



A Concentrated Wound Interior Permanent Magnet Machine for Direct-Drive Wind Turbine Applications

Author:

Ahsanullah, Kazi

Publication Date:

2015

DOI:

<https://doi.org/10.26190/unsworks/18391>

License:

<https://creativecommons.org/licenses/by-nc-nd/3.0/au/>

Link to license to see what you are allowed to do with this resource.

Downloaded from <http://hdl.handle.net/1959.4/54902> in <https://unsworks.unsw.edu.au> on 2024-04-27

A Concentrated Wound Interior Permanent Magnet Machine for Direct- Drive Wind Turbine Applications



By

Kazi Ahsanullah

A thesis submitted to

THE UNIVERSITY OF NEW SOUTH WALES

in partial fulfilment of the

requirements for the degree of

Doctor of Philosophy

School of Electrical Engineering and Telecommunications
March, 2015

PLEASE TYPE

THE UNIVERSITY OF NEW SOUTH WALES
Thesis/Dissertation Sheet

Surname or Family name: Ahsanullah

First name: Kazi

Other name/s:

Abbreviation for degree as given in the University calendar: PhD

School: Electrical Engineering & Telecommunications

Faculty: Engineering

Title: A Concentrated Wound Interior Permanent Magnet
Machine for Direct-Drive Wind Turbine Applications

Abstract 350 words maximum: (PLEASE TYPE)

In direct-drive wind turbine systems, intermediate gearboxes are eliminated to increase the efficiency and reliability of the system. This also reduces maintenance downtimes. The direct-drives necessitate the generator to have a low rated speed. Therefore, permanent magnet machines with high number of poles are favourable for direct-drive wind turbine applications. An interior PM synchronous machine (IPMM) offers a number of advantages such as the availability of reluctance torque, extended constant power speed range. These machines also present an economic edge with the reduced use of expensive rare earth magnet materials. This makes this IPM machine a promising candidate for direct drive wind turbine application.

This thesis presents a systematic approach to design an interior permanent magnet machine with concentrated windings for direct-drive wind turbine applications. The initial phase of this work investigates and compares the performances of the interior PM synchronous machine with fractional-slot concentrated winding and the distributed winding in stators and the flat-shaped or V-shaped magnets in the rotor respectively. The design criteria are set to achieve a low cogging torque, low torque ripple, and high efficiency. The cogging torque and the torque ripple are reduced by improving the rotor and stator geometry utilizing the Finite Element Analysis. It was found that the fractional-slot concentrated wound interior permanent magnet synchronous machine can provide comparable performance as that of a distributed wound interior permanent magnet synchronous machine and even perform better on attributes like the cogging torque, power density, torque ripple and the copper loss. The fractional-slot concentrated wound interior permanent magnet synchronous machine with flat-shaped magnet structure is constructed to validate the findings experimentally.

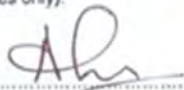
This thesis is the only detailed literature so far that investigates and presents experimental validation of the performance of a fractional-slot concentrated wound interior permanent magnet synchronous machine as a generator for direct-drive wind turbine system. This thesis also analyzes the dynamic performance of the prototype machine. The result shows that the existing dynamic control strategies of the distributed wound IPM machine can be easily adopted in a concentrated wound IPMM without any significant changes.

The work done in this thesis creates a strong benchmark for future work on fractional-slot concentrated wound IPM machines suitable for direct-drive wind turbine application

Declaration relating to disposition of project thesis/dissertation

I hereby grant to the University of New South Wales or its agents the right to archive and to make available my thesis or dissertation in whole or in part in the University libraries in all forms of media, now or here after known, subject to the provisions of the Copyright Act 1968. I retain all property rights, such as patent rights. I also retain the right to use in future works (such as articles or books) all or part of this thesis or dissertation.

I also authorise University Microfilms to use the 350 word abstract of my thesis in Dissertation Abstracts International (this is applicable to doctoral theses only).


Signature


Witness

24/08/15
Date

The University recognises that there may be exceptional circumstances requiring restrictions on copying or conditions on use. Requests for restriction for a period of up to 2 years must be made in writing. Requests for a longer period of restriction may be considered in exceptional circumstances and require the approval of the Dean of Graduate Research.

FOR OFFICE USE ONLY

Date of completion of requirements for Award:

THIS SHEET IS TO BE GLUED TO THE INSIDE FRONT COVER OF THE THESIS

CERTIFICATE OF ORIGINALITY

I hereby declare that this submission is my work and to the best of my knowledge it contains no material previously published or written by another person, nor material which to a substantial extent has been accepted for the award of any other degree or diploma at UNSW or any other educational institution, except where due acknowledgment is made in the thesis. Any contribution made to the research by others, with whom I have worked at UNSW or elsewhere, is explicitly acknowledged in the thesis. I also declare that the intellectual content of this thesis is the product of my own work, except to the extent that assistance from others in the project's design and conception or in style, presentation and linguistic expression is acknowledged.

Signed..........
Date.....24/08/15.....

ACKNOWLEDGEMENTS

I would like to express my sincere gratitude to my team of supervisors-my herculean mentors- Prof. Faz Rahman and Dr. Rukmi Dutta for their valuable guidance, encouragement and financial support, without which this would never have become a reality. Their dedication and a keen interest to help their students had been the sole reason for completing my work on time. They gave me the opportunity to perform research work of my interest, for which I will be forever grateful.

This thesis is dedicated to my mother who passed away battling cancer. This one is for you mom!

I would like to gratefully acknowledge various people who have been my support system in recent years as I have worked on this research. First, I owe an enormous debt of gratitude to my father, my two sisters, Meghna and Samiya, my niece, Mahira and my cousin Rezwan. Through the struggles and trials of this thesis, they have been a constant source of joy. I am also indebted to my grandmother, who passed away the very year I started my research. She raised and fed me with the life knowledge to become the person I am.

I am very grateful to the wonderful laboratory staff in the group of Power Electronics and Drives, especially Mr. Liyadipitiya Gamini, Mr. Puthanveetil Subash and Mr. Liu Zhenyu for their untiring support, guidance and valuable comments that benefited the completion and success of this study. Special acknowledgement is given to Dr. Dan Xiao for his constant support and suggestions during the experimental setup. I am very grateful to all my colleagues in the Energy Systems Research Group at the School of Electrical Engineering and Telecommunications, UNSW for their cooperation and helpful discussions: Mohammad Farshadnia, Ali Cheema, Hansika Ratnayake, Merlin Chai, Dr. Dai Nguyen, David Tan, Alan Quan, Ali Reza etc. I gratefully acknowledge the help and input from Dr. Howard Lovatt (CSIRO) and Mr. Karl Wilson (CSIRO) during the construction of the prototype machine.

I also take this opportunity to thank my friends for bearing with me through the rough patches. Their relentless encouragement has helped me keep focusing on my goals.

Lastly, and most of all, I would like to begin and end in the name of Allah, most gracious, most merciful. It has been both a delight and privilege to have fused together research with creation.

ABSTRACT

In direct-drive wind turbine systems, intermediate gearboxes are eliminated to increase the efficiency and reliability of the system. This also reduces maintenance downtimes. The direct-drives necessitate the generator to have a low rated speed. Therefore, permanent magnet machines with high number of poles are favourable for direct-drive wind turbine applications. An interior PM synchronous machine (IPMM) offers a number of advantages such as the availability of reluctance torque, extended constant power speed range. These machines also present an economic edge with the reduced use of expensive rare earth magnet materials. This makes this IPM machine a promising candidate for direct drive wind turbine application.

This thesis presents a systematic approach to design an interior permanent magnet machine with concentrated windings for direct-drive wind turbine applications. The initial phase of this work investigates and compares the performances of the interior PM synchronous machine with fractional-slot concentrated winding and the distributed winding in stators and the flat-shaped or V-shaped magnets in the rotor respectively. The design criteria are set to achieve a low cogging torque, low torque ripple, and high efficiency. The cogging torque and the torque ripple are reduced by improving the rotor and stator geometry utilizing the Finite Element Analysis. It was found that the fractional-slot concentrated wound interior permanent magnet synchronous machine can provide comparable performance as that of a distributed wound interior permanent magnet synchronous machine and even perform better on attributes like the cogging torque, power density, torque ripple and the copper loss. The fractional-slot concentrated wound interior permanent magnet synchronous machine with flat-shaped magnet structure is constructed to validate the findings experimentally.

ABSTRACT

This thesis is the only detailed literature so far that investigates and presents experimental validation of the performance of a fractional-slot concentrated wound interior permanent magnet synchronous machine as a generator for direct-drive wind turbine system. This thesis also analyzes the dynamic performance of the prototype machine. The result shows that the existing dynamic control strategies of the distributed wound IPM machine can be easily adopted in a concentrated wound IPMM without any significant changes.

The work done in this thesis creates a strong benchmark for future work on fractional-slot concentrated wound IPM machines suitable for direct-drive wind turbine application.

Table of contents

ACKNOWLEDGEMENTS.....	iv
ABSTRACT.....	v
TABLE OF CONTENTS	vii
LIST OF FIGURES.....	xii
LIST OF TABLES	xxii
Nomenclature	xxiv
Abbreviations	xxxii
CHAPTER 1: Introduction	1
1.1 General Background	1
1.2 Direct-Drive & Geared Generator System.....	3
1.3 Motivations	8
1.4 Research Objectives	11
1.5 Main contributions	12
1.6 Outline of Thesis.....	13
CHAPTER 2: Literature Review	15
2.1 Introduction.....	15
2.2 Wind Turbine Topology.....	15
2.2.1 Wind Energy	15
2.2.2 HAWT (lift type)	16
2.2.3 VAWT.....	17
2.3 PM Generators for Wind Application.....	20
2.3.1 PMSG's category with respect to the flux path	20
2.3.2 PMSG's category with respect to magnet structure	25
2.4 General background of Interior Permanent Magnet Machines	27
2.5 IPMM for wind turbine applications.....	30
2.6 Interior permanent magnet topology.....	32
2.7 Distributed and Concentrated windings	33
2.8 Finite Element Method (FEM).....	35
2.8.1 Mathematical formulations of the Physical Model	36
2.8.2 Mesh Formation.....	38

2.8.3	Boundary Conditions	40
2.8.4	Matrix Equations of Elements.....	42
2.8.5	Solving Finite Element Equations.....	44
2.9	FEA for determining the Machine Parameters and characteristics of the IPMM	44
2.9.1	Construction of the geometry and assigning the mesh.....	44
2.9.2	Assigning Physics	46
2.9.3	External Electric circuit	48
2.9.4	Parameter Calculation	49
2.10	Conclusion	53
CHAPTER 3: Design of a High-Pole Number IPMM with Distributed		
Windings		
		54
3.1	Introduction.....	54
3.2	Initial analysis of a 4-pole IPMM configuration.....	54
3.3	42 pole IPMM with Distributed windings (DW)	61
3.3.1	Selection of rotor design	63
3.3.2	Air-gap length and Aspect ratio	65
3.3.3	Stator design.....	65
3.3.4	Selection of Magnet structure	67
3.3.5	Selection of pole magnet configuration	69
3.3.6	Minimization of Cogging torque.....	73
3.3.7	Design optimization for low Cogging torque.....	75
3.3.8	Torque ripple minimization	77
3.3.9	Simulation results.....	83
3.3.10	Losses in the DW IPMM	86
3.3.11	Inductance and saliency ratio of the DW IPMM	89
3.4	Conclusion	91
CHAPTER 4: Design of a High-Pole Number IPMM with Fractional-Slot		
Concentrated Wound Stator.....		
		93
4.1	Introduction.....	93
4.2	Fractional-Slot Concentrated winding (CW) and its structure.....	93
4.3	Performance analysis of using FSCW over DW	96
4.3.1	Choice of slot and pole combination.....	98
4.3.2	Winding factor	101
4.3.3	MMF	106
4.4	42 pole IPMM with Concentrated windings	108

4.4.1	Stator design for FSCW IPMM	109
4.4.2	Winding layout of the FSCW IPMM	109
4.4.3	Cogging torque optimization for FSCW IPMM	111
4.4.4	Torque ripple minimization for FSCW IPMM	113
4.4.5	Comparison of FSCW IPMM and DW IPMM	118
4.4.6	Efficiency	121
4.4.7	Inductance and saliency ratio comparison between DW and FSCW IPMM's ..	122
4.5	Conclusion	127
CHAPTER 5: Final Design Selection and Prototyping of the		
FSCW IPMM-F.....		
		129
5.1	Introduction.....	129
5.2	Choice of materials	129
5.2.1	Core material.....	130
5.2.2	Selection of Permanent Magnet material	136
5.2.3	Stator coil	141
5.3	Final winding Configuration.....	145
5.3.1	End winding inductance.....	146
5.3.2	Slot fill factor	148
5.4	Rotor of the final design.....	149
5.5	3-D FEA of the FSCW IPMM-F design	150
5.6	Mechanical stress analysis	152
5.7	Final FSCW IPMM-F design.....	155
5.8	Losses of the final design.....	158
5.8.1	Mechanical losses	158
5.8.2	Magnet losses	162
5.8.3	Stray load loss	165
5.8.4	Final Efficiency for the FSCW IPMM-F	167
5.9	Conclusion	169
CHAPTER 6: Experimental Verification of the Steady State Performance		
of the Prototype FSCW IPMM-F.....		
		170
6.1	Introduction.....	170
6.2	Open Circuit Parameters	170
6.2.1	PM Flux Linkage	174
6.2.2	Friction co-efficient and Rotor Inertia	174
6.2.3	Cogging torque.....	176

6.3	Developed Torque.....	180
6.4	Inductance and Saliency ratio	182
6.5	Generator Efficiency	186
6.6	Conclusion	190
CHAPTER 7: Dynamic Performance of the Prototype		
FSCW IPMM-F.....		191
7.1	Introduction.....	191
7.2	Flux oriented control.....	192
7.2.1	Effect of current angle variation	194
7.2.2	The d - q current plane	195
7.2.3	Circle diagram.....	196
7.3	Maximum torque Per Ampere (MTPA):.....	197
7.4	Field weakening region.....	199
7.5	Transition of control modes	203
7.6	De-coupling current controllers	203
7.7	Control as a Generator	204
7.8	MTPA control during motoring condition	205
7.9	Generation.....	207
7.9.1	MTPA control during generating condition:.....	210
7.9.2	FW control during generating condition:.....	212
7.10	Wind profile simulation using back-to-back PWM converter	214
7.11	Conclusion	221
CHAPTER 8: Conclusion and Future Works.....		222
8.1	Conclusions.....	222
8.2	Future Works	225
Reference		227
Appendix A: Loss Minimization Control and Modelling in MATLAB-SIMULINK.....		241
A.1	Loss minimization.....	241
A.2	Core loss resistance.....	242
A.3	Control algorithm for LM.....	243
A.4	Loss minimization control during motoring condition	246
A.5	Modelling in Matlab-Simulink for various control strategies	247
Appendix B: Construction Process of the 42 pole FSCW IPMM-F		249

B.1	Construction Process.....	249
Appendix C: Thermal stress analysis.....		255
Appendix D: Search coils in the winding		258
D.1	Search coils	258
D.2	Phase voltage measurement using search coils.....	259
Appendix E: Final Machine Drawings.....		261
E.1	3-D view of the FSCW IPMM-F	261
E.2	Rotor of the FSCW IPMM-F	262
E.3	Stator of the FSCW IPMM-F.....	263
E.4	Cover plate of the FSCW IPMM-F.....	264
E.5	End plate front of the FSCW IPMM-F	265
E.6	End plate back of the FSCW IPMM-F.....	266
E.7	Shaft of the FSCW IPMM-F.....	267
E.8	Encoder Mount and Keeper plate of the FSCW IPMM-F	268
Appendix F: Space Vector Modulation		269
F.1	Drive system	269
F.2	Space Vector Modulation scheme.....	271
Appendix G: Experimental setup.....		274
G.1	The Experimental setup	274
G.2	Regenerative Dynamometer System.....	276
G.3	Mechanical Drawing of the MEA loading motor	280
G.4	Initial Displacement Angle between the Rotor and Incremental Encoder	281
G.5	Control algorithm.....	282
G.6	3-phase IGBT inverter	287
Appendix H: Publication list		290

LIST OF FIGURES

Fig. 1.1	Generic generator types for wind turbine application	2
Fig. 1.2	Various wind turbine topology	4
Fig. 1.3	Drive-train topology	5
Fig. 1.4	Converter system for the PMSG	6
Fig. 2.1	C_p Versus λ of a HAWT for various pitch angles	17
Fig. 2.2	Power curve of HAWT when $\beta=0^\circ$	17
Fig. 2.3	Various VAWT topologies: (a) Savonius wind turbine; (b) Darrieus wind turbine and (c) H-rotor wind turbine	18
Fig. 2.4	C_p Versus λ of an H-Rotor VAWT	19
Fig. 2.5	Power Curve for the H-rotor VAWT	19
Fig. 2.6	Various rotor configurations of PM machines	20
Fig. 2.7	PM machine rotor according to magnet structure	26
Fig. 2.8	Magnetic flux paths of an IPMM in (a) d-axis and (b) q-axis	28
Fig. 2.9	Wind energy conversion system using IPM machine	31
Fig. 2.10	Various Magnet structure of the IPMM	33
Fig. 2.11	(a) Distributed and (b) Concentrated winding structure	34
Fig. 2.12	Typical elements used for mesh formation in FEA	39
Fig. 2.13	1/4th of a 4 pole IPMM displaying the nodes and Dirichlet's boundary	41
Fig. 2.14	IPMM with quarter cyclic-symmetry	42
Fig. 2.15	Distributed and Concentrated Wound 42 pole IPMM	45
Fig. 2.16	Meshing of the prototype 42 pole IPMM	46
Fig. 2.17	Magnetic property of (a) Soft magnetic material and (b) Permanent Magnet	47
Fig. 2.18	Current excitation circuit in FEA	49
Fig. 2.19	Flow chart for the time-stepping finite element process	50
Fig. 2.20	EMF circuit in FEA	51
Fig. 2.21	Meshing of a 3-layer air-gap	52

Fig. 3.1	4 pole IPM machines with (a) Flat-shaped Magnets ; (b) V-shaped Magnets and (c) Segmented Magnets	55
Fig. 3.2	Flux distribution of a four pole segmented IPMM (one pole)	57
Fig. 3.3	Air-gap flux density of a 4 pole non-segmented IPMM, Segmented IPMM and a V-shaped IPMM	57
Fig. 3.4	Cogging torque comparison between the 4 pole non-segmented, segmented and the V-shaped IPMM	58
Fig. 3.5	Flux distribution of V-shaped IPMM's for various V-angles	59
Fig. 3.6	Air-gap flux density of a V-shaped IPMM for various V-angles (30°,60°,90°,130°,155°)	60
Fig. 3.7	FFT spectrum of the air-gap Flux density of 4 pole V-shaped IPMM	60
Fig. 3.8	Variation in cogging torque with the change in V-angle for the V-shaped IPMM	61
Fig. 3.9	Winding layout of (a) Full pitch DW and (b) 1 slot short pitch DW	66
Fig. 3.10	Slot dimension of the DW IPMM	68
Fig. 3.11	One pole of the flat shaped DW IPMM showing flux density in various regions with color shades.	69
Fig. 3.12	Cross-sectional view of (a) DW IPMM-F and (b) DW IPMM-V	70
Fig. 3.13	Change in peak Air-gap flux density and Cogging torque with the variation in IPMM rotor structures with magnet arc angle being constant	71
Fig. 3.14	(a)Variation in air-gap flux density with the variation in IPMM rotor structures with constant magnet volume while varying the magnet arc angle; (b) Peak air-gap flux density (Zoomed in)	72
Fig. 3.15	Change in peak Air-gap flux density and Cogging torque with the variation in IPMM rotor structures with constant magnet volume while varying the magnet arc angle	72
Fig. 3.16	Cogging torque in PM machines	75
Fig. 3.17	Cogging torque of D-1 and D-2	76
Fig. 3.18	Flux barrier designs	78
Fig. 3.19	Variations in torque ripple with the change in flux barrier design and slot opening for D-1	78
Fig. 3.20	Air-gap flux density of the prototype machine for three flux barrier designs mentioned in Fig. 3.18	79
Fig. 3.21	FFT analysis of air-gap flux density for D-1 with a flux barrier Design 'B' at various slot openings.	80
Fig. 3.22	Variations in torque ripple with the change in flux barrier design and slot opening	80

	for D-2	
Fig. 3.23	Variation in 6th and 12th order torque ripple with the change in the number of conductors per slot (N)	82
Fig. 3.24	FFT of the developed torque for D-1 when N=6 and N=7	82
Fig. 3.25	FFT of the developed torque for D-2 when N=6 and N=7	82
Fig. 3.26	Air-gap flux density of D-1 & D-2	84
Fig. 3.27	Line-Line Back EMF	84
Fig. 3.28	Spectrum analysis of the L-L EMF of D-1 and D-2	84
Fig. 3.29	Total developed torque	85
Fig. 3.30	FFT of the developed torque	86
Fig. 3.31	Variation in peak electrodynamic torque with respect to the torque angle for D-1	86
Fig. 3.32	(a) B-H characteristics curve and (b) loss characteristics of non-oriented silicon steel M270-35A	87
Fig. 3.33	Individual loss elements of the Bertotti loss model using M270-35A silicon steel for D-1	88
Fig. 3.34	Cu. losses & Iron losses versus percentage of loading for D-1	89
Fig. 3.35.	Cu. losses & Iron losses versus percentage of loading for D-2	89
Fig. 3.36	Efficiency versus P.U. of rated speed for DW IPMM-F (black) and DW IPMM-V (blue)	89
Fig. 3.37	42-pole DW IPMM-F with flux being channeled to (a) d-axis and (b) q-axis	90
Fig. 3.38	Basic phasor diagram of the IPM machine	91
Fig. 4.1	Single layer and double layer concentrated winding layout	95
Fig. 4.2	Modular concentrated winding layout	95
Fig. 4.3	54-slot, 42 pole single-layer FSCW design	96
Fig. 4.4	54-slot, 42 pole double-layer FSCW design	96
Fig. 4.5	Configuration of IPMM with (a) Distributed windings and (b) Concentrated winding structure	97
Fig. 4.6	A 2 pole (a) Distributed winding structure and (b) Concentrated winding structure	98
Fig. 4.7	42 pole IPMM with various slot and pole combinations in FSCW layout	99
Fig. 4.8	An IPMM with $1/7 S_{pp}$ showing a stator pole	100

Fig. 4.9	Cogging torque of the 42 pole IPMM with various S_{pp} combinations.	100
Fig. 4.10	(a) 18-slot,14 pole IPMM showing phase coils and (b) Phasor diagram indicating the construction of each phasor using EMF phasor diagram	102
Fig. 4.11	Winding factor for $2/5 S_{pp}$	103
Fig. 4.12	Winding factor for $3/7 S_{pp}$	104
Fig. 4.13	Winding factor for $3/8 S_{pp}$	104
Fig. 4.14	MMF obtained by FEA for various slots and poles combination	107
Fig. 4.15	MMF harmonic spectrum for DW IPMM-F and FSCW IPMM-F	108
Fig. 4.16	Flux distribution of a portion of (a) FSCW IPMM-F and (b) FSCW IPMM-V with V-angle of 120°	109
Fig. 4.17	Slot and air-gap dimension of the FSCW IPMM	110
Fig. 4.18	Winding layout for 42 pole FSCW IPMM	111
Fig. 4.19	Cogging torque of FSCW IPMM's	113
Fig. 4.20	Cross-sectional view of a flat shaped IPMM with different flux barrier shapes	115
Fig. 4.21	Rotor air-gap field for various flux barriers in the FSCW IPMM-F	115
Fig. 4.22	Variation in torque ripple with the change in slot openings in the stator slots for the FSCW IPMM-F	116
Fig. 4.23	Variation in torque ripple with the change in slot openings in the stator slots for the FSCW IPMM-V	117
Fig. 4.24	Flux density in the tooth of the stator for (a) DW IPMM-F and (b) FSCW IPMM-F	119
Fig. 4.25	L-L Back EMF of DW IPMM-F, FSCW IPMM-F, and FSCW IPMM-V	120
Fig. 4.26	Spectrum analysis of DW IPMM-F, FSCW IPMM-F, and FSCW IPMM-V	120
Fig. 4.27	Total developed torque of DW IPMM-F, FSCW IPMM-F and FSCW IPMM-V	120
Fig. 4.28	FFT analysis of developed torque for the DW IPMM-F, FSCW IPMM-F, and FSCW IPMM-V	121
Fig. 4.29	Cu. losses & Iron losses versus percentage of loading for FSCW IPMM-F	121
Fig. 4.30	Cu. losses & Iron losses versus percentage of loading for FSCW IPMM-V	122
Fig. 4.31	Efficiency versus P.U. of rated speed for DW IPMM-F and FSCW IPMM-F	122
Fig. 4.32	Circuit for AC standstill test for the DW IPMM-F	123
Fig. 4.33	Self-inductance of the DW IPMM-F, FSCW IPMM-F, and FSCW IPMM-V	125
Fig. 4.34	Mutual-inductance of the DW IPMM-F, FSCW IPMM-F, and FSCW IPMM-V	125

Fig. 4.35	Harmonics of self and mutual inductance	125
Fig. 5.1	B-H characteristics curves of 35CS300 and 50CS350 (Manufacturer datasheet)	130
Fig. 5.2	Loss characteristics curve for the 35CS300 and the 50CS350	131
Fig. 5.3	Core loss and efficiency for FSCW IPMM-F with two different core materials	132
Fig. 5.4	Individual loss elements of the Bertotti loss model using 50CS350 silicon steel	133
Fig. 5.5	B-H loop of typical non-oriented silicon steel (Bipolar curve)	133
Fig. 5.6	The steel tester method	133
Fig. 5.7	Copper wound toroid	134
Fig. 5.8	Experimental hysteresis loop of 50CS350	135
Fig. 5.9	Experimental B-H characteristics curve of 50CS350	135
Fig. 5.10	Flux density in various segments of the prototype FSCW IPMM-F using different core materials	136
Fig. 5.11	B-H Hysteresis loop for a permanent magnet	137
Fig. 5.12	(a) Effect of temperature on PM demagnetization curve, (b) Demagnetization curves of standard permanent magnets at 20° C	137
Fig. 5.13	NdFeB 32SH coercivity versus the change in i_d current	138
Fig. 5.14	Dimension of each Magnet piece for the prototype FSCW IPMM-F	139
Fig. 5.15	Magnet Fields for various magnets at 2m and 4m distance	140
Fig. 5.16	Effect on Flux density and L-L voltage of FSCW IPMM-F with the change in B_r	141
Fig. 5.17	A portion of FSCW IPMM-F showing the orientation of the magnets	142
Fig. 5.18	Winding with a 0.6 mm copper wire for double layer CW stator	143
Fig. 5.19	Resistivities of selected metals	144
Fig. 5.20	Resistance per phase as temperature increases for the FSCW IPMM-F	144
Fig. 5.21	Slot dimension of the final FSCW IPMM-F design	145
Fig. 5.22	Winding layout of the FSCW IPMM-F	145
Fig. 5.23	Estimated End winding length for (a) Single layer DW; (b) Single layer CW and (c) Double layer CW	146
Fig. 5.24	(a) Dimension of an end winding and (b) End winding of the FSCW IPMM-F (side view)	147
Fig. 5.25	Manual winding methods	149

Fig. 5.26	Position of magnet in the rotor for the FSCW IPMM-F (all values are in mm)	150
Fig. 5.27	3-D model of the FSCW IPMM-F	151
Fig. 5.28	Flux density and its FFT analysis of the FSCW IPMM-F using 3-D FEA	151
Fig. 5.29	Flux density in the z-axis direction of the FSCW IPMM-F using 3-D FEA	152
Fig. 5.30	Deflection Contour of the FSCW IPMM-F	153
Fig. 5.31	VON-MISES Stress and SHEAR Stress for rotor core and Magnets of the FSCW IPMM-F at Rated Speed (Fig. a & b); 4500 rpm (Fig. c & d)	154
Fig. 5.32	Flux density of the Final design (FSCW IPMM-F) conducted in FEA	156
Fig. 5.33	Cogging torque of the Final design	156
Fig. 5.34	(a) L-L Back EMF & (b) FFT analysis of the L-L and phase Back EMF of the Final Design	156
Fig. 5.35	Losses in an IPM machine	158
Fig. 5.36	Drawing of the rotor and bearings to calculate the bearing friction loss	160
Fig. 5.37	Power loss due to bearing friction at various speeds	160
Fig. 5.38	Hysteresis and eddy current loss for sintered NdFeB at 50 Hz	164
Fig. 5.39	Extrapolated values of measured hysteresis and eddy current loss	164
Fig. 5.40	Magnet eddy current losses at various frequencies with the variation in the number of segment in the magnets.	164
Fig. 5.41	Magnet losses versus frequency in the final design of the FSCW IPMM-F	165
Fig. 5.42	Ratio of R_{ac}/R_{dc} versus frequency for different sizes of copper wire (at 25°C)	167
Fig. 5.43	Various losses of the prototype at different load setting during rated speed condition	167
Fig. 5.44	Surface plot of the efficiency at rated speed for the FSCW IPMM-F	168
Fig. 5.45	(a) Power loss of the FSCW IPMM-F at full load with the variation in speed; (b) Variation in efficiency with the change in speed for full- and half load	168
Fig. 6.1	The electro-dynamometer coupled to the prototype FSCW IPMM-F	171
Fig. 6.2	Experimental setup to determine the new machine parameters	171
Fig. 6.3	Phase voltage of the prototype	172
Fig. 6.4	Frequency spectrum of the phase voltage for the prototype	172
Fig. 6.5	Three phase voltages of the prototype	173
Fig. 6.6	Frequency spectrum of the L-L voltage for the prototype	173

Fig 6.7	Phase voltage versus Speed of the prototype	174
Fig. 6.8(a)	Power versus square of the speed of the prototype	175
Fig. 6.8(b)	Rotational speed from rated to zero with respect to time	175
Fig. 6.9	Static measurement test to obtain cogging torque	176
Fig. 6.10	Experimental setup for cogging torque measurement	178
Fig. 6.11	Measured cogging torque for various rotor positions	179
Fig. 6.12	Curve fitted cogging torque waveform	179
Fig. 6.13	Developed Electromagnetic Torque (Experimental)	180
Fig. 6.14	FFT spectrum of Electromagnetic Torque (Experimental)	181
Fig. 6.15	Developed torque of the prototype in FE	181
Fig. 6.16	3-phase current waveform of the prototype FSCW IPMM-F – (a) During motoring at full load and rated speed; (b) During generating at full load and rated speed; (c) During motoring at half load and rated speed; (d) During generating at half load and rated speed; (e) During motoring at full load and half the rated speed; & (f) During generating at full load and half the rated speed	183
Fig. 6.17	Locking mechanism for the AC standstill saliency test	184
Fig. 6.18	Self- and mutual-inductance waveform of the FSCW IPMM-F at rated current	184
Fig. 6.19	Phase voltage and current during AC standstill saliency test	185
Fig. 6.20	FFT spectrum of phase voltage and current during AC standstill saliency test	186
Fig. 6.21	Variation in d - and q -axis inductances and saliency with the change in phase current	186
Fig. 6.22	Efficiency calculation of the CW IPMM for three different rotating speed	188
Fig. 6.23	Efficiency map of the CW IPMM during generating condition	188
Fig. 6.24	Iron and Mechanical loss of the prototype CW IPMM	189
Fig. 6.25	Power loss of the prototype CW IPMM at rated speed	189
Fig. 7.1	Reference frame for a 4-pole IPM machine	191
Fig. 7.2	Equivalent circuit of an IPMM	192
Fig. 7.3	Calculated torque comprising of alignment and reluctance torque from Eq. (7.4)	193
Fig. 7.4	Block diagram of Flux oriented control (FOC)	194
Fig. 7.5	Steady-State Space vector d - and q -axis phasor diagram	194
Fig. 7.6	Constant-torque loci of an IPMM	195

Fig. 7.7	Voltage limit ellipses and current limit circle of an IPMM	197
Fig. 7.8	Circle diagram showing torque hyperbolas	198
Fig. 7.9	Vector control during field-weakening	200
Fig. 7.10	Classification of IPM machine type by characteristic current; (a) Circle diagram for Type-1 IPMM; (b) Circle diagram for Type-2 IPMM	202
Fig. 7.11	FOC control algorithm	203
Fig. 7.12	Decoupling current controllers	203
Fig. 7.13	Block diagram of the FOC scheme during generation	205
Fig. 7.14	Speed response for speed step of -100 to 100rpm	206
Fig. 7.15	q - axis current response for speed step of -100 to 100rpm	206
Fig. 7.16	MTPA trajectory achieved experimentally (Blue points) with the current trajectory obtained analytically	206
Fig. 7.17	Overall system efficiency and CW IPMM efficiency during MTPA operation during motoring	207
Fig. 7.18	Experimental setup for generation	208
Fig. 7.19	Measured response of the DC bus for a load step change from no load to full load	208
Fig. 7.20	Measured response of i_q for a load step change from no load to full load	209
Fig. 7.21	Measured response of i_d for a load step change from no load to full load	209
Fig. 7.22	Torque transient when the prototype CW-IPMM is loaded from zero to full load at rated speed	209
Fig. 7.23	DC bus response for speed step change of 80 to 120 rpm	210
Fig. 7.24	i_d and i_q current response for speed step change of 80 to 120 rpm	211
Fig. 7.25	MTPA current trajectory from experiment during generation	211
Fig. 7.26	Efficiency calculation of the FSCW IPMM with MTPA during generation	211
Fig. 7.27	Field-weakening current trajectory from experiment during generation	212
Fig. 7.28	Outcome of terminal voltage and torque with increasing speed	213
Fig. 7.29	Field-weakening range of the prototype IPMM (Experimental)	213
Fig. 7.30	Field-weakening range of the FSCW IPMM-F conducted in FEA	214
Fig. 7.31	Schematic diagram of the FSCW IPMM-F controlled by a back-to-back PWM converter	215

Fig. 7.32	(a) Wind turbine power versus shaft speed for various wind speed; (b) Power-wind speed of a typical small wind turbine generator	216
Fig. 7.33	Variation in power and torque with respect to speed	217
Fig. 7.34	Efficiency and L-L voltage	217
Fig. 7.35	Change in d - and q -axis current of the FSCW IPMM-F	218
Fig. 7.36	Step change in speed at full load	218
Fig. 7.37	d - and q -axis current during step change in speed from 62 RPM -143 RPM	219
Fig. 7.38	Dynamic performances at 143 RPM with load disturbances	219
Fig. 7.39	(a) Grid side phase current during load disturbance; (b) Magnified portion of the box shown in (a)	220
Fig. 7.40	Response of the IPMM with a rapid change from generating to motoring action	220
Fig. A.1	Equivalent circuit of the IPMM taking into account the iron loss resistance	241
Fig. A.2	Electrical losses with varying i_{od} under different loading conditions for the prototype IPMM	245
Fig. A.3	i_q versus i_d for different torque conditions during LM control	245
Fig. A.4	LM trajectory achieved experimentally (Blue points) with current trajectory	247
Fig. A.5	Efficiency calculation of the FSCW IPMM-F during LM operation and when $i_d=0$	247
Fig. A.6	MTPA operation in generating mode for CW IPMM implemented in MATLAB-Simulink	248
Fig. A.7	Variation in i_d - i_q current with respect to the developed torque during MTPA condition	248
Fig. B.1	Steps of the Construction process	249
Fig. B.2	Final rotor configuration	251
Fig. B.3	Laser cut rotor and stator laminations	252
Fig. B.4	Stacking of all rotor laminations	252
Fig. B.5	Position of search coils, thermistor, and leads in the CW slot layout	253
Fig. B.6	Complete winding of the stator	253
Fig. B.7	FSCW IPMM-F machine assembly	254
Fig. C.1	Lumped parameter network of the FSCW IPMM-F showing the temperature of various nodes	256
Fig. C.2	Change in stator laminations temperature with respect to time (measured	257

	experimentally)	
Fig. D.1	Arrangement of search coils for (a) d,q axis search coils and (b) Leakage search coils	259
Fig. E.1	3-D view of the FSCW IPMM-F	261
Fig. F.1	Schematic diagram of the IPMM during motoring operation	269
Fig. F.2	Schematic diagram of the FSCW IPMM-F generator system	270
Fig. F.3	Schematic diagram of the FSCW IPMM-F connected to back-to-back inverters	270
Fig. F.4	Phase voltage space vectors	271
Fig. F.5	Switching pattern for sector 1	273
Fig. G.1	Complete experimental setup	275
Fig. G.2	<i>d-space control desk</i>	276
Fig. G.3	Loading motor	277
Fig. G.4	Screen shot of Torque mode option available in MEA RDS	279
Fig. G.5	Measured line-to-line back emf of the prototype FSCW IPMM-F at 143 rpm	281
Fig. G.6	Back-to-back 3-phase IGBT inverter (casing off)	287
Fig. G.7	IGBT inverter schematic	288
Fig. G.8	Interconnection between the IGBT inverter and the control boards	289

LIST OF TABLES

Table 1.1	Commercial Wind Turbine with Synchronous Machine	7
Table 1.2	Three types of generators used for large Wind Turbines	8
Table 2.1	Design parameters of the H-rotor wind turbine	18
Table 2.2	Steps for analyzing a domain in FEM	36
Table 2.3	Material of each region	47
Table 2.4	Mechanical set for the region during FEA	48
Table 3.1	Main dimension of the 4 pole IPMM with DW	56
Table 3.2	Variation in flux density, Cogging torque and EMF by varying the pitch in DW	66
Table 3.3	Permitted flux densities for standard salient-pole synchronous machines	68
Table 3.4	Main dimension of the DW IPMM	70
Table 3.5	Effect of cogging torque with the variation in magnet arc length	76
Table 3.6	Difference in volume for both the DW IPMM's	77
Table 3.7	Variation in torque ripple with the change in shoe thickness for D-1	83
Table 3.8	Key parameters of the DW IPMM	84
Table 4.1	Winding functions for different S_{pp}	103
Table 4.2	Winding factor for different S_{pp}	105
Table 4.3	Induced EMF and winding factor for different combinations of S_{pp} and winding type	105
Table 4.4	Change in the cogging torque with respect to the variations in magnet length for the FSCW IPMM-F	112
Table 4.5	Change in the cogging torque with respect to the magnet length for FSCW IPMM-V	112
Table 4.6	Change in torque ripple with the change in flux barrier shape and size for FSCW IPMM-F	116
Table 4.7	Magnet area, Flux barrier design, Slot opening, Cogging torque, Torque ripple and peak air-gap flux density for all of the four designed machines	117
Table 4.8	Output Parameters for DW IPMM-F, FSCW IPMM-F, and FSCW IPMM-V	119
Table 4.9	Inductance and saliency of DW IPMM-F, FSCW IPMM-F, and FSCW IPMM-V	127
Table 5.1	Properties of compared core grades	131

Table 5.2	Properties of various PM's	138
Table 5.3	Testing of individual magnets using HALL probes	140
Table 5.4	Change in Fundamental component of flux density and the L-L voltage of FSCW IPMM-F with the change in B_r	141
Table 5.5	Mechanical stress limit for the rotor core	154
Table 5.6	Specifications of the final design	157
Table 5.7	Reynolds number, torque coefficient and winding loss at various speeds	161
Table 6.1	Components associated with the experimental setup	171
Table 6.2	d- and q- axis inductances at this rated condition	184
Table 7.1	Maximum speed for flux weakening	214
Table B.1	Variation in torque and power with the change in the tolerance across each magnet	250
Table C.1	Specifications for thermal modelling of the FSCW IPMM-F	255
Table C.2	Temperature data for various elements of the FSCW IPMM-F at 8.48 A current after running for three straight hours	256
Table F.1	Space vector modulation look-up table	272
Table G.1	Key parameters of the loading motor	279

NOMENCLATURE

A

A	Intercepting area of the turbine	[m ²]
A_a	Electrical loading	[A/m]
\vec{A}	Magnetic vector potential	
A_g	Air-gap surface area	[m ²]
A_w	Cross-sectional area of the wire	[m ²]

B

B	Magnetic flux density	[T]
B_δ	Air-gap flux density due to the magnets	[T]
B_{max}	Peak air-gap flux density	[T]
B_r	Magnet remanent flux density	[T]
B_s	Flux density produced by the stator	[T]
\vec{B}	Magnetic field	[T]

C

C_p	Power co-efficient	
c	Denominator of S_{pp}	
c_l	Chord length	[m]

D

d	Magnet thickness	[m]
d_i	Thickness of steel iron	[m]
D	Armature diameter	[m]
$D-1$	Distributed wound flat shaped IPMM	
$D-2$	Distributed wound V-shaped IPMM	
\vec{D}	Electric displacement	
D_r	Rotor outer diameter	[m]
D_b	Bearing inner diameter	[m]

NOMENCLATURE

<i>d</i>-axis	Direct axis		
		E	
E_{ph}	Induced EMF per phase		[V]
\vec{E}	Maxwell's electric field		
$\overline{E_n}$	Reference EMF phasor element		
E_g	Stored magnetic energy in the air-gap		[J]
		F	
f	Frequency [HZ]		[Hz]
f_s	Sampling frequency		[Hz]
F	Force acting on the bearing		[N]
F_s	MMF produced by stator coils		[A-t]
		G	
g^{-1}	Inverse air-gap function		
		H	
h	Depth of buried magnet		[m]
H_c	Coercivity of magnet		[A/m]
\vec{H}	Magnet field strength		[A/m]
		I	
i_s	Supply current to the stator coils		[A]
i_a	Phase A current		[A]
i_b	Phase B current		[A]
i_c	Phase C current		[A]
i_d	<i>d</i> -axis current		[A]
i_q	<i>q</i> -axis current		[A]
I_{cr}	Characteristic current		[A]
I_r	Rated current		[A]
I_{am}	Current limit		[A]
		J	
J	Electric current density		[A/m ²]
J_a	Equivalent electric current density from armature coils		[A/m ²]

NOMENCLATURE

J_m Equivalent electric current density from magnets [A/m²]

K

k Proportionality constant

k_b Bearing loss constant

k_{cu} Slot-fill factor

k_e Eddy current loss constant [W(Ts⁻¹)^{-3/2}m⁻³]

k_h Hysteresis loss constant [WsT⁻²m⁻³]

k_f Fill factor

k_w Winding factor

$k_{w,n}$ Winding factor of the n order harmonic component

k_p Pitch factor

k_d Distribution factor

L

l Stack length [m]

l_{ew} Height of the end winding [m]

L_s Stator inductance [H]

L Differential operator

L_d d -axis inductance [H]

L_q q -axis inductance [H]

L_a Self-inductance of *phase A* winding [H]

L_{end} End winding leakage inductance [H]

M

m No. of phases

M_{ab} Mutual inductance between *phase A* and *B* winding [H]

N

N No. of conductors per slot

N_a Winding function of phase A

N_n Nodes

N_{ph} Number of turns per phase [Turns]

N_{coil} No. of turns per coil

N_s Total No. of turns of the conductor

NOMENCLATURE

N_{coil}	Number of turns per coil	[Turns]
n	Harmonic order	
n_i	Slot no.	

P

P	Total no. of poles	
P_w	Wind power	[W]
P_m	Mechanical power from wind	[Pa]
P_e	Electrical loss	[W]
P_{eddy}	Eddy Current Loss	[W]
P_{hys}	Hysteresis Loss	[W]
P_{iron}	Total core/iron loss	[W]
P_{cu}	Copper loss	[W]
$P_{bearing}$	Bearing loss	[W]
$P_{windage}$	Windage loss	[W]
P_{mag}	Magnet loss	[W]
P_{stray}	Stray loss	[W]
P_p	Pole pairs	

Q

q -axis Quadrature axis

R

r	Radius	[m]
R	Conductor resistance	[Ω]
R_a	Coil resistance of phase A	[Ω]
R_{air}	Air-gap reluctance	[AT/Wb]
R_{ro}	Radius of the rotor	[m]
R_{si}	Inner radius of the stator	[m]
R_T	Resistance of the conductor at T operating temperature	[deg.]
r_g	Airgap radius	[m]

NOMENCLATURE

R_c	Core loss resistance	[Ω]
R_{ac}	AC resistance	[Ω]
R_{dc}	DC resistance	[Ω]
\mathcal{R}	Reluctance	[AT/Wb]
R_e	Reynold's number	

S

S_{cs}	Conductor area	[m]
S_{us}	Total coil area	
S_{pp}	Slots per pole per phase	
S_{ff}	Slot fill factor	
s	Slots	

T

T	Operating temperature	[deg.]
T_{out}	Torque	[Nm]
T_v	Load torque	[Nm]
t	Time	[s]
t_p	Periodicity	
t_{ini}	Initial value of time step	[s]
T_e	Electro-magnet/alignment torque	[Nm]
T_{rel}	Reluctance torque	[Nm]
T_{cog}	Cogging torque	[Nm]
T_{ripple}	Torque ripple	[Nm]
T_{cfreq}	Frequency of cogging torque	[Hz]

U

u	Unbalanced magnetic pull	
-----	--------------------------	--

V

v_i	Interpolating function	
V_{am}	Voltage limit	[V]

NOMENCLATURE

V_{om}	Voltage limit of the inverter	[V]
V_{oc}	Open circuit voltage	[V]
V_v	Kinematic air viscosity	[m ² /s]
v	Wind speed/velocity	[m/s]
v_q	q -axis voltage	[V]

W

w	Width of the pole face	[m]
W_{ew}	Width of the end winding	[m]
W_{air}	Energy in the air around the end windings	[J]
ω_r	Rated speed	[RPM]
ω_e	Electrical speed	[rad/s]
ω_{ref}	Reference speed	[rad/s]
ω_b	Base speed	[Elec. rad/s]
ω_c	Critical speed	[Elec. rad/s]
ω_{max}	Maximum speed	[Elec. rad/s]
w_m	Rated speed	[rad/s]
$W_{m,n}$	Amplitude of the n th order harmonic component	

NOMENCLATURE

Greek Letters and Symbols

δ	Air-gap length	[m]
δ_{skin}	Skin depth	
α_{25}	Temperature co-efficient at 25°C	
β	Blades pitch angle	[deg.]
Φ	Fundamental flux per pole	[Wb]
ϕ	Function/Electric scalar potential	
ψ_{pm}	Permanent magnet flux linkage	[Wb]
ω_m	Mechanical speed	[rad/s]
θ	Relative position of the permanent magnet	[degrees]
θ_r	Rotor position	[Elec. degrees]
θ_m	Rotor mechanical position	[Mech. degrees]
μ	Permeability	[H/m]
μ_0	Permeability of free space	[H/m]
μ_{rec}	Magnet recoil permeability	[H/m]
ρ	Density of air	[kg/m ³]
ρ_r	Conductor resistivity	[Ω-m]
σ	Conductivity	[S/m]
τ_p	Pole pitch	[m]
τ_s	Slot pitch	
λ	Tip-speed ratio	
λ_d	<i>d</i> -axis flux linkage	
λ_q	<i>q</i> -axis flux linkage	
τ_D	Domain volume	
λ_{cpmax}	Tip-speed ratio for maximum C_p	
γ	Current displacement angle/torque angle/Gamma	[degrees]
γ_d	Current phase angle measured from <i>d</i> -axis	[degrees]
ξ	Saliency ratio	

Numbers

2D	Two-dimensional
3D	Three-dimensional

ABBREVIATIONS

AC	Alternating current
AFPM	Axial flux permanent magnet machine
AWG	American wire gauge
BLDC	Brushless DC machine
CPSR	Constant power speed range
CW	Concentrated non-overlapping winding
D-D	Direct-drive
DC	Direct current
DTC	Direct torque control
DW	Distributed winding
DW IPMM-F	Distributed wound Interior permanent magnet machine with flat-shaped magnets in the rotor
DW IPMM-V	Distributed wound Interior permanent magnet machine with V-shaped magnets in the rotor
DFIG	Doubly fed induction generator
EMF	Electromotive force
EESG	Electronically excited synchronous generator
FE	Finite element
FEA	Finite element analysis
FEM	Finite element method
FOC	Field oriented control
FFT	Fast Fourier transform
FRT	Fault ride through
FSCW	Fractional-slot Concentrated windings
FSCW IPMM-F	Fractional-slot Concentrated wound Interior permanent magnet machine with flat-shaped Magnets in the rotor
FSCW IPMM-V	Fractional-slot concentrated wound Interior permanent magnet machine with V-shaped magnets in the rotor

ABBREVIATIONS

HAWT	Horizontal axis wind turbine
HVRT	High voltage ride through
IM	Induction machine
IPM	Interior permanent magnet
IPMM	Interior permanent magnet machine
LCM	Lowest common multiple
LM	Loss minimization
LVRT	Low voltage ride through
MMF	Magnetomotive force
MTPA	Maximum torque per ampere
NdFeB	Neodymium magnet
PM	Permanent magnet
PMSM	Permanent magnet synchronous machine
PMSG	Permanent magnet synchronous generator
PWM	Pulse width modulated
RFPM	Radial flux permanent magnet machine
SEG	Segmented
SM	Synchronous machine
SPM	Surface permanent magnet
SVM	Space vector modulation
SPWM	Sinusoidal pulse width modulation
SCIG	Squirrel cage induction generator
SOR	Stator outer radius
THD	Total harmonic distortion
TFPM	Transversal flux permanent magnet machine
VAWT	Vertical axis wind turbine

CHAPTER 1: Introduction

1.1 General Background

Wind energy is among the fastest growing renewable energy sources in the world. With an annual growth rate of nearly 20%, the total installed capacity of wind turbines has reached 370 GW by the end of 2014 [1]. This indicates a global demand for the wind energy, making this market open to new and more efficient designs.

Different types of electric generators are commercially available for use in wind turbine systems. Early wind turbine systems used a multi-stage gearbox coupled with a squirrel cage generator to achieve a constant speed when the power level was below 1.5 MW [2]. Main drawback of such topology is the severe mechanical stress on the wind turbine, low efficiency, the need for a reactive power compensator on the electric side, and poor power quality. In order to achieve maximum aerodynamic efficiency over a wide range of wind speeds, variable speed wind turbines that utilize a doubly-fed induction generator was introduced to the market. Compared to fixed speed wind turbines, variable speed wind turbines offer many advantages such as less mechanical stress, better efficiency, increased energy capture and a better power quality. This kind of a system uses a gearbox to couple the generator and rotor shaft. It also uses a power electronic converter rated at 30% of the nominal power in the rotor. The rotor of a typical wind turbine rotates at a speed of 20-100 rpm [3]. The gearbox has the role of increasing the wind turbine shaft speed to the acceptable range suitable for the DFIG operation [4]. DFIG based wind turbines consist about 50% of the whole wind energy market. Many companies have manufactured DFIG based wind turbines, such as Negmicon in Denmark, General Electric in the United-States, and Nordex in Germany

[5]. DFIGs are widely used in the wind energy sector since they offer many advantages as independent control of active and reactive powers, robustness, low overall manufacturing cost, and a simple structure. The stator of a DFIG is directly connected to the grid and are strongly affected by grid side disturbances such as faults. Grid faults are capable of causing unbalanced current flow in the machine, overheating, and severe torque pulsations [6]. Hence, DFIGs operating in weak grids are not suitable candidates in a wind generation system.

The most common generic types of generators used for wind turbine applications are reported in Fig. 1.1. To account for the drawbacks of variable-speed DFIG-based systems, direct-driven electrically excited synchronous machines were utilized in the wind turbines. ENERCON is among the leading manufacturers that utilize this topology. In this scenario, the stator of the machine is connected to the grid through a full-rated power converter. This improves the reliability of the system and makes it immune to grid side disturbances [2].

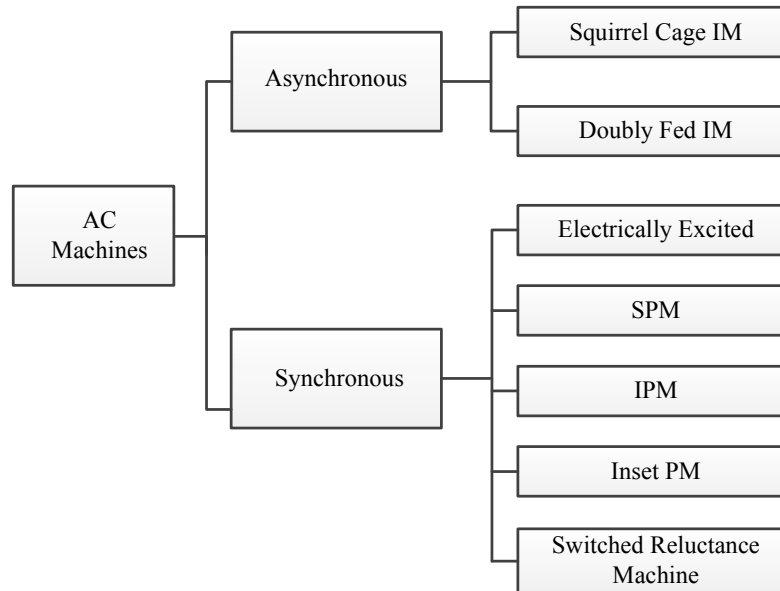


Fig. 1.1 Generic generator types for wind turbine applications

An electrically excited direct-drive synchronous generator (EESG) is almost twice as heavy and more expensive than a permanent magnet synchronous generator (PMSG) of the same power rating. The PMSG is also more efficient compared with the EESG when field loss is eliminated [7].

To increase the efficiency, reduce the weight, and to keep the end-winding losses small, direct-drive generators are designed with a large diameter and small pole pitch [8]. Compared with an electrically excited synchronous generator, the requirement of a larger pole number can be met with permanent magnets that allow small pole pitch.

PMSG's are self-excited, and they do not need to draw reactive power from the grid. Also, it is well suitable for low-speed applications because their efficiency and power factor does not depend on the rotational speed unlike induction machines [9]. Several researchers have already pointed out that PM synchronous machines with radially magnetized surface mounted magnets are a good choice for the design of direct-drive wind turbines [10-12].

1.2 Direct-Drive & Geared Generator System

Most wind turbine generators consist of a gearbox connected to the turbine and the generator. Power loss in gearboxes and gearbox failures are a primary concern in these topologies as gearbox failures often lead to long downtimes. Also, the gearbox needs regular maintenance, hence increasing the annual maintenance costs particularly in offshore wind turbines. Some studies suggest that the maintenance cost for gearbox connected to offshore wind turbines can go up to more than 20% of the total cost of the wind farm [13]. Fig. 1.2 shows the various wind turbine topology available in the market.

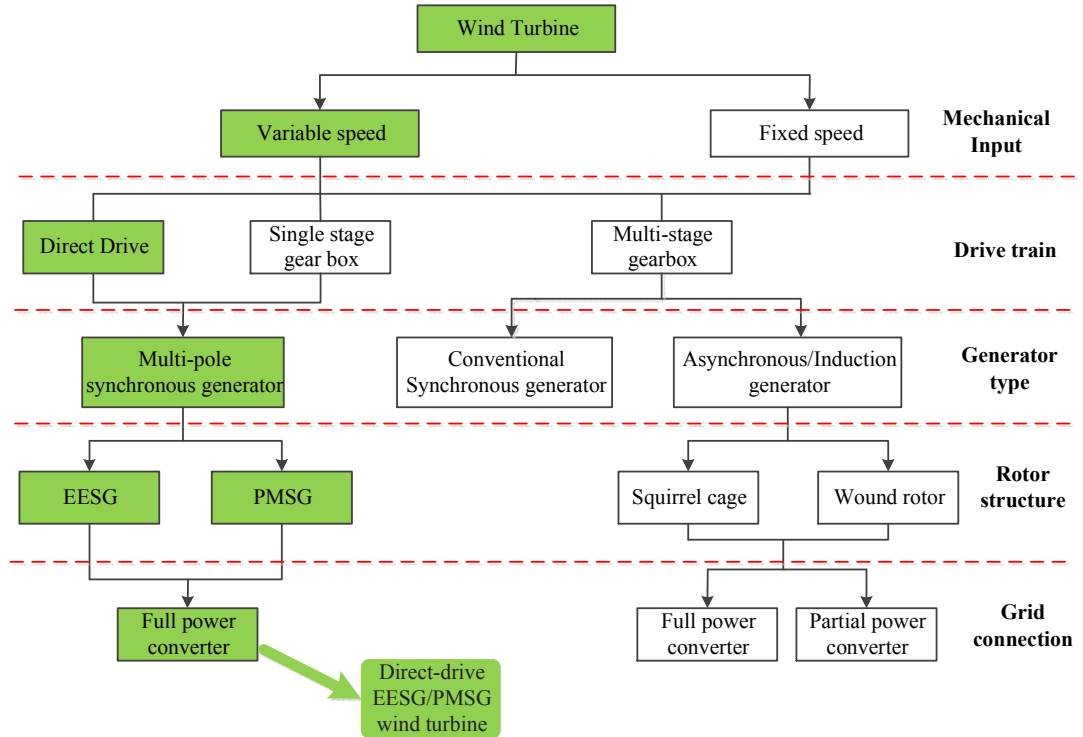


Fig. 1.2. Various wind turbine topology [14]

Doubly fed induction generators use gearbox in order to connect to the wind turbine. Because of this, manufacturers are moving towards gearless generator systems, known as the direct-drive wind turbine systems. The advantages of direct-drive wind turbines over gear-box-based wind turbines are as follows:

- Simplified drive train
- High overall efficiency
- High reliability

Fig. 1.3 shows the drive-train topology of a wind turbine configuration. A direct-drive (D-D) system requires a power electronic converter with full power rating. An induction machine (IM) does not qualify for direct-drive applications. Direct-drive configurations require a large number of poles and large diameters; this is not easily achievable in an IM.

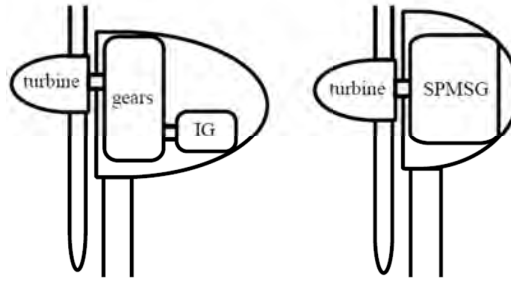


Fig. 1.3. Drive-train topology

The most suitable option for direct-drive wind turbine systems is the use of a permanent magnet synchronous generator (PMSG) which has a lower power loss compared to wound-rotor synchronous generators. Direct-driven PM machines are nowadays mostly used for wind turbine and boat propulsion [15]. The main drawback of direct-drive topology is the high torque rating that affects the mass of the electrical machine. For direct-drive wind generators, the machine has low rotational speed. The speed is determined by

$$\omega_r = \frac{60f}{P_p} \quad (1.1)$$

where, P_p = pole pairs;

The elimination of the gearbox from the drive train means a low rotational speed for the generator (typically 20-100 rpm [3]). This will produce electricity in a typical frequency range of 30-80 Hz. In order to maintain this speed, the number of poles has to be increased for any machine types as seen in Eq. (1.1). For induction machines, the efficiency is seen to decrease with the rise of pole numbers. Thus it does not qualify for such applications [16]. Induction generators used in direct-drive configurations require large number of poles and diameters which lead to high magnetizing currents.

The number of pole pairs is defined by

$$P_p = \frac{\pi D}{\tau_p} \quad (1.1)$$

where,

D = Armature diameter;

τ_p =Pole pitch;

An increase in the number of pole pairs would require either the increase of the armature diameter or a reduction of the pole pitch. Increasing the armature diameter would mean an increase of the overall volume and consequently total cost. On the other hand, reducing the pole pitch has some feasibility issues as the armature teeth will become too narrow and the small slot width to depth ratio will reduce the slot fill factor and increase slot leakage [17]. Extremely high pole numbers could cause excessive magnet flux leakage.

Recent observation in the wind energy market shows that the usage of PMSG in wind turbines has become more prevalent compared to other generators. Some of the commercialized Synchronous generators for wind turbines are summarized in Table 1.1 [7]. For a direct-drive PM generator, the amplitude and frequency of the output voltage are not constant due to the variable speed and fixed excitation of the permanent magnets [3]. This means that the output power needs to be converted into AC power with constant voltage and constant frequency through AC/DC/AC converter. For AC/DC conversion, a 3-phase diode rectifier is used whereas for DC/AC conversion, an SPWM (sinusoidal pulse width modulated) inverter with filter is used. Fig. 1.4 shows the direct-drive permanent magnet full-power rectification system.

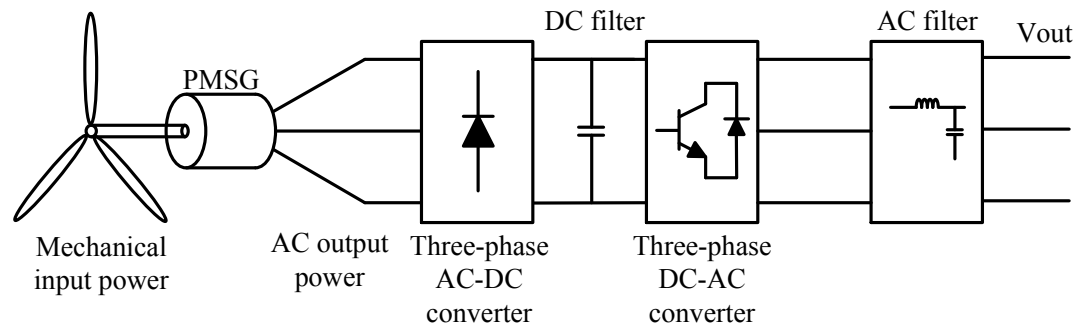


Fig. 1.4. Converter system for the PMSG

Table 1.1 Commercial Wind Turbine with Synchronous Machine

Manufacturer	Power level (MW)	Generator type	Drive-train type	Model
Alstom,USA	6	PMSG	Direct drive	
Dewind, Germany	2	EESG	Gearbox	Dewind D9.2/D8.2
EWT,Netherland	2	PMSG	Direct Drive	DirectWIND90/96
Enercon,Germany	7.5	EESG	Direct Drive	E126
	3			E-101
	2			E-82
GE,USA	4.1	PMSG	Direct Drive	GE 4.1-113
Leitwind, Italy	3	PMSG	Direct Drive	LTW101
	2			LTW70
Siemens,Germany	2.3	PMSG	Direct Drive	SWT-2.3-113
	3			SWT-3.0-101
	6			SWT-6.0-154
Vestas,Denmark	8	PMSG	Gearbox	V164
Gamesa,Spain	4.5	PMSG	Gearbox	G128/G136
Vensys,Germany	1.5	PMSG	Direct Drive	Vensys 70/77/82
	2.5			Vensys 90/100
NPS,USA	2.3	PMSG	Direct-Drive	NPS 2.3
Nordex,Germany	6	PMSG	Direct Drive	NordexN150
EWT,Netherland	2	PMSG	Direct Drive	DirectWind90/96
The Switch,Finland	4.25	PMSG	Direct-Drive	PMG4250-16

The principal advantages of the direct-drive permanent magnet full-power rectification technology are as follows:

- *High power generates efficiency and a better power curve*

The Permanent Magnet (PM) generator avoids all rotor windings and mechanical energy losses associated with gearboxes and couplings. The full power converter provides the flexibility to optimize rotational speed for maximum energy capture, which reduces transmission loss and allows higher generation levels, especially in low wind velocities. The grid side converter can operate reactive-neutral with the power system to improve the power factor. The converter can also be ordered to control reactive power and voltage in the grid within a range.

Table 1.2 Three types of generators used for large Wind Turbines

Type	Drive train	Stator radius	Total cost estimation	Power loss	Ride through performance
DFIG	3 stage geared	100%	100%	100%	Bad
EESG	D-D	600%	120%	95%	Good
PMSG	D-D	600%	105%	65%	Good

- *Lower maintenance costs and less downtime*

The absence of the gearbox in the system reduces the overall maintenance thus reducing the maintenance cost of the whole wind turbine system.

- *Better grid connectivity*

A bi-product advantage of direct-drive generators is the noise reduction achieved when the gearbox is removed from the wind turbine system. A superior low-voltage ride-through can be performed using a full power converter allowing high levels of reactive power control. In reference [2, 18], a direct-drive synchronous generator (SG), a PMSG and a DFIG with a 3-stage gearbox are compared where the DFIG was taken as the base as shown in Table. 1.2. It can be seen that the most efficient generator is the direct-drive PMSG with power losses of about 65% of that of a typical DFIG-based wind turbine. In addition, the ride through capability is better for Direct-Drive synchronous generators compared with DFIGs. However, in terms of costs and size, the DFIG has advantages over direct-drive generators. Nevertheless, the reliability issues associated with the DFIG system is making the wind turbine manufacturers adopt synchronous generators for wind energy systems.

1.3 Motivations

In the past, most of the wind turbine manufacturers used an SCIG for wind application that had the following weaknesses:

- ❑ Uncontrollable reactive power consumption.

- Fixed speed operation.
- Requirement of a multi-stage gearbox.
- Limited power quality control.

A DFIG-based wind turbine is vastly used in the market with the following drawbacks:

- Vulnerability to grid side voltage sags and short circuits.
- Requirement of a multi-stage gearbox.
- The need for slip ring and brushes.

Manufacturers for wind application are looking for more efficient and robust generators for wind energy. The previous generation system had many flaws that need to be addressed in order to achieve an efficient wind power system. Manufacturers are moving towards Direct-Drive Permanent Magnet Synchronous generator for wind application because it has the following advantages:

- Higher power to weight ratio.
- Wider speed range than DFIG
- The grid side converter can operate reactive-neutral with the power system to improve the power factor
- The converter can control reactive power and voltage in the grid within a range.
- Lower maintenance costs and less downtime
- Better grid connectivity
- A full power converter enables superior low-voltage ride-through

Radially laminated PM machines have proven to be a better option for large-scale wind turbines compared to its peers. In the current global wind power generation

market, all radially laminated PM machines are constructed with surface permanent magnet structure. A PM machine with surface permanent magnet structure in the rotor has already shown great potential as a wind turbine generator. The present research trend is focused on designing surface mount Permanent magnet synchronous generators (SPM) for wind turbine applications. On the other hand, very few people have worked with Interior Permanent Magnet Machine (IPMM) for wind application. Compared to SPM, the IPM machine has the following advantages:

- ❑ Less demagnetisation risk of the permanent magnets as they are surrounded by ferromagnetic iron and fixed relatively far from the air-gap [19].
- ❑ More robust rotor structure because the magnet is buried in the rotor iron
- ❑ Additional reluctance torque component
- ❑ The presence of saliency makes it more suitable for sensorless application
- ❑ A wider constant power speed range compared to conventional SPM machine

This makes an IPM machine a compelling candidate for wind turbine generation. IPMM in wind energy is very new. More research has been focused on IPM machines applicable for traction drives. In literature, IPMMs have been found to have high field-weakening behavior with significant reluctance torque component. All these machines have been designed for high-speed applications. A D-D wind turbine generator will incur a very low rated speed. Designing an efficient IPMM for low-speed applications will play a significant role in IPMM research.

1.4 Research Objectives

The goals of this thesis are as follows:

- Investigate an IPMM with various magnet structures for a low-speed direct-drive wind turbine.
- A systematic design of the IPMM with in-depth analysis on the effect of different winding structures of the machine. The IPMM will be designed with both Distributed and Fractional-slot Concentrated Wound layout in the stator slots, and an extensive comparison will be conducted.
- All the IPMM's modelled in this thesis will be optimized according to three basic criteria. They are:
 - Low cogging torque ($< 1\%$ of rated torque)
 - Low torque ripple ($< 5\%$ of rated torque)
 - High efficiency ($> 90\%$)

These design goals are set explicitly for IPMM in wind turbine generation. In a direct drive wind turbine, the cogging torque should not be more than 1.5% to 2% of rated torque as mentioned in [13, 20]. Particular emphasis has to be placed on the reduction of cogging torque in IPM machines. The primary target for the optimization of the IPMM is to reduce the cogging torque and torque ripple in the machine so that direct-drive wind turbines can tolerate it [20]. To increase the wind turbine system efficiency, the efficiency of the generator plays a vital role. This thesis focuses on designing an IPMM with machine efficiency greater than 90%.

1.5 Main contributions

The main contributions of this thesis are as follows:

- **A systematic analysis of an ideal magnet structure of the IPMM for low-speed applications.**

The radial magnet structure of an IPMM can be of segmented, non-segmented and V-shaped IPMM with different V-angles. These structures provide various magnetic loading to the machine and changes the overall characteristics of the IPMM. This thesis focuses on designing low-speed IPMM with different magnet structures using Finite Element Analysis (FEA) and comparing the results with respect to the designing goals mentioned in the previous section.

- **Investigation of the suitability of implementing fractional-slot concentrated wound layout on Interior Permanent Magnet Machines with a high number of poles.**

Most major wind turbine manufacturers use distributed windings to configure the permanent magnet synchronous machine for wind turbines [21]. In recent times, the fractional-slot concentrated winding layout has gained popularity in machines for application in hybrid electric vehicles and traction motors. The use of concentrated windings in IPM machines for low-speed wind turbine applications is considerably a new field. The existing demerits of concentrated wound machine can be eliminated by employing an appropriate winding configuration while retaining the advantages of the winding at the same time. An extensive comparison between both the windings was conducted to get a proper understanding.

- **Construction of a fractional-slot concentrated wound Interior Permanent Magnet Machine with high efficiency, low cogging torque and torque ripple for direct-drive wind turbine applications.**

Initially, a systematic construction of the IPMM is done with a conventional distributed wound layout in the stator. The primary dimension of this design is used to construct an IPMM with fractional-slot concentrated wound IPMM, which is then compared to the base distributed wound IPMM in FEA. Based on the findings, a concentrated wound IPMM machine was built and tested. The prototype IPMM was found to have a higher efficiency and lower cogging torque and torque ripple in comparison to wind turbine generators of the same rating available in the market.

1.6 Outline of Thesis

This thesis is structured as follows:

Chapter 2 presents the general background of the relevant technology. It provides an in-depth review of past work related to this field. This chapter also examines various wind turbine topologies. A brief overview of the Finite Element Method (FEM) used to analyze different machine models are illustrated in this chapter. Lastly, the use of 2D FEA for calculating the machine parameters is also shown.

Chapter 3 illustrates a systematic design optimization process of a 4 KW IPMM with distributed windings (DW) for low-speed wind application. It studies various parameter optimization methods based on surface permanent magnet machines. FEA verifies the suitability of these methods. The minimization technique on cogging torque and torque ripple of IPM machines has been discussed extensively in this chapter. Core losses of an IPMM have been comprehensively analyzed in chapter 3.

Chapter 4 presents a comparative study to investigate the suitability of the fractional-slot concentrated winding (FSCW) structure in the stator and the flat or V-shaped magnets in the rotor poles. This chapter illustrates the calculation of the inductance and saliency ratio of both DW and FSCW IPMMs using an AC standstill test

condition. The overall machine parameters and performance characteristics are predicted using 2D FEA and the output characteristics are compared with the ones found in chapter 3 for the DW design.

Chapter 5 builds upon the findings of chapter 4 to construct a prototype FSCW IPMM with flat shaped magnet structure. This chapter gives a detailed specification of the optimal model built for verification purposes. The selection of materials and its effect on the performance of the machine is also studied here. The mechanical stress analysis is provided before prototyping the final design. The 3-D FE analysis of the final design is examined in this chapter to ensure leakages kept to negligible in the axial direction. Lastly, various kinds of losses in a PM machine are considered and analyzed for the prototype IPMM.

Chapter 6 presents the performance analysis of the constructed 42 pole FSCW IPMM as a generator. This chapter verifies the experimental results with the FEA results achieved in chapter 5. The design goals set for the IPMM are verified using the prototype. Lastly, the saliency ratio and the open loop efficiency are calculated for the constructed IPMM.

Chapter 7 discusses the control methodology and the controller architecture that were applied to the constructed FSCW IPMM. Vector control strategies had been implemented to the prototype during motoring and generating operation. The efficiency calculation during various modes of operation is also shown in chapter 7.

Chapter 8 concludes the work presented in this thesis and scopes suggestions for future expansion of the current work.

CHAPTER 2: Literature Review

2.1 Introduction

This chapter provides an introduction to the permanent magnet synchronous machine where the main focus is on the interior permanent magnet (IPM) machine for direct-drive wind turbine applications. It summarizes various literature relevant to this research. Different structures of the wind turbine are also studied in this chapter. Lastly, a general overview of the FE method used for the analysis of electromagnetic systems is given here.

2.2 Wind Turbine Topology

2.2.1 Wind Energy

The wind power can be expressed as

$$P_w = \frac{1}{2} \rho A v^3 \quad (2.1)$$

where,

ρ = air density (kg/m^3),

v = wind speed (m/s) and

A is the intercepting area of the turbine.

The mechanical power from the wind is lesser than P_w and is defined by the power coefficient (C_p) that also represents the aerodynamic turbine efficiency. It is defined as

$$P_m = \frac{1}{2} \rho A v^3 C_p \quad (2.2)$$

The maximum (theoretical) C_p is 0.59. C_p depends on the tip-speed ratio (λ) and the blade pitch angle (β).

$$C_p = C_p(\lambda, \beta) \quad (2.3)$$

where, $\lambda = \frac{R \cdot w_m}{v}$; R = radius of the blades and w_m is the rotor speed ($rad.s^{-1}$);

Depending on the structure of rotation, a wind turbine can be classified as (a) Horizontal axis wind turbine (HAWT) and (b) Vertical axis wind turbine (VAWT). HAWT's are commercially more available in the market than the later one. However, in recent years, researchers have highlighted that VAWT's can achieve significant improvements in efficiency [22, 23]. Both of these structures have been described in the following sections.

2.2.2 HAWT (lift type):

Numerical approximations have been developed by researchers for various HAWTs to calculate C_p based on the tip speed ratio. A commonly used approximation to calculate C_p is expressed as

$$C_p(\lambda, \beta) = 0.22 \left(\frac{116}{\lambda'} - 0.4 * \beta - 5 \right) e^{\frac{-12.5}{\lambda'}} \quad (2.4)$$

where, $\frac{1}{\lambda'} = \frac{1}{\lambda + 0.08 * \beta} - \frac{0.035}{\beta^3 + 1}$;

Using Eq.(2.4), power speed versus tip-speed ratio is plotted for various pitch angles as shown in . For $\beta=0^\circ$, the power coefficient is 0.432 when the tip-speed ratio is 5.8. The power curve is plotted in Fig. 2.2 using these values. The wind speed to achieve rated power of 4 KW is found to be 8 m/s as seen in Fig. 2.2.

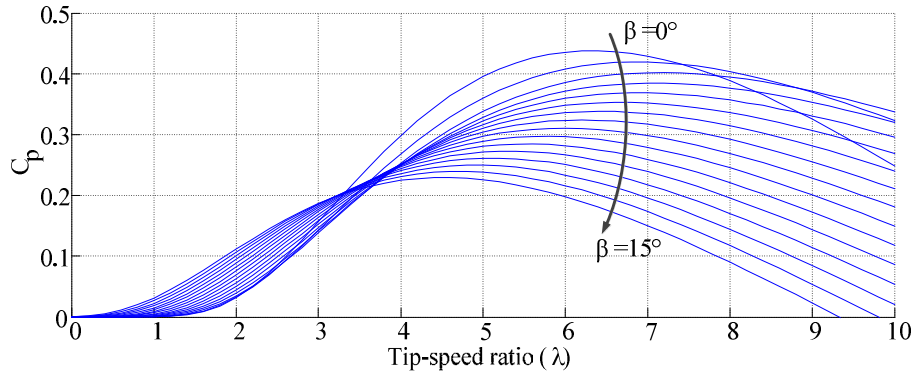


Fig. 2.1. C_p Versus λ of a HAWT for various pitch angles

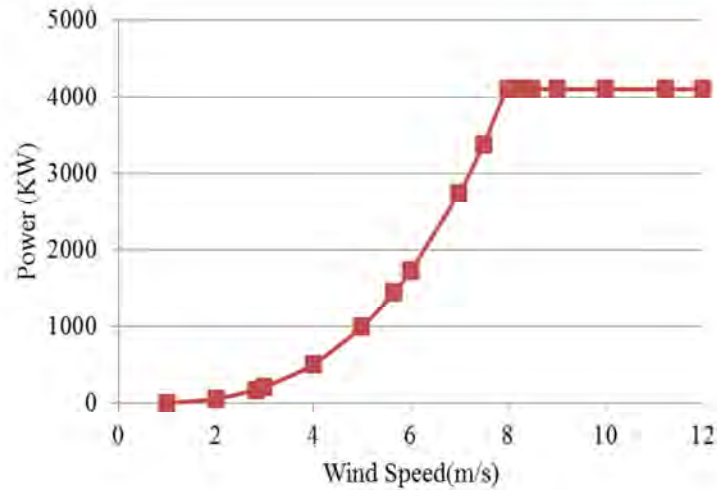


Fig. 2.2. Power curve of HAWT when $\beta=0^\circ$

2.2.3 VAWT:

A vertical axis wind turbine can operate in the wind of any direction. It is not as frequently used as its counterpart HAWT as the VAWT requires a starter motor to achieve operating speed. For a small scale direct-drive wind turbine, the VAWT can be advantageous as the generator can be placed on the ground that significantly reduces the weight that had to be supported otherwise. This reduces the noise of the overall system and furthermore decreases the need for maintenance. Common VAWT type includes the Darrieus turbine and the Savonius wind turbine. Commercially available Darrieus lift wind turbine that is also referred to as H-rotor is gaining some attention due to its ability

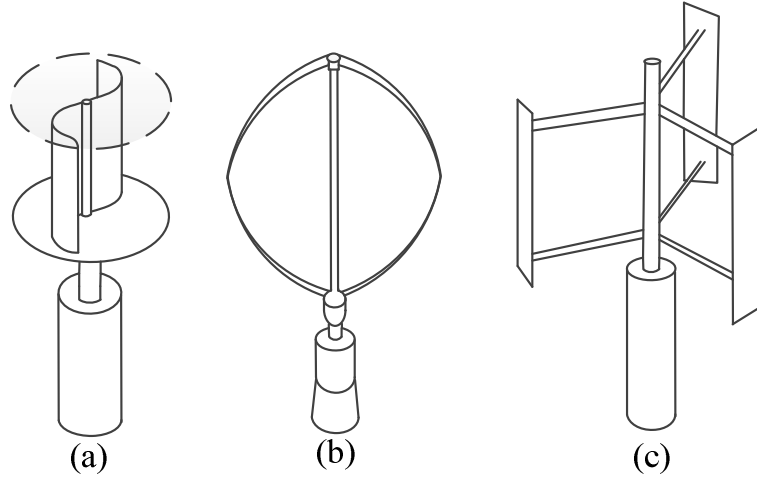


Fig. 2.3. Various VAWT topologies: (a) Savonius wind turbine; (b) Darrieus wind turbine and (c) H-rotor wind turbine

Table 2.1 Design parameters of the H-rotor wind turbine

Turbine Parameters	
Swept area (m ²)	30
Hub Height (m)	6
Turbine radius (m)	3
Blade length(m)	5
Chord length(m)	0.25
Solidity	25%

to accept the wind from any direction and simplified system structure. shows various VAWT topologies. In this research, the H-rotor vertical axis wind turbine had been chosen for further analysis purposes.

The analysis is based on a three bladed H-rotor VAWT designed in for a direct drive PM synchronous machine. NACA0018 airfoil with a tip speed ratio of four is selected as it is extensively used in various VAWTs, and the experimental data is readily available [24]. Fig. 2.3 shows the design parameters of the H-rotor wind turbine [25].The power coefficient curve [25] is plotted in Fig. 2.4. Reynolds number greatly influences C_p which is expressed in Eq. (2.5).

$$Re = \frac{c_l v \lambda_{cpmax}}{V_v} \quad (2.5)$$

where,

c_l = chord length,

V_v = kinematic air viscosity = $1.46 \times 10^{-5} \text{ m}^2/\text{s}$ and

λ_{cpmax} = Tip-speed ratio for maximum C_p .

The blades Reynolds number for this study is about 3×10^6 at low wind speed within limits. The aspect ratio of 20 for this H-Rotor is the optimum value, as reduced aspect ratio increases local Reynolds number and at the same time decreases rotational velocity [26]. Using the above analysis, the power curve for the H-Rotor VAWT is plotted in Fig. 2.5. The wind speed to achieve rated power for the H-rotor VAWT is found to be 7.8 m/s as seen in Fig. 2.5.

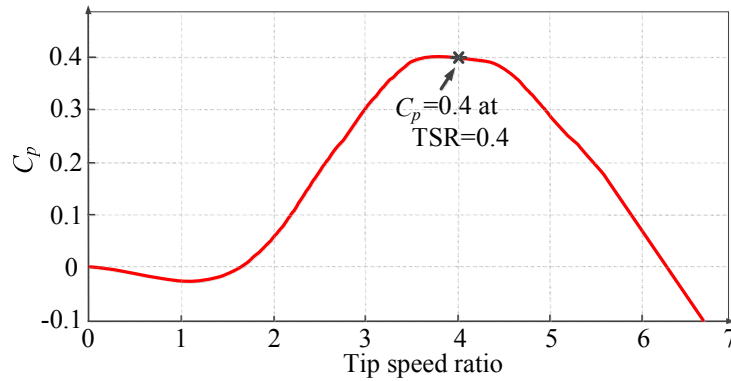


Fig. 2.4. C_p Versus λ of an H-Rotor VAWT

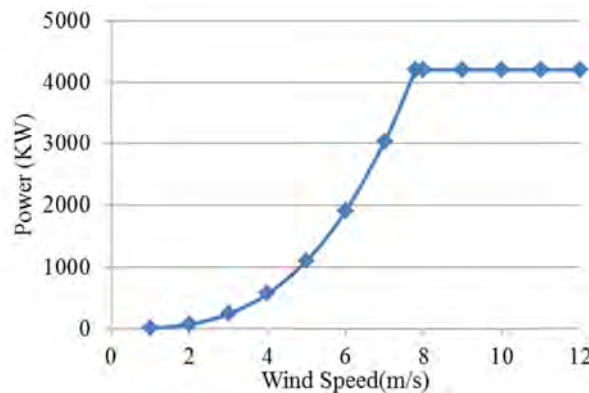


Fig. 2.5. Power Curve for the H-rotor VAWT

2.3 PM Generators for Wind Application

Permanent Magnet Synchronous machines can be categorized according to the direction of the flux path. It can also be categorized according to the magnet structure.

2.3.1 PMSG's category with respect to the flux path

According to the direction of flux path, PM structure can be sub-categorized to

- Radial flux permanent magnet (RFPM) machine (Fig. 2.6(a))
- Axial flux permanent magnet (AFPM) machine (Fig. 2.6(b))
- Transversal-flux permanent magnet (TFPM) machines (Fig. 2.6(c))

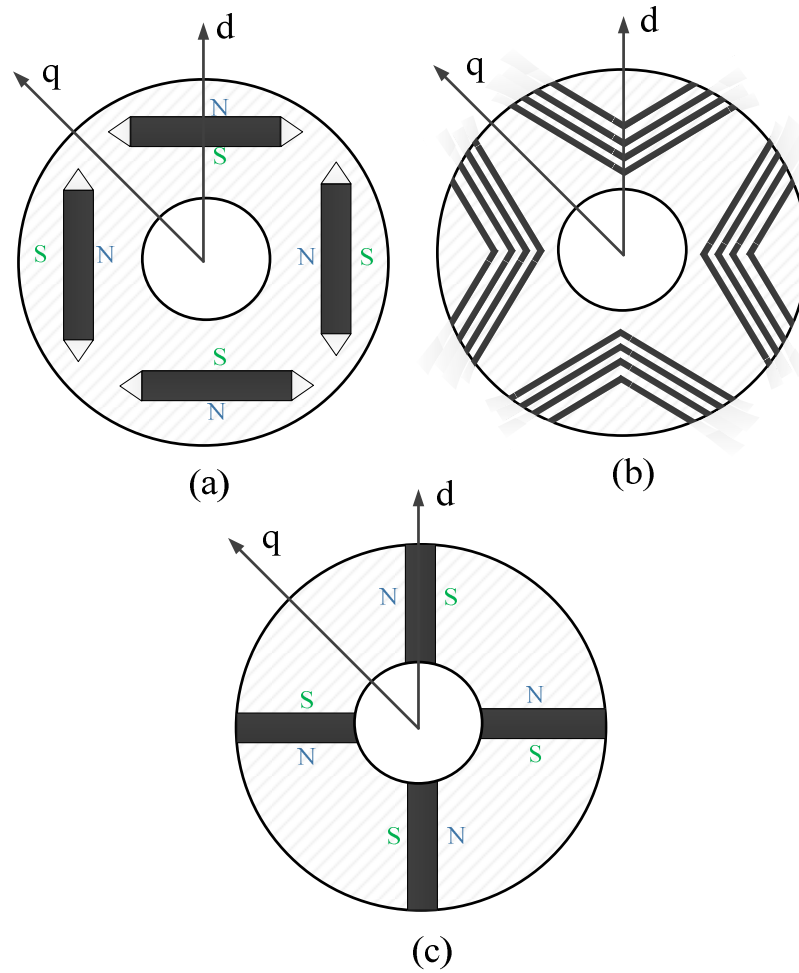


Fig. 2.6. Various rotor configurations of PM machines; (a) RFPM; (b) AFPM and (c) TFPM

2.3.1.1 Radial flux permanent magnet machine

RFPM is the most common type of PM machine used for the design of large-scale direct-drive wind turbines [10, 11, 27, 28]. They produce magnetic flux in the radial direction with permanent magnets that are radially oriented. These machines have a higher torque capability than typical induction machines as well as an electrically excited synchronous generator. The efficiency is higher than IM because it does not have rotor windings that also suggest that it has higher power and torque density. These machines can be easily designed with a large pole number required for low-speed operations. However, this type of machine has a long end-windings leading to higher copper loss the flux density is reduced due to the large air gap. These machines are economically better off for large-scale wind turbines compared to the axial flux machine.

The advantages and disadvantages of an RFPM are given below:

Advantages:

- ❑ Higher torque capability than IM and electrically excited SM.
- ❑ Greater efficiency and power density than IM due to the absence of rotor windings
- ❑ Construction is easy for high pole number.

Disadvantages:

- ❑ High copper loss as the diameter over the axial length is small.
- ❑ Less flux density due to large air-gap.
- ❑ Unattractive power to weight ratio.

2.3.1.2 Axial flux permanent magnet machine

In all axial flux machines, the rotor rotates relative to the stator with the flux crossing the air gap in the axial direction. There are many types of axial flux machine

configuration. These machines can have slot-less windings that allow larger air-gap length. The AFPM usually requires larger magnet than RFPM leading to higher magnet costs. There are many types of AFPM configurations:

- Single rotor and stator
- Double - Stator
- Double-Rotor
- Toroidal Winding (TORUS machine)

The stator core orientation for this machine is longitudinal.

Structure with one rotor and one stator

In this structure, a large attractive force exists between the stator and the rotor. A special thrust bearing is used to prevent the rotor from moving in the axial direction that makes the construction more complicated in this structure. To balance this attractive force, an additional stator can be added to the structure by which the force produced by the rotor and the additional stator can balance the force of the rotor and slotted machine stator. Instead of using the stator an extra rotor with a mounted magnet can also be inserted in the construction to balance out the attractive force.

Double-Stator Slotted Axial-Flux Machine

This kind of AFPM machines consists of 2 external stators and one inner rotor. The permanent magnet is axially magnetized and is surface mounted or inset into a cut window on the rotor disc. As this structure does not require a rotor yoke, so the overall axial length is quite short.

Double-Rotor Slotted Axial-Flux Machine

This configuration is similar to the previous one except that there is one stator located in the middle of the two rotors. In this machine, there is no need for the stator back yoke.

Axial-Flux machine with Toroidal Winding

Axial flux machines have a short axial length and thus have a high power-to-weight ratio. The absence of slots leads to a negligible cogging torque. According to [29], this configuration has large air-gap width due to the lack of teeth, leading to large magnet height and high magnet costs. In [17], the authors compared these axial flux machine with radial flux machines, which showed that with the same ratings, the axial flux machines have greater power density. This is because axial flux machines have smaller volume for a given power rating. The results also showed that the double rotor axial flux configurations have the highest torque density while the axial flux with one rotor and one stator has the lowest. With respect to the magnet weight, for all axial-flux configurations except the Torus machine, the use of magnets is better than that of radial-flux constructions. As far as the volume of the machine is concerned, double-stator axial-flux requires the least space, as in this construction does not need rotor back yoke, and the axial length is very short. The highest efficiency exists in the double rotor axial flux machine, as the iron loss in this construction has the lowest efficiency. The radial flux configurations have the lowest efficiency. The author showed that the single sided axial-flux constructions were not efficient due to the lower pole number and the increased axial length.

Construction of a TORUS machine requires considerable magnet weight. This is due to the presence of the additional air gap for accommodating stator windings. As the power rating increases, both the air gap and the air gap reluctance due to the magnet and winding become larger. So this construction is more suitable for small power rating generators. In [5], using 2D FEA the author showed that the axial flux machine with surface-mounted magnets was a more attractive alternative in applications that require high torque values and low electrical loading values.

In [17] a comparison performed between AFPM and RFPM showed that AFPM have greater power density. The results also showed that the double rotor AFPM has the highest torque density, and the single rotor-stator configuration has the lowest. On the other hand, the double stator AFPM design results in a very compact structure because of elimination of the rotor yoke; the axial length can be made very short. A double rotor AFPM has higher iron losses that indicate greater efficiency. The torus or slotless structure is very simple in construction but requires larger magnet because of longer air-gap length. This structure is not suitable for larger power ratings.

In summary, the advantages AFPM over RFPM are:

- Higher power density, hence requires less core material.
- They have an uniform and easily adjustable air-gap.
- The noise and vibration are less.
- Low cogging torque in the slotless structure.

The major disadvantages of AFPM include structural instability because of the large diameter discs, high magnet cost in slotless design and requirement of a large outer diameter that makes it difficult to be used in wind turbines. AFPM machines have gained much attention from their disc-type structure. Researchers have already investigated them for small wind turbine applications and have seen satisfactory performance [30-33]. However, the feasibility of the AFPM's for large wind farms are yet to be investigated.

2.3.1.3 *Transversal-flux PM machines*

Previously for the RFPM and the AFPM machines, the stator cores were longitudinal but for the TFPM machine, the stator core has transverse orientation, with surface-mounted magnets and has a radial orientation of its air gap. For these machines,

the path of the magnetic flux is perpendicular to the direction of rotor rotation. There are different rotor structures for this kind of PM machines, such as the rotor with single-sided surface magnets with single-sided flux concentration and double-sided flux concentration. TFPM's have a high power density compared with traditional induction generator [6]. Multi-pole generator Aps (Denmark Company) has worked intensively on transversal-flux PMG for wind turbines. The current loading of a transverse machine increases as the pole pitch decreases [9]. High current loading will lead to large armature reaction that will also result in higher rating of the electronic rectifier connected to the generator and thus would increase the overall system costs. The construction of TFPM is also very complicated compared to the AFPM and RFPM since it has the flux path of three dimensions [34]. Thus, this machine is less attractive to the wind turbine manufacturers.

2.3.2 *PMSG's category with respect to magnet structure*

There are many different brushless PM machine configurations used for wind applications. They can be categorized according to magnet structures. They are

- Surface permanent magnet (SPM) machine (Fig. 2.7(a))
- Interior permanent magnet (IPM) machine (Fig. 2.7(b))
- Inset permanent magnet machine (Fig. 2.7(c))

In a surface magnet rotor, the magnet poles are glued to the rotor whereas in an interior magnet rotor structure; the magnet poles are buried inside the rotor. The inset PM machine is very similar to the structure of surface magnet rotor except for the fact that there is an iron tooth present between each couple of adjacent PM's [35]. Both the IPMM and the inset magnet structure produce additional reluctance component to the torque compared to the SPM, which is non-salient [36].

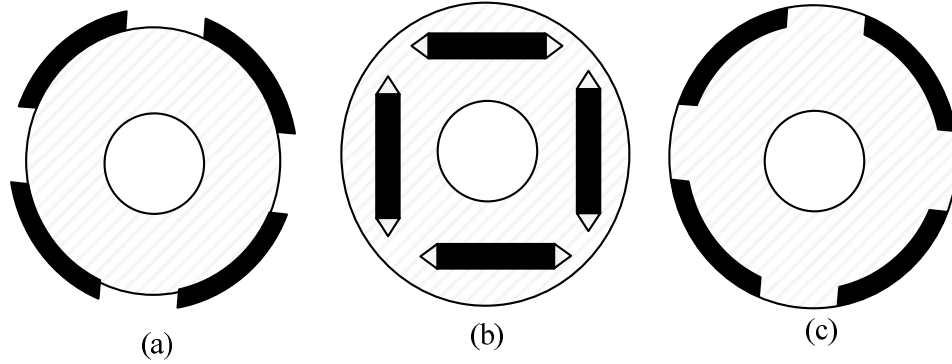


Fig. 2.7. PM machine rotor according to magnet structure; (a) SPM; (b) IPM and (c) Inset PM machine

Most of the radial flux permanent magnet wind turbine generators are surface permanent magnet machine [21]. A good example of commercialized SPM wind turbine generator with optimum performance is the one used in Siemens SWT-3.0-101 [14]. However, in recent years, some researchers have focused on designing IPM machines for wind application [37]. An SPMM is a conventional non-salient pole synchronous machine with no reluctance torque component. Whereas for IPMM, the reluctance torque component adds up to the total torque of the machine. This is because, for an IPMM, there is a variation in d - q axis inductances making it a salient pole synchronous machine. Analysis on inset PM has not been studied throughout this thesis. With surface mounted magnets in the machine, the remanent flux density must be higher than the air-gap flux density. Magnets with higher remanent flux density are needed in the machine to achieve a sufficient amount of air-gap flux density. The use of magnets such as NdFeB or Alinco that has higher remanent flux density is costlier than ferrite magnets thus making the overall cost of the machine higher. While this is not the case for IPM machine in which the air-gap flux density of the pole piece is given by:

$$B_{\delta} = \frac{B_r}{\frac{w}{h} + \frac{2\mu_{rec}}{d}\delta} \quad (2.6)$$

where,

B_δ = Air-gap flux density;

B_r = Magnet material remanence;

w = Width of the pole face;

h = depth of buried magnet;

μ_{rec} = Magnet recoil permeability;

δ = air-gap and

d = magnet thickness;

By selecting suitable values of w and h , it is possible to use low-cost ferrite magnets to generate high air-gap flux density. As SPM machine is magnetically non-salient, there is no reluctance torque component available unlike an IPM machine. SPM machines are more vulnerable to demagnetization compared to IPMM. This is because for SPMM, the rotor magnets are directly exposed in the air-gap to the demagnetizing stator field. The advantages of an IPMM over SPMM has been already discussed in chapter 1.

2.4 General background of Interior Permanent Magnet Machines

In an IPM machine, the magnets are buried inside the rotor for an IPMM that makes it mechanically robust and is more capable of withstanding higher speeds. The magnetic flux of the IPMM is shown in Fig. 2.8. From the figure, it is seen that the magnetic flux of the IPMM passing through the d -axis magnetic circuit has to cross two magnet depths and two air-gaps. This is not the case for magnetic flux passing through the q -axis magnetic circuit. For this reason, the q -axis inductance is higher than the d -axis inductance in an IPMM. Thus, the IPMM is of a salient pole structure that gives the machine to utilize its reluctance torque in combination with its magnetic torque. This gives the machine optimum field weakening capability.

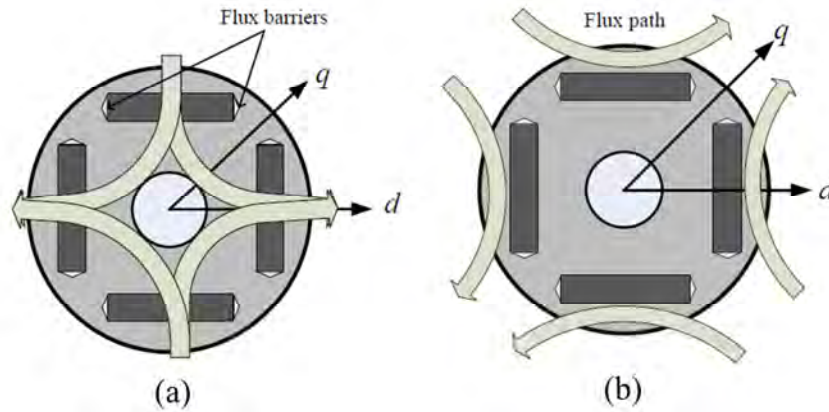


Fig. 2.8. Magnetic flux paths of an IPMM in (a) d -axis and (b) q -axis

For the last three decades, IPM machines have attracted much interest due to their high efficiency, embedded magnet structure, high torque & power density and the presence of the reluctance torque. Research on various aspects of IPM machines conducted at present that includes design, control, machine parameters and flux weakening operation. In 1982, Hosinger [38] submitted his research on deriving the direct and quadrature axis inductances and the open circuit voltage for an interior type permanent magnet machine. Parameters and performance of an IPMM were first presented by Chalmers et al. [39] for variable frequency operation. The paper explained a way to obtain the q -axis inductance with saturation taken into account.

T. M. Jahns [40] was one of the first authors to publish an in-depth analysis on IPMM's. Soon after, Schiferl and Lipo [41] with the help of finite element analysis (FEA) inquired about the variable speed performance and operating limits of 'buried' type permanent magnet machines. Steen et al. [42] was the first to patent several geometrical configurations on a synchronous machine with buried permanent magnets in 1979. Rahman et al. [43] developed simple analytical expressions to determine the direct and quadrature axis reactance of an IPMM.

Much research has been conducted on IPMM in flux weakening applications. Jahns [44] revealed the effectiveness of the interior PM synchronous machine for adjustable speed operations and extending it to constant power speed range at high speeds. Schiferl and Lipo [41] presented the basis for determining the optimum flux weakening performance in IPMM with the variation of its equivalent circuit parameters. Soong et al. [45] compared the field-weakening performance of a standard 2.2 KW induction machine with that of synchronous reluctance and IPM machines. It was found that the multiple barrier IPMM have the most promising rated and field weakening characteristics. The authors also developed an axially laminated IPMM in [46] with high saliency capable of achieving very high saliency and an extreme wide constant power speed range exceeding 7.5:1. Zhu et al. [47] derived the stator iron loss between a SPMM and an IPMM and came up to the conclusion that the IPMM has higher flux weakening range with the cost of having a higher iron loss in that range due to the higher harmonic content in the armature reaction field.

An investigation done by Honda [48] for various rotor configuration of an IPMM showed that the double layered IPMM with two PM's per pole has the best configuration for reluctance torque utilization and maximized total generated torque. Further research on the double layered IPMM with different rotor structures in [49] concluded that concentrated winding is inferior to distributed winding in terms of generated torque and the constant power region size for a double layer IPMM. Fratta et al. [50] concluded that the IPMM would be more suitable for spindle drives in comparison to induction machines due to its higher torque density and flux weakening ability provided the mechanical and magnetic issues in the rotor are resolved.

2.5 IPMM for wind turbine applications

Interior Permanent Magnet Machine (IPMM) is a newly emerging technology and its application in the wind energy sector has only recently been investigated. It has been already cited in this thesis, that the most common type of PM machines used in the wind industry are radial flux permanent magnet (RFPM) machines with surface mounted magnets (SPM). Analysis conducted between a surface and an interior permanent magnet synchronous generator for wind turbine application in [51] showed that, efficiency is higher for the IPMM due to better power factor in comparison to the SPMM.

In [52], the author analyzed different types of rotor structure for high-power performance for small-scale wind power permanent magnet synchronous generator and the results showed that the tangentially magnetized IPM structure with a magnet width of 33.9 mm was the most suitable rotor structure for achieving high power performance. Whereas, the SPM structure with a magnet width/ pole pitch of 90% was found to be the most appropriate for high efficiency, low voltage and high power output. For inset PM structures, the magnet torque reduces when magnet width/pole pitch decreases. However, the average torque of the inset PM machine is increased to the same magnet width/pole pitch of the SPM machine due to its salient characteristics that incorporate the reluctance torque component. For radially laminated IPM machine, decreasing the magnet width and also increasing the insertion depth of the magnets decrease the magnet torque but the reluctance torque increases. The machine delivered a maximum average torque when the magnet was near the rotor surface that was less compared to tangentially-magnetized IPM but was greater than SPM and Inset PM. For the V-shaped IPM structure, it did not exhibit much difference in the average torque when the angle

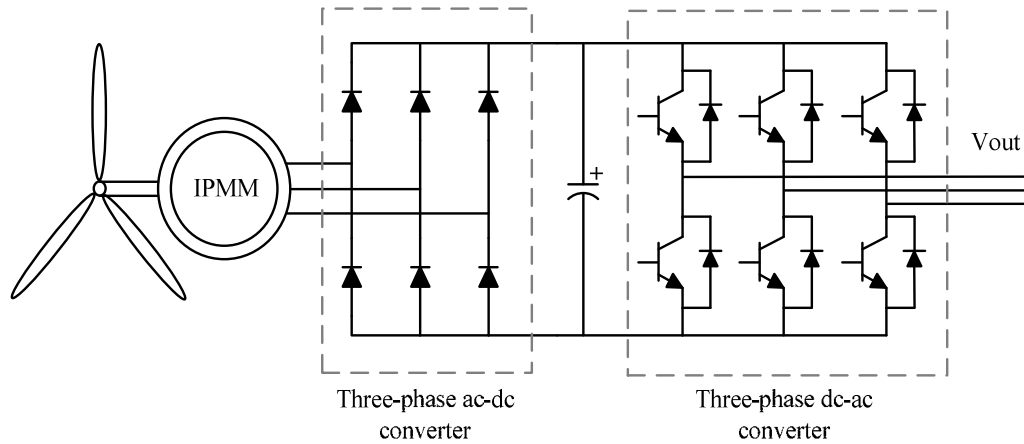


Fig. 2.9. Wind energy conversion system using IPM machine

of the magnets was increased, and the value was slightly smaller than the tangentially magnetized IPM.

In [53], for high-power performance of the PMSG in a large scale direct-drive wind power generation system, the author compared four types of rotor structures, a SPM, a tangentially-magnetized IPM, a radially magnetized IPM and an inset PM using 2D-FEM. The results exhibited that the inset PM structure is suitable rotor structure out of the four examined. The inset PM structure with optimum salient part width has high power performance and high efficiency at the rated condition. In this case, the maximum torque of tangentially-magnetized IPM is less than that of SPM. Whereas, the radially-magnetized IPM requires less reluctance torque compared with the tangentially-magnetized IPM. Another interesting fact is that the average torque decrease if the pole shoe becomes larger for the radially magnetized IPMM. This is because flux leakage occurs in the pole shoe. According to [54], the use of IPM machine provides quicker return on investment and more money profit during a period compared with a SPM machine for a small wind turbine with a wind speed of 5 *m/s*. Two 7 MW fractional slot concentrated wound SPM and IPM machines were designed and compared in [55]. The results in FE suggested that the IPM generator has higher torque per volume and less

magnet loss than the SPM machine. On the other hand, the SPM machine has lower torque ripple and better demagnetization performance with lesser weight and cost in comparison to the IPM generator.

2.6 Interior permanent magnet topology

The developed torque for an IPM machine can be expressed as follows:

$$T_{out}(i_s, \theta_r, \psi_{PM}) = \frac{1}{2} i_s^2 \frac{dL_s}{d\theta_r} - \frac{1}{2} \psi_{PM}^2 \frac{d\mathcal{R}}{d\theta_r} + N_{ph} i_s \frac{d\psi_{PM}}{d\theta_r} \quad (2.7)$$

where,

ψ_{PM} = Flux from permanent magnets;

i_s = Supply current (to the stator coils);

L_s = Stator inductance;

θ_r = Rotor position and

\mathcal{R} = Reluctance.

The first term in Eq. (2.7) is known as the reluctance torque and is related to the variation of stator inductance with rotor position. This variation of stator inductances is caused by pole saliencies or flux barriers. Efficient utilization of this reluctance torque is crucial for higher power and more stable operation and relatively higher efficiency improvement in IPM wind generators [37]. The second term is known as cogging torque. It is caused by the interaction of magnet flux and stator slots, resulting in the variation of reluctance (\mathcal{R}). The last term is referred to as electro-dynamic torque or alignment torque that is the main contributor to the useful torque produced by the machine.

In IPM machine, the subcategory has been done according to the orientation of the magnets in the rotor. They are

- Conventional/Flat IPM machine (Fig. 2.10(a))
- Segmented IPM machine (Fig. 2.10(b))
- V-shaped magnet IPM machine (Fig. 2.10(c))

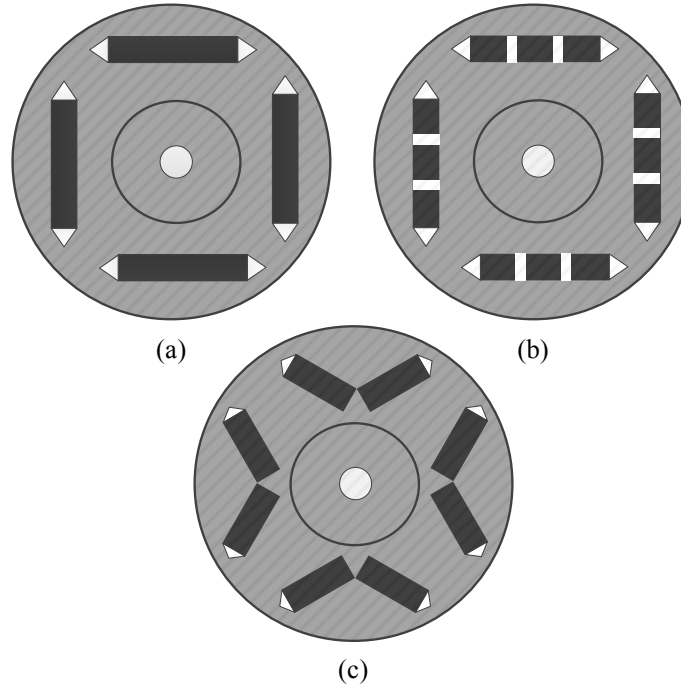


Fig. 2.10. Various Magnet structure of the IPMM

2.7 Distributed and Concentrated windings

The majority of 3-phase radial-field IPM machines are designed with overlapping distributed windings (DW). Almost all the main wind turbine manufacturers' use distributed windings to configure the permanent magnet synchronous machine for wind turbines [21]. Although, recently the concentrated wound PM machines are gaining popularity in direct-drive wind generation systems [56].

Before the 21st century, concentrated windings were mostly used in small BLDC motors and AC servomotors due to their simple structure. CW structures present a fractional number of slots per pole per phase with irregular distribution of slots. Recently these windings have gained popularity in machines for application in hybrid electric vehicles and traction motors. The fractional-slot concentrated winding (FSCW) for the IPMSM is getting attention from the research community due to its high slot-fill factor, high tolerance to phase fault, simplified manufacturing process, non-overlapping coils resulting in shorter end windings and reduced copper usage [57-62].

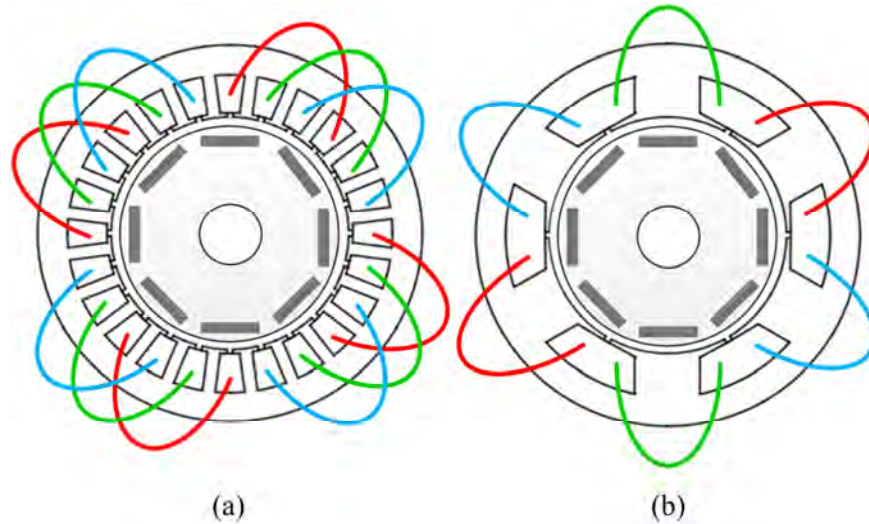


Fig. 2.11. (a) Distributed and (b) Concentrated winding structure

Despite having these advantages, the FSCW was not widely used in the past due to its characteristics in producing EMF and MMF waveforms with unacceptably high total harmonic distortion. However, in recent years, it has been proved that through appropriate choice of slot and pole combinations [63], the CW can produce sinusoidal EMF waveform. Magnussen and Sadarangani [64] were one of the first to design a high-performance PM machine with concentrated windings. Various PM machines equipped with fractional slot concentrated windings are discussed in [65-69] that are not addressed in this thesis. A low speed direct-drive permanent magnet dynamo-electric machine with concentrated windings was designed for wind power generation that showed satisfactory performance [70]. Examples of IPMM's with eight poles showing both distributed windings (DW) and concentrated windings (CW) are shown in Fig. 2.11.

High pole conventional distributed wound PM machines lead to the high slot numbers in the stator that increases the copper loss in the machine. As a result, the copper loss for this high pole PM machine dominates the total loss of the machine resulting in low efficiency. Furthermore, the total manufacturing cost of the machine

increases as a result of more copper wires being used in the production of the high pole PM machines. These issues can be resolved by the use of fractional slot concentrated wound in the stator of the high pole PM machines. This is because, fractional slot concentrated winding layout does not require high slot numbers, even though, the pole numbers are high, resulting in lower copper losses in the machine.

In FSCW, the opposite polarity of the corresponding phase coil is located in the next slot, which makes the end windings to not overlap. This makes the lengths of the end windings for an FSCW at least three times smaller than DW. As a result of this, the stack length of FSCW machine can be increased leading to a higher developed torque. This leads to study the concentrated windings in IPMM with high pole numbers applicable for low-speed applications. Theoretically, distributed windings have shown to have lower torque ripple than concentrated windings because of the distributed magnetic flux through the teeth [71]. On the other hand, cogging torque is lower in concentrated winding structure in comparison to DW structure [72, 73]. This research investigates the application of both DW and FSCW to IPMSM with high pole number for the low-speed application.

2.8 Finite Element Method (FEM)

In the finite element method, the whole domain is subdivided into a fixed number of subdomains thus minimizing the complexity of the problem. The interpolating functions v_i are defined on each sub-domain, and the function ϕ is approximated by v_i for each subdomain whose coefficients are the unknown quantities. In order to determine the coefficients, the field problem is solved using the following general steps [74]:

- *Partition of the domain:* The domain is divided into subdomains.

- *Choice of interpolating functions:* The functions v_i are chosen.
- *Formulation of the system to resolve the field problem:* With the use of Galerkin's method or Rayleigh-Ritz method, the field problem is solved by determining ϕ for nodes of each element.
- *Solution of the problem:* Common numerical algorithms are used to compute ϕ_i in the N_n nodes of the domain and thus solving the problem.

The finite element analysis (FEA) of a domain consists of steps shown in Table 2.2.

Table 2.2 Steps for analyzing a domain in FEM

Pre-processing	<ul style="list-style-type: none"> • Construction of the geometry • Mesh formation of the study domain • Assigning material properties to various regions • Assigning sources of excitation (if present) • Assigning an electrical circuit (if needed) • Assigning boundary conditions
Solving	<ul style="list-style-type: none"> • Derivation and assembling of element matrix equations • Solving the equations for unknown variables
Post-processing	<ul style="list-style-type: none"> • Analysis of results obtained

2.8.1 Mathematical formulations of the Physical Model

The laws of electromagnetic field problems can be expressed by Maxwell's equation. These equations are given below in differential form,

$$\vec{\nabla} \times \vec{H}(\mathbf{P}, t) = \vec{J}(\mathbf{P}, t) + \frac{\delta D(\vec{\mathbf{P}}, t)}{\delta t} \quad (2.8)$$

$$\vec{\nabla} \times \vec{E}(\mathbf{P}, t) = \frac{\delta \vec{B}(\vec{\mathbf{P}}, t)}{\delta t} \quad (2.9)$$

$$\vec{\nabla} \cdot \vec{B}(\mathbf{P}, t) = 0 \quad (2.10)$$

where,

$\vec{H}(\mathbf{P}, t)$ = Magnetic field strength,

$\vec{J}(\mathbf{P}, t)$ = Electric current density,

$\vec{D}(\mathbf{P}, t)$ = Electric displacement,

$\vec{B}(\mathbf{P}, t)$ = Magnetic flux density,

$\vec{E}(\mathbf{P}, t)$ = Maxwell's electric field;

And, $\vec{\nabla} = \vec{1}_x \frac{\delta}{\delta x} + \vec{1}_y \frac{\delta}{\delta y} + \vec{1}_z \frac{\delta}{\delta z}$; \mathbf{P} is the point where the vector is considered, and t indicates the time dependence.

In steady state, $\frac{\delta}{\delta t}$ is zero and for such condition Maxwell's equation can be expressed as,

$$\vec{\nabla} \times \vec{H}(\mathbf{P}, t) = \vec{J}(\mathbf{P}, t) \quad (2.11)$$

Initially for determining the equation of the permanent magnet machine, only a current source excitation is considered. The magnetic field can be represented as,

$$\vec{B} = \mu \vec{H} \quad (2.12)$$

where, μ = Permeability of the material;

By substituting Eq.(2.12) into Eq.(2.11), we get :

$$\vec{\nabla} \times \frac{1}{\mu} \vec{B} = \vec{J} \quad (2.13)$$

In [75], the solving of the field problem were conducted using field potentials rather than the field that simplified the overall solving process. A magnetic vector potential (\vec{A}) and electric scalar potential (ϕ) is introduced to simplify the electromagnetic problem. The flux density can be represented in terms of the magnetic vector potential as,

$$\vec{B} = \vec{\nabla} \times \vec{A} \quad (2.14)$$

$$\vec{E} + \frac{\delta \vec{A}}{\delta t} = -\vec{\nabla} \phi \quad (2.15)$$

Using the Equations stated in this section, the equation of the permanent magnet machine can be expressed as [73],

$$-\frac{1}{\mu} \nabla^2 \vec{A} + \sigma \frac{\partial \vec{A}}{\partial t} - \nu \times \sigma (\nabla \times \vec{A}) = -\sigma \nabla \Phi \quad (2.16)$$

where,

σ = Conductivity of the material;

ν = Velocity of a material with respect to a given reference frame;

Considering the permanent magnet excitation in addition to the current excitation, Eq. (2.16) transforms to

$$-\frac{1}{\mu} \nabla^2 \vec{A} + \sigma \frac{\partial \vec{A}}{\partial t} - \nu \times \sigma (\nabla \times \vec{A}) = -\underbrace{\sigma \nabla \Phi}_{J_a} + \underbrace{\nabla \times \vec{M}}_{J_m} \quad (2.17)$$

where,

J_a = Equivalent current density due to armature current;

J_m = Equivalent current density due to PM;

To eliminate the velocity term in Eq.(2.17), the moving frame is considered the reference that makes the relative velocity become zero. Eq.(2.17) becomes

$$-\frac{1}{\mu} \nabla^2 \vec{A} + \sigma \frac{\partial \vec{A}}{\partial t} = -\sigma \nabla \Phi + \nabla \times \vec{M} \quad (2.18)$$

In a 2D plane, the magnetic vector potential is only non-zero in the z-axis. The governing system equation for 2D analysis is given by [73],

$$-\frac{1}{\mu} \nabla^2 A_z + \sigma \frac{\partial A_z}{\partial t} = -J_a + J_m \quad (2.19)$$

2.8.2 Mesh Formation

The 2D domain is sub-divided into a finite and sufficiently high number of elements. The behavior of each of this element is defined by the partial differential function shown in Eq.(2.19). These elements can be of various forms characterized by each vertex. Each vertex is referred to as nodes, and all of the nodes set up the mesh.

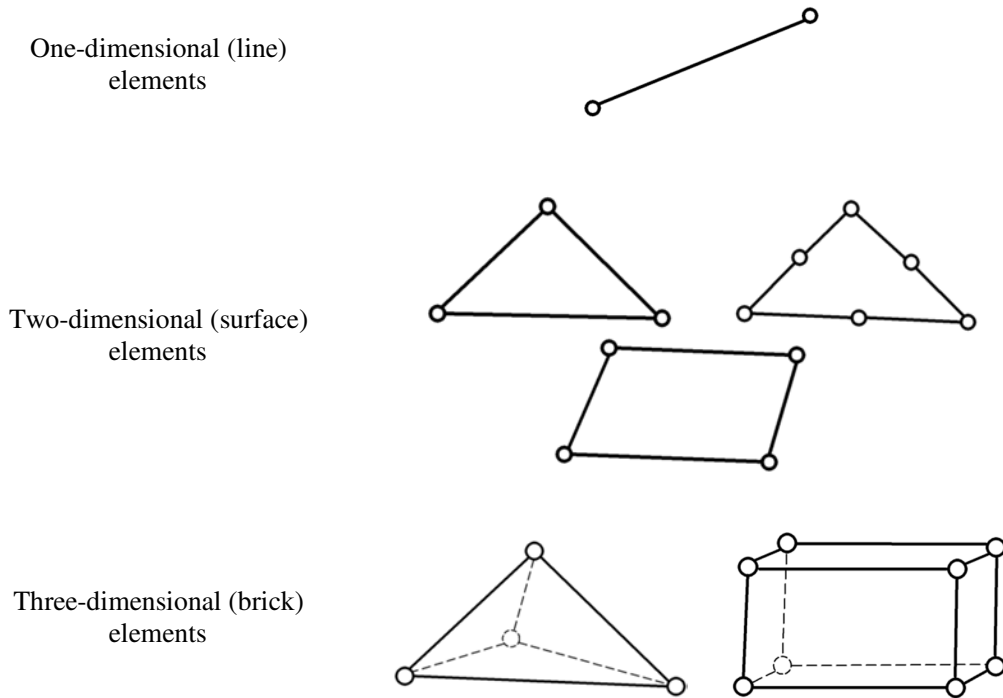


Fig. 2.12. Typical elements used for mesh formation in FEA

The primary task in FEM is to solve for all unknown node potentials in the element. Fig. 2.12 shows the typical elements used for mesh analysis in Finite element study. Each of these elements can be represented by a polynomial function. A lesser number of nodes in each element makes the function simple with fewer unknown variables. The most commonly used element is the 2D surface triangular element that can represent any shape of a 2D plane with the help of a combination of triangles.

Assuming the primary domain has been sub-divided into N_m finite elements, the magnetic vector potential at m -th triangular element can be represented as,

$$A_m(x, y) = a + bx + cy \tag{2.20}$$

where, a , b , and c are constants that will be determined in terms of their interpolated field variables.

In the three nodes of the triangular element, the potential function is given as,

$$\begin{cases} A_1 = a + bx_1 + cy_1 \\ A_2 = a + bx_2 + cy_2 \\ A_3 = a + bx_3 + cy_3 \end{cases} \quad (2.21)$$

Evaluating the expression at the nodes:

$$\begin{cases} A_1 \\ A_2 \\ A_3 \end{cases} = \frac{1}{2} \begin{bmatrix} 1 & x_1 & y_1 \\ 1 & x_2 & y_2 \\ 1 & x_3 & y_3 \end{bmatrix} \begin{cases} a \\ b \\ c \end{cases} \quad (2.22)$$

Solving for a , b and c using Cramer's rule:

$$\begin{aligned} a &= \frac{1}{2A_m} \left[A_1 \underbrace{(x_2 y_3 - x_3 y_2)}_{p_1} + A_2 \underbrace{(x_3 y_1 - x_1 y_3)}_{p_2} + A_3 \underbrace{(x_1 y_2 - x_2 y_1)}_{p_3} \right] \\ b &= \frac{1}{2A_m} \left[A_1 \underbrace{(y_2 - y_3)}_{q_1} + A_2 \underbrace{(y_3 - y_1)}_{q_2} + A_3 \underbrace{(y_1 - y_2)}_{q_3} \right] \\ c &= \frac{1}{2A_m} \left[A_1 \underbrace{(x_3 - x_2)}_{r_1} + A_2 \underbrace{(x_1 - x_3)}_{r_2} + A_3 \underbrace{(x_2 - x_1)}_{r_3} \right] \end{aligned} \quad (2.23)$$

Substituting (2.23) into (2.21):

$$A_m(x, y) = \left(\frac{1}{2A_m} \sum_{i=1}^3 p_i A_i \right) + \left(\frac{1}{2A_m} \sum_{i=1}^3 q_i A_i \right) \cdot x + \left(\frac{1}{2A_m} \sum_{i=1}^3 r_i A_i \right) \cdot y \quad (2.24)$$

$$= \sum_{i=1}^3 v_i(x, y) \cdot A_i \quad (2.25)$$

where, v_i is the interpolating function for i -th sub domain.

2.8.3 Boundary Conditions

Boundary conditions are assigned to study domains to increase the accuracy and efficiency of the FE analysis [73, 74, 76]. There are three main groups of boundary conditions:

- Dirichlet's Condition
- Neumann's Condition
- Periodic Condition

Dirichlet's Condition

This condition corresponds to assigning a magnetic vector potential (\vec{A}) on a given part of the boundary. \vec{A} is a constant meaning the boundary line will have the same value throughout. It is common to assign $\vec{A} = 0$ considering the leakage flux beyond the boundaries is zero. This assumption is valid as the flux lines are confined within the stator back iron. This condition is equivalent to an external material place outside the study domain for which the magnetic permeability is null. Fig. 2.13 shows the Dirichlet's boundary of a 1/4th of a four pole IPMM. It can be seen that the stator outer radius and the rotor inner radius are imposed with this condition.

Neumann's Condition

Neumann's condition is imposed to a region that has symmetry. This condition is satisfied by imposing a given value to the derivative of \vec{A} normal to the boundary. This makes the flux lines to have a particular incidence angle with the boundary. In this research, Neumann's boundary condition is not applied to 2D FE analysis. The 3D FE analysis conducted in chapter 5 considers Neumann's condition in the domain.

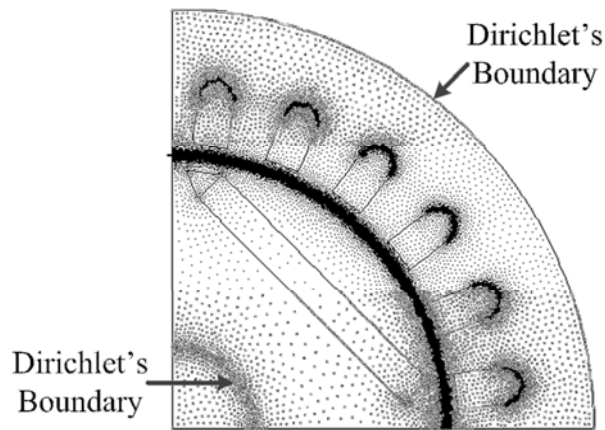


Fig. 2.13. 1/4th of a 4 pole IPMM displaying the nodes and Dirichlet's boundary

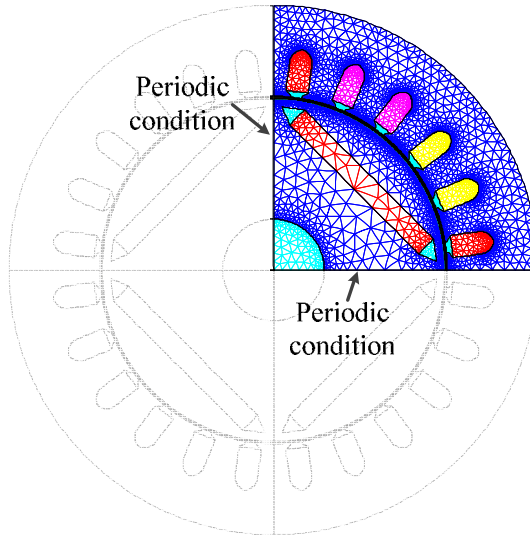


Fig. 2.14. IPMM with quarter cyclic-symmetry

Periodic Condition

The periodic condition is applied to structures that exhibit a repetition of electromagnetic fields. It is assigned to two boundary lines using symmetries in the geometry. These boundary conditions are useful in structures as the overall geometry can be scaled down, and the analysis on one part of it will provide accurate results with less computational time. Fig. 2.14 shows an IPMM with a quarter cyclic-symmetry. The symmetry of a domain can be either even or odd symmetry. For the prototype CW machine as well as the machine shown in Fig. 2.14, even cyclic boundary conditions are applied.

2.8.4 Matrix Equations of Elements

The two primary methods used in deriving the matrix equations of elements in order to solve the field problems are:

- The weighted residual method
- Variational method

Both these methods provide high accuracy by minimizing the error to null. Galerkin's method is a general form of the weighted residual method that is one of the most commonly used technique in FE. In Galerkin's method, a trial function A^* that approaches the exact solution A in a domain D with a forcing function f corresponds to a residual (shown in Eq.(2.26)) equal to zero (near zero) in the whole domain [73, 74, 77].

$$r = LA^* - f \quad (2.26)$$

where, L is a differential operator.

By the use of the weight function (w_i), the residual method forces the integrals of the residuals to be zero. This can be expressed over the domain volume (τ_D) as

$$R_i = \int_{\tau_D} w_i(LA^* - f)d\tau \quad (2.27)$$

The weight functions are chosen to be equal to interpolating functions according to Galerkin's method. Taking the approximation found in Eq.(2.25), Eq.(2.27) becomes

$$R_i = \int_{\tau_D} v_i L \left(\sum_{j=1}^N A_j v_j \right) - v_i f d\tau \quad i = 1, 2, 3, \dots, N \quad (2.28)$$

This equation generates a system of equations that can be expressed as [74]

$$[ss][A] = [T] \quad (2.29)$$

where, $[A]$ = Column vector of the unknown coefficients A_i .

$[ss]$ is a global coefficient matrix depends on the interpolating functions. Eq.(2.29) describes a deterministic system where there exists an excitation. The elements of these interpolating functions in the i^{th} column and j^{th} row can be expressed as,

$$s_{ij} = \frac{1}{2} \int_{\tau_D} (v_i L v_j + v_j L v_i) d\tau \quad (2.30)$$

$[T]$ in Eq.(2.29) is a column vector whose elements are dependent on the forcing function (f). It is expressed as

$$t_i = \frac{1}{2} \int_{\tau_D} v_i f d\tau \quad (2.31)$$

2.8.5 Solving Finite Element Equations

The linear algebraic equations can be solved by either direct method or iterative method. For PM machines, the electromagnetic characteristics have non-linear characteristics that need to be solved using numerical iterative methods. In this thesis, the FE analysis is conducted by solving the non-linear equations using iterative methods. The most commonly used iterative method for solving FE problems is the Newton-Raphson method. The formulation of Newton-Raphson iteration method for FEA analysis is widely documented and analyzed [75, 78, 79].

2.9 Finite Element Analysis for determining the Machine Parameters and characteristics of the IPMM

All machine modelled in this thesis were created and optimized with FEA. This section describes the steps taken to model the final 42 pole 54 slot concentrated wound IPMM with flat shaped magnets (FSCW IPMM-F) and to determine its performance characteristics. The design process is modelled using CEDRAT-Flux 2D.

The stages of the primary design process are given below:

- Construction of the geometry and assigning the mesh
- Assigning Physics
- Solving the scenario
- Performance Analysis

2.9.1 Construction of the geometry and assigning the mesh

To reduce heavy processing and computational time, a designer needs to determine the symmetry of the model. Basic symmetry can be of two kinds [74].

- xy symmetry: In this case, the magnetic phenomena are assumed to be identical with x,y plane normal to the z -axis.
- Axial symmetry (r,z)/Periodicity: The magnetic phenomena are considered to be identical on each semi-plane (r,z) obtained by a rotation around the z -axis.

For 2-D FEA, x,y symmetry was not applied to the design. For rotational machines, axial symmetry can be employed in almost all cases. The two IPMM's developed in this thesis had two different periodicities. For the distributed wound 42 pole IPMM, the axial symmetry was found to be 17.14° that is one pole pitch of the machine. This means that for every 17.14° , the stator, and the rotor will have the same configuration. For every 17.14° , the phase coils are equally distributed around the stator. This means the geometry of the IPMM can be designed to just $1/42$ of the full machine. As for the concentrated wound 42 pole IPMM, the axial symmetry was found to be 120° . Fig. 2.15 shows the geometry of both the machines drawn with respect to the axial symmetry.

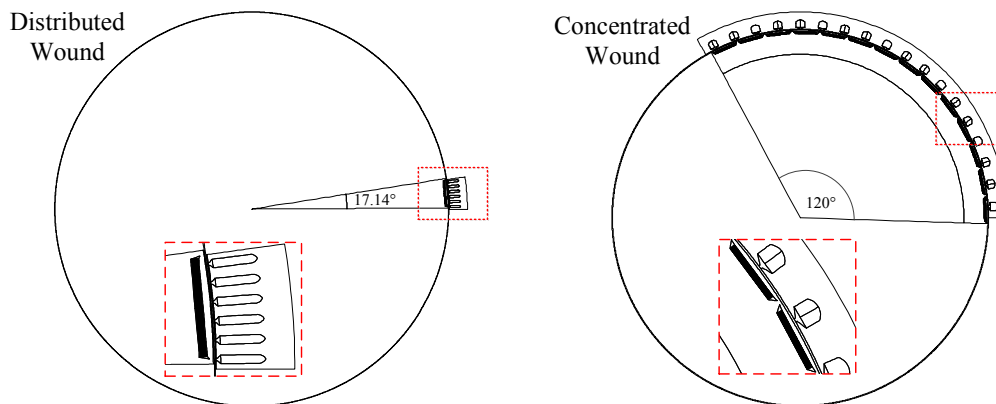


Fig. 2.15. Distributed and Concentrated Wound 42 pole IPMM

After completion of the geometry, a mesh is created. Assigning the right value of elements in the geometry for forming the mesh is important as it affects the accuracy of the solution. A smaller mesh results in higher accuracy but requires more elements in the geometry thus take longer computational time. On the other hand, large meshing of

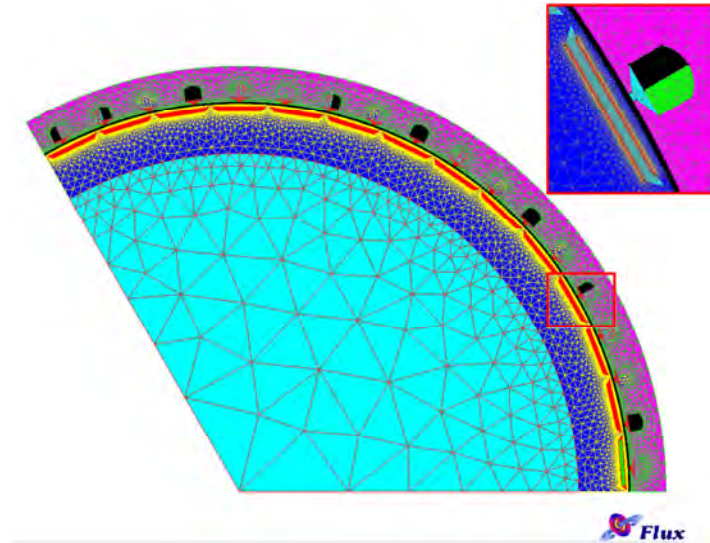


Fig. 2.16. Meshing of the prototype 42 pole IPMM

the geometry could end up giving imprecise results. For this reason, the designer has to analyze in the region of the machine that has the highest ramp in field variation. This means, the mesh should be dense in areas where the field variation is high (i.e. the air-gap region, slot opening, magnet edges, etc.) and least dense where the change in field is comparatively constant (i.e. near the boundary region, inner shaft region, etc). The mesh across the geometry should be well proportioned to avoid imbalance in the results. Fig. 2.16 shows the mesh structure for the prototype 42 pole concentrated wound IPMM.

2.9.2 Assigning Physics

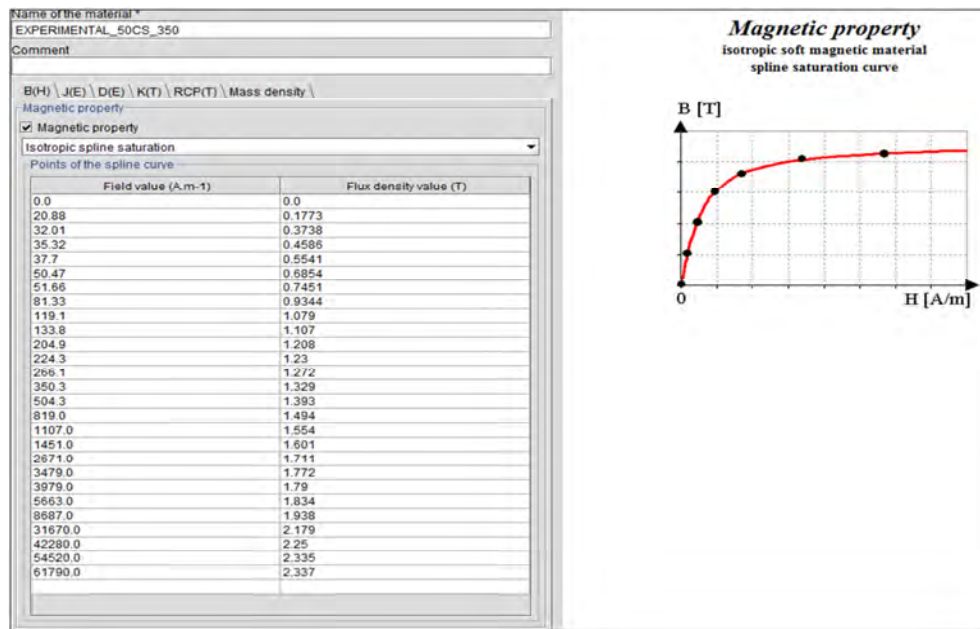
The physical properties are assigned to each region after the completion of the mesh. Table 2.3 shows the material of each region that was applied to the FSCW IPMM-F.

The magnetic materials are characterized by the B-H curve. The magnetic property of the isotropic soft magnetic material is defined by a spline saturation curve shown in Fig. 2.17(a). This soft magnetic material (for this case is non-oriented silicon steel) is

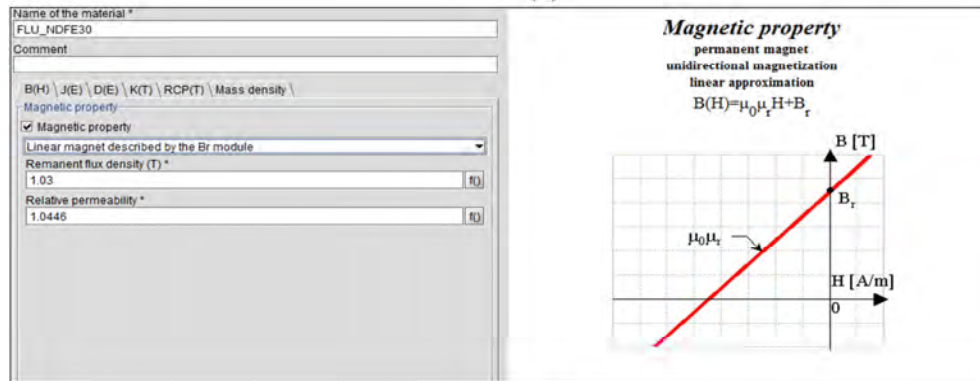
assigned to the rotor and the stator of the prototype. As for PM's, the magnetic property is defined in the second quadrant of the B-H curve shown in Fig. 2.17(b).

Table 2.3. Material of each region

Region	Material
Stator & Rotor	Non-oriented silicon steel
Permanent Magnets	NdFeB
Stator slots	Copper
Shaft	Air
Air-gap, Flux barrier	Air



(a)



(b)

Fig. 2.17. Magnetic property of (a) Soft magnetic material and (b) Permanent Magnet

Table 2.4 Mechanical set for the region during FEA

Mechanical set	Type	Regions to assign
Fixed Stator	Fixed	Stator, Slots
Moving Air-gap	Compressible	Air-gap
Moving Rotor	Rotation around one axis	Shaft, Rotor, Magnets, Flux barriers

After the declaration of the B-H characteristics, the magnet orientation has to be defined. The common orientation of the magnets includes radial and ortho-radial. In this research, each magnet was oriented individually. Extensive analysis of material properties has been done in chapter 5.

All the regions of the machine need to be assigned to three different mechanical set. Table 2.4 points out each region to its mechanical set.

2.9.3 External Electric circuit

The current/voltage sources related to the stator winding can be assigned to an external electrical circuit. Each phase of the IPM machine can be represented by a stranded coil in the electrical circuit. A typical 3- ϕ star connected current excitation circuit is shown in Fig. 2.18.

It can be seen from Fig. 2.18, end winding leakage inductance is in series with each phase of the winding. This is because FE 2D analysis cannot represent the effect of end-turn. The value of end turn inductance is calculated by some empirical formula separately and included in the electrical circuit. The dot in every component of Fig. 2.18 represents the direction of current entering the component. In FEA, the two-phase current sources represent the actual three-phase model.

The current sources are described as,

$$i_a = I_{rms}\sqrt{2}\sin(2\pi ft + \gamma) \quad (2.32)$$

$$i_b = I_{rms}\sqrt{2}\sin(2\pi ft + \gamma - 120^\circ) \quad (2.33)$$

where, γ is the torque/current angle.

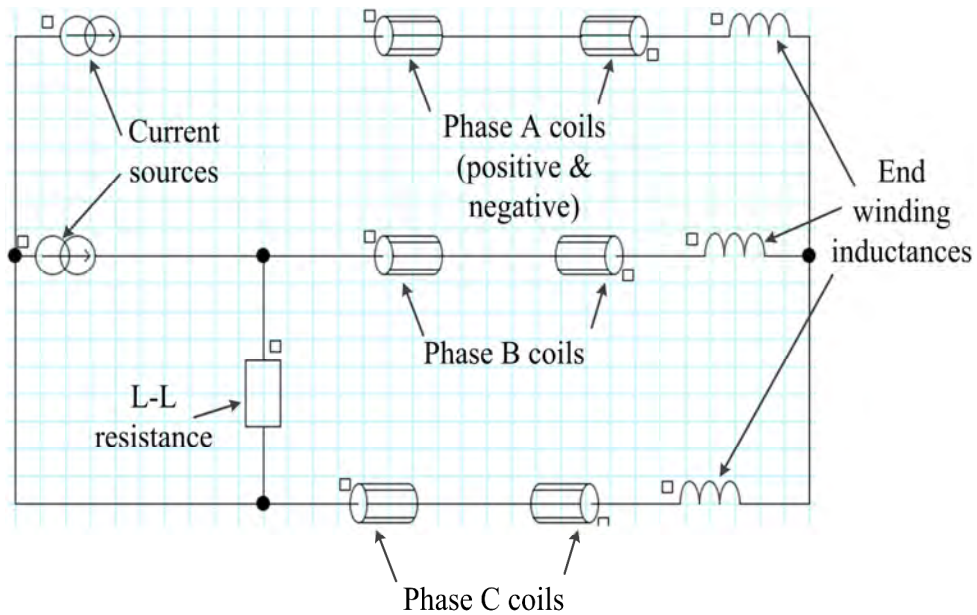


Fig. 2.18. Current excitation circuit in FEA

2.9.4 Parameter Calculation

There are two magnetic applications used for the analysis of the model in FEM.

They are:

- **Magneto-static 2D:** In this application, the input sources are time invariant. The Magneto-static application is used for the analysis of flux density and the MMF for the IPMM. The flux density is measured in a path specified by the designer. For measuring MMF in the prototype, stranded coil conductors with an imposed current is assigned to each phase and the magnets are replaced with air. The post processing of the MMF is done in the same manner as the flux-density, which is by assigning a path in the geometry and measuring the field across it.
- **Transient Magnetic 2D:** In this case, the sources are time-variant. This means that the whole problem consists of solving the problem at discrete time intervals. All the performance analysis of the IPMM's can be conducted using this application. The flowchart for the time stepping solving process is shown in Fig. 2.19.

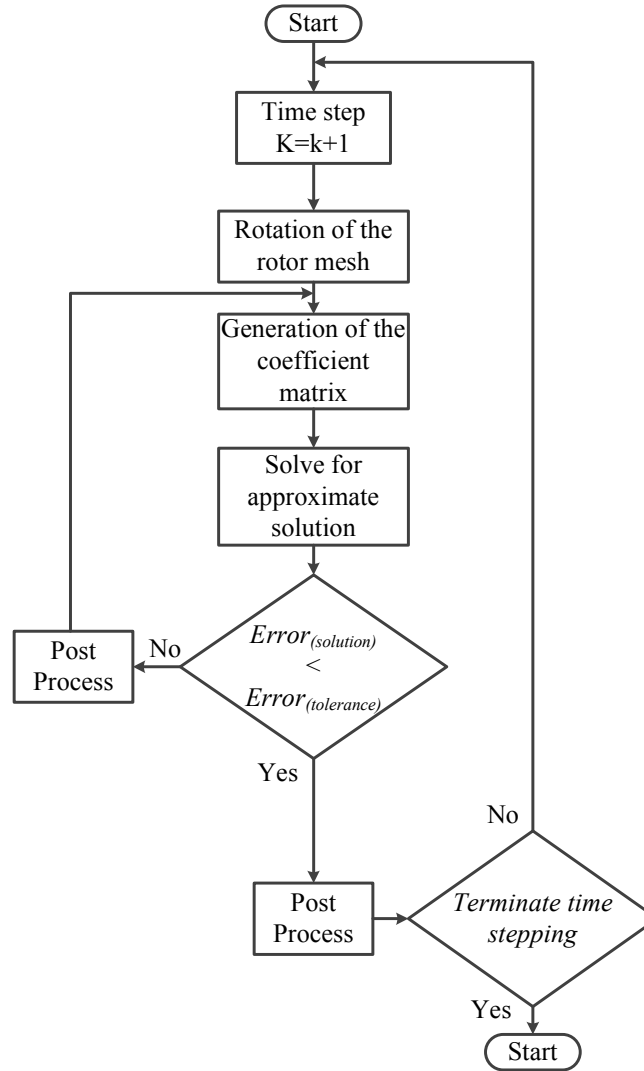


Fig. 2.19. Flow chart for the time-stepping finite element process

Various performance calculations using transient Magnetic 2D are shown below:

Back EMF:

For the analysis of the open circuit back EMF, a fixed rotor speed is assigned to the mechanical set of the rotor. The electrical circuit for the EMF calculation is given in Fig. 2.20. The phase and the L-L resistance are of infinite values of resistance.

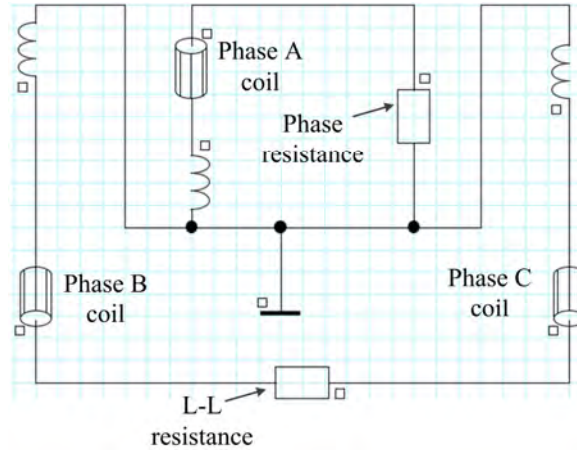


Fig. 2.20. EMF circuit in FEA

In Cedrat-Flux 2D, the value of time steps needs to be given correctly in order to get the correct results. The three parameters of time step are:

- *Initial value of time step:* If a computation has 48 time-steps over an electrical period (180°), the initial value of time step is calculated as

$$t_{ini} = \frac{360^\circ / P_p}{\omega_r \times 48 \times 6} \quad (2.34)$$

where,

P_p = Pole pairs;

ω_r = Rated speed (RPM);

For the prototype CW IPMM design, the value of time step is found to be $4.166e-4$ s.

- *Study time limit:* The study time limit is fixed to 1 for solving all scenarios.
- *Limit number of time steps:* The study time steps are limited to 48 steps.

Cogging torque:

The analysis of cogging torque requires no external electrical circuit. As the cogging torque values are quite small, special consideration is needed to limit the influence of finite element numerical errors due to meshing of the domain. Cogging

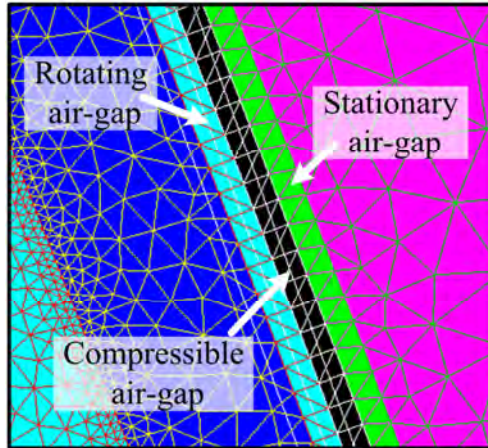


Fig. 2.21. Meshing of a 3-layer air-gap

torque is produced by the magnet flux linked across the air-gap. For this reason, a fine mesh needs to be done across the air-gap to achieve the exact cogging torque. A 3-layer air-gap with a moving air-gap between the two layers is drawn in FE to analyze the cogging torque, thus giving accurate cogging torque values. Fig. 2.21 shows the evenly sub-divided 3-layer air-gap for the prototype design.

In Cedrat-Flux 2D, the cogging torque is found by rotating the rotor slowly at 1/6 rpm. The computation is conducted for two slot pitches of the prototype. For the 54 slot machine, 2 slot pitches corresponds to 13.33° mechanical degrees. For 60 time steps, 1 second corresponds to 1 mechanical degree with an imposed rotor speed of 1/6 rpm. The time step turns out to be 0.222s with a maximum number of time steps to 61s. The study time limit is set to 100 seconds.

Developed torque:

The generated torque/power can be calculated by using the electrical circuit shown earlier in Fig. 2.18. The current sources have been already described in Eq.(2.32) and Eq.(2.33). The frequency of each sinusoidal current is dependent on the rotating speed of the rotor.

It is calculated as,

$$f = \frac{w_r \times P_p}{60} \quad (2.35)$$

The time steps for solving a scenario to achieve torque/power are of the same value as solving the EMF scenario.

2.10 Conclusion

In this chapter, various PM synchronous machines for wind turbine application were reviewed in detail. Two main research areas that are relevant to this work are studied: the IPM machine topology, and various winding layout of the IPMM.

This chapter also provides the wind turbine characteristics of both HAWT and VAWT. For D-D topology, the machine rotating speed is equal to the turbine speed. Due to the elimination of the gearbox, the number of poles has to be increased to decrease the rated speed of the machine. Using the power-speed curves of the HAWT & VAWT, the rated speed of the turbine is determined which in turns gives the number of poles of the machine at rated frequency. The selection of rotor poles has been discussed in chapter 3.

Finally, a brief overview on 2D Finite element analysis of the electric machine is presented. The process of developing the FE models for the studied machines is described in steps. The FE model of each machine design was used to estimate various performance indicators such as the cogging torque, L-L EMF, Power, Losses, etc.

CHAPTER 3: Design of a High-Pole Number IPMM with Distributed Windings

3.1 Introduction

This chapter presents a systematic design optimization process of a 4kW interior permanent magnet machine (IPMM) with distributed windings (DW) for low-speed applications. It discusses various steps that were taken to minimize the cogging torque, torque ripple and the overall size of the machine. All critical parameters and output characteristics for all designs are compared using CEDRAT FLUX 2D FEA. To increase the accuracy level of the FE computation results, the air gap region is meshed using three layers of finite elements.

3.2 Initial analysis of a 4-pole IPMM configuration

According to the basic electrical machine theory, the torque of an electric machine is directly proportional to the air gap flux density. To have a good dynamic response and high torque density, air gap flux density should be maximized. The aim of this study is to understand the air-gap flux density of the IPM machine with a small pole pitch angle that is due to the large pole numbers. Initially, in order to determine the most suitable magnet pole configuration, the air-gap flux density of the conventional flat-shaped IPM machine, segmented IPM machine and a V-shaped IPM machine of 4-pole were calculated and compared.

The air-gap flux density of a 4-pole conventional flat-shaped IPM machine, flat-shaped segmented IPM machine, and V-shaped IPM machine were calculated in their respective FE model. Since, the primary aim is to determine the most suitable magnet

configuration, the calculation of the air-gap flux density was carried out for open circuit condition. Fig. 3.1 shows the IPMM having the above mentioned magnet configurations. The geometrical dimensions of the stator and basic rotor were taken from an equivalent industrial induction motor from ABB. The key dimensions of the rotor and stator are listed in Table 3.1.

The material for stator and rotor is chosen to be non-oriented electrical steel. The permanent magnet material is NdFeB with a remanence of 1.1 T. The flux barriers on the edge of the magnets as seen in Fig. 3.1 are provided to prevent the magnetic short circuit between adjacent magnet poles.

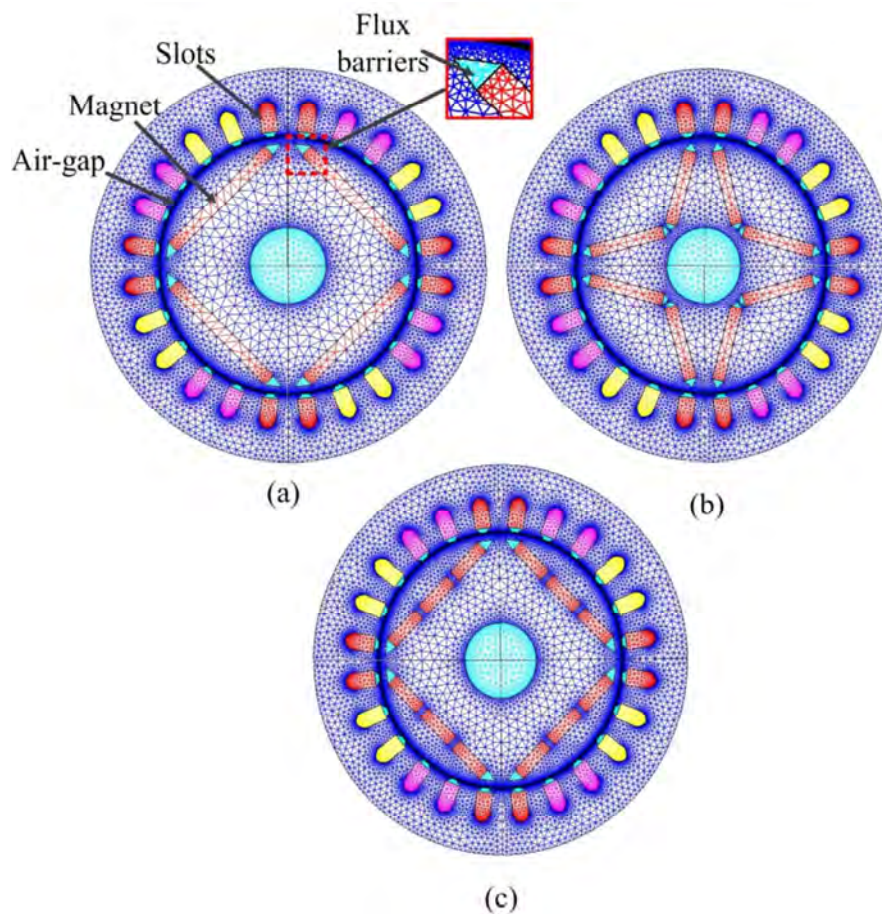


Fig. 3.1. 4 pole IPM machines with (a) Flat-shaped Magnets; (b) V-shaped Magnets and (c) Segmented Magnets

Table 3.1 Main dimension of the 4 pole IPMM with DW

Dimension	Value (mm)
Outer diameter of stator	125
Inner diameter of stator	82
Outer diameter of rotor	81
Diameter of shaft	24
Total number of pole	4
Length of magnets	43.58
Thickness of magnets	5
Number of slots per pole	6
Width of slots	5.3
Slot opening	2.56
Slot Depth	11.45
Stack/Axial length	50.308

The main difference between the conventional IPMM and the segmented IPMM is in the shape of the magnets. For segmented IPMM, the magnets are split into 2 or more sections for one pole. The iron bridges between the magnet sections provide an additional path for the magnet flux canalization during flux weakening operation as found in [80] and shown in Fig. 3.1. A segmented IPMM was designed with the same dimension as described in Table 3.1, but with 3 segmented magnets in one pole as shown in Fig. 3.2. Two iron bridges between the magnet segments are of the same size each with a width of 2mm.

V-shaped IPMM consists of a segmented magnet in one pole with a V-angle between the two magnets as seen in Fig. 3.1. Initially the flux density and the cogging torque of the V-shaped IPMM with a V-angle of 155° was analyzed with the conventional flat shaped IPMM and the segmented flat shaped IPMM.

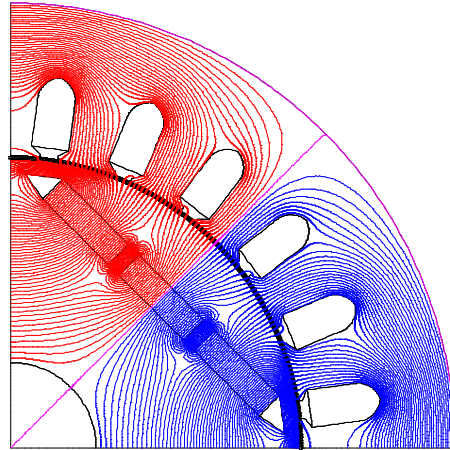


Fig. 3.2. Flux distribution of a four pole segmented IPMM (one pole)

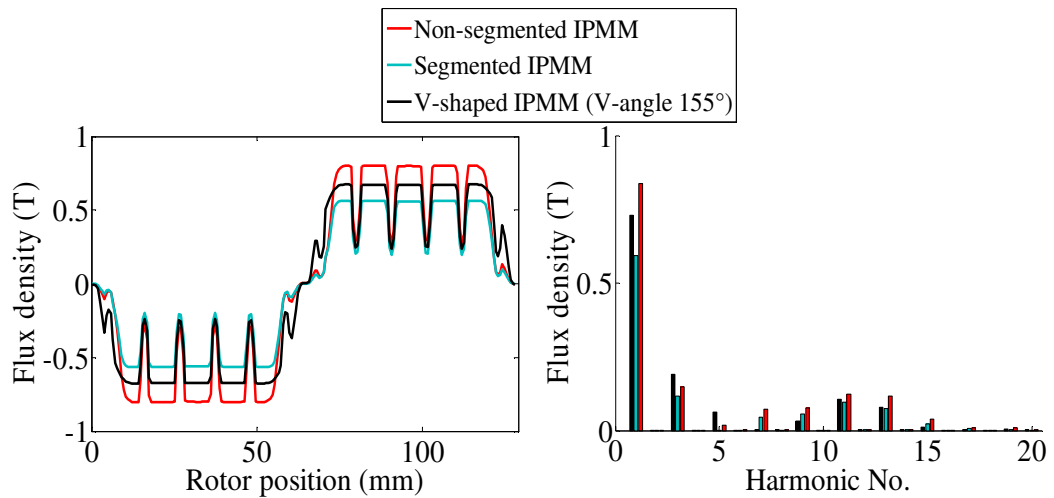


Fig. 3.3. Air-gap flux density of a 4 pole non-segmented IPMM, Segmented IPMM and a V-shaped IPMM

Fig. 3.3 shows a comparison of the air-gap flux density between a four pole non-segmented IPMM, Segmented IPMM and a V-shaped IPMM (V-angle 155°). As seen from Fig. 3.3, the non-segmented conventional flat shaped IPMM generates the highest fundamental component of the flux density of 0.84 T in the air-gap. The fundamental component of air-gap flux density of the segmented IPMM was found to be 0.59 T that is 30% less than the flux density achieved with a flat shaped IPMM of similar dimension.

The segmented IPMM showed relatively less flux density in the air-gap as the magnets are segmented into 3 pieces having iron bridges in between which causes lesser flux to reach the air-gap. As for the V-shaped IPMM, the flux density is found to be 0.73, which is significantly lower than the non-segmented IPMM. Fig. 3.4 shows the variation in cogging torque for all three designs.

The cogging torque of a V-shaped IPMM is found to be very low compared to the other two designs. The non-segmented flat shaped IPMM generates the highest cogging torque of 0.1 Nm peak. It can be seen from Fig. 3.4 that the IPMM with segmented magnets develops lesser cogging torque in comparison to the non-segmented flat shaped IPMM. This is because cogging torque is proportional to the air-gap flux and, in this case, the air-gap flux density is substantially lower for the segmented IPMM.

In the previous study, the V-angle for the V-shaped IPMM was chosen to be 155°. Altering the V-angle will change the air-gap flux density as well as the developed cogging torque of the machine. The next study focuses on the effect of V-angle on the flux density and cogging torque of an IPMM. The flux distribution for all V-shaped IPMM designed for this analysis is shown in Fig. 3.5.

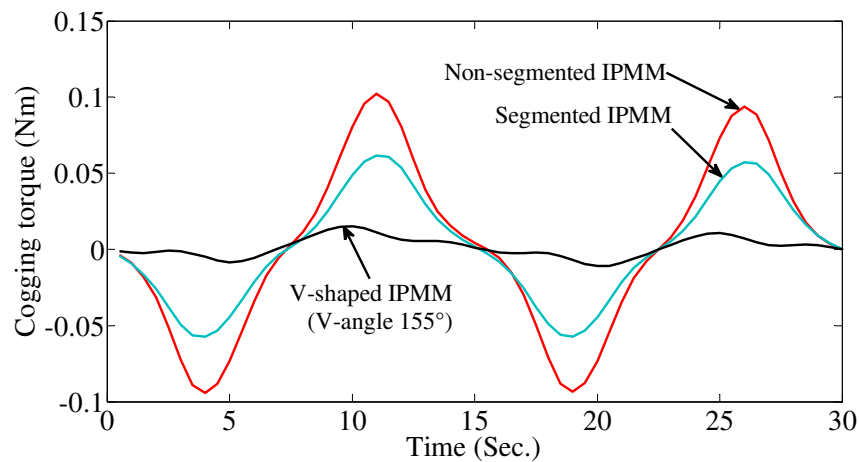


Fig. 3.4. Cogging torque comparison between the 4 pole non-segmented, segmented and the V-shaped IPMM

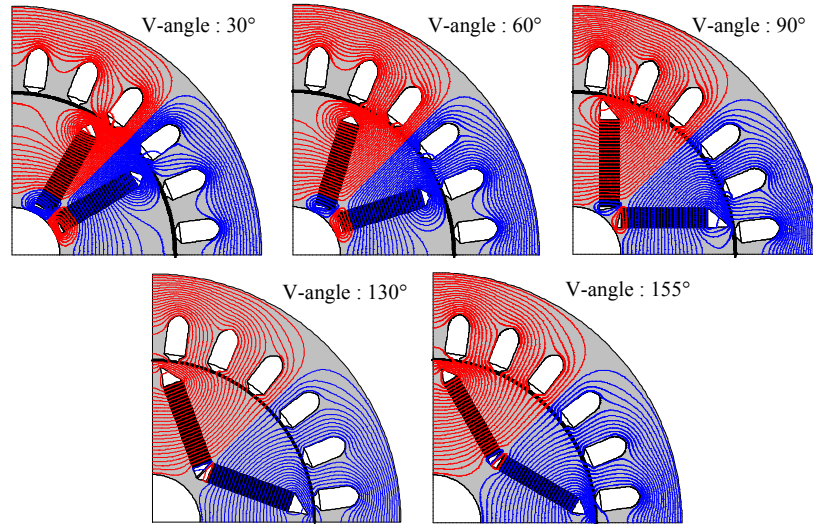


Fig. 3.5. Flux distribution of V-shaped IPMM's for various V-angles

Different air-gap flux density can be obtained for a V-shaped IPM machine by changing the position and V-angle of the magnet in the rotor pole. Fig. 3.6 shows the air-gap flux density plot of the V-shaped magnet IPMM for different V-angle. The FFT plot of the air-gap flux density is given in Fig. 3.7.

In this study, while decreasing the V-angle between the magnets, the magnet volume is kept constant which makes the distance between magnets of two adjacent poles higher. At this particular region between two adjacent magnet poles, no flux is crossing the air-gap, and the flux density becomes zero as seen in Fig. 3.6. This makes the average flux density to be lower for the v-shaped IPMM's with smaller V-angles. On the other hand, V-shaped IPMM with small V-angle generates higher peaks in their air-gap flux density waveform. The study of the V-shaped IPMM with various V-angles with the same magnet volume exhibits that there exists an optimum V-angle for which the fundamental component of flux density is maximum. As for this case, the four-pole V-shaped IPMM with a V-angle of 90° is the optimum angle at which the fundamental component of flux density is maximum at 0.83T.

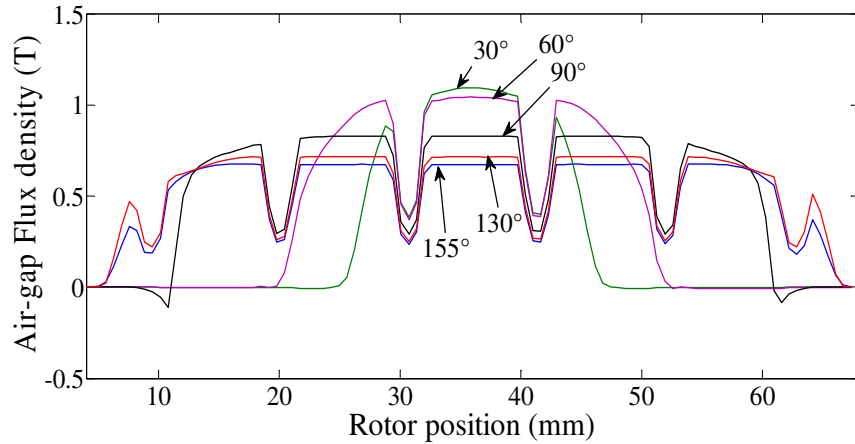


Fig. 3.6. Air-gap flux density of a V-shaped IPMM for various V-angles (30°,60°,90°,130°,155°)

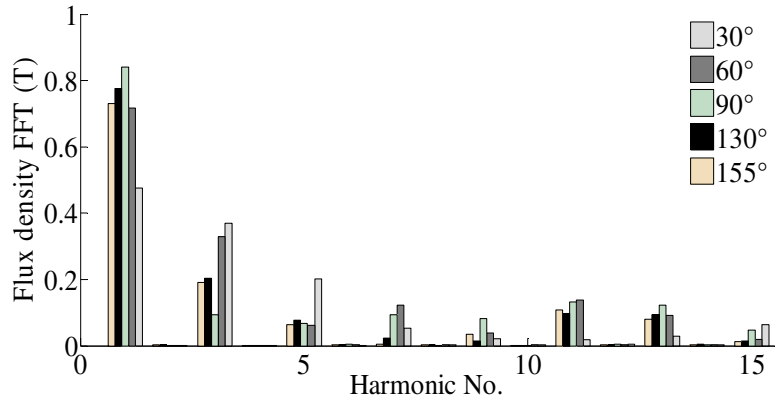


Fig. 3.7. FFT spectrum of the air-gap Flux density of 4 pole V-shaped IPMM

This comparison indicates that the fundamental component of flux-density reaches its peak at a certain V-angle. It should be noted here that due to mechanical limitation, V-angle cannot be made too small. According to [81], decreasing the value of V-angle will increase the air-gap flux density and will have a smaller optimal split ratio for higher torque. A small optimal split ratio leads to a large slot area and a higher electrical loading that increases the probability of demagnetization of the magnets [82]. Fig. 3.8 shows the variation in cogging torque with the change in V-angle for the V-shaped IPMM. It can be seen that the peak cogging torque increases with the reduction of V-angle. The V-shaped IPMM with a V-angle of 155° produces the lowest amount of cogging torque as seen in Fig. 3.8.

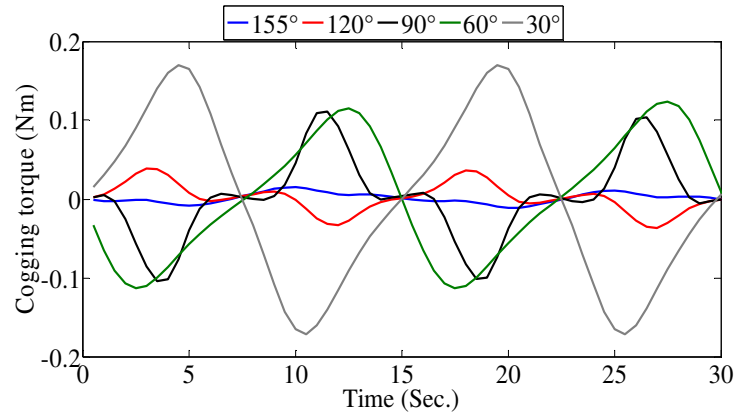


Fig. 3.8. Variation in cogging torque with the change in V-angle for the V-shaped IPMM

The primary focus of this study is to achieve a high air-gap flux density with low cogging torque for various rotor configurations in the IPMM. The flat shaped IPMM was able to provide maximum flux density in the air-gap but with highest developed cogging torque. The segmentation of flat shaped magnets reduces the overall flux crossing the air-gap. This means the overall power rating of the IPMM will be considerably lower. For these reasons, no further analysis has been done with an IPMM with flat shaped segmented magnets. The study shows promising results on the V-shaped IPMM with various V-magnets. More analysis on the V-angle for these machines has been conducted in section 3.3.4.

3.3 42 pole IPMM with Distributed windings (DW)

Pole number is a critical design parameter in machine design. For direct-drive PM machines, the pole number can vary in a very wide range. In chapter two, the wind turbines were designed to obtain a rated power of 4 KW at 8 m/s of wind speed. From the analysis conducted in chapter 2, the wind speed of 8 m/s corresponds to 143 rpm for the direct-drive IPM machine.

The number of poles needed for the IPMM to achieve 143 rpm at 50 Hz can be calculated by,

$$p_p = \frac{60f}{\omega_r} \quad (3.1)$$

where, ω_r is the rated speed of the IPMM and p_p is the number of pole pairs.

From Eq.(3.1), the number of pole pairs was calculated to be 21. Initially, stator and the rotor dimensions were expanded based on the initial 4 pole IPMM. There are a substantial number of free parameters when designing a machine. Some of these parameters need to be restricted in order to have an optimal solution. For initial designing of the IPMM with distributed windings, some of the parameters were limited to a particular value so that other parameters could be optimized to achieve an optimal IPM machine. The following parameters were restricted to the designers' desired values:

- Power of the IPMM is set to 4 KW.
- Rated L-L voltage is fixed in the range of 350-400 volts (RMS).
- Air-gap Flux density range between 0.75- 0.85 T.
- Stack length in the range of 150-200 mm.
- 21 Pole pairs and rated frequency at 50 Hz.

The power and the voltage are set to a certain value depending on the availability of instruments in the lab for experimentation of the machine. The air-gap flux density is directly proportional to the mechanical loading of the machine. The air-gap flux density range is chosen based on existing salient pole machines in the market. All the other free parameters are somehow related to the above restricted parameters. The selection procedures for all of these free parameters are discussed in detail in the forthcoming sections.

3.3.1 Selection of rotor design

For high pole machines, the rotor design has a significant influence on the performance and structure. The rotor radius of the machine was first carefully determined based on magnetic and electric loading of the proposed DW IPM machine. It is a established fact that the induced EMF is a function of the rotor radius as given by the following expression,

$$E_{ph} = \frac{\pi}{2\sqrt{2}} \times \frac{B_{\max} \times l \times \omega \times R_{ro} \times N_s \times K_w}{P_p} \quad (3.2)$$

where,

B_{\max} = Peak air-gap flux density;

l = Stack length;

$\omega = 2\pi f$;

R_{ro} = Radius of the rotor;

N_s = Total Number of turns of the conductor;

K_w = Winding factor and

P_p = Pole pairs;

It can be seen from Eq.(3.2), that if the air-gap flux density is kept constant, the EMF solely depends on the R_{ro} , N_s and P_p . A typical l/R_{ro} ratio of a synchronous machine is around 0.35 [83]. The flux density in the air-gap, tooth and the stator yoke at no-load of a machine calculated from the finite element model should be in permissible limits at all times based on the design of the insulation of the machine. At the early design stage, the electromagnetic torque of the IPMM is calculated from the Eq.(3.3) [62].

$$T_e = \sqrt{2}\pi.B_g.l.R_{si}.A_a \quad (3.3)$$

where,

B_g = air-gap flux density;

R_{si} =Stator inner radius;

A_a =electrical loading;

An expression for air-gap flux density, B_δ of the machine can be derived for a constant EMF:

$$B_\delta = \frac{\phi}{2 \times k_1 \times R_{ro} \times l} \quad (3.4)$$

where, k_1 =proportionality constant; ϕ =fundamental flux per pole;

Using analytical equations to determine open-circuit air-gap flux density is difficult for IPMM's as the machine has significant leakage flux and magnetic saturation. In this research, the flux density distribution is obtained using FEA. The electrical loading of the machine can also be defined in terms of number of turns and rotor radius [84],

$$A_a = k_2 \frac{N_s}{2R_{ro}} \times I_r \quad A/m \quad (3.5)$$

where, k_2 =proportionality constant;

The linear current density for small PM machine should be less than 35 kA/m according to [85]. Initially, the IPMM was designed with an electrical loading of 18.8 kA/m calculated using Eq.(3.3) at full load torque. It should be noted here that torque ripple is related to the electric loading of the machine. Electrical loading can be optimized for minimum torque ripple for a given rating of the machine [86]. A detailed analysis of this minimization technique for the proposed machine is discussed in the latter part of this chapter. The winding factor of 1-slot short pitch distributed winding is 0.96. Increasing the dimension of the machine will increase the mass as well as the cost of the overall machine whereas increasing the number of turns will increase the copper loss. Thus, the optimum dimensions and number of turns can be found by minimizing copper loss and volume for a given rated voltage and power.

3.3.2 Air-gap length and Aspect ratio

The length of the air gap of a machine has a significant influence on any PM machine. The air-gap length can be characterized as [85]

$$\delta \geq 7 \times 10^{-7} \times \tau_p \times \frac{A_a}{B_{max}} \quad (3.6)$$

where,

δ = air-gap length;

τ_p = pole pitch and

A_a = Electrical loading;

The air-gap length for all constructed designs in this research varies from 1.1 mm ~ 1.3 mm depending on the desired peak air-gap flux density range of 0.75-0.85T. In machine terms, the aspect ratio is defined as the stack length (l) to the air-gap diameter (D_i) of the machine. For large scale direct-drive PM generators, the optimal aspect ratios are usually lower than 0.6 [87]. Typically, smaller aspect ratios result in greater torque density per volume. In the initial DW IPMM design, the aspect ratio is set to 0.3.

3.3.3 Stator design

Usually, a full pitch winding (i.e. 3 slots per pole) is commonly used in a high pole number machine. However, a full pitch winding also results in higher space harmonics in the magnetomotive force (MMF). Such stator structures are also known to produce higher cogging torque in the PM machine due to the position of the slots with respect to rotor magnet poles. For the selection of appropriate pitch in the DW winding, the air gap flux density and cogging torque were compared between a full pitch (i.e. 3 slot per pole) and 1-slot short pitch winding (i.e. 6 slots per pole). Both the winding layout is shown in Fig. 3.9 for two pole pitch of the DW IPMM. This winding pattern should be repeated 21 times to represent the entire winding. It should be pointed out that for a full pitch DW the fundamental winding factor is 1, whereas, for 1-slot short pitch DW, it is

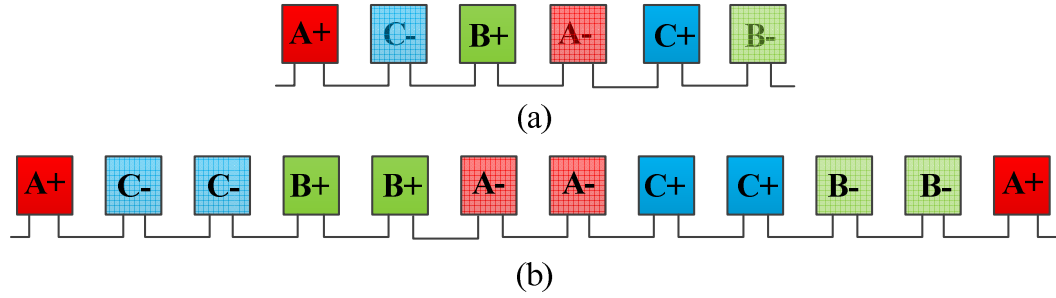


Fig. 3.9. Winding layout of (a) Full pitch DW and (b) 1 slot short pitch DW

Table 3.2 Variation in flux density, Cogging torque and EMF by varying the pitch in DW

	DW-full pitch	DW-1 slot short pitch
Flux density (T)	0.877	0.877
Cogging torque (Nm)	16.27	10.5
Winding factor	1	0.966
L-L EMF (volts)	450.8	440.4

0.966. This shows that an IPMM with full pitch DW winding will generate higher back EMF as compared to a 1 slot short pitch DW of the same geometry.

The comparison of cogging torque conducted by varying the pitch of the DW shows an increase in cogging torque for both flat-shaped and V-shaped IPMM when the windings are full pitched and with the same air-gap flux density. It was found that the air-gap flux density was not significantly affected by the winding pitch, but the cogging torque was higher in a full pitch DW winding. Due to the lower winding factor, the IPMM with 1-slot short pitch winding generates lesser EMF in comparison to the IPMM with full pitch winding. Table 3.2 summarizes these results. As it was found that the set goal of the cogging torque can be achieved by the 1-slot short pitch winding while maintaining the same air-gap flux density as the full pitch winding, therefore, 6-slots per pole i.e. 1-slot short-pitch winding structure was selected.

For a fixed slot depth, the stator outer radius (SOR) increases proportionally with the rotor outer radius. The increase of stator radius is necessary to maintain 6 slots per pole configuration. A reasonable slot and tooth width must be selected so that an

acceptable level of slot fill factor and tooth saturation can be preserved. The thickness of the yoke depends on the dimension of the slots and slot area must suffice to hold required number of conductors of a certain size. The required current density determines the conductor size. Total coil area in a slot can be defined as

$$S_{us} = \frac{N \times S_{cs}}{k_{cu}} \quad (3.7)$$

where,

N = Number of conductors per slot;

S_{cs} = Conductor area;

k_{cu} = Slot-fill factor;

Slot area and geometry were selected based on the required numbers of conductors in the slot to induce the rated voltage and current rating. A typical slot fill factor of 0.35 was considered to calculate the required slot area. A detailed analysis of slot fill factor will be done in chapter 5. It was found that number of conductors per slot is 6 and based on current rating the size of conductors was selected as 3.31 mm. Thus, the required area of the slot was calculated as 55.6 mm². Fig. 3.10 shows the slot dimension in the stator for one slot short pitch distributed winding structure. As the structure of the slots affects the torque ripple, which suggests the optimization of the slot dimensions were necessary for the minimization of torque ripple. This will be discussed in section 3.3.8.

3.3.4 Selection of Magnet structure

For PM machines, various steps need to be taken for optimization of the magnetic loading to have the most compact design. Magnetic loading is directly linked to the structure and the material of the magnets.

3.3.4.1 Selection of Magnet grade:

Magnet remanence is directly proportional to the magnetic loading in PM synchronous machines. This makes the selections of magnet remanence and coercivity a

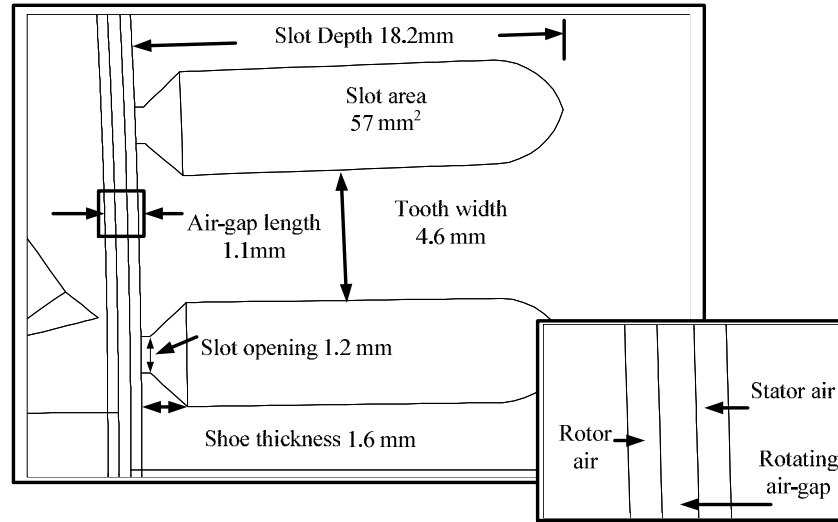


Fig. 3.10 Slot dimension of the DW IPMM

paramount aspect in the design of IPM machine. The varying range of magnet remanence depends on the saturation level of the PM machine. This saturation point depends on the material used for laminating the rotor and stator of the machine.

Table 3.3 shows the permitted flux densities of the magnetic circuit for a standard salient-pole synchronous machine. This table was used as a benchmark for adjusting the magnet remanence and machine dimensions to limit different regions of the machine to become saturated. Fig. 3.11 shows the flux density in the air-gap, tooth and the stator yoke at no-load for the flat shaped 42 pole IPMM calculated from the finite element model that are in permissible limits according to Table 3.3. The V-shaped IPMM with DW also shows similar flux density pattern as of Fig. 3.11.

Table 3.3. Permitted flux densities for standard salient-pole synchronous machines

	Flux density (T) range
Air-gap	> 0.8
Stator yoke	1.0-1.5
Tooth	1.6-2.0
Rotor yoke	1.0-1.5

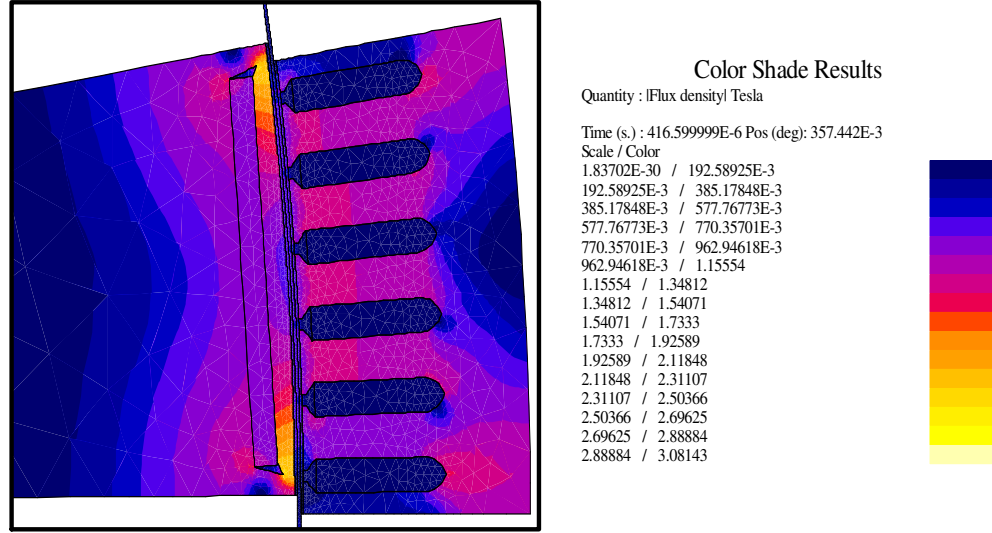


Fig. 3.11. One pole of the flat shaped DW IPMM showing flux density in various regions with color shades.

3.3.5 Selection of pole magnet configuration

The geometric restriction for the value of magnet length is defined by,

$$t_m \leq (R_r - d) \times \tan \frac{\pi}{2P_p} \quad (3.8)$$

where,

t_m =magnet length,

R_r = radius of the rotor,

d =magnet thickness.

According to Eq.(3.8), increasing the pole pairs will reduce the magnet length while by increasing the rotor radius, more geometrical space for magnets with larger length will be possible. To select the right magnet configuration for the 42 pole DW IPMM, the IPMM with V-shaped magnet for various V-angles were analyzed and compared with an IPMM with flat-shaped magnets of the same dimension. The analysis was based on the achieving high air-gap flux density that affects the magnetic loading of the machine and low cogging torque that is one of the primary design goals. Table 3.4 shows the principal dimensions of the machines studied.

Table 3.4. Main dimension of the DW IPMM

Dimension	Values (mm)
Stator Outer diameter	340
Rotor Outer diameter	310
Air-gap length	1.1
Stack length	162
Magnet Volume	$0.11e-3 \text{ m}^3$
Magnet Remanence	1.16 T

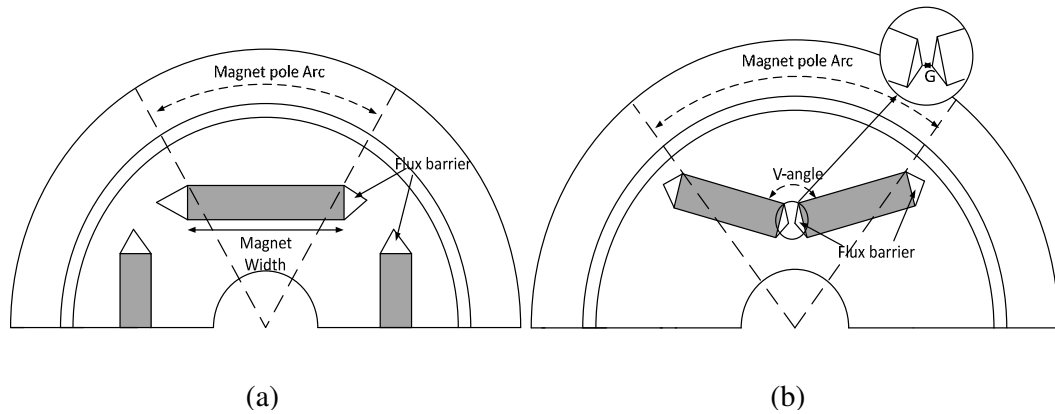


Fig. 3.12. Cross-sectional view of (a) DW IPMM-F and (b) DW IPMM-V

Fig. 3.12 shows the pole pitch of (a) an IPMM with flat-shaped (DW IPMM-F) magnet and (b) V-shaped (DW IPMM-V) magnet. From Fig. 3.12(b), it can be seen that if the magnet pole arc is kept constant while decreasing the V-angle, the width of the iron bridges between the two magnets legs (referred to as “G” in Fig. 3.12(b)) will widen. A large iron bridge in this area will result in leaking of the magnet flux. Therefore, to keep the magnet pole arc and G constant while decreasing the V-angle, the magnet width increases according to Fig. 3.12. Thus, the comparison has been conducted in 2 different stages. Firstly, the magnet pole arc as well as the magnet width is kept constant while changing the gap width between the magnets (G). Secondly, the magnet volume and gap width “G” were held constant while the magnet pole arc was varied. Fig. 3.13 compares the air-gap flux density and the cogging torque of different IPM rotor structures for the first case. It can be seen from Fig. 3.13, that air-gap flux density is the highest for the

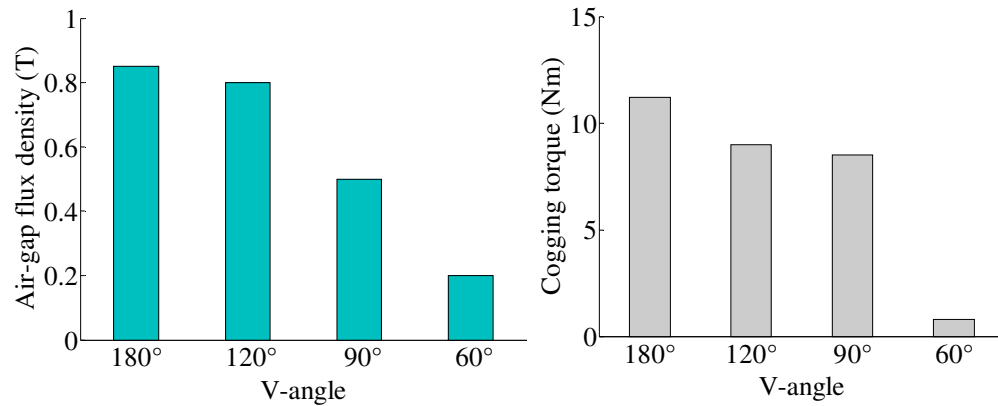


Fig. 3.13. Change in peak Air-gap flux density and Cogging torque with the variation in IPMM rotor structures with magnet arc angle being constant

flat-shaped magnet (it can be considered as a magnet shape with the V-angle of 180°). This is because there is no additional leakage path of G in this configuration. However, the cogging torque is also the highest for this rotor. The minimum cogging torque is found to be 0.8 Nm for a V-shaped IPMM with a V-angle of 60° but the air-gap flux density is unacceptably low (> 0.29 T). Therefore, a trade-off between magnetic loading and cogging torque of the machine is needed. In the second case, the magnet pole arc is varied, but the magnet volume and the gap width between the magnets (G) for the V-shaped rotor structure were kept constant. The variation in air-gap flux density for different rotor structures under this condition is shown in Fig. 3.14. The difference in the fundamental component of air-gap flux density and cogging torque for various rotor structures under this condition is compared in Fig. 3.15. It can be concluded from the comparison that a higher pole pitch produces high fundamental component of air-gap flux density. On the other hand, the peak of the air-gap flux density reduces with higher pole pitch in the machine. By varying the magnet pole arc, it is seen that the cogging torque for the V-shaped IPMM with 120° of V-angle has been reduced to 6.46 Nm while the air-gap flux density remains the same as seen in Fig. 3.13.

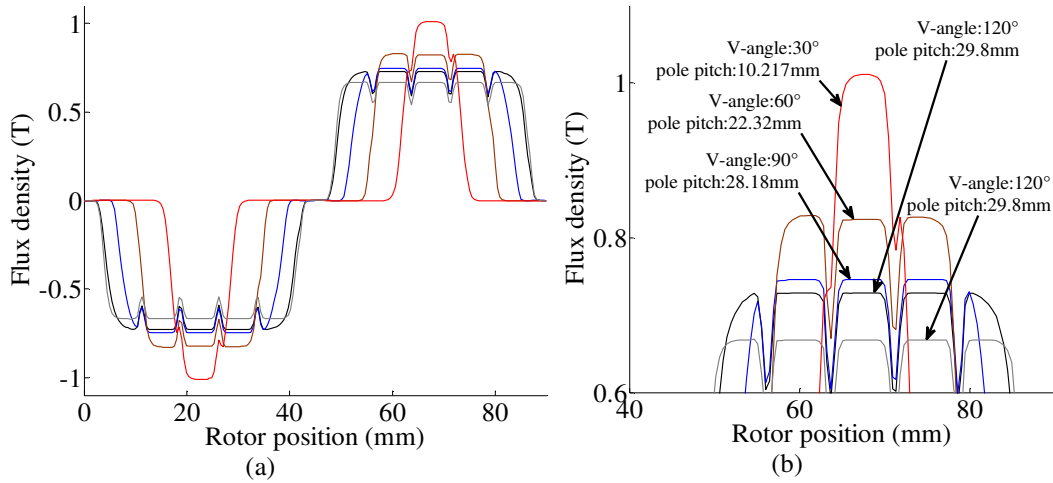


Fig. 3.14. (a) Variation in air-gap flux density with the variation in IPMM rotor structures with constant magnet volume while varying the magnet arc angle; (b) Peak air-gap flux density (Zoomed in)

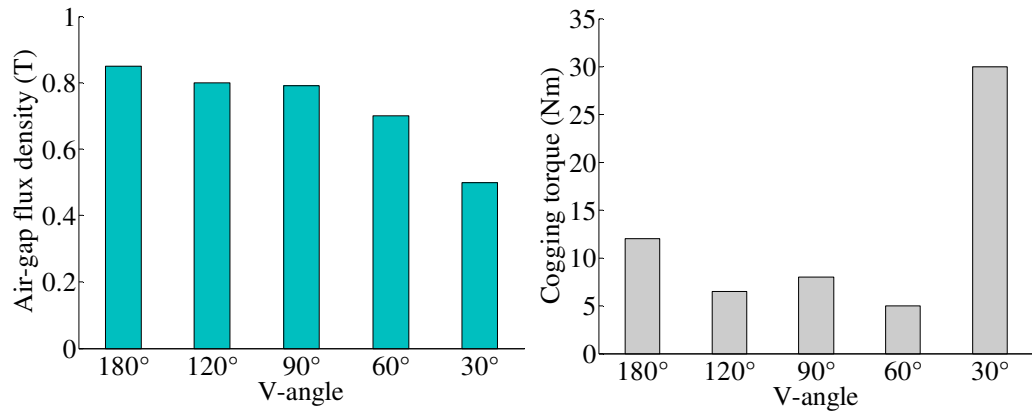


Fig. 3.15. Change in peak Air-gap flux density and Cogging torque with the variation in IPMM rotor structures with constant magnet volume while varying the magnet arc angle.

The minimum cogging torque of 4.18 Nm was found in the V-shaped IPMM with a V-angle of 60° and with a lesser flux density of 0.7 T compared to that of a flat shaped and a V-shaped IPMM with 120° of V-angle. From the above preliminary comparison, there are two clear choices - flat-shaped magnet and V-shaped magnet with 120° V-angle. Further design optimizations were carried out in the finite element models of these two designs to achieve following design objectives:

- Cogging torque (<1% of rated torque)

- low torque ripple (<5% of rated torque)
- High efficiency (>90%)

3.3.6 Minimization of Cogging torque

There are two torque components that affect the output performance of a machine. The first, called Cogging torque, is produced in permanent magnet machine by the magnetic attraction between the rotor mounted permanent magnets and the stator teeth. It contributes to torque ripple, vibration and noise that are undesirable for any machine design. The second component is referred to as torque ripple that will be discussed in the next section.

The PM machines produce a significant cogging torque that causes both vibrations and noise. The effect of cogging torque is the most severe when speed is very low. Minimization of cogging torque is crucial for a direct-drive wind turbine. In a direct-drive wind turbine, at cut-in speed, the wind needs to overcome the cogging torque before any useful electric power can be developed at the terminal of the generator. Cogging torque is higher for compact machines with stronger permanent magnets and smaller air gap [88]. Cogging torque in an IPMM is greater compared to an SPM machine due to the unbalanced magnetic reluctance between the stator and the rotor [89]. The cogging torque is produced in the machine by the magnetic attraction between the permanent magnet poles of the rotor and the stator teeth. A small variation of flux density distribution significantly affects the cogging torque [90]. It can also be defined as the circumferential component of the attractive force that attempts to maintain the alignment of the stator teeth and the permanent magnets [91], shown in Fig. 3.16. Thus, the position of the magnets with respect to the teeth is critical to minimize the cogging torque. Cogging torque is produced when the magnet flux of leading and trailing edge of a permanent magnet enters a slot.

The cogging torque can be approximated as follows [88, 89]:

$$T_{cog} = -\frac{dE_g(\theta)}{d\theta} \quad (3.9)$$

where,

θ = relative position of the PM with respect to the iron core, and

$E_g(\theta)$ = Stored magnetic energy in the air gap of the motor.

Since the magnet pole arc and θ are directly related, the variation of the magnet pole arc length influences the resultant cogging torque. Various cogging torque minimization techniques can be applied in order to reduce its adverse effect on the machine. The conventional cogging torque reduction methods include pole pitch adjustment, PM asymmetry adjustment process, and semi-closed and auxiliary slots of the stator core [92]. Cogging torque can be reduced simply by reducing magnet strength, but it was not considered in this study, as weak magnets will significantly reduce power/torque density of the machine. Another commonly used technique to reduce cogging torque is skewing of the magnets that were also not considered here as it will complicate the manufacturing process. In [91], the cogging torque of an SPM machine has been analyzed by varying the magnet strength, varying the magnet arc length and shifting magnet poles. The results show that cogging torque increases with the rise in magnet arc length and magnet strength in SPM machines. The cogging torque of an IPMM can also be reduced by choosing an optimum flux barrier shape, as stated in [93]. The two methods that were applied in the proposed design to minimize cogging torque were: magnet pole arc variation and flux- barrier variation. As the flux barrier shape also have a significant effect on minimization of the torque ripple, the optimization of flux barrier shape has been conducted in order to minimize both the cogging torque and torque ripple in section 3.3.8.

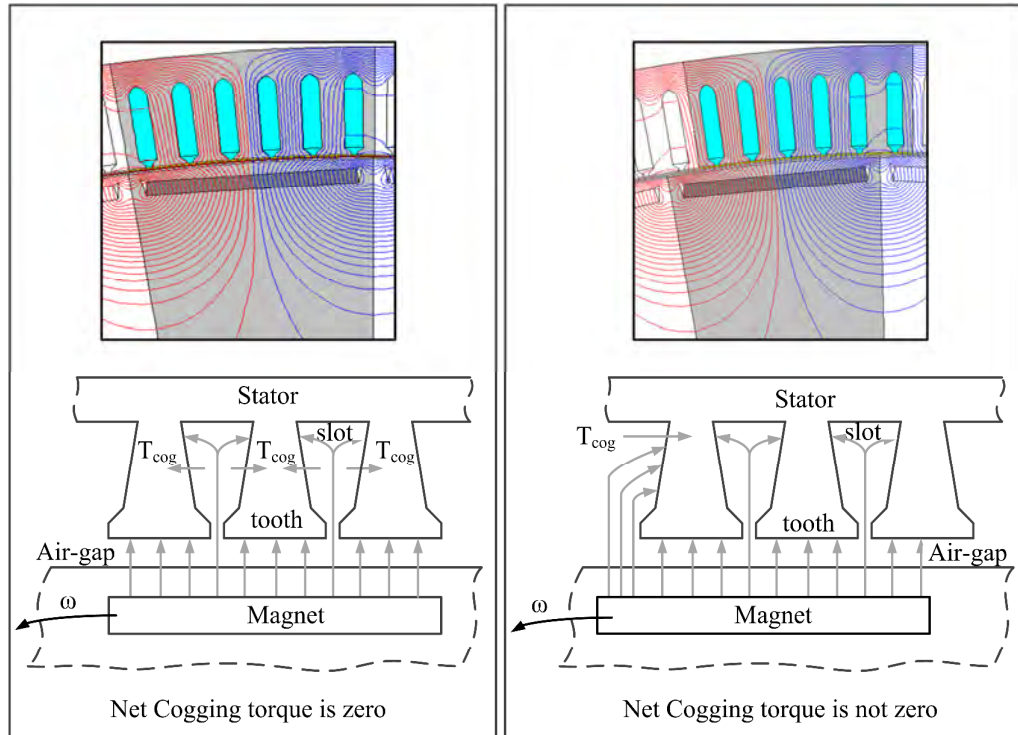


Fig. 3.16. Cogging torque in PM machines

3.3.7 Design optimization for low Cogging torque

The IPMM with the flat shaped magnet rotor structure will be referred here as D-1, and the one with a V-shaped rotor structure with a V-angle of 120° will be referred as D-2. To achieve the same power as of D-1, the stack length of D-2 was increased to 173mm. Except for the difference in the stack length both designs have the same key dimensions as shown in Table 3.4. The winding layout for both the designs is a DW with 1 slot short pitch winding as discussed in section 3.3.3. The reduction of the cogging torque is achieved by changing the magnet arc length in the rotor of the machine. The analysis had been conducted for D-1 to get the optimum magnet arc length to achieve minimum cogging torque in the machine. Table 3.5 shows the change in the cogging torque with various magnet arc lengths for D-1.

The optimum magnet arc length for D-1 was found to be 40.84 mm with a minimum cogging torque of 2 Nm, which is less than 1% of rated torque. Similarly, for

Table 3.5 Effect of cogging torque with the variation in magnet arc length

Magnet arc length (mm)	Cogging torque (Nm)	Air-gap flux density (T)
38.92	10.46	0.785
39	11.1	0.79
40.84	2	0.8
42.2	5.83	0.837

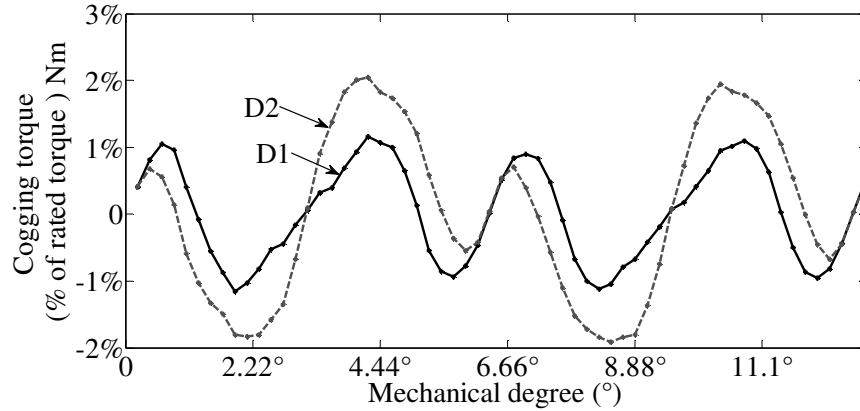


Fig. 3.17. Cogging torque of D-1 and D-2

D-2, the minimum cogging torque was found to be at 4.53 Nm with an optimum magnet arc length of 38.09mm. Fig. 3.17 shows the cogging torque for D-1 and D-2 as a percentage of rated torque with optimum magnet arc found in Table 3.5.

It was found that although the overall magnet arc length of a D-2 was smaller than that of the D-1, the cogging torque is nearly two times higher in the D-2. Thus, in terms of cogging torque, DW IPMM-F (D-1) has better performance. Although pole arc length of DW IPMM-V (D-2) is lower, the total machine volume as well as the magnet volume in this machine is found to be higher to obtain similar performance as the DW IPMM-F (D-1), shown in Table 3.6. Hence, it can be concluded that in terms of cogging torque optimization and also to achieve a more compact design in an IPMM with large pole number flat-shaped magnet with the DW stator i.e. D-1 is a better choice.

Table 3.6 Difference in volume for both the DW IPMM's

	D-1 mm^3	D-2 mm^3
Machine volume	58.8e-3	62.82e-3
Magnet volume	0.8e-3	0.86e-3

3.3.8 Torque ripple minimization

Torque ripple is critical at low speed due to the damping effect of the rotor mass inertia. This ripple is mainly caused by the harmonics in the air-gap flux density. Besides, the saturation in the rotor and stator core due to the magnetic and electrical loading increases the torque ripple component in the developed torque. Typically, the cogging torque and the harmonic contents in the back EMF are minimized to reduce the torque ripple in the developed electromagnetic torque in PM machines [94, 95]. The harmonics in the air-gap flux density are introduced by the slot openings of the stator and the magnet flux-barrier of the rotor in an IPMM. Hence, both the slot opening and the design of flux barriers influence the minimization of the torque ripple. Moreover, in an IPMM, the design of the flux barrier is also essential to reduce unnecessary magnet flux leakage in the iron parts next to the bridges. The effect of flux-barriers on the rotor MMF harmonics has been discussed in chapter 4.

Fig. 3.18 shows three flux barrier design variations proposed in order to reduce torque ripple for D-1 and D-2. As the slot opening has a direct influence on torque ripple, an analysis had also been carried out with various slot opening values along with the three flux barrier designs shown in Fig. 3.18 to achieve reduced torque ripple. In this thesis, the three flux-barrier design for D-1 IPMM are referred to as A, B and C and for D-2 IPMM, it is called a, b and c.

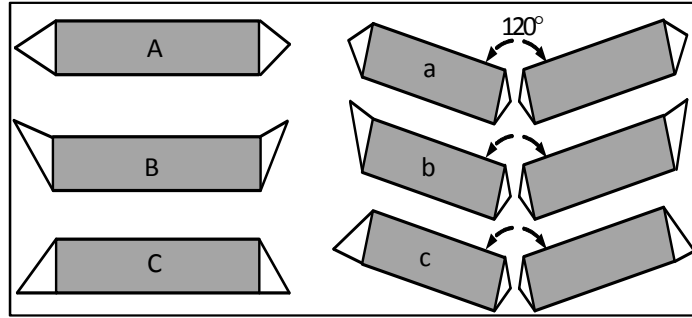


Fig. 3.18. Flux barrier designs

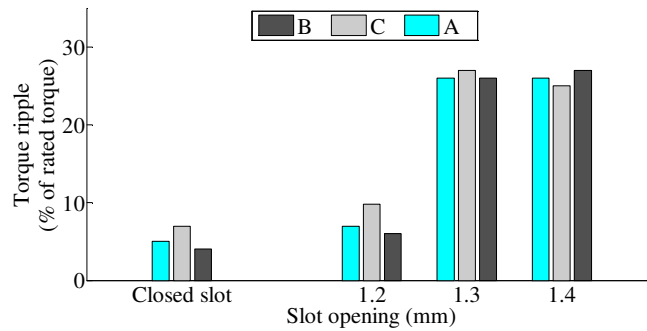


Fig. 3.19. Variations in torque ripple with the change in flux barrier design and slot opening for D-1

The variation in torque ripple for D-1 with the three flux barrier designs shown above is compared in Fig. 3.19. The analysis also included the effect of closed slot in the stator on the torque ripple. The results shown in Fig. 3.19 indicates that the closed stator slots will reduce the torque ripple in comparison to open stator slots. However, the constructions of closed stator slots are troublesome making the insertion of the windings in the slots very difficult. For this reason, closed slots in the stator were not considered in this research.

For all three flux barrier designs in open slot stators, the torque ripple is found to be the lowest when the slot opening is 1.2 mm. The minimum torque ripple for D-1 was found to be 6% of the total rated torque with a flux barrier design of “B” and a slot opening of 1.2 mm. The air-gap flux density of D-1 under this condition is compared in Fig. 3.20 with a slot opening of 1.2 mm to ensure that the air-gap flux density is still

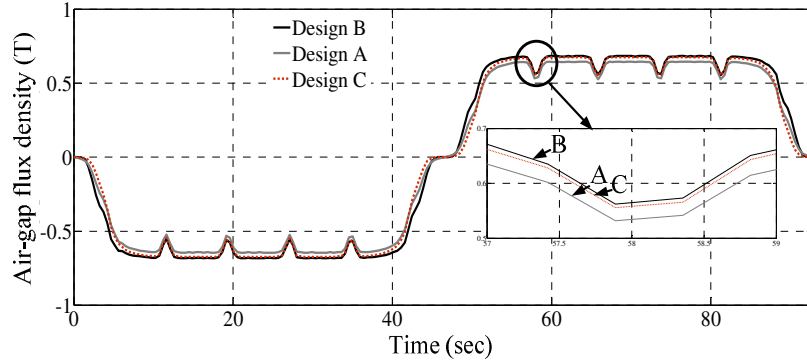


Fig. 3.20. Air-gap flux density of the prototype machine for three flux barrier designs mentioned in Fig. 3.18

within the design range with the selected barrier design and slot opening. The FFT analysis of the air-gap flux density for Design “B” with all three slot opening is showed in Fig. 3.21. Design “B” produces the minimum total harmonic distortion (THD) in the air-gap with a slot opening of 1.2 mm.

The fundamental component of Design “B” is 0.8 T, which is found to be higher than the other two flux barrier designs (A and C). Thus, it can be concluded from this study that the flux barrier design “B” reduces the unnecessary flux leakage in the iron ribs and will be able to generate higher torque than design A and C while producing the lowest torque ripple. The variations in torque ripple for D-2 with the three flux barrier designs shown in Fig. 3.18 are compared with respect to three different slot openings in Fig. 3.22. As for D-2, the minimum torque ripple was 14.4% of the rated torque with the flux barrier design of “b” and a slot opening length of 1.3 mm. However, this value of torque ripple is still much higher than the set design goal discussed in section 3.3.4. The ripple of torque can also be expressed with respect to the EMF harmonics. If the cogging torque and the magnetic saturation is neglected, the torque ripple can be shown as [96],

$$T_{ripple} = 2\sqrt{(\hat{E}_7 - \hat{E}_5)^2 + (\hat{E}_{13} - \hat{E}_{11})^2 + (\hat{E}_{19} - \hat{E}_{17})^2 + (\hat{E}_{25} - \hat{E}_{23})^2} / \hat{E}_1 \quad (3.10)$$

where, E_n is the amplitude of the n^{th} order harmonic component of the phase back-EMF.

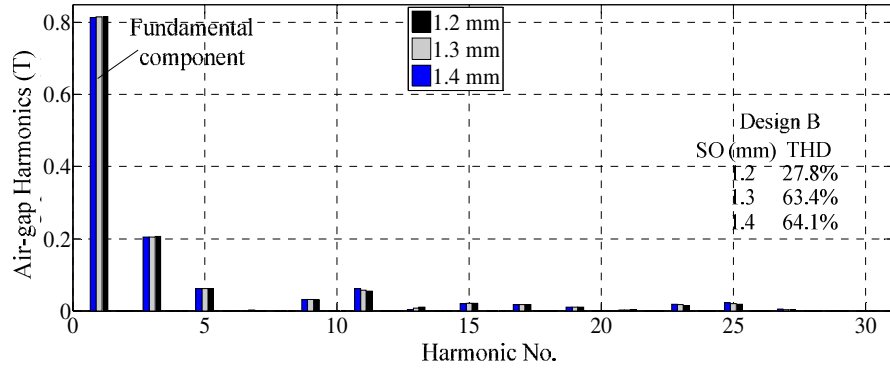


Fig. 3.21. FFT analysis of air-gap flux density for D-1 with a flux barrier Design ‘B’ at various slot openings.

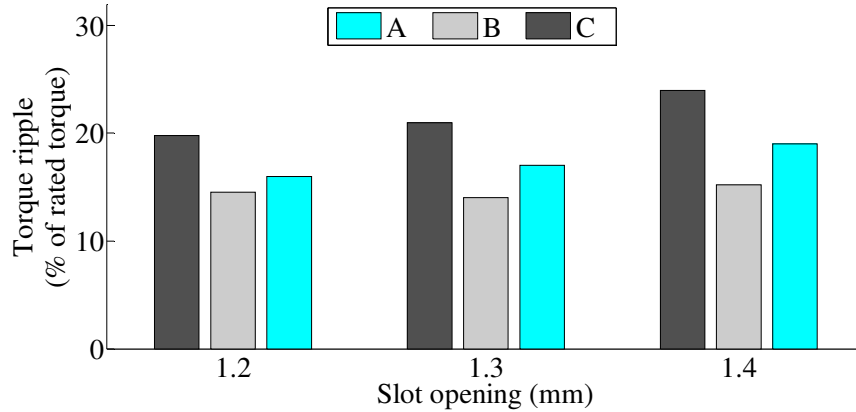


Fig. 3.22. Variations in torque ripple with the change in flux barrier design and slot opening for D-2

Assuming the back-EMF consists of only fundamental, 5th, 7th, 11th and 13th harmonics, it will induce a 6th and 12th order harmonic ripple in the torque waveform [84]. This means that the torque harmonics will be influenced by the 6th and the 12th order torque ripple. According to [84], the trade-off between electrical and magnetic loading influences the EMF harmonics which in turn affect the torque ripple. An analysis has been conducted for D-1 by varying the electrical loading of the machine. As mentioned earlier in the definition of electrical loading given in Eq.(3.5), it is the function of rated current and number of turns per phase. By keeping the rated current constant but by changing the number of turns per phase, electrical loading can be varied.

However, reduction of the number of turns will affect the induced voltage and torque unless the active length of the machine is increased. Hence, the active length was adjusted to get the same RMS voltage and torque output as before while reducing the number of turns per phase. To accommodate the conductors in the slots, the slot depth was also adjusted. Fig. 3.23 shows the change in the 6th and 12th order harmonic component of torque ripple with the variation in the number of conductors per slot (N) for D-1.

The plot in Fig. 3.23 shows that the 6th order harmonic content is lowest when the number of conductors per slot is 6. On the other hand, the 12th order harmonic content is highest when N=6. Further FFT plot of the torque waveform when N=6 (Design A) & N=7 (Design B) is shown in Fig. 3.24. In the FFT of the Fig. 3.24, the DC component of the torque is excluded to show the harmonics clearly. From Fig. 3.24, it can be seen that the 12th order harmonic is higher for Design B that produces a peak-peak torque ripple of 9% of the rated torque. On the other hand, Design A has higher 6th order harmonic but the peak-peak torque ripple is 6% of the rated torque. Hence, it can be concluded that the reduction of 6th order harmonic is more important for reducing peak-peak torque ripple. This suggests in keeping the number of conductors per slot to its previous value of 6 which produces a torque ripple of 6% of rated torque for D-1. The FFT plot of the torque waveform for D-2 when N=6 & 7 is shown in Fig. 3.25. The minimum torque ripple was found to be 14.4 % at N=6 turns per slot.

The effect of slot dimension on the 6th order EMF harmonics has been analyzed in [84]. This means that the torque ripple can also be optimized by varying the slot dimensions in the stator. The stator slot depth was previously adjusted according to the slot area needed to accommodate the coils. The slot opening has been adjusted in this section to minimize the torque ripple.

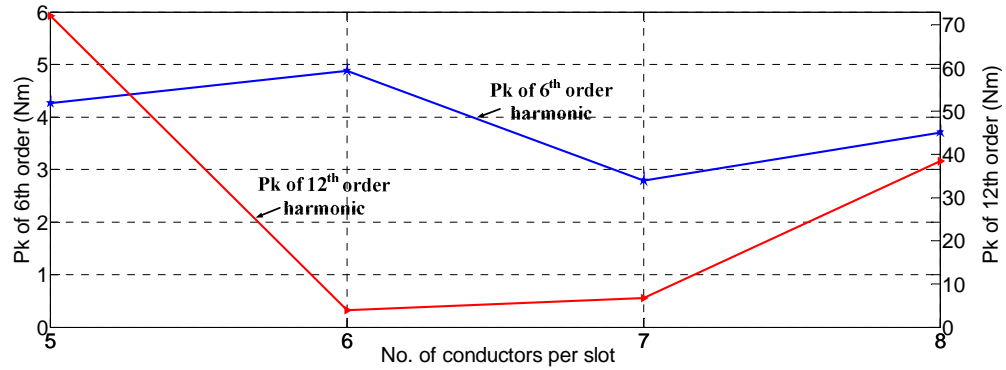


Fig. 3.23. Variation in 6th and 12th order torque ripple with the change in the number of conductors per slot (N)

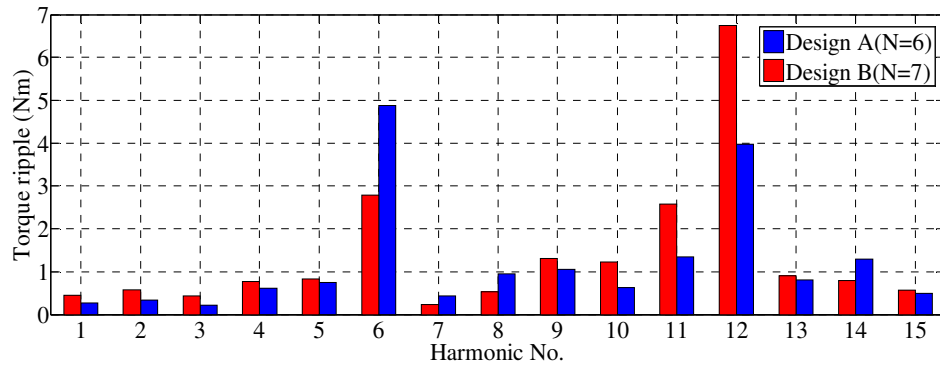


Fig. 3.24. FFT of the developed torque for D-1 when N=6 and N=7

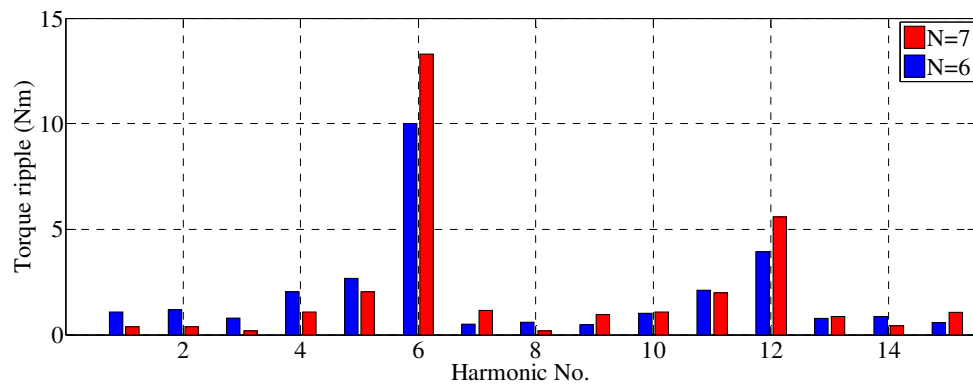


Fig. 3.25. FFT of the developed torque for D-2 when N=6 and N=7

The effect of shoe thickness (shown in Fig. 3.10) on torque ripple was also investigated in this research. Table 3.7 displays the variation of the torque ripple due to the change in the 6th order harmonic content in back EMF for various shoe thickness. The minimum torque ripple for the proposed D-1 was found to be 6% of the rated

Table 3.7 Variation in torque ripple with the change in shoe thickness for D-1

Shoe thickness (mm)	1.6	1.7	1.9
6th order EMF Harmonic	4.9%	5.2%	5.3%
Torque ripple	6%	6.8%	6.8%

torque with a shoe thickness of 1.6mm. Similarly for D-2, the shoe thickness for lowest torque ripple was found to be at 1.6 mm.

3.3.9 Simulation results

After appropriate optimization of the barrier and slot opening, the air-gap flux density, EMF and the developed power were recalculated for both designs- D-1 and D-2 using FE model. Table 3.8 shows the key specifications and typical parameters of both models. As mentioned earlier, to achieve the same power rating in the two designs, the stack length of the design D-2 was increased by 6.8%. The chosen rotor and stator core material (grade M270-35A), is a non-oriented silicon steel with a thickness of 0.35mm. It has a saturation point at 1.6T and core losses of 2.7 W/kg at 1.5T/50Hz [97]. The flux density waveforms of both the machines designed are shown in Fig. 3.26. The peak fundamental air-gap flux density is found to be 0.8 T for D-1 and for D-2, it is 0.76 T. Fig. 3.27 displays the L-L back EMF of D-1 and D-2. The line to line back EMF of D-1 is found to be 370 volts (RMS) with a total harmonic distortion (THD) of 4.82%. As for the L-L EMF voltage for D-2, it is 360 volts with a THD of 4.96%. Fig. 3.28 shows the L-L EMF spectrum analysis of D-1 and D-2.

The RMS line current is set to 6.5 A for both the designs. The maximum torque per ampere (MTPA) condition under current control was simulated in the FE model to calculate the developed power and torque at rated speed.

Table 3.8 Key parameters of the DW IPMM

Items	
Rated Power	4 KW
Rated Voltage	370 V
Rated Current	6.5 A
Speed	143 RPM
Number of poles	42
Number of slots	252
Number of conductors per slot	6

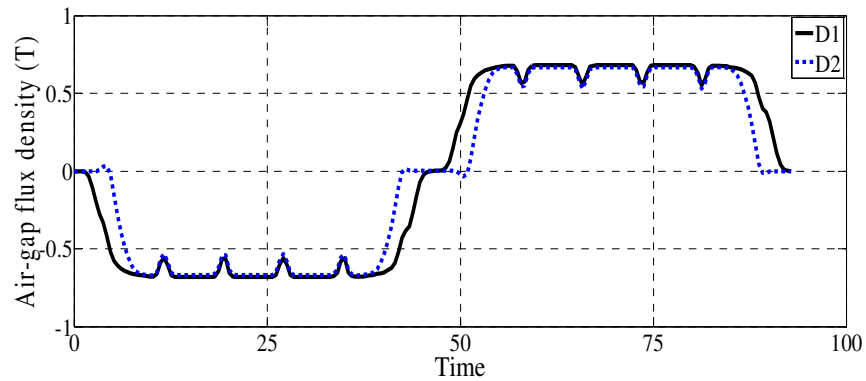


Fig. 3.26. Air-gap flux density of D-1 & D-2

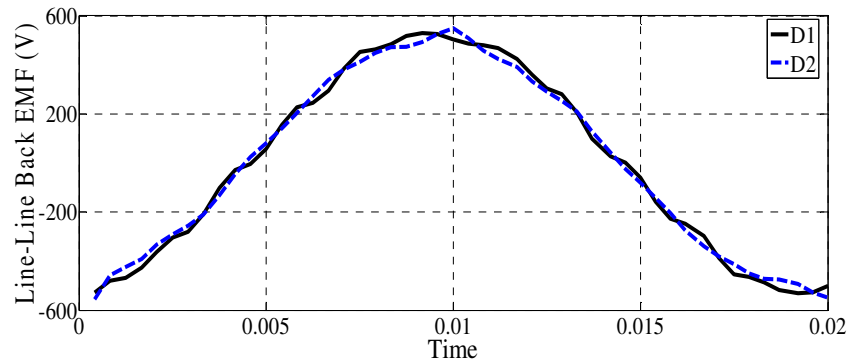


Fig. 3.27. Line-Line Back EMF

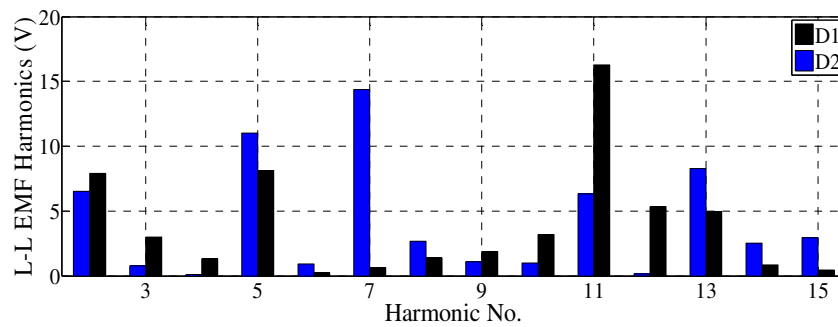


Fig. 3.28. Spectrum analysis of the L-L EMF of D-1 and D-2

The coupled circuit and the analysis procedure for simulating the developed torque have been already shown for an IPMM machine in chapter 2. The current angle for MTPA is found to be 3° for D-1 and 5° for D-2. This indicates that the saliency in both machines is low. Fig. 3.29 shows the electrodynamic torque of both the machine design. The total developed power of D-1 is 4137W with a total torque of 276 Nm at rated speed. D-2 has a total power of 4048 W with a total torque of 270 Nm at rated speed. This indicates that even with a larger machine volume for D-2, it generates 2.1% less power than D-1. Fig. 3.30 shows FFT of the developed torque for D-1 and D-2. The variation in peak of the developed torque with respect to the torque angle (Γ) for D-1 is shown in Fig. 3.31. As stated before, the torque ripple for D-1 is 6% of rated torque, whereas the torque ripple for D-2 is 14.4%.

From Fig. 3.30, it can be seen that 6th harmonic component has the highest magnitude that is dominating in production of torque ripple. This is due to the fifth and seventh harmonics of the back-EMF [86], already explained in section 3.3.8. The next highest torque harmonic is of 12th order.

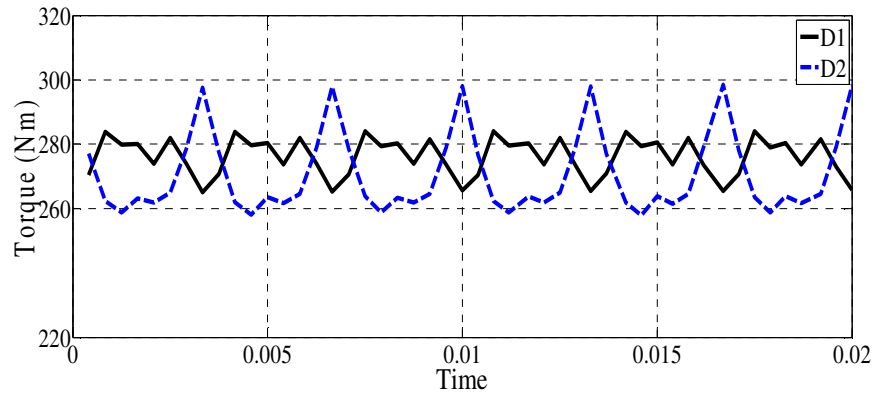


Fig. 3.29. Total developed torque

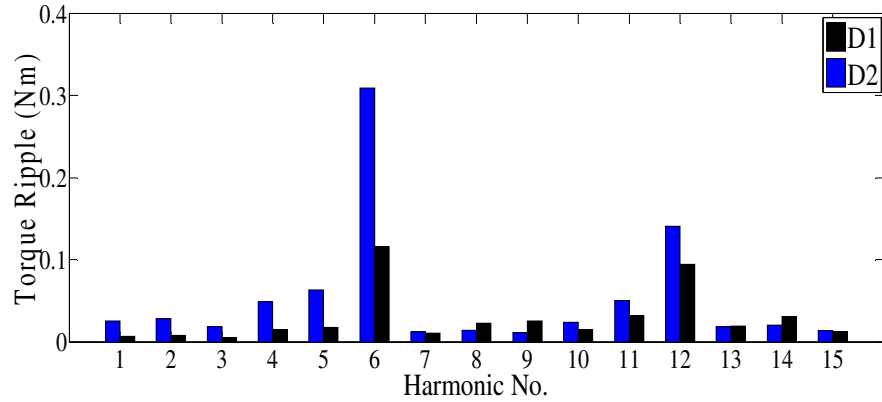


Fig. 3.30. FFT of the developed torque

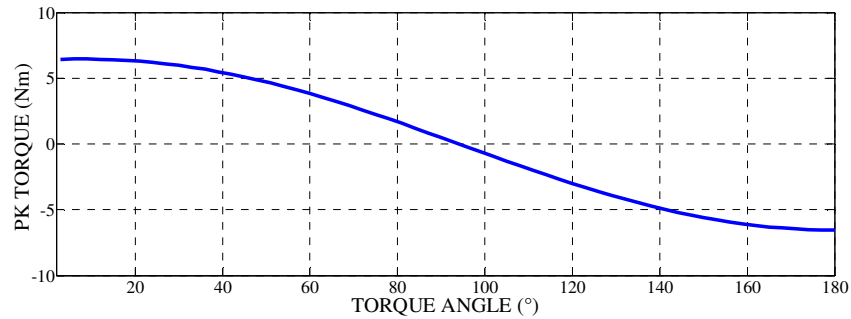


Fig. 3.31. Variation in peak electrodynamic torque with respect to the torque angle for D-1

Torque ripple produced by these 6th and 12th order harmonics can be eliminated in principle by generating an inverse torque component through appropriate modulation of the stator current as described in [98] where a very high bandwidth current controllers were proposed for high-frequency torque ripple compensation. However, this study has not been conducted in this research. The torque ripple can be minimized further by applying various design technique explained in [98, 99]. It can also be reduced by using particular winding layout in stator [86]. Future research will focus on analyzing these techniques into reducing the torque ripple for DW IPM machines.

3.3.10 Losses in the DW IPMM

In this section, the iron losses in the stator and rotor and resistive losses in the conductors of the winding were studied. No mechanical losses were investigated. Fig.

3.32 shows the B-H characteristics curve and the loss characteristics of M270-35A (Core material of the stator and the rotor for D-1 and D-2).

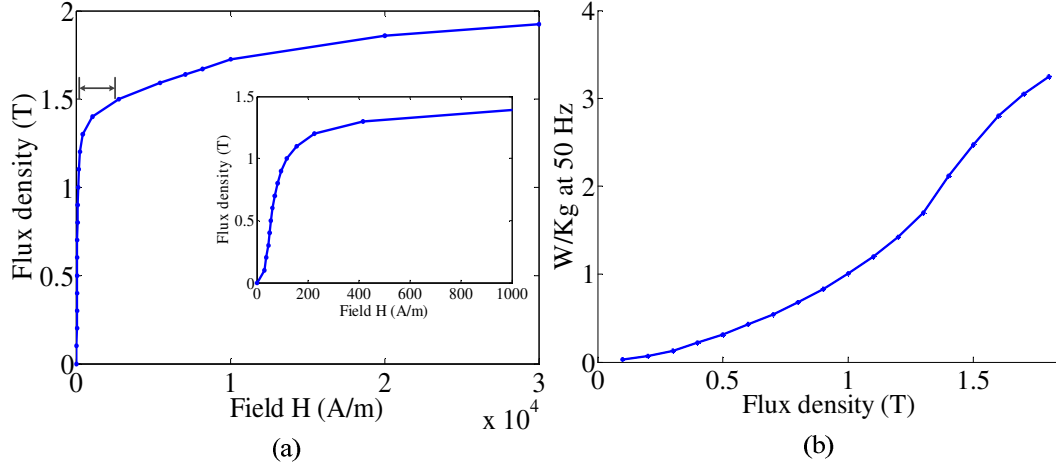


Fig. 3.32. (a) B-H characteristics curve and (b) loss characteristics of non-oriented silicon steel M270-35A

The stator and rotor iron loss in the machine can be estimated using Bertotti's loss model as given below,

$$p_{iron} = \underbrace{k_f k_h B_{max}^2 f}_{\text{Losses by hysteresis}} + \underbrace{k_f \frac{\pi^2 \sigma d_i^2}{6} B_{max}^2 f^2}_{\text{Classical losses}} + \underbrace{8.67 k_f k_e B_{max}^{1.5} f^{1.5}}_{\text{Losses in excess}} \quad (3.11)$$

where,

k_h = Hysteresis loss coefficient;

k_f = Fill factor = 0.97;

k_e = Loss in excess coefficient;

B_{max} = Peak air-gap flux density;

f = electrical freq = 50 Hz;

σ = Conductivity = 1923077 s/m;

d_i = Thickness of steel iron = 0.35e-3 m.

The density of silicon steel M270-35A is 7650 Kg/m³. The coefficients of Bertotti's loss model have to be accurate in order to achieve the correct core loss of the machine

in FE. Applying the formula to 2 different points in Fig. 3.32 will give two set of equations for two unknowns. k_h and k_e are found to be $50.069 \text{ W s T}^2 \text{ m}^{-3}$ and $1.383 \text{ W (T s}^{-1})^{-3/2} \text{ m}^{-3}$ respectively. The loss curve of silicon sheet steel M270-35A is plotted in Fig. 3.33 with the new coefficient, which is then compared with the loss curve found in CEDRAT Flux-2D material database.

The coefficients found using Bertotti loss model are used to analyze the core loss of the machine in FE. The resistive losses in the copper conductors can be expressed as,

$$P_{cu} = 3I^2 R \quad (3.12)$$

where,
 R =Conductor resistance;
 I^2 = Stator Current;

Fig. 3.34 & Fig. 3.35 show the calculated copper losses and iron losses for D-1 and D-2 for different load settings at rated speed. It can be seen that 94% efficiency can be achieved at full load for D-1, whereas for D-2 it is 93.78%. Efficiency and power at full load for various speeds were also calculated for both the machines and shown in Fig. 3.36. For both the machines, the maximum efficiency is achieved at rated speed as can be seen in Fig. 3.36.

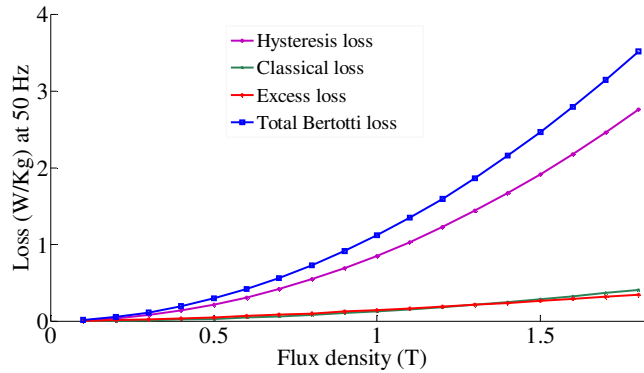


Fig. 3.33. Individual loss elements of the Bertotti loss model using M270-35A silicon steel for D-1

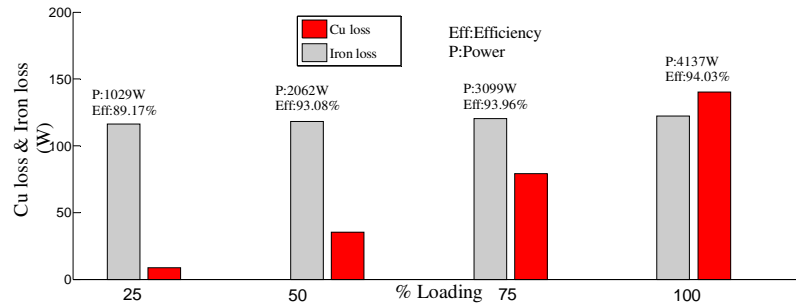


Fig. 3.34. Cu. losses & Iron losses versus percentage of loading for D-1

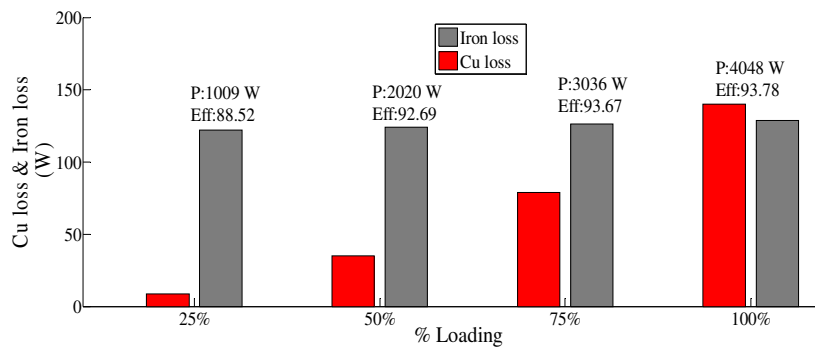


Fig. 3.35. Cu. losses & Iron losses versus percentage of loading for D-2

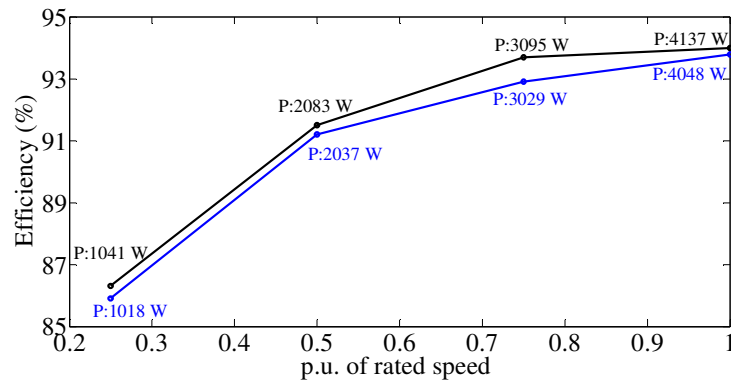


Fig. 3.36. Efficiency versus P.U. of rated speed for DW IPMM-F (black) and DW IPMM-V (blue)

3.3.11 Inductance and saliency ratio of the DW IPMM

Saliency ratio (ξ) given by Eq.(3.13), contributes to the additional reluctance torque that is additive to the total machine torque. In an IPMM, the saliency is greater than 1.

It is defined as,

$$\xi = \frac{L_q}{L_d} \quad (3.13)$$

where,

L_q = q-axis inductance;

L_d = d-axis inductance;

Measuring the inductance in distributed winding IPMM is a straight forward task as the rotor can be easily positioned according to the d - and q -axis flux paths shown in Fig. 3.37. By measuring the flux linkage at these particular locations, the inductances can be measured easily. The equation for calculating L_d and L_q are given below:

$$L_d = \frac{\lambda_d - \psi_{pm}}{i_d}, i_q = 0 \quad (3.14)$$

$$L_q = \frac{\lambda_q}{i_q}, i_d = 0 \quad (3.15)$$

where, $\lambda_{d,q}$ = d,q axis flux linkage, $i_{d,q}$ = d,q axis current and ψ_{pm} = PM flux linkage;

In IPM machines, the flux linkages are influenced by self-saturation and cross saturation effects [100]. Thus, it is crucial to consider these impacts while estimating the flux linkages to calculate the inductance. The calculation of the inductances has been only conducted for the distributed wound flat shaped IPMM. In FE, by varying the

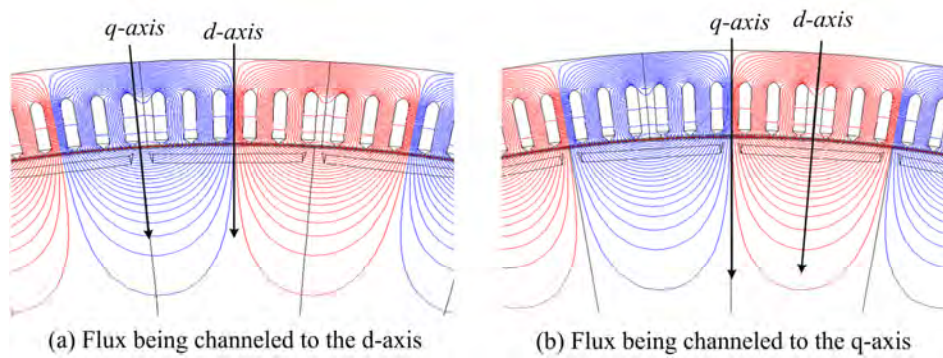


Fig. 3.37. 42-pole DW IPMM-F with flux being channeled to (a) d -axis and (b) q -axis

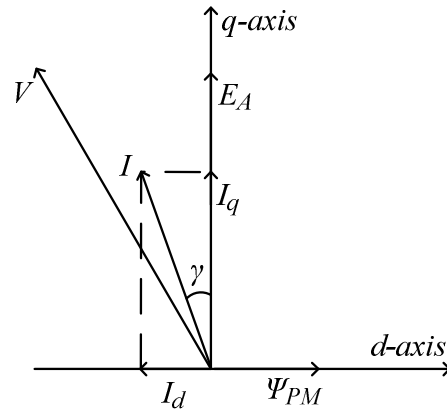


Fig. 3.38. Basic phasor diagram of the IPM machine

current angle (γ shown in Fig. 3.38) from 0° to 90° , the IPMM is excited with q - or d -axis current, respectively.

Using, Eq.(3.14) and (3.15), the value for L_d and L_q of the DW IPMM-F are found to be 6.5 mH and 15mH respectively. This makes ξ to be 2.3 for the DW IPMM-F. The calculation of inductance by applying the AC standstill test for DW and CW IPMM's are shown in the chapter 4.

3.4 Conclusion

This chapter presents the design of a low-speed distributed wound IPMM with minimum cogging torque and torque ripple. At first, design comparisons between various rotor geometries of an IPMM were performed. Analysis of the results showed that the flat shaped IPMM and the V-shaped IPMM with a V-angle of 120° were clear choices for the proposed designs for achieving an optimal design.

The selection process of each design parameter was described in this chapter to model an efficient IPM machine. The procedure for determining these key parameters have helped us to design all IPMM's that are modelled in the thesis. In the latter part, the study conducted in FE analysis displayed that the flat shaped IPMM shows overall

better performance with respect to the V-shaped IPMM when designed for low-speed applications. Compared to the commercially available direct-drive PM machine of similar power rating, the optimized DW IPMM design shows significant advantages. Several steps were taken to minimize the cogging torque and torque ripple. It was shown that the DW IPMM-F has reduced cogging torque, low torque ripple, higher efficiency and lesser dimension as compared to a DW IPMM-V. The torque ripple for DW IPMM-V is high and may not be able to satisfy design specifications of low-speed applications. Hence, no further analysis was conducted with this model. The presented comparison brings to the conclusion that the DW IPMM-F is an attractive solution for low-speed applications.

The next chapter will build upon the findings of the IPMM key parameters to model an IPMM with a concentrated wound structure.

CHAPTER 4: Design of a High-Pole Number IPMM with Fractional-Slot Concentrated Wound Stator

4.1 Introduction

The chapter presents the design process of an interior permanent magnet machine (IPMM) with fractional-slot concentrated windings (FSCW) for high pole numbers. The primary aim of this study is to investigate the suitability of the concentrated winding structure in the stator and the flat-shaped or V-shaped magnets in the rotor poles. For a fair comparison, the selection of the key dimensions of the proposed FSCW IPMM was kept similar to that of the DW IPMM described in chapter 3. Various steps were taken to minimize the cogging torque and torque ripple for the FSCW IPMM so that design goals can be achieved. An extensive comparison was conducted between the FSCW IPMM modelled in this chapter with the DW IPMM designed in chapter 4. This chapter also presents the calculation of the inductances and saliency ratios of both DW and FSCW IPMM's using an AC standstill test like condition in the 2D finite element analysis.

4.2 Fractional Slot Concentrated winding (FSCW) and its structure

The Concentrated winding (CW) had not been popular in the past since an FSCW machine produces higher harmonic contents in the armature MMF distribution compared with a DW machine. These harmonics cause flux variations in the air-gap, and, as a result, increases rotor losses, vibrations, and extra heating. In case of a low-speed induction machine, the rotor cage actively interacts with these stator MMF

harmonics which is not preferable for acceptable performance [72]. However, for a PMSG, only the principal harmonic of the stator MMF interacts with the main harmonic of rotor PM flux density. The unwanted MMF harmonics in an FSCW PMSG increases the leakage inductance. This increase in leakage inductance results in higher core losses. The leakage inductance also results in a lower characteristic current that extends the flux weakening region in the IPMM [64]. Distributed winding stators have a higher winding factor compared to the concentrated winding stator resulting in a higher electromagnetic torque compared to FSCW design. However, in recent years, it has been shown that through appropriate choice of slot and pole combinations [58], the FSCW stator can produce sinusoidal EMF waveform with a high winding factor and smooth average torque. As for FSCW layout, the stator windings can be of

- Single layer

Advantage: Single layer produces high self-inductance and almost zero mutual-inductance leading to good fault-tolerant capability [57, 101].

- Double layer

Advantage: Double-layer FSCW has smaller torque ripples and lower magnet eddy current losses due to lower air-gap MMF harmonic components as compared to a single layer FSCW [102, 103].

Fig. 4.1 shows the winding layouts for a single and double layer FSCW. Double layer FSCW machines can be further categorized as traditional FSCW and modular FSCW. The winding arrangement for traditional FSCW is as shown in Fig. 4.1. Fig. 4.2 shows the winding arrangement for a modular FSCW. In comparison to traditional FSCW, modular FSCW has a higher winding factor. For an 8pole/12slot traditional FSCW machine, the winding factor is 0.866. As for a 10pole/12slot modular FSCW machine, the winding factor is 0.933 [104].

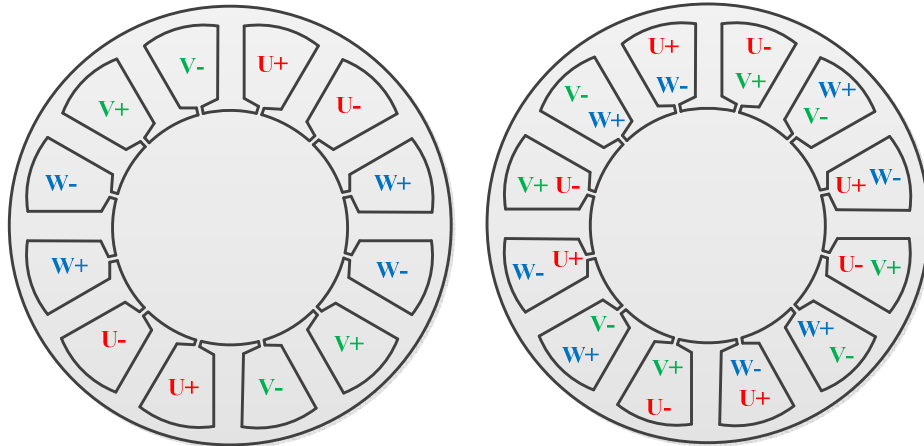


Fig. 4.1. Single layer and double layer concentrated winding layout

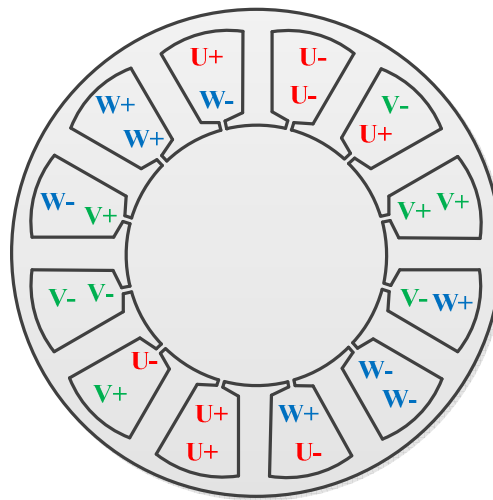


Fig. 4.2. Modular concentrated winding layout

Modular FSCW machines also have low cogging torque as the lowest common multiple (LCM) between the slot and the pole number being large [104]. On the other hand, modular FSCW machines have higher sub-harmonics in the MMF as compared to the traditional FSCW machines [105]. These sub-harmonics cause saturation in the core, rotor losses, higher inductance and unbalanced radial magnetic forces. This thesis focuses on traditional concentrated windings; thus, the modular FSCW structures have not been discussed further. Air-gap flux waveforms and their corresponding harmonic spectrums for a single and double layer, 54-slots, 42-pole FSCW IPMM are shown in

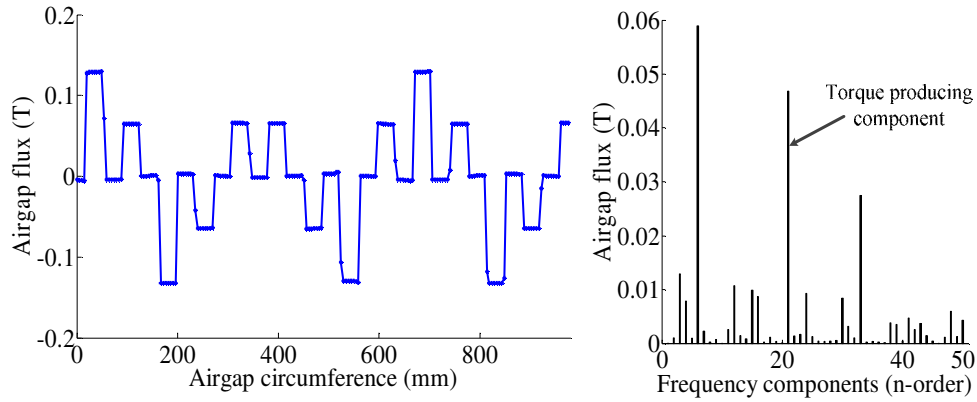


Fig. 4.3. 54-slot, 42 pole single-layer FSCW design

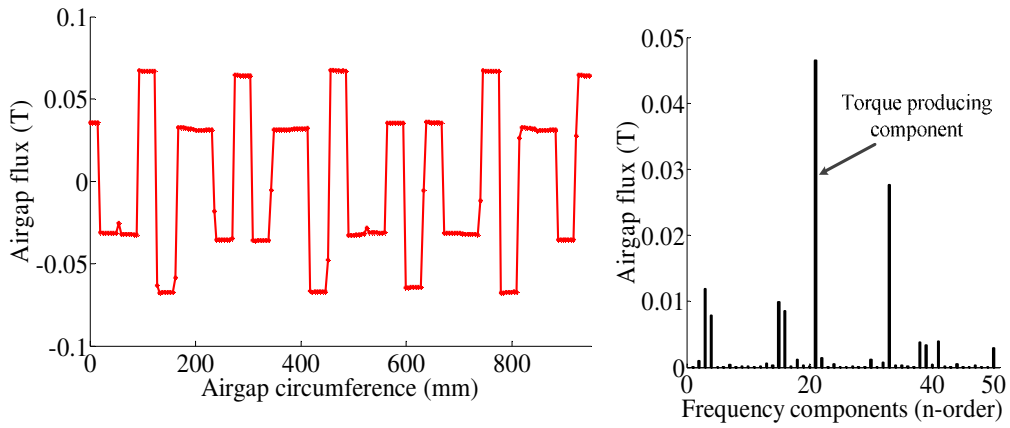


Fig. 4.4. 54-slot, 42 pole double-layer FSCW design

Fig. 4.3 and Fig. 4.4 respectively, as an example. The double layer FSCW shows fewer air-gap harmonics in the DW arrangement in comparison to the single layer FSCW arrangement shown in Fig. 4.4. These harmonics contribute to core and magnet eddy current losses. For this reason, the double layer FSCW was selected as the base layout in this research.

4.3 Performance analysis of using FSCW over DW

Fig. 4.5 shows the cross-sections of a typical 4-pole IPMM's with DW and FSCW. It can be seen from Fig. 4.5 that the number of slots is 24 for DW as compared to 6 in FSCW for the same rotor configurations.

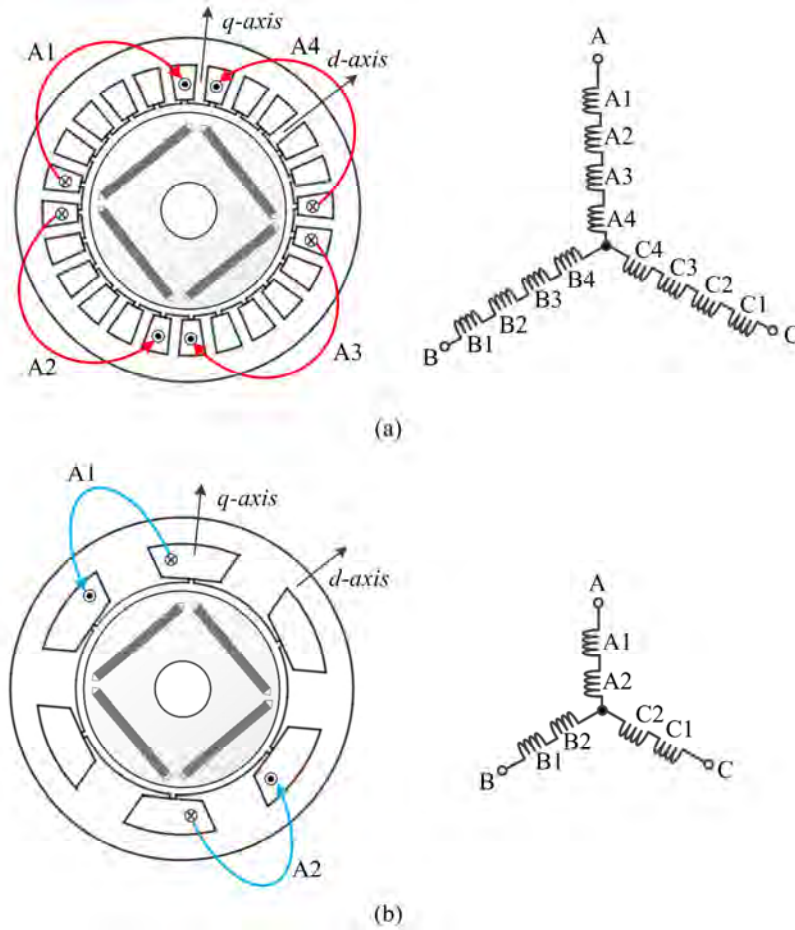


Fig. 4.5. Configuration of IPMM with (a) Distributed windings and (b) Concentrated winding structure

In FSCW, the opposite polarity of the corresponding phase coil is located in the next slot. This makes the end windings not to overlap, in contrast to DW structure resulting in longer end windings for DW IPMM as seen in Fig. 4.6. As a result of end winding length, the axial length of the DW IPMM becomes longer than that of the FSFSCW IPMM of equal torque and power rating.

The key favorable characteristics of an FSCW stator are :

- High slot-fill factor [106, 107]: Typical slot-fill factors of a DW design is around 35%, whereas it can go up to 45% for a conventional FSCW design.
- Simplified manufacturing process.
- Low cogging torque [72, 73].

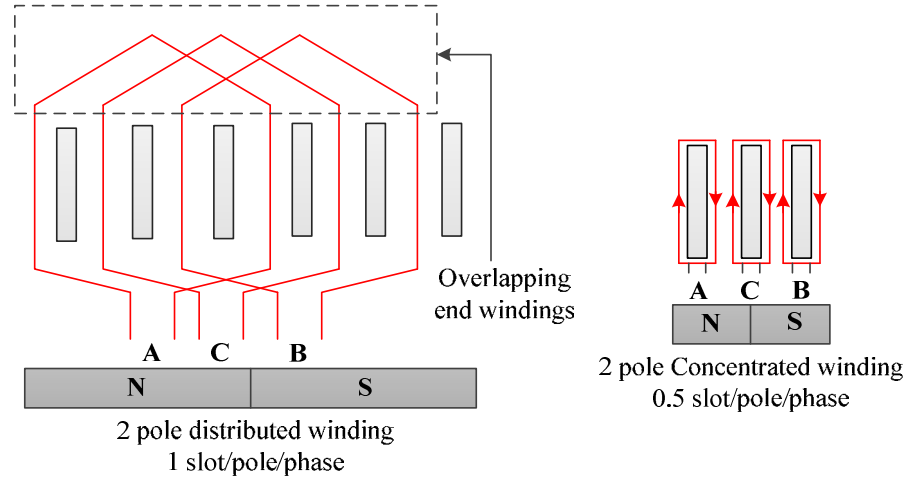


Fig. 4.6 A 2 pole (a) Distributed winding structure and (b) Concentrated winding structure

- High tolerance to phase fault: An FSCW machine has high leakage inductance as compared to the DW machine but has a small or zero mutual inductance that makes it ideal for fault tolerant applications [108].
- Non-overlapping coils resulting in shorter end-windings: reduced copper usage, resulting in lower copper losses [58].
- Higher power density [19].

4.3.1 Choice of slot and pole combination

Through the selection of an appropriate number of slots per pole per phase (S_{pp}), the output torque can be increased while cogging torque can be further reduced for a PM machine with FSCW stator. S_{pp} for an FSCW machine is calculated using the equation below,

$$S_{pp} = \frac{\text{Total No. of slots}}{\text{Total No. of poles} \times \text{total number of phase}}$$

For example, in Fig. 4.5, a 3-phase IPMM with 24 slots, 4 poles would have an integral-slot distribution of $S_{pp} = 2$, whereas, an IPMM with 6 slots/4-poles would have

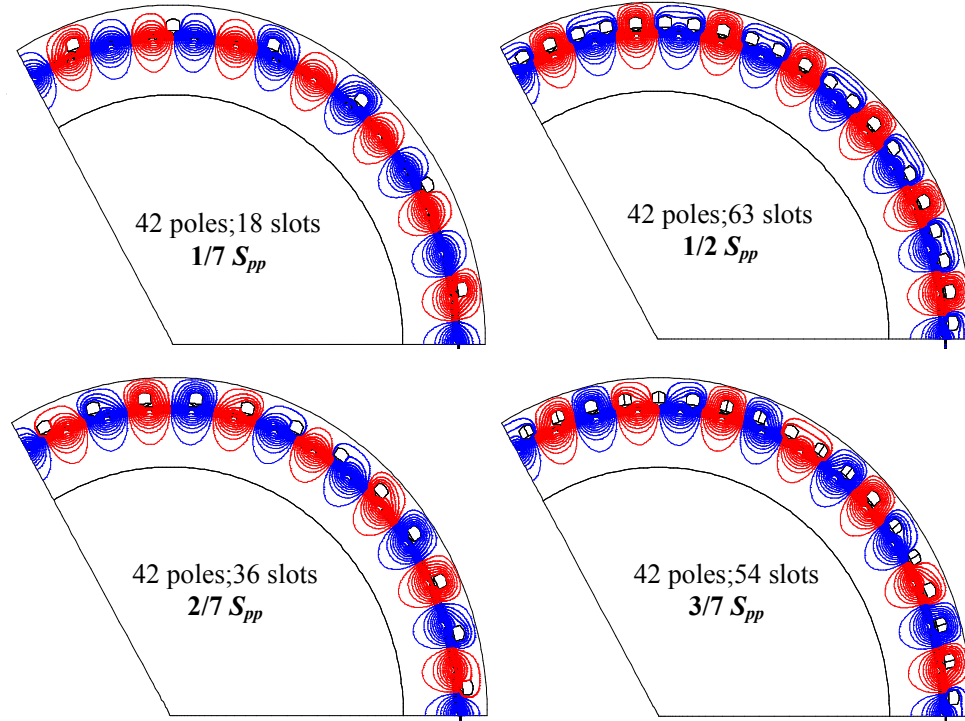


Fig. 4.7. 42 pole IPMM with various slot and pole combinations in FSCW layout

an $S_{pp} = 0.5$ a fractional-slot distribution. Fig. 4.7 shows 42 pole IPMM with fractional-slot concentrated windings having $1/2, 1/7, 2/7$ and $3/7 S_{pp}$.

Fig. 4.8 shows a stator pole for $1/7 S_{pp}$, where a large portion of a rotor pole of opposite polarity falls under the same stator pole. This reduces the total EMF generated in that phase. Thus, it can be concluded that the selection of lower values of S_{pp} in FSCW machines will reduce the total developed EMF. This means the selection of appropriate S_{pp} is very crucial in producing a sinusoidal EMF of the desired magnitude.

For an FSCW stator, the cogging torque has high-frequency fluctuations due to its fractional slot distribution. The periodicity of the cogging torque can easily be determined by

$$T_{cfreq} = \frac{360^\circ}{LCM} \quad (4.1)$$

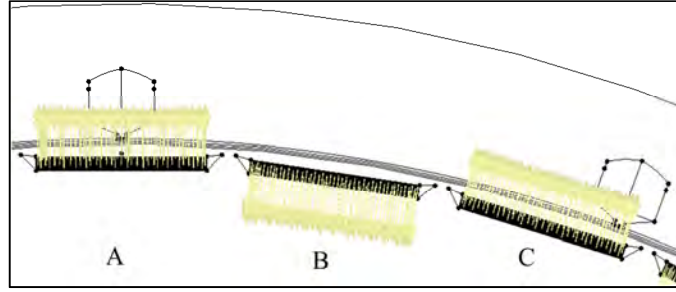


Fig. 4.8. An IPMM with $1/7 S_{pp}$ showing a stator pole

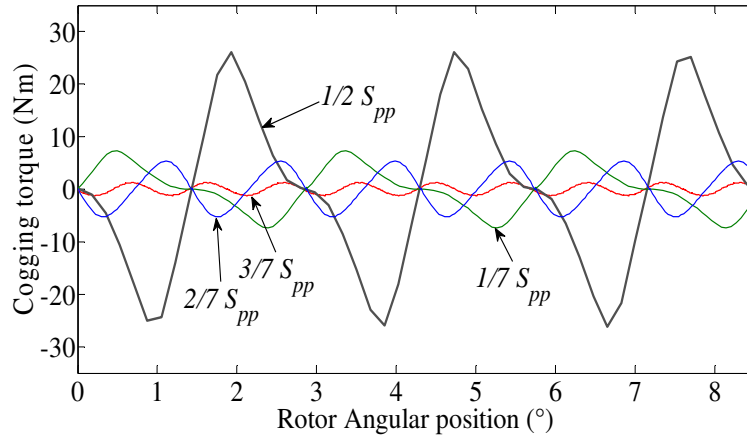


Fig. 4.9. Cogging torque of the 42 pole IPMM with various S_{pp} combinations.

Eq.(4.1) indicates that the frequency of cogging torque will vary based on the lowest common multiple (LCM) of the IPMM. The value of LCM is associated with S_{pp} of an IPMM. The lowest common multiple (LCM) of a 42 pole, 36 slots IPMM is 252. This makes the periodicity to be 1.42° . For the four designs of 42-pole IPMM shown in Fig. 4.7, the calculated cogging torques are compared in Fig. 4.9.

It is seen from Fig. 4.9 that the peak cogging torque value changes with the change in the S_{pp} value. This is expected since the change of S_{pp} is related to LCM. According to Eq.(4.1), a high value of LCM results in higher frequency fluctuations. On the other hand, it also yields in lower peak value in the cogging torque waveform [72, 109], which is reflected in Fig. 4.9. In this case, the 42 pole FSCW IPMM has a LCM value of 378 which is the maximum compared to the other designs. It also has the

lowest peak value of cogging torque.

4.3.2 Winding Factor

EMF is induced in the phase coils when the flux varies across the air-gap. Its magnitude depends on three main variables-rotor speed (w_m), flux-density (B_{max}), winding factor(k_w) and number of series turns per phase (N_{ph}).

$$E = w_m N_{ph} B_{max} k_w \quad (4.2)$$

Eq.(4.2) shows that the winding factor directly affects the generated EMF. The total EMF of a phase is the sum of all EMF produced by each coil. The winding factors are mostly expressed for each space harmonic. The ratio of flux linked by a winding compared to flux that would have been linked by a single-layer full-pitch DW winding with the same number of turns and one single slot per pole per phase is referred to as winding factor [64]. It can be written as,

$$k_w = k_p . k_d \quad (4.3)$$

where,

k_p =pitch factor &

k_d = distribution factor.

The skewing factor is neglected in Eq.(4.3) as FSCW machines are usually not skewed. Winding factor can be computed by determining k_p and k_d using the EMF phasor method [64]. A simple example of this approach is demonstrated using a 14 pole, 18 slot FSCW IPMM is shown in Fig. 4.10. Each winding in a particular slot represents an EMF phasor element. Each of this EMF phasors is represented by:

$$\overline{E}_n = e^{j\left(\frac{\pi \cdot p}{s} n_i\right)} \quad (4.4)$$

Where,

\overline{E}_n = Reference EMF phasor element,

n_i = Slot number

p = Total number of poles,

s = Total number of slots.

Fig. 4.10 shows the sum of EMF phasors that makes up phase A in the IPMM. Vectors $V_{a/b/c}'$ are achieved when all the winding elements corresponding to a particular phasor are in phase.

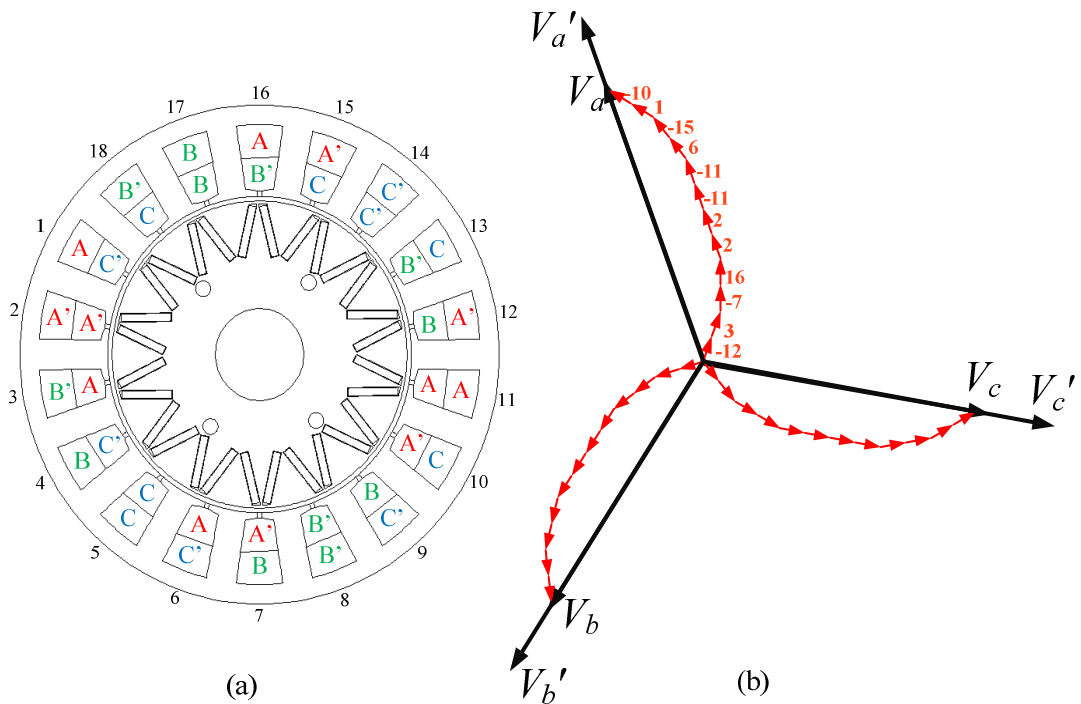


Fig. 4.10. (a) 18-slot, 14 pole IPMM showing phase coils and (b) Phasor diagram indicating the construction of each phasor using EMF phasor diagram

From Fig. 4.10, the winding factor can be easily calculated by dividing vectors $V_{a/b/c}$ by $V_{a/b/c}'$ respectively. The winding factor found for this 14 pole, 18 slot IPMM is 0.903.

Another approach to calculating the winding factor is to use the winding function.

The winding factor with respect to the winding function is given by [110],

$$k_{w,n} = \frac{W_{m,n}}{W_{m,n,b}} \quad (4.5)$$

Where,

$k_{w,n}$ = Winding factor of the n^{th} order harmonic component

$W_{m,n}$ = is the amplitude of the n^{th} order harmonic component of the actual winding function for the winding of interest

$W_{m,n,b}$ = is the amplitude of the n^{th} order harmonic component of the base winding function

Table 4.1 shows the winding functions that are used to determine the winding factor for different S_{pp} [111]. The winding factor can now be easily calculated using Eq.(4.5) for various slot-pole combinations, plotted in Fig. 4.11 - Fig. 4.13.

Table 4.1 winding functions for different S_{pp}

S_{pp}	1/5,1/7,1/11	2/5,2/7	3/7,3/11
$W_{m,n}$	$\frac{2}{n\pi} \frac{P}{c} \sin\left(\frac{n\pi}{s}\right) \left(2\cos\left(\frac{7\pi}{s}n\right)\right)$	$\frac{2}{n\pi} \frac{P}{c} \sin\left(\frac{n\pi}{s}\right) \left(1+2\cos\left(\frac{10\pi}{s}n\right)\right)$	$\frac{2}{n\pi} \frac{P}{c} \sin\left(\frac{n\pi}{s}\right) \left(1-2\cos\left(\frac{2\pi}{s}n\right)\right)$
$W_{m,n,b}$	$\frac{2s}{mn\pi}$		

where,

c= Denominator of S_{pp} ;

n=Harmonic order and

m= Number of phases

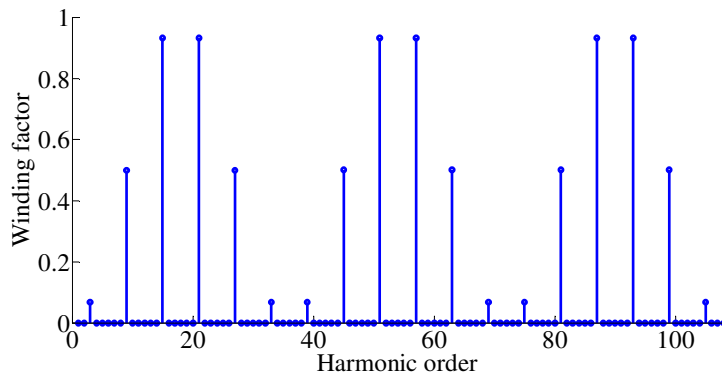


Fig. 4.11. Winding factor for 2/5 S_{pp}

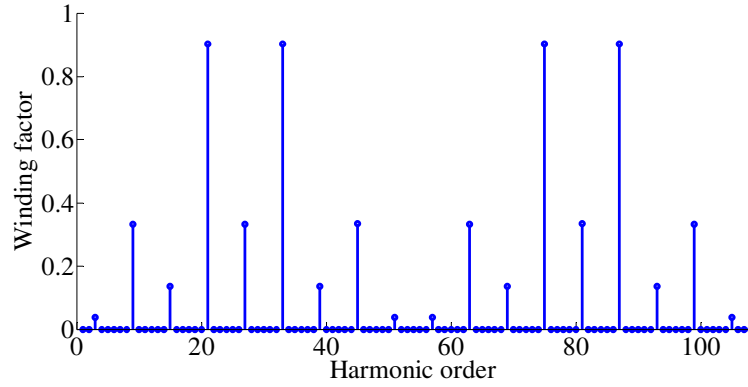


Fig. 4.12 Winding factor for $3/7 S_{pp}$

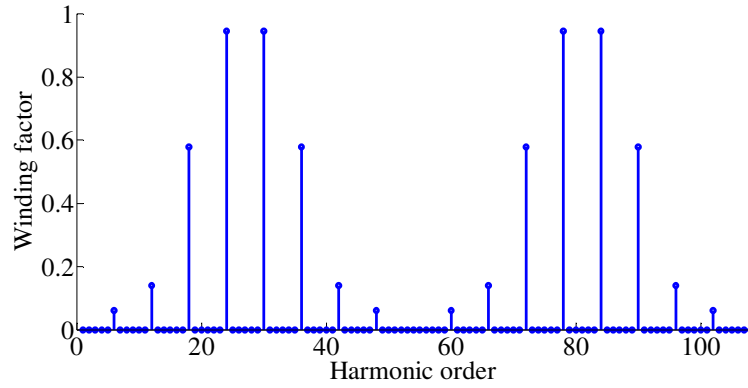


Fig. 4.13 Winding factor for $3/8 S_{pp}$

Unity winding factor is not achievable for fractional-slot concentrated windings. However, by adjusting slots and poles combination, a value very close to unity can be achieved. Table 4.2 shows the winding factors of double layer windings with various slot and pole combinations. Table 4.3 summarizes the results of the investigation conducted in [112] for various S_{pp} of a 14 pole IPMM. The maximum value for k_w is found to be 0.945 when the S_{pp} is either 3/8 or 3/10 according to Table 4.2. However, both these winding layout has unbalanced magnetic pull (UMP) [113]. Avoiding UMP is important as it affects the wear of the bearings as well as the noise and vibrations [113, 114]. Neglecting the S_{pp} related to UMP, the highest k_w is found to be 0.933 when the S_{pp} is either 2/5 or 2/7.

Table 4.2 Winding factor for different S_{pp}

Poles Slots		4	6	8	10	12	14	16	18
6	S_{pp} K_w	1/2 0.866		1/4 0.866	1/5 0.5		1/7 0.5	1/8 0.866	
9			1/2 0.866	3/8 0.945	3/10 0.945	1/4 0.764	3/14 0.473	3/16 0.175	
12				1/2 0.866	2/5 0.933		2/7 0.933	1/4 0.866	
15					1/2 0.866		5/14 0.951	5/16 0.951	
18						1/2 0.866	3/7 0.902	3/8 0.945	
21							1/2 0.866	7/16 0.851	
24								1/2 0.866	
27									1/2 0.866

Integral product of no. of phase
 Unbalanced magnetic pull

Table 4.3 Induced EMF and winding factor for different combinations of S_{pp} and winding type

S_{pp}	Type	Winding layer	EMF (RMS volts)	EMF harmonic contents	Winding factor
2	DW	Double	28.4	Very low	0.933
1/7	CW	Single	14.5	High	0.866
2/7	CW	Double	21	Low	0.933
3/7	CW	Double	27.6	Very low	0.902

From Table 4.3, it can be seen that with an S_{pp} of 3/7, an FSCW machine can produce an EMF with low harmonic content and magnitude of EMF is close to an equivalent DW machine. Apart from this, a very low cogging torque and a wider flux-weakening range were also achieved in this FSCW machine [112]. This justifies the fact

that by an appropriate selection of slot and pole combination, FSCW can produce sinusoidal EMF with a small THD in an IPMM.

For a 42-pole IPMM, $S_{pp} = 3/7$ was selected based on the previous research conducted in [115]. Under such a structure, the slot number will be 54.

4.3.3 MMF

As previously discussed, an FSCW machine produces higher harmonic contents in the armature MMF distribution compared with a DW machine. These harmonics cause flux variations in the air-gap and, as a result, increases rotor losses. The flux variations in the air-gap also result in higher leakage inductance that contributes to the self-inductance of the machine [116]. The number of slots (s) and pole pairs (P_p) in an FSCW machine has an effect on MMF distribution [117]. Periodicity of a machine is given as

$$t_p = GCD \quad (4.6)$$

where, GCD refers to the greatest common divisor.

According to [117], if s/t_p is even, only the odd order harmonics will be present in the MMF distribution. The developed MMF in the air-gap is profoundly related to S_{pp} . A base winding distribution exists for each S_{pp} which is based on the minimum possible number of poles and slots. To achieve a winding distribution for the higher number of slots and poles for the same S_{pp} , the core winding function is reproduced $P/(2 * \text{denominator of } S_{pp})$ times. Fig. 4.14 shows the MMF waveform for different S_{pp} . The prototype FSCW machine with $3/7 S_{pp}$ for this thesis has a periodicity of 3 which makes $s/t_p=18$ an even number. This suggests only the odd order harmonics will be present in the MMF distribution.

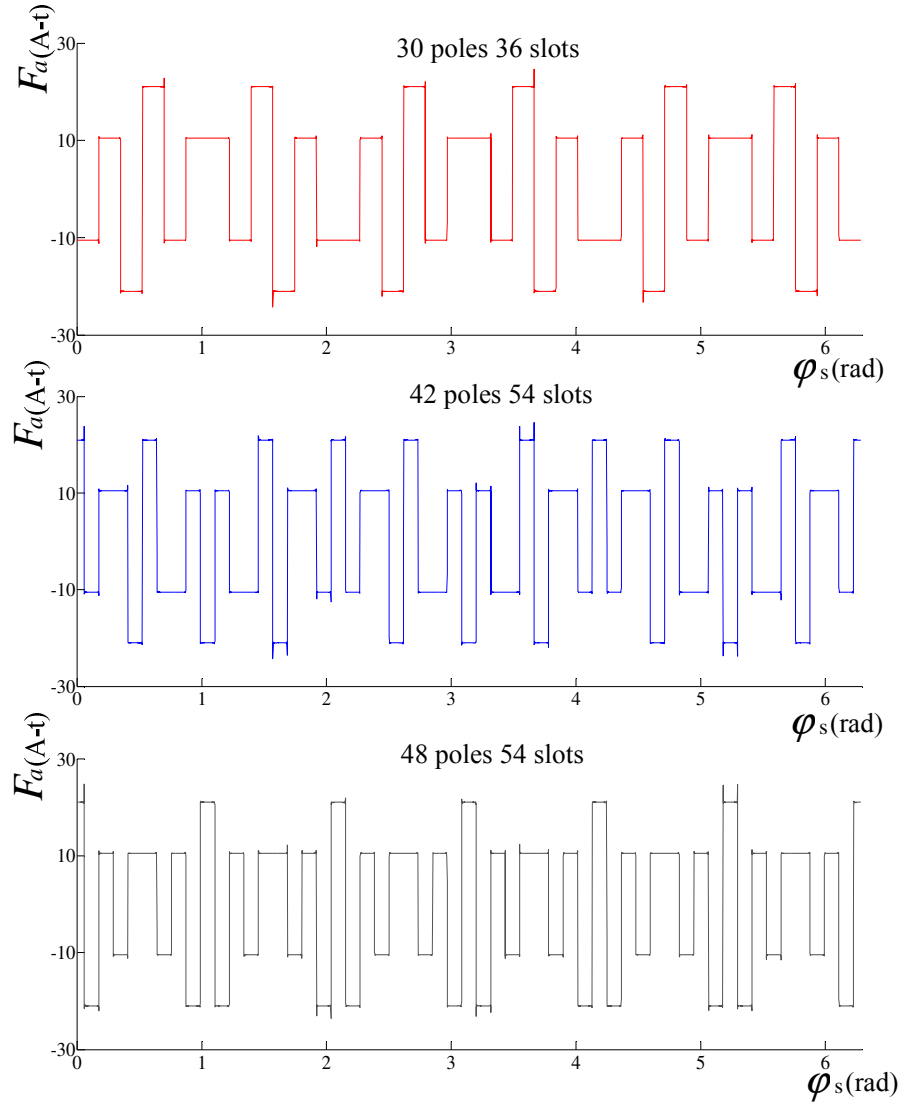


Fig. 4.14. MMF obtained by FEA for various slots and poles combination.

The MMF produced by stator coils can also be expressed as

$$F_s = B_s A_g R_{air} \quad (4.7)$$

where,

B_s = Flux-density produced by the stator

A_g = Air-gap surface area

R_{air} = Air-gap reluctance.

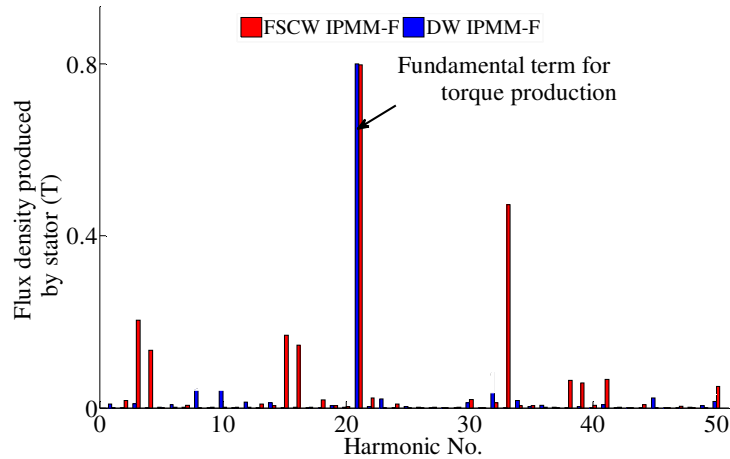


Fig. 4.15. MMF harmonic spectrum for DW IPMM-F and FSCW IPMM-F

If the air-gap length and overall slot opening widths are kept constant, then the MMF of the machine is proportional to the air-gap flux density produced by the stator coils. Fig. 4.15 shows the harmonic spectrum of the flux density produced by stator coils for the DW IPMM-F and the FSCW IPMM-F of same dimensions. The main harmonic order is equal to the number of pole pairs that is 21 for both the prototype machines as seen in Fig. 4.15. No notable sub-harmonics are present in the DW machines. As for the FSCW machine, significant odd order harmonics are present in the MMF distribution. Due to the imperfections in the machine i.e. slot openings and reluctance of the flux path, some even order harmonics are also present in the spectrum that are negligible.

4.4 42 pole IPMM with Concentrated windings

In chapter 4, the DW machine was designed to achieve a very low cogging torque, low torque ripple, and high efficiency. The geometry of the optimized DW IPMM is taken as the base model for the FSCW IPMM. Apart from the different stator winding configuration, the two IPMM's have identical rotor and stator dimensions, air-gap length, magnet length and stack length for a fair comparison. Two rotor geometries: flat

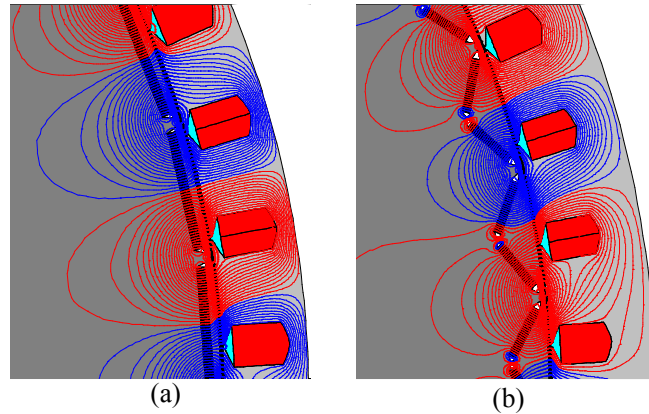


Fig. 4.16. Flux distribution of a portion of (a) FSCW IPMM-F and (b) FSCW IPMM-V with V-angle of 120°

shaped IPMM and V-shaped IPMM (V-angle of 120°) has been modelled with fractional-slot concentrated windings having $3/7 S_{pp}$ as shown in Fig. 4.16.

4.4.1 Stator design for FSCW IPMM

As compared to 252 slots in the DW IPMM, the number of slots has been reduced to 54 slots for the FSCW IPMM having an S_{pp} of $3/7$. A typical slot-fill factor of 0.4 was assumed for the FSCW machine. A study on slot-fill factor on DW and FSCW machines has been conducted in chapter 5. The number of conductors per slot needed to produce the rated voltage of 360 volts was found to be 15. Similar to DW design, the required slot area was calculated based on number of conductors, the cross-sectional area of the conductors based on the current rating. It was calculated as 124 mm^2 . Fig. 4.17 shows the slot dimensions of the proposed FSCW IPMM. Note that the total amount of copper used for the FSCW IPMM is kept same as of the DW IPMM.

4.4.2 Winding layout of the FSCW IPMM

The arrangement of phase coils in FSCW to achieve the desired winding factor is not as straight forward as the DW design.

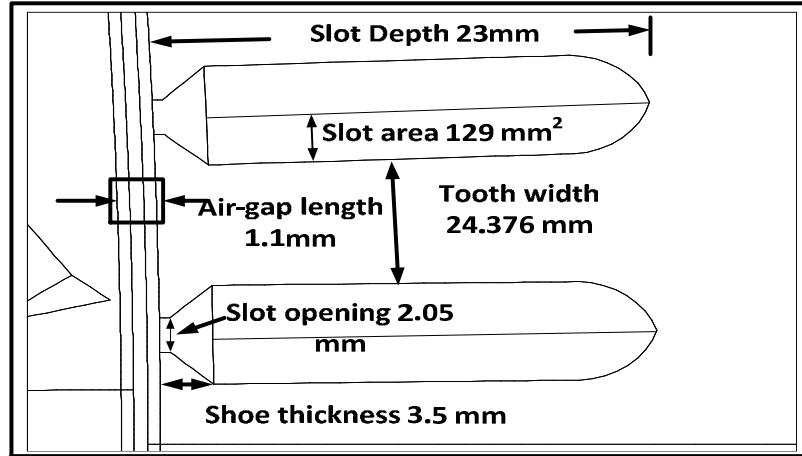


Fig. 4.17. Slot and air-gap dimension of the FSCW IPMM

Methods of finding the optimal winding layout in FSCW to achieve the highest possible flux linkage is shown in [58, 64]. In this thesis, these methods are used to obtain the optimal winding arrangement for the FSCW IPMM. Since, the periodicity of a 42 pole, 54 slot FSCW IPMM is 3, the winding pattern is studied for 120° ($1/3^{\text{rd}}$ of the machine) which will be repeated three times to represent the entire winding.

The method of determining the optimal winding pattern based on [58, 64] is explained as follows:

- a. A repeatable sequence of 1s and 0s can be determined by using S_{pp} :

$$S_{pp} = \frac{3 \rightarrow \text{Total no. of 1s}}{7}$$

Total no. of 0s \rightarrow numerator-denominator $\rightarrow 4$

- b. The optimum repeatable sequence is found by alternating the 1s and 0s with 1s being the first integer. The sequence for the test machine is,

$$1\ 0\ 1\ 0\ 1\ 0\ 0$$

- c. The optimum sequence is repeated until the total number of 1s is equal to the total number of slots in the machine. For $1/3^{\text{rd}}$ of the machine, the number of slots is 18. This means the sequence should be repeated 6 times.

- d. Each integer in the sequence is assigned to a particular winding conductor of a phase. The usual winding sequence is:

PA MC PB MA PC MB.....

The first alphabet of each conductor represents the orientation. Here P is referred to as positive, and M is referred to as minus that is the return conductor. The second alphabet of each conductor refers to the phase. The integers under 1s are selected to form the first layer of the winding. The second layer is obtained by shifting the first layer in the neighboring slot and reversing the conductor's direction. This process is shown below:

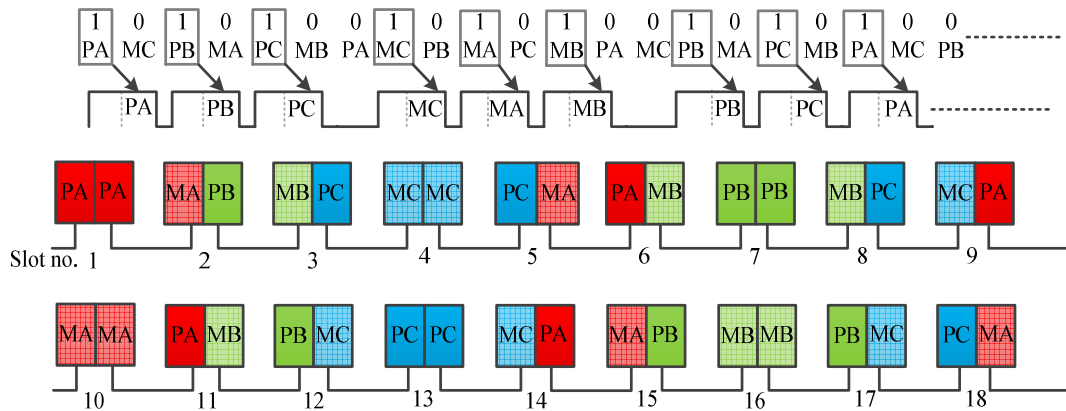


Fig. 4.18. Winding layout for 42 pole FSCW IPMM

4.4.3 Cogging torque optimization for FSCW IPMM

The IPMM with concentrated winding is less affected by cogging torque than its counterpart distributed winding mainly due to the discontinuous reluctance variation in the rotor and stator. The reduction of the cogging torque is crucial for low-speed IPM machines [118]. The optimization of the magnet arc length and flux barrier were considered as the two main cogging torque minimization techniques in chapter 4 for the DW IPMM. The same minimization techniques were investigated for the FSCW IPMM-F and the FSCW IPMM-V. Initially, the magnet arc length of the proposed flat shaped FSCW-IPMSM was kept to 40.84 (for which the magnet length is 39.78 mm),

that is the same magnet length as the DW IPMM-F, so that cogging torque of the FSCW machine can be compared fairly with the DW machine. The cogging torque calculated for the FSCW IPMM with the same magnet arc as the DW IPMM-F was found to be 2.8 times higher in comparison to the DW IPMM-F. This high value of cogging torque is due to the misalignment of the stator teeth and the permanent magnets of the FSCW IPM machine. This indicates that further magnet arc optimization will be necessary for the FSCW IPMM to minimize cogging torque. It should be noted here that the change of the magnet arc length results in a change in the overall magnet volume which in turn results in the variation of the air-gap flux density. Table 4.4 summarizes the outcome of this investigation. Table 4.5 shows the change in the cogging torque with various magnet lengths for the FSCW IPMM-V. The optimum magnet length of the FSCW IPMM-F is found to be 36.6 mm which is 7.6% less than that of the DW IPMM-F designed in chapter 3. As for the FSCW IPMM-V, the optimum magnet length is found to be 38.7 mm, slightly higher than that of FSCW IPMM-F.

Table 4.4 Change in the cogging torque with respect to the variations in magnet length for the FSCW IPMM-F

Magnet length (mm)	% Reduction in magnet volume with respect to DW IPMM-F	Cogging torque (Nm)	B_{\max} (T)
39.78	0	5.67	0.837
38.7	2.5	4.89	0.82
37.6	5	3.06	0.8
36.6	7.6	0.5	0.794
35.5	10	1.47	0.77

Table 4.5 Change in the cogging torque with respect to the magnet length for FSCW IPMM-V

Magnet length (mm)	% Change in magnet volume with respect to DW IPMM-F	Cogging Torque (Nm)
37.7	5% reduction	0.66
38.7	2% reduction	0.63
39.7	0	3
40.7	2% increase	5.4
41.7	4.8% increase	6.5

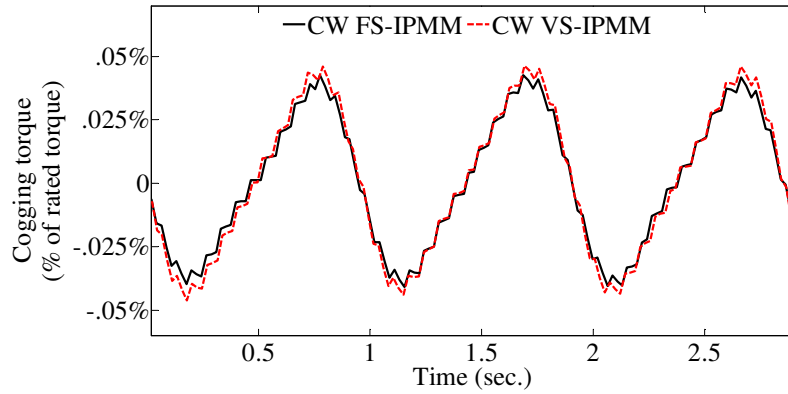


Fig. 4.19. Cogging torque of FSCW IPMM's

Fig. 4.19 shows the cogging torque waveforms of both FSCW designs. Both the FSCW IPMM's produce significantly less cogging torque compared with the DW machines. This is because FSCW eliminates periodicity between slots and poles which aids in the reduction of the cogging torque. Also, it should be noted here that the cogging torque of the FSCW IPMM has a higher frequency than the DW IPMM and easier to filter out.

4.4.4 Torque ripple minimization for FSCW IPMM

The torque ripple is mainly caused by the stator and rotor MMF harmonics. Many pieces of literature have highlighted the effect of the structure of flux barriers on the overall torque ripple of the machine [119-121]. The torque ripple of the DW IPMM-F and the DW IPMM-V were optimized in chapter 3 by varying the flux barrier designs with respect to the slot opening in the stator. Bianchi *et al.*[119] developed an expression to clearly highlights the stator-rotor harmonic interactions on the torque ripple. It is given as,

$$T_{ripple} = -\frac{P}{2} \frac{\mu_0}{\delta} r_g l \pi \sum_{\substack{n=6m\pm 1 \\ m=1,2,3,\dots}} (n f_{s,n} f_{r,n} \sin((n\pm 1)\theta_r \pm \gamma_d)) \quad (4.8)$$

where,

p =Number of poles;

CHAPTER 4: Design of a High-Pole Number IPMM with Fractional-Slot Concentrated Wound Stator

r_g = Air-gap radius;
 l = Stack-length;
 δ = Air-gap length;
 n = Harmonic Number;
 θ_r = Rotor angular position (electrical);
 γ_d = Current phase angle measured from d -axis;
 $f_{s,n}$ = n^{th} -order stator MMF harmonic;
 $f_{r,n}$ = n^{th} -order rotor MMF harmonic;

It can be seen from Eq.(4.8), that the harmonic order of torque ripple waveform are a multiple of 6. Also, the same order of stator and rotor MMF harmonics interacts and contributes to the overall torque ripple. The stator and rotor unwanted harmonics are caused by the winding structure, stator slotting and the flux barriers in the rotor. It is already seen in Fig. 4.15 that the FSCW IPMM-F has significant harmonics in the stator MMF distribution which cannot be avoided. In order to reduce the overall torque ripple, the rotor MMF distribution has to overcome unwanted harmonics that can be done by adjusting the flux barriers and the slot opening of the slots.

In FSCW IPMM, the positioning of the slots with respect to flux barrier is not the same as the DW IPMM. Initially, for the FSCW IPMM-F, the magnet length is kept identical as that of the DW IPMM-F for a fair comparison. The variation in the dimensions of x and y of the flux barriers (as shown in Fig. 4.20) were required to minimize torque ripple in the FSCW IPMM-F. The effect of rotor air-gap field with the change in flux barrier is shown in Fig. 4.21.

It can be seen from Fig. 4.21 that the fundamental rotor air-gap field is maximum when the flux barriers are of ‘Design B’. This indicates that the machine designed with this geometry will produce maximum torque. On the other hand, ‘Design C’ has a lower magnitude of unwanted spatial MMF harmonics in the stator.

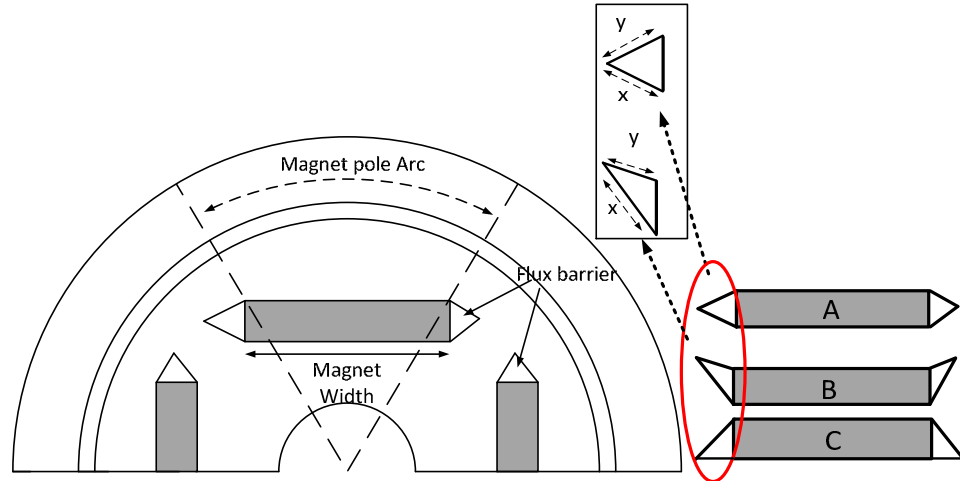


Fig. 4.20. Cross-sectional view of a flat shaped IPMM with different flux barrier shapes

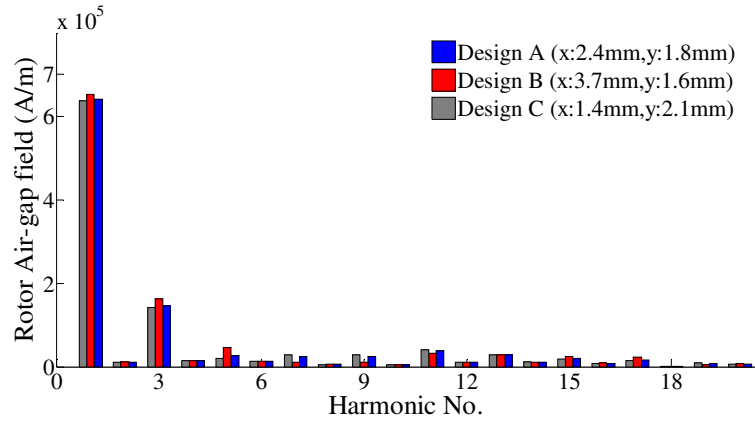


Fig. 4.21. Rotor air-gap field for various flux barriers in the FSCW IPMM-F

Table 4.6 summarizes the effect of the changes in the flux barrier dimension on the torque ripple for the FSCW IPMM-F with a constant slot opening length. It can be seen from Table 4.6 that Design B generates more torque as compared to Design ‘A’ and ‘C’. Although Design ‘C’ causes the least amount of torque ripple, it has not been taken into account because it produces less overall torque compared to the other two designs. Thus, design ‘B’ was chosen for the FSCW IPMM-F for further analysis.

A further torque ripple analysis of FSCW IPMM was carried out by using the flux barrier design ‘B’ while varying the slot openings. The analysis has been conducted using two different magnet lengths in the rotor; (a) magnet length of 39.788mm which

Table 4.6 Change in torque ripple with the change in flux barrier shape and size for FSCW IPMM-F

Design A				
x	y	Area of the flux barrier	Total torque	Torque ripple
2.469	1.882	2.34	274.2	5.67%
2.588	2.056	2.62	274.5	5.7%
2.8	2.4	3.2	274.8	5.84%
Design B				
3.7	1.2	1.6	279	6.98%
3.8	1.5	2.2	280.5	6.09%
3.8	1.7	2.5	281	5.7%
Design C				
1.4	3.3	2.1	272.31	4.9%
1.59	3.49	2.4	272.49	4.97%

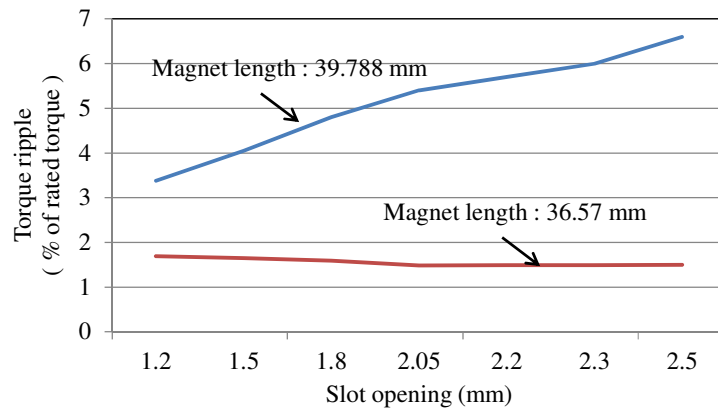


Fig. 4.22. Variation in torque ripple with the change in slot openings in the stator slots for the FSCW IPMM-F

is the same as in the DW IPMM-F and (b) optimized magnet length of 36.57 mm in which the cogging torque is the minimum. The variations in torque ripple for the FSCW IPMM-F under these conditions are compared in Fig. 4.22. The minimum torque ripple for FSCW IPMM-F was found to be 1.48% of the total rated torque with a flux barrier design of “B” and a magnet length of 36.57mm. The slot opening at this condition is 2.05 mm.

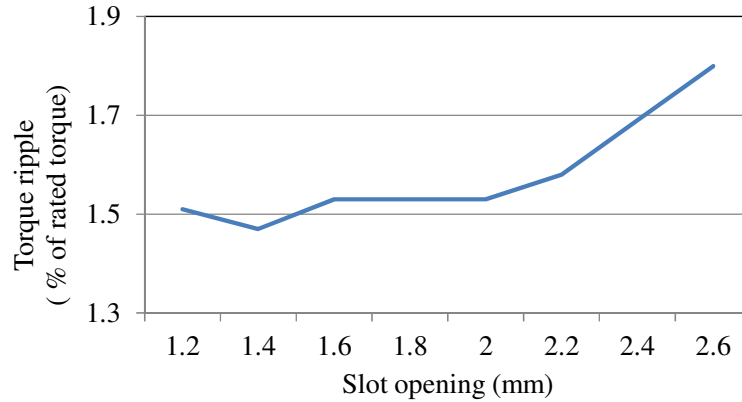


Fig. 4.23. Variation in torque ripple with the change in slot openings in the stator slots for the FSCW IPMM-V

This indicates that the reduction of cogging torque is of primary importance when reducing the overall torque ripple of an IPMM. A similar analysis has been conducted for the FSCW IPMM-V, which shows that Design ‘A’ generates the least amount of torque ripple for the FSCW IPMM-V. This is because Design ‘A’ reduces the flux leakage significantly compared to the other two designs that in turns reduces the rotor MMF harmonics in the air-gap that causes torque ripple for the FSCW IPMM-V. The effect of slot opening on FSCW IPMM-V with a flux barrier of design ‘A’ is shown in Fig. 4.23. Table 4.7 compares the cogging torque and torque ripple of all four designs investigated in this thesis. It can be concluded from Table 4.7 that the FSCW IPMM-F and the FSCW IPMM-V are the best choices as they have the lowest torque ripple and cogging torque.

Table 4.7 Magnet area, Flux barrier design, Slot opening, Cogging torque, Torque ripple and peak air-gap flux density for all of the four designed machines

Machine type	Magnet Area mm^2	Flux barrier design	SO	Cogging torque Nm	Torque ripple (% of rated torque)	B_{\max} (T)
DW IPMM-F	119	B	1.2	2	6%	0.8
DW IPMM-V	114	B	1.3	4.53	14.4%	0.76
FSCW IPMM-F	110	B	2	0.5	1.48%	0.77
FSCW IPMM-V	116	A	1.4	0.63	1.47%	0.71

4.4.5 Comparison of FSCW IPMM and DW IPMM

This section compares some of the key performance characteristics of the FSCW IPMM with the DW IPMM-F. As shown in Table 4.7, air-gap flux densities of the FSCW IPMM's are slightly lower than the DW IPMM-F due to reduced magnet volume in these machines. The optimum magnet arc length of the FSCW IPMM-F to achieve the minimum cogging torque is about 7.6% less than that of the DW IPMM-F. The magnet volume for an FSCW IPMM-F is 7.6% less than the DW IPMM-F, but the power is only 3.7% lower than that of the DW IPMM-F. In order to achieve the design specification of the rated power, the stator outer diameter of the FSCW IPMM were increased by 2.9%. It should be noted that the increase in the stator outer radius also increases the cogging torque and torque ripple marginally.

The rated current is set to 6.5 A (RMS) for both the designs to achieve 4 KW at rated speed. Fig. 4.24 shows the flux density at the tooth of the slots for both machines. Table 4.8 compares the main outcomes of the three IPMM designs. It is seen that the DW IPMM-F has higher flux density of 1.2T in the tooth, which is close to saturation for the material that has been used in the stator core. As for the FSCW IPMM-F, the flux density is 0.8T in the tooth which suggests that the rated current can be increased to a higher value without making the stator core saturated. This suggests that the power density of the FSCW IPMM-F can be increased to a higher value to achieve higher rated power than that of the DW IPMM-F. Throughout this thesis, the rated current is kept to 6.5 A (RMS) to have a fair comparison between all the IPMM's modelled.

It can be seen from the Table 4.8 that the overall volume of the FSCW IPMM is larger by 2.9%, and cogging torque is smaller by 68.5% than that of the DW IPMM-F. Thus, it can be concluded that the selection of the DW versus FSCW stator for the high

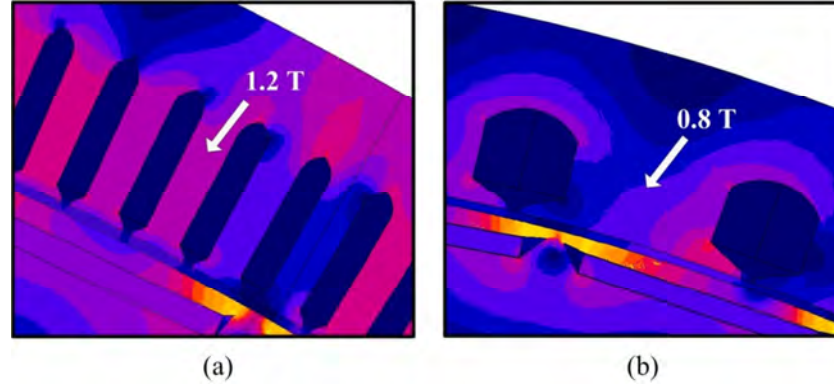


Fig. 4.24. Flux density in the tooth of the stator for (a) DW IPMM-F and (b) FSCW IPMM-F

Table 4.8 Output Parameters for DW IPMM-F, FSCW IPMM-F, and FSCW IPMM-V

Machine type	Stator outer radius mm	L-L EMF V	EMF THD	Total torque Nm	Total power W
DW IPMM-F	340	363	4.18%	276	4137
FSCW IPMM-F	350	360	0.76%	270	4038
FSCW IPMM-V	350	340	0.67%	260	3890

pole number IPMM will be influenced by the reduction of the cogging torque rather than by the increase in overall volume.

The Line-Line EMF voltage waveforms of all three designs are shown in Fig. 4.25. Fig. 4.26 plots the L-L EMF harmonics of all the machines. It can be seen, that the THD of the FSCW IPMM-V is at a much lower level compared to the other ones. Fig. 4.27 and Fig. 4.28 show the total power and the FFT of the developed torque for these three machine designs. Fig. 4.28 shows that the torque ripple is small at low frequencies for the FSCW IPMM that can easily be eliminated by speed control loop using vector control system [122]. The 6th and 12th harmonics of torque in a DW IPMM-F are much higher than the FSCW IPMM that is considered to be the dominating harmonic in the torque ripple. For the DW IPMM-F, the 6th order harmonic component has the highest

magnitude of 4.88 Nm. As for the FSCW IPMM-F, the magnitude of the 6th order harmonic is 0.93 Nm.

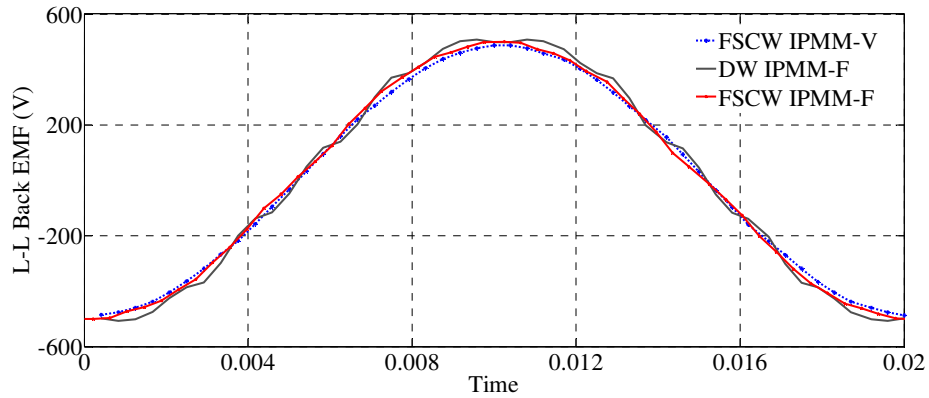


Fig. 4.25. L-L Back EMF of DW IPMM-F, FSCW IPMM-F, and FSCW IPMM-V

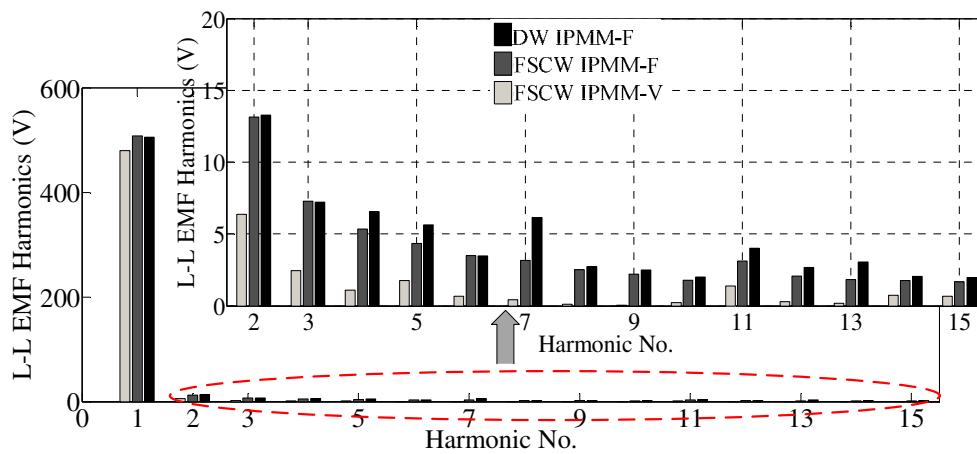


Fig. 4.26. Spectrum analysis of DW IPMM-F, FSCW IPMM-F, and FSCW IPMM-V

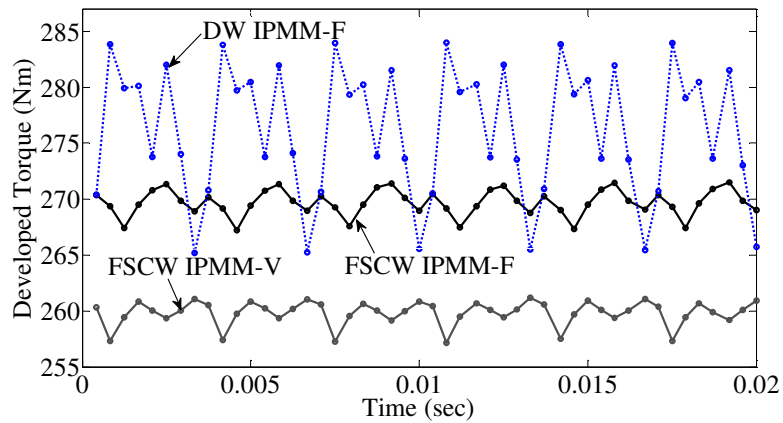


Fig. 4.27. Total developed torque of DW IPMM-F, FSCW IPMM-F and FSCW IPMM-V

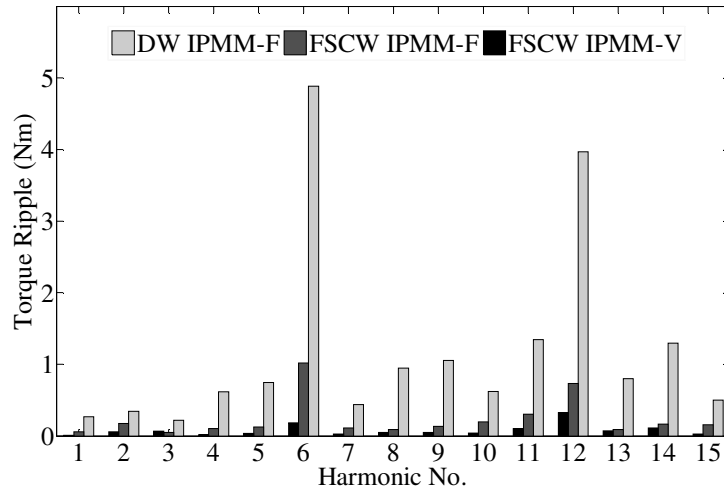


Fig. 4.28. FFT analysis of developed torque for the DW IPMM-F, FSCW IPMM-F, and FSCW IPMM-V

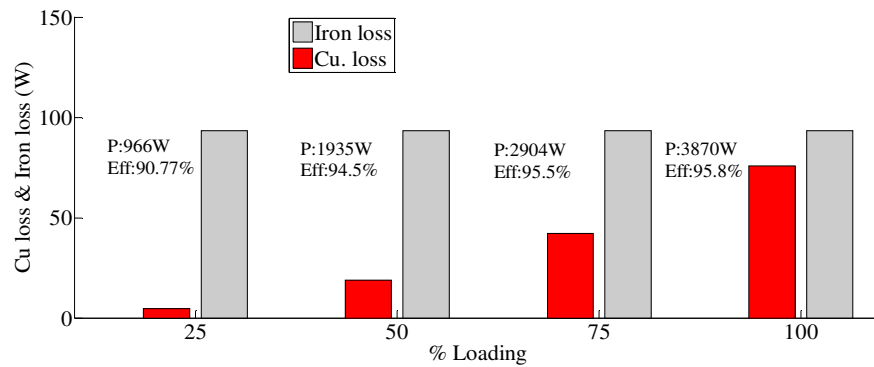


Fig. 4.29. Copper losses & Iron losses versus percentage of loading for FSCW IPMM-F

4.4.6 Efficiency

The efficiency and loss calculation for the FSCW IPMM has been conducted in the same manner as for the DW IPMM shown in chapter 4. Fig. 4.29 and Fig. 4.30 show the losses for the IPMM-F and FSCW IPMM-V, respectively. It can be seen that both the machines achieve maximum efficiency at full load. Efficiency at full load for various speeds was calculated for the FSCW IPMM-F and compared with the DW IPMM-F shown in Fig. 4.31. About 94% efficiency was achieved at full load in the DW IPMM-F, whereas, for FSCW IPMM-F, it is 95.56%. The efficiency of the FSCW IPMM-F is more than that of DW IPMM-F because of lower resistive losses.

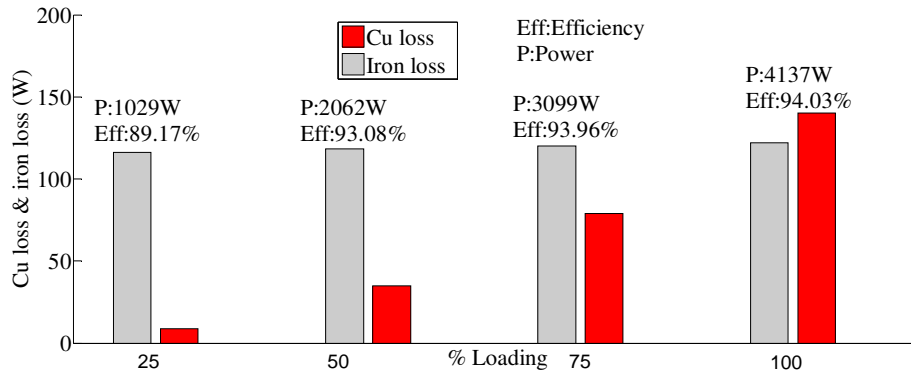


Fig. 4.30. Copper losses & Iron losses versus percentage of loading for FSCW IPMM-V

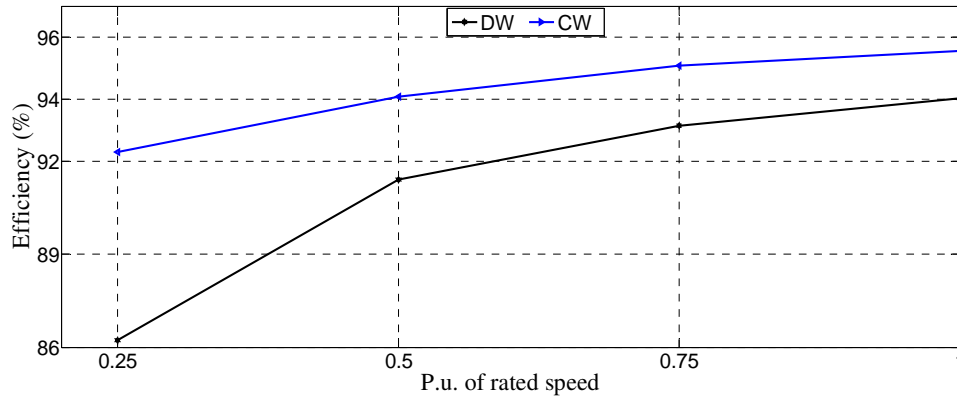


Fig. 4.31. Efficiency versus P.U. of rated speed for DW IPMM-F and FSCW IPMM-F

4.4.7 Inductance and saliency ratio comparison between DW and FSCW IPMM's

The measurement of L_d and L_q are usually carried out by the AC standstill test method. The conventional method applied to the DW IPMM (shown in chapter 4) for calculating inductances is not applicable for FSCW IPMM's. This is because of the fact that the d- and q-axis flux paths are not obvious for FSCW IPMM's due to the aperiodicity between slots and poles. For the FSCW IPMM, an AC standstill test like condition is simulated to calculate L_d and L_q . Although this method takes longer computational time, it is found to be more accurate than various magneto-static methods available in

the literature, in particular for the FSCW-IPMM. This process is conducted by exciting one of the phase coils with an AC source at a specified frequency.

The circuit model for this test is shown in Fig. 4.32.

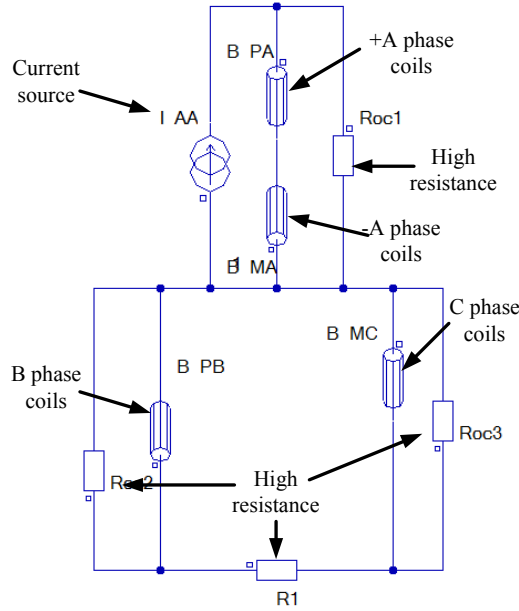


Fig. 4.32. Circuit for AC standstill test for the DW IPMM-F

The voltage drop across the excited winding and the neighboring phase winding are measured for various rotor positions (θ_r). For accuracy of the results the simulations are conducted every 0.1° (mechanical) and the self-inductance (L_a) and mutual inductance (M_{ab}) at each rotor position are calculated by Eq.(4.9) and Eq.(4.10) respectively.

$$L_a(\theta_r) = \frac{\sqrt{\left(\frac{V_a}{i_s}\right)^2 - R_a^2}}{2\pi f} \quad (4.9)$$

$$M_{ab}(\theta_r) = \frac{V_b}{2\pi f \cdot i_s} \quad (4.10)$$

where,

i_s = Input current

V_a = Voltage drop across the excited phase

R_a = A phase resistance

V_b = Voltage drop across another phase

Fig. 4.33 and Fig. 4.34 show the self- and mutual inductances of the two FSCW IPMM's designed in this chapter and compares it to the DW IPMM-F developed in chapter 4. Even with similar FSCW structure, the FSCW IPMM-F and the FSCW IPMM-V shows different self-inductance values. This can be easily explained by analytical self-inductance formula for conventional salient-pole machine given as [123],

$$L_a(\theta_r) = \mu_0 R_{si} l \int_0^{2\pi} N_a^2(\theta_r) g^{-1}(\theta_r) d\theta_r \quad (4.11)$$

Where,

R_{si} = Stator inner radius,

l = Effective stack length,

N_a = Winding function of phase A and

$g^{-1}(\theta_r)$ = Inverse air-gap function.

The effective air-gap length is different for both the FSCW machines due to their dissimilar pole pitch [124], making the self-inductance non-identical for the FSCW machines. The high self-inductance for the FSCW IPMM-V will provide the machine with high fault-tolerant capability in comparison to the other two designs. The self-inductance for the DW IPMM-F is low due to its lower harmonic contents [116] in the MMF waveform as seen in Fig. 4.33. However, the mutual inductance is much higher for the DW IPMM-F seen in Fig. 4.34.

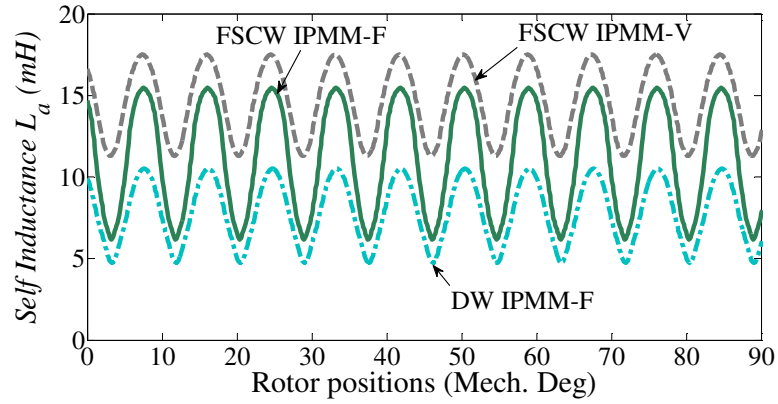


Fig. 4.33. Self-inductance of the DW IPMM-F, FSCW IPMM-F, and FSCW IPMM-V

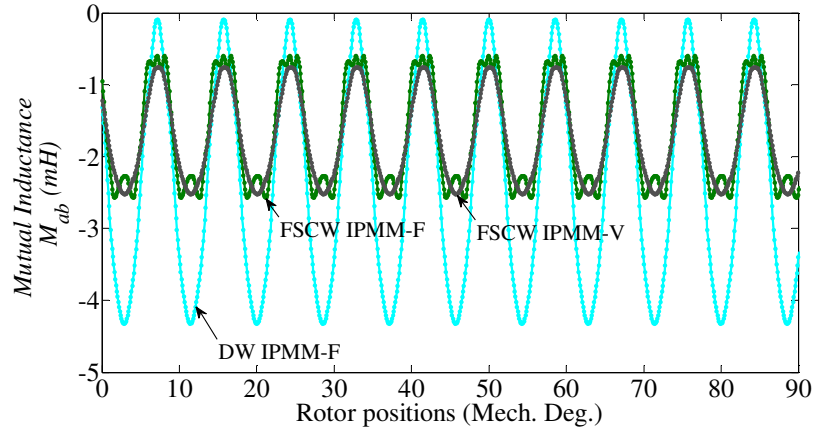


Fig. 4.34. Mutual-inductance of the DW IPMM-F, FSCW IPMM-F, and FSCW IPMM-V

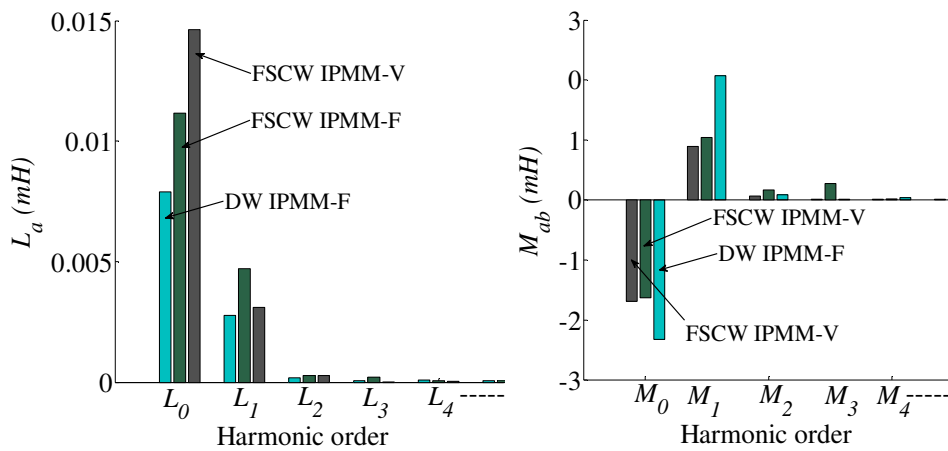


Fig. 4.35. Harmonics of self and mutual inductance

This is due to the presence of mutual coupling between phases. Fig. 4.35 shows the harmonic spectrum of self- and mutual inductances, respectively. From the harmonic

components of L_a and M_{ab} values, L_d and L_q can be determined by Eq.(4.12) and Eq.(4.13), respectively. Conventionally with DW, L_d and L_q are calculated from self-inductance using equations Eq.(4.14) and Eq.(4.15) [123].

$$L_d = (L_0 - M_0) - \left(\frac{L_1}{2} + M_1\right) - \left(\frac{L_2}{2} + M_2\right) - \dots \quad (4.12)$$

$$L_q = (L_0 - M_0) + \left(\frac{L_1}{2} + M_1\right) + \left(\frac{L_2}{2} + M_2\right) + \dots \quad (4.13)$$

$$L_d = \frac{3}{2}(L_0 - L_1) \quad (4.14)$$

$$L_q = \frac{3}{2}(L_0 + L_1) \quad (4.15)$$

Table 4.9 compares the L_d and L_q values that were calculated using the above equations from the measured self- and mutual inductances. It should be noted here that the saliency ratio is slightly different when L_d and L_q are calculated using Eq.(4.14) and Eq.(4.15), which neglects mutual inductance. Here, the mutual inductance is much larger in DW IPMM-F that should be included in the calculation of d - and q -axis inductances.

The comparison in Table 4.9 also shows that FSCW machine has slightly lower saliency ratio compared to the DW machine. This is due to a significant increase in the d -axis inductance that becomes comparable to q -axis inductance resulting in a lower saliency ratio. A comparison of inductances between the two FSCW designs reveals that saliency ratio is the lowest in the FSCW IPMM-V. This indicates reluctance torque component of such a machine will be lower compared to that of the FSCW IPMM-F.

Table 4.9 Inductance and saliency of DW IPMM-F, FSCW IPMM-F, and FSCW IPMM-V

Machine type	Phase A current (A)	Resistance in phase A (Ω)	L_d (mH)	L_q (mH)	ξ	ξ (excluding M_{ab})
DW IPMM-F	6.5	0.56	6.3	14.1	2.22	2.07
FSCW IPMM-F	6.5	0.6	8.4	17.1	2.04	2.46
FSCW IPMM-V	6.5	0.6	13.5	19	1.4	1.54

However, the wider constant power speed range is still possible in a PM machine with low or nil saliency, if its characteristic current as defined in Eq.(4.16) is equal or close to rated current (I_r).

The characteristic current is defined as,

$$I_{cr} = \frac{\psi_{PM}}{L_d} \quad (4.16)$$

where, ψ_{PM} is PM flux linkage.

As for the DW IPMM-F, the saliency ratio is higher than the other two but with smaller d-axis inductance values. Therefore, its characteristic current will be larger compared to two FSCW designs. In this study, the end winding leakage inductance has been neglected as 2D FEA does not consider end winding leakage inductance. The effect of end winding leakage inductance is examined in chapter 6.

4.5 Conclusion

Chapter 4 has investigated the suitability of implementing FSCW layout on IPMM's with high number of poles. The FSCW designs were then compared to a DW IPMM, which had been developed in the previous chapter. It is seen that the FSCW IPMM-F and the FSCW IPMM-V are the best choices as they have the lowest torque ripple and cogging torque. The FSCW designs also achieved sinusoidal back EMF waveform with low THD. However, the winding factor of the concentrated winding

IPMM is slightly lower than the DW design. As for the FSCW design, the FSCW IPMM-F was chosen for prototyping for the following reasons:

- For FSCW design, the flat shaped IPMM provides higher air-gap flux density as compared to the V-shaped IPMM for the same pole arc.
- A comparison of inductances between the two FSCW designs in [125] reveals that saliency ratio is lower in the FSCW IPMM-V. This indicates reluctance torque component of such a machine will be lower compared to that of the FSCW IPMM-F.
- The overall cost of manufacturing is more in the FSCW IPMM-V due to its segmented magnets in the rotor. The cost of laser cutting the rotor would also increase for the FSCW IPMM-V due to the small air-gap between the magnets in the same pole.

The next chapter will build upon the findings in this chapter to construct a prototype flat-shaped IPMM with FSCW structure.

CHAPTER 5: Final Design Selection and Prototyping of the FSCW IPMM-F

5.1 Introduction

The work done in chapter 4 already provided an optimal design of a 42-pole/ 54-slot FSCW IPMM with flat-shaped magnets in the rotor (FSCW IPMM-F). A prototype machine was constructed based on this design for experimental verification. Construction of this prototype FSCW IPMM-F was carried out by the Energy Systems Group, EET, UNSW in collaboration with the Commonwealth Scientific and Industrial Research Organization (CSIRO), Linfield.

This chapter focuses initially on the selection of materials for each region of the FSCW IPMM-F. The final rotor and stator dimensions were selected based on the study carried out to minimize the cogging torque and torque ripple as described in chapter 4. The FSCW winding configuration designed for the prototype was presented and analyzed in chapter 4. The FE analysis conducted in chapter 3 and 4 was in 2-dimension. A 3-D FE analysis was conducted to investigate leakage fluxes in the axial direction of the machine. The 3-D FEA results are presented in this chapter. A step by step construction process of the machine described in this chapter will provide an overview of the manufacturing process of the prototype FSCW IPMM-F.

5.2 Choice of materials

Three different active materials are considered for the core, coil, and rotor magnet poles. The materials were selected based on the properties such as low losses,

saturation, operating temperature, demagnetization, and mechanical stress. The next few sections describe the selection process of the active materials.

5.2.1 Core material

The lamination sheet made of silicon steel is the most commonly used core material for electric machines. First choice for the prototype machine was non-oriented silicon steel grade M270-35A of thickness 0.35mm. It has a high saturation point at 1.6 T and relatively low core losses 2.7 W/kg at 1.5T/50Hz. However, the availability of the lamination sheet of 0.35 mm turned out to be an issue during the construction phase. This has prompted an investigation for other equivalent steel grades. It was found that two radially available non-oriented steel grades (i) 35CS300 (According to EN 10106: M300-35A) and (ii) 50CS350 (According to EN 10106: M350-50A) could replace M270-35A without any compromise to the optimized design. The B-H characteristics curves of these two materials are shown in Fig. 5.1. Some of the key features of these non-oriented silicon steel grades are given in Table 5.1. The loss characteristics curve for the 35CS300 and the 50CS350 obtained from the manufacturer are shown in Fig. 5.2.

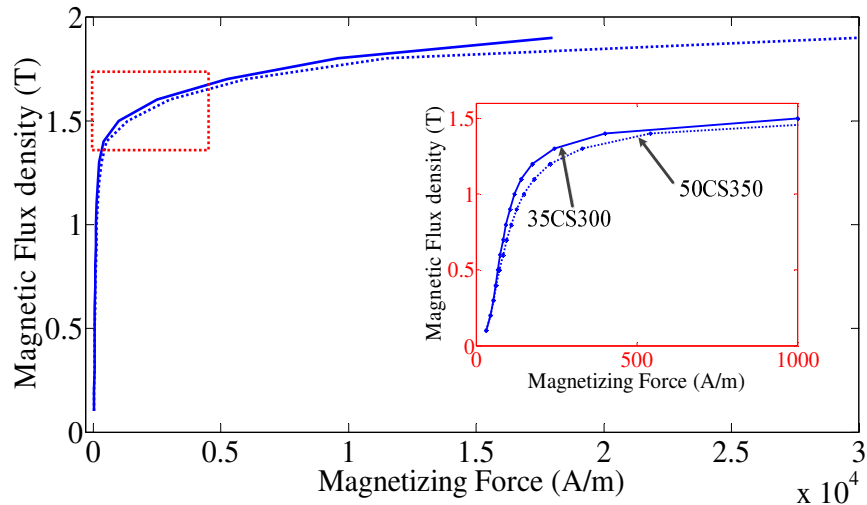


Fig. 5.1. B-H characteristics curves of 35CS300 and 50CS350 (Manufacturer datasheet)

Table 5.1 Properties of compared core grades

Material Type		Lamination thickness	Stacking Factor	Max power loss (W/kg) at 50 Hz at 1.5 T(from datasheet)	Loss (W/kg) at 50 Hz at 1.7 T(from Manufacturer's Test)
EN 10106:2007	JISC 2552 :2000				
M270-35A	35A270	0.35	95%	1.1	N/A
M300-35A	35CS300	0.35	95%	1.2	2.56
M350-50A	50CS350	0.50	97%	1.5	2.65

In chapter 4, was shown that the core loss in the FSCW IPMM-F makes up approximately 27% of the total loss of the machine at full load. A more in-depth analysis was conducted to see the effect on the overall efficiency of the prototype FSCW IPMM-F by selecting the 50CS350 as the core material. Fig. 5.3 shows the core loss and the efficiency of the FSCW IPMM-F with two different core materials.

It can be seen from Fig. 5.3 that the difference in core loss between the two materials is approximately 10 watts during full load. However, this difference does not have a considerable influence on the efficiency, as both materials produce an efficiency of 93% under full load conditions. This suggests that the use of 50CS350 will not decrease the efficiency to a significant level.

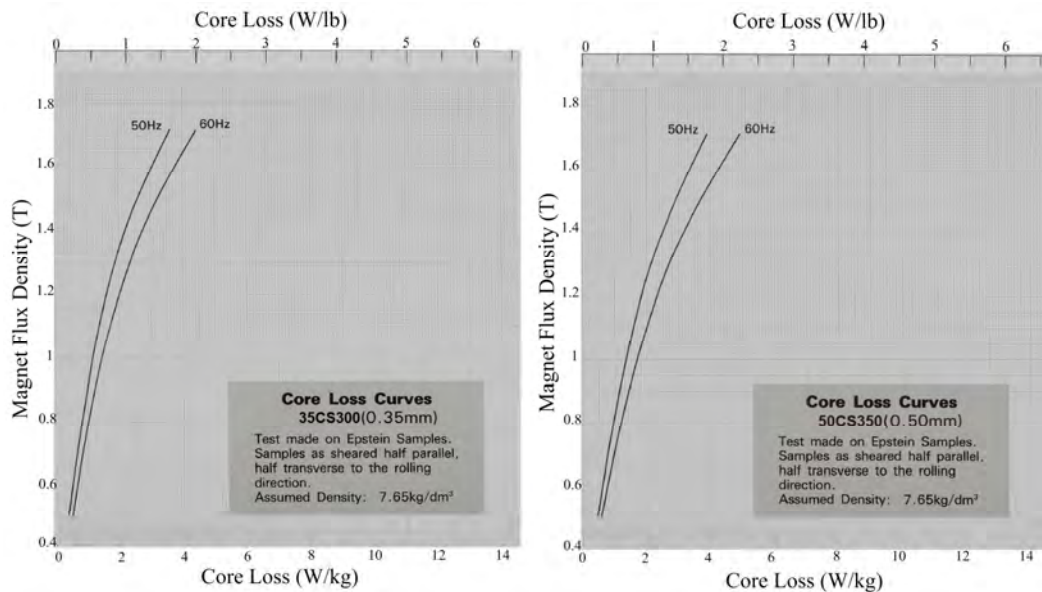


Fig. 5.2. Loss characteristics curve for the 35CS300 and the 50CS350

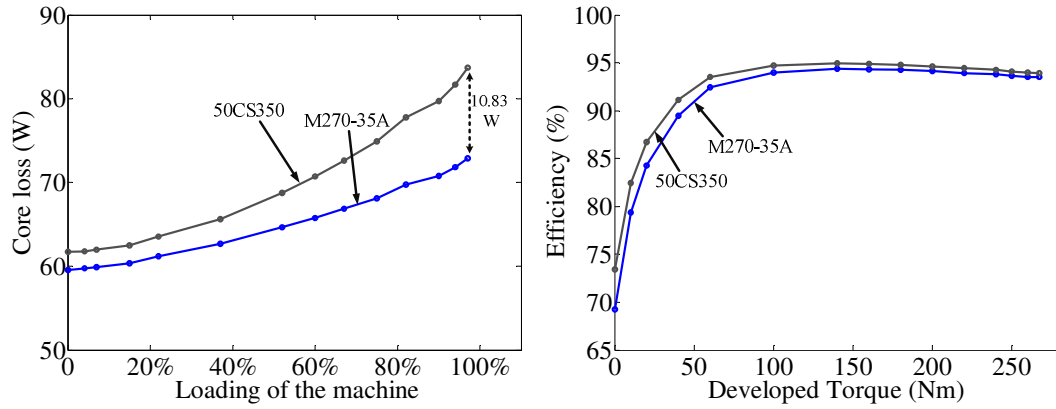


Fig. 5.3. Core loss and efficiency for FSCW IPMM-F with two different core materials

In order to select 50CS350 as the core material of the rotor and the stator for the prototype machine, some further analysis was conducted. The Bertotti loss coefficients, k_h and k_e were found for 50CS350 in the similar manner as it was found for M270-35A as discussed in chapter 3. The coefficient values of 50CS350 are given below:

$$k_h = 35.647 \text{ W s T}^2 \text{ m}^{-3};$$

$$k_f = 0.97;$$

$$k_e = 2.227 \text{ W (T s}^{-1})^{-3/2} \text{ m}^{-3};$$

$$\sigma = 2272727 \text{ s/m};$$

The calculated loss curve of silicon sheet steel 50CS350 using the Bertotti loss model is compared with that of the manufacturer's datasheet in Fig. 5.4. It can be seen that the Bertotti loss curve is following the loss curve provided by the manufacturer, suggesting that the coefficients calculated can be used in FE to determine the iron loss.

In this research, a steel tester method is used to accurately define the 50CS350 material in FEA. Using the steel tester method, the B-H loop of the 50CS350 can be easily determined from which the B-H characteristics curve is originated. Fig. 5.5 shows the B-H loop of typical non-oriented silicon steel. The block diagram for the steel tester method is shown in Fig. 5.6.

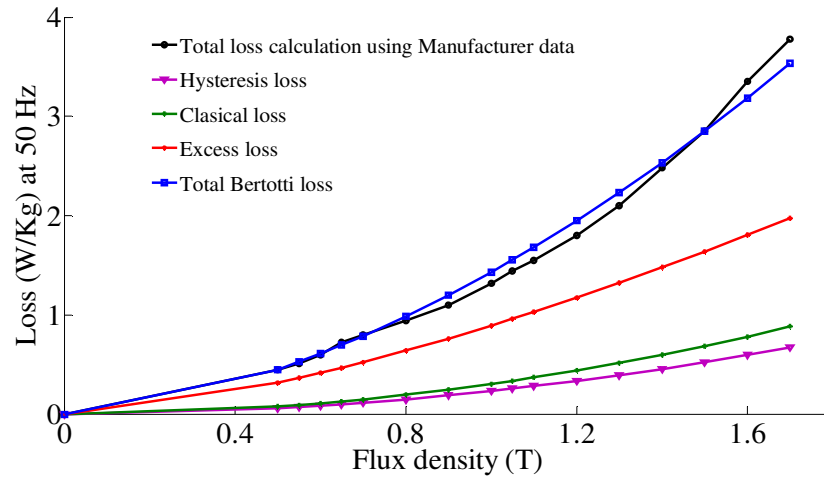


Fig. 5.4. Individual loss elements of the Bertotti loss model using 50CS350 silicon steel

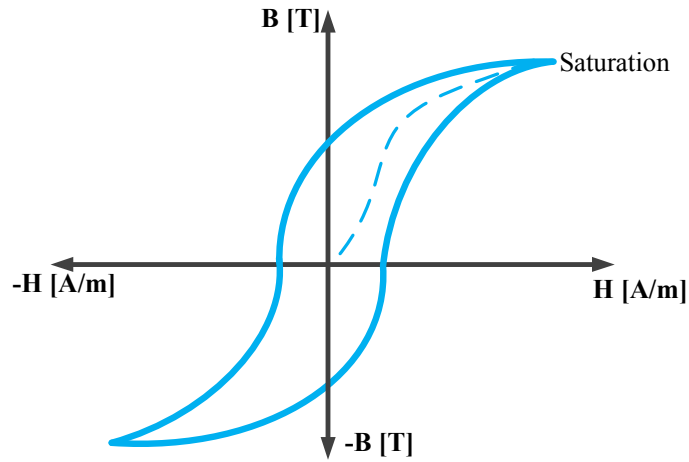


Fig. 5.5. B-H loop of typical non-oriented silicon steel (Bipolar curve)

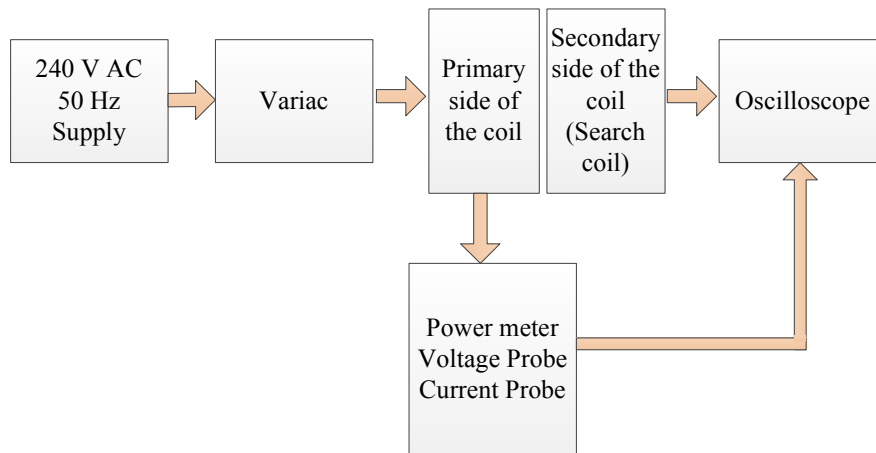


Fig. 5.6. The steel tester method

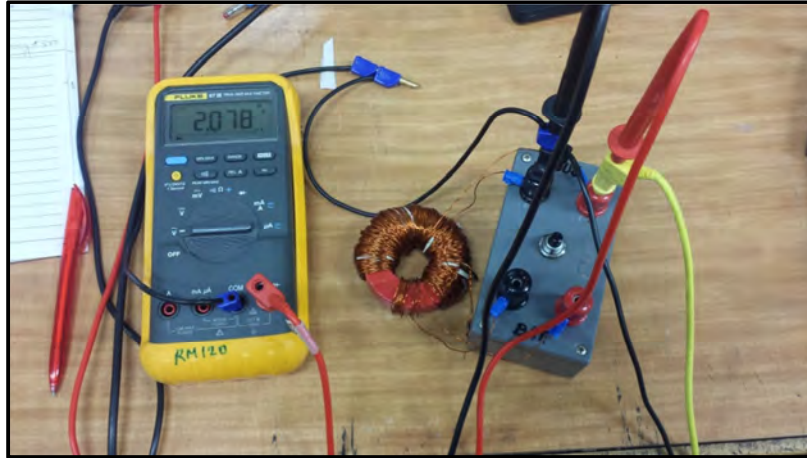


Fig. 5.7. Copper wound toroid

For this study, a toroid was constructed using laminated sheets of 50CS350 for which the inner diameter was 35 mm, and the outer diameter of the toroid was 64mm. The number of turns on the primary side was 209, and for the secondary side it was 48. Both the primary and secondary winding coils are copper wires of grade AWG 22. Fig. 5.7 shows the copper wound toroid used in this experiment.

The equation used to determine B and H are given as,

$$B = \frac{I}{A.N'} \int e_2 dt \quad (5.1)$$

$$\text{And } \int H.dl = N.I \quad (5.2)$$

Where,

B= Magnetic flux density;

A =Cross sectional area of the toroid;

N' = Number of turns in the secondary;

e_2 = Secondary induced voltage;

H = Magnetic field strength;

N = Number of turns in the primary and

I = Current induced in the primary side of the toroid;

A program was used in MATLAB based on Eq.(5.1)-Eq.(5.2) to determine the hysteresis loop of 50CS350 (plotted in Fig. 5.8). The B-H characteristics curve is found

by taking the maximum value of B and H from each of the hysteresis loop shown in Fig. 5.8. The experimental B-H characteristics curves of 50CS350 together with the B-H characteristic curve given in the datasheet are plotted in Fig. 5.9.

It is seen from Fig. 5.9 that the experimental B-H characteristics curve differs slightly from the manufacturer's one. The experimental B-H curve was used in the FE model so that the FE result would closely resemble the experimental results.

Fig. 5.10 shows the FEA flux density color plot of the highly saturated regions of the prototype machine at full load for the three core materials considered here. They were found to be within permissible limits for all three materials.

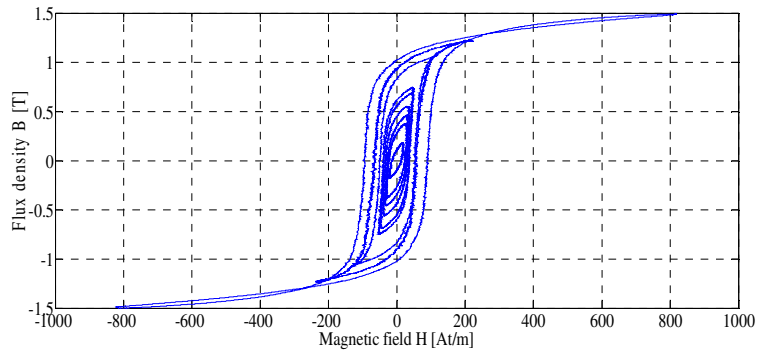


Fig. 5.8. Experimental hysteresis loop of 50CS350

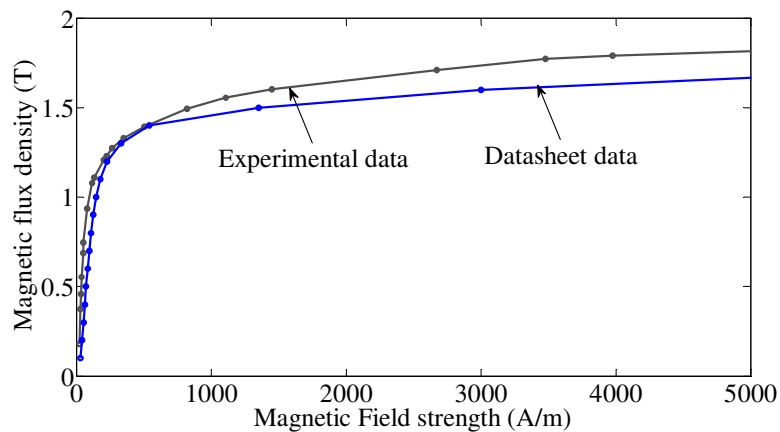


Fig. 5.9. Experimental B-H characteristics curve of 50CS350

5.2.2 Selection of Permanent Magnet material

Like any ferromagnetic material, Permanent Magnet materials can be characterized using a B-H loop. Fig. 5.11 shows a typical B-H Hysteresis loop and characteristic parameters for a permanent magnet. The primary parameters that characterize a Permanent magnet are described below [126]:

- Remanence (B_r): It is the magnetic flux density at zero magnetic field.
- Coercivity (H_c): This point is defined as the negative field at which the magnetic flux density is zero.
- Recoil Magnetic Permeability: $\mu_{rec} B = B_r + \mu_{rec} \mu_0 H$.

The first and third quadrants in the B-H loop of Fig. 5.11 are defined as magnetizing and demagnetizing quadrants respectively. The characteristics of PM's are often described by the quadrant II as they mostly operate in this region. PM's are designed to function in the recoil line (see Fig. 5.11). The recoil line is linear till B reaches B_{knee} . If $B < B_{knee}$, the magnet becomes partially demagnetized and will fall under a new recoil line. It should be noted here that demagnetization of PM's is irreversible.

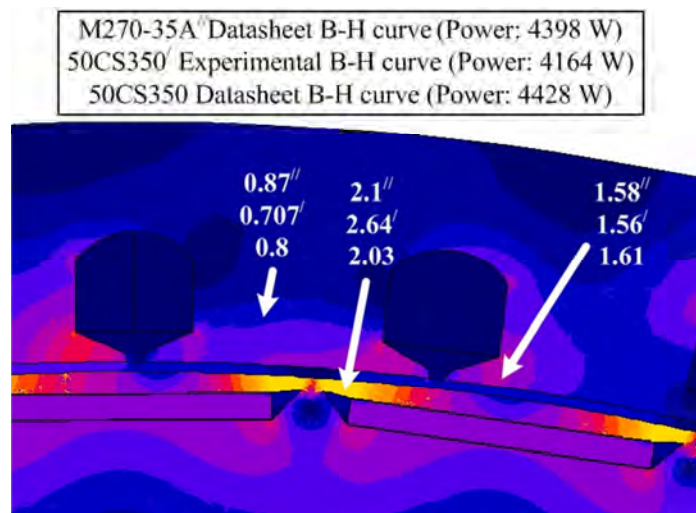


Fig. 5.10. Flux density in various segments of the prototype FSCW IPMM-F using different core materials

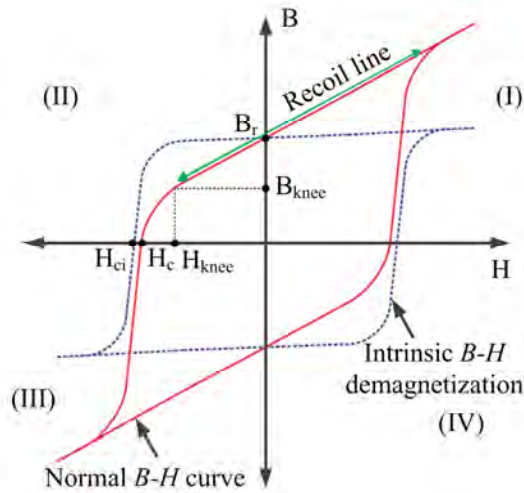


Fig. 5.11. B-H Hysteresis loop for a permanent magnet [127]

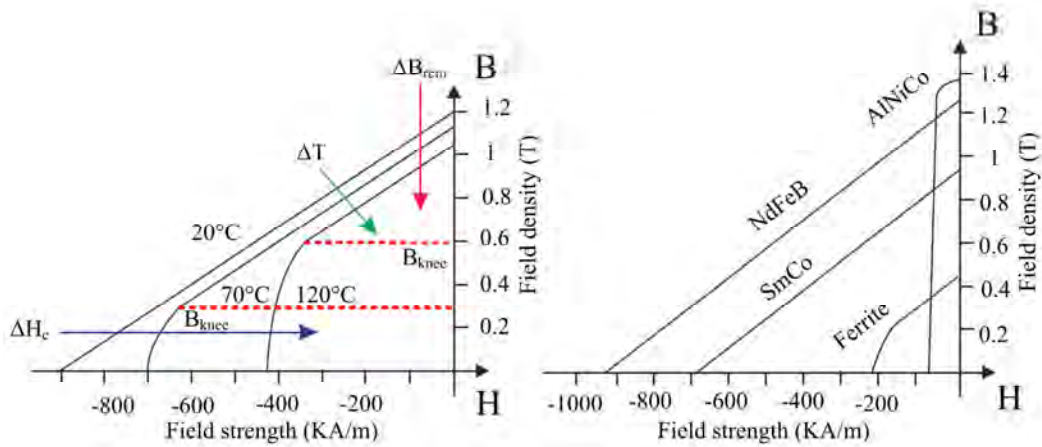


Fig. 5.12. (a) Effect of temperature on PM demagnetization curve, (b) Demagnetization curves of standard permanent magnets at 20° C [127].

Fig. 5.12 shows the demagnetization curves of standard permanent magnets at 20°C. It also displays the effect of temperature on B_{knee} . As seen from Fig. 5.12, the increase in temperature increases the demagnetization risk as B_{knee} reduces. PM's are classified as either soft or hard based on their hysteresis characteristics. A soft magnetic material has a small hysteresis loop that indicates the material has high initial permeability and a low coercivity. On the other hand, a hard magnetic material has wider hysteresis loop [127]. Permanent magnet synchronous generators are designed with hard magnetic material as they have higher coercivity and thus have less chance of demagnetization.

In Fig. 5.12, AlNiCo has the highest remanent flux density. Due to its small hysteresis loop, there is a high possibility of magnetization as well as demagnetization. The rare-earth PM materials, SmCo, and NdFeB, have large remanence and coercivity as seen in Fig. 5.12. Both of these PM's have superior magnetic properties. The general properties of the most common permanent magnets are displayed in Table 5.2. It can be seen that the maximum allowable temperature for SmCo is higher than NdFeB, which indicates lesser chances of corrosion. However, NdFeB magnets are the most preferred choice for present day PM machines due to its lower cost in comparison to SmCo. It has maximum operating temperatures of between 80°C to 220°C. NdFeB magnets also have a high coercivity of approximately 844KA/m. Fig. 5.13 shows the effect of negative i_d current on the coercivity of the magnets of the prototype FSCW IPMM-F. This shows that the magnets will not be demagnetized even after applying high negative i_d current during field-weakening.

Table 5.2 Properties of various PM's

	B_r (T)	H_c (KA/m)	T_{curie} (°C)	T_{max} (°C)	Hysteresis Loss (KJ/ m ³)
Fe	0.38	250	450	300	0.27
AlNiCo	1.2	50	860	540	36
SmCo	0.85	570	775	250	170
NdFeB	1.15	880	310	180	255

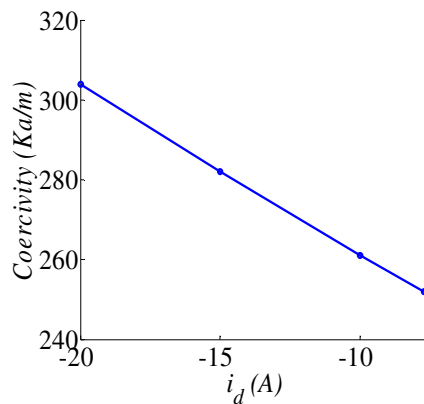


Fig. 5.13. NdFeB 32SH coercivity versus the change in i_d current.



Fig. 5.14. Dimension of each Magnet piece for the prototype FSCW IPMM-F

The chosen grade of NdFeB magnet is N32SH with a remanent flux density of 1.13~1.17 T and maximum operating temperature of 230°. This grade was chosen based on the required air-gap flux density to produce 4 KW at 143 RPM. The dimension and the orientation of one magnet piece are shown in Fig. 5.14. In chapter 3 and 4, the magnet remanence was chosen to be 1.16 T with a relative permeability of 1.0446. In FEA, the magnet property was considered to have linear approximation. This is defined by,

$$B(H) = \mu_0 \mu_r H + B_r \quad (5.3)$$

where, $\mu_r = 4\pi \times 10^{-7}$ H/m.

In order to represent the PM's accurately in FE, the magnets were tested using a Gaussmeter. Ten random magnets were chosen out of 42 magnets and were placed in an open atmosphere so that no outside field can influence the experiment. Using axial and transversal HALL probes connected to the Gaussmeter, the remanant flux density was measured. An axial HALL probe measured the flux parallel to the probe holder whereas the transversal probe measured the flux perpendicular to the probe holder. It is should be note here that the position of the probe related to magnet must be exactly the same between each sample. Fig. 5.15 shows the magnetic field for the ten magnets under test at 2 m and 4 m distance from the HALL probes. The Flux density for each magnet can

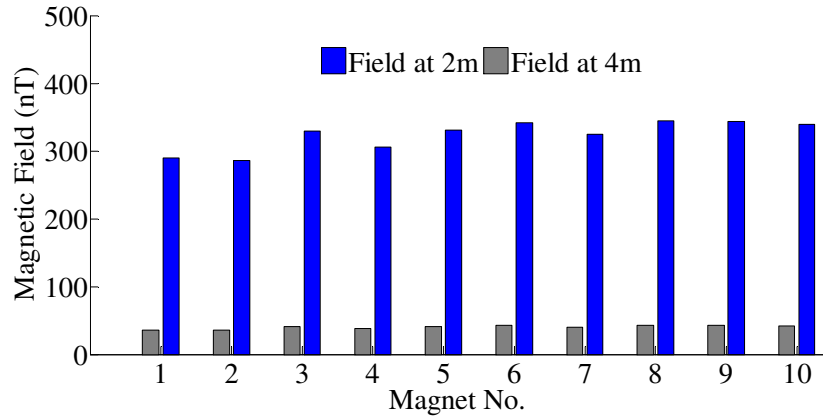


Fig. 5.15. Magnet Fields for various magnets at 2m and 4m distance

Table 5.3. Testing of individual magnets using HALL probes

Magnet	Field ratio=	Magnetic moment ($A.m^2$)	Current (A)	H (A/m)	B_r (T)
	Field at 2m Field at 4m				
1	8.03	11.53	1958	-652654	0.86
2	8.04	11.39	1934	-644683	0.85
3	8.09	13.02	2212	-737247	0.97
4	8.01	13.77	2339	-772569	1.03
5	8.01	13.22	2245	-748296	0.99
6	7.99	13.71	2329	-776192	1.02
7	8.04	12.94	2198	-732718	0.97
8	8.01	13.77	2339	-772569	1.03
9	8.06	13.65	2318	-772569	1.02
10	8.01	13.77	2339	-772569	1.03
Average	8.04	12.89	2188	-729440	0.96
Std. Dev.	0.03	0.89	151	50480	0.07

be calculated easily as shown in Table 5.3 using the above data achieved from the HALL probes.

From Table 5.3, it can be seen that there are discrepancies in B_r for each piece of permanent magnet. The average value for B_r is found to be 0.96 T which is almost 18% lower than the expected value of 1.16 T. B_r is proportional to magnetic loading and slight change in remanence significantly affects the parameters of machine design. Fig. 5.16 shows the change in flux density and L-L voltage for the FSCW IPMM-F with the

change in B_r . The impact of B_r on the main fundamental component of flux density and the generated EMF is shown in Table 5.4 for the FSCW IPMM-F.

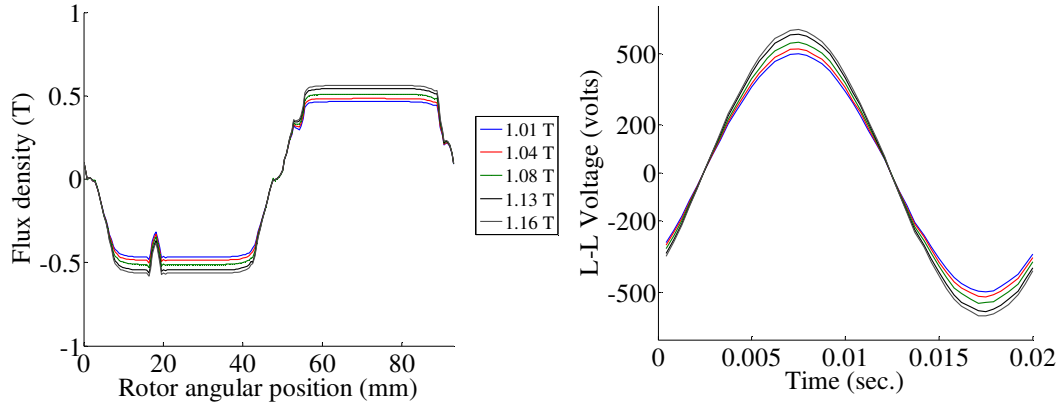


Fig. 5.16. Effect on Flux density and L-L voltage of FSCW IPMM-F with the change in B_r

Table 5.4. Change in Fundamental component of flux density and the L-L voltage of FSCW IPMM-F with the change in B_r

Magnet Remanence (T)	Fundamental Flux density, B_δ (T)	L-L Voltage (RMS) (Volts)
1.01	0.56	352.6
1.04	0.59	366.94
1.08	0.62	386.3
1.13	0.65	410.43
1.16	0.68	424.87

From Table 5.3, it is seen that 3 out of 10 magnets have a B_r of 1.03 T. Some more discussion on the magnet remanence with the magnet manufacturer and considering the accuracy of the test methods, it was decided that use of $B_r = 1.03$ T in the FE model would be reasonable. Fig. 5.17 shows the magnet orientation of the FSCW IPMM-F.

5.2.3 Stator coil

The use of copper is a common choice for coil material due to its high melting point, low cost, high conductivity, and excellent flexibility. The selection of the proper grade of copper wire is important as it significantly affects the copper loss that makes

up around 65 % of the total loss of the FSCW IPMM-F at full load. In chapter 3 and 4, the copper wire was assumed to be AWG 17 during FE analysis. AWG 17 has a maximum ampere rating of 19A with a resistance of 16.6 *ohms/km*.

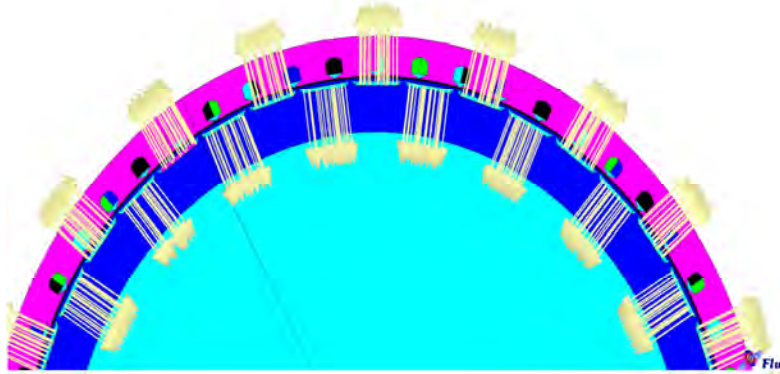


Fig. 5.17. A portion of FSCW IPMM-F showing the orientation of the magnets.

The amount of copper loss can be calculated as,

$$P_{cu} = 2N_{coil}\rho_r I^2 \frac{l}{A_w} \quad (5.4)$$

where,

N_{coil} = Number of turns per coil

ρ_r = Conductor resistivity

A_w = Cross-sectional area of the wire

l = Machine stack length

A copper material grade for winding is characterized by its resistivity, cross-sectional area, and its ability to carry maximum current. All 3 of these parameters affect the copper loss of the machine according to Eq.(5.4). For the prototype FSCW IPMM-F, the maximum current in the stator is 9.2A. In order to minimize the stator resistance while keeping the current carrying capacity unaltered, paralleling of copper wires to form one coil is an excellent option. A test was conducted by using six conductors in parallel to form one coil. Two sets of wires were used in the test – one set with a diameter of 0.56mm for each conductor and another set with a diameter of 0.6mm for each conductor. It was found that the slot-fill factor achieved using a 0.6mm copper wire

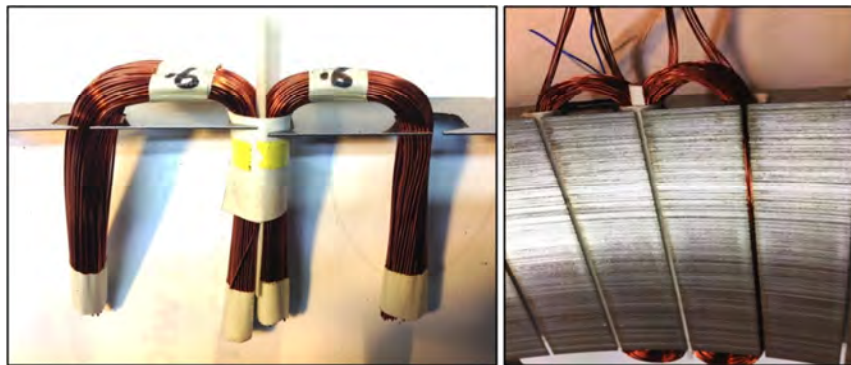


Fig. 5.18. Winding with a 0.6 mm copper wire for double layer CW stator

was higher than that of 0.56mm. Using a 0.56mm wire will allow a current density of $8.16A/mm^2$ for a 12A load. As for the same condition, the current density would be $7.1 A/mm^2$ for a 0.6mm wire. The required current rating of the prototype machine to achieve 4kW at 143 rpm is 6A. Hence, the 0.6mm copper wire was selected for the winding. The one coil of the winding will consist of 6 conductors in parallel. Fig. 5.18 shows the winding with a 0.6mm diameter copper wire that form the double layer CW stator of the prototype machine. The nominal resistance of the copper wire with 0.6mm diameter is $60.46 \Omega/km$ at $20^\circ C$. The use of 6 parallel strands to form one coil reduces the resistance to $10.08 \Omega/km$. As compared to AWG 17 used previously for designing the DW and CW IPMM's in chapter 3 and 4, the resistance of the wire decreases by almost 60% with the use of 0.6mm copper wire.

Resistivities of the materials and thus the resistance of conductors vary with temperature. Fig. 5.19 shows the graphs of resistivity versus temperature for various metals. It is seen from Fig. 5.19 that the change in resistivity for copper is lower than that of Aluminum, Gold, and Tungsten. Resistance of a conductor due to temperature rise can be estimated using the equation below

$$R_T = R_{25}[1 + \alpha_{25}(T - T_{25})] \quad (5.5)$$

Where,

R_T =Resistance of the conductor at T operating temperature;

R_{25} = Resistance of the conductor at 25°C ambient temperature;

T= Operating temperature;

T_{25} =25°C ambient temperature; and

α_{25} =Temperature co-efficient (TCR) at 25°C ambient temperature (4.138×10^{-3} for copper);

The variation in resistance per phase of the final model with the increase in temperature is shown in Fig. 5.20.

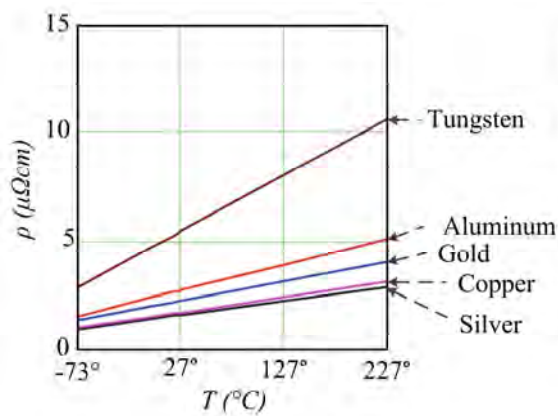


Fig. 5.19. Resistivities of selected metals [128]

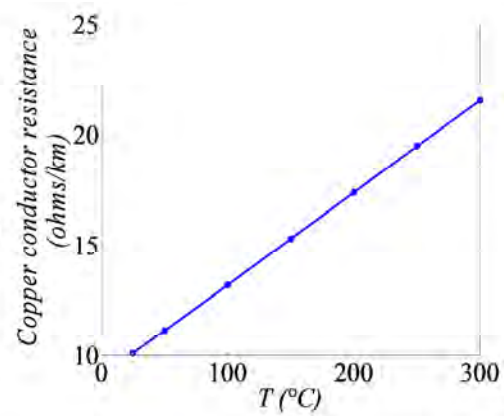


Fig. 5.20. Resistance per phase as temperature increases for the FSCW IPMM-F

The resistance for each phase in the FSCW IPMM-F can be calculated easily using datasheet provided by the manufacturer that specifies the resistance of the copper wire per km length. It is shown below:

The average turn length of one coil is found to be 0.433m.

The average length of each coil = 0.433 x 21(total number of turns per coil) = 9.07 m;

Total length of each phase = 9.07 x 18(coils per phase) = 0.163 km;

From the datasheet, the resistance of the copper wire with 0.6 mm diameter is determined to be 60.46 Ω/km. The use of 6 parallel strands to form one coil reduces the resistance to 10.08 Ω/km. So the resistance of one phase in the FSCW IPMM-F is 0.163 x 10.08 = 1.65 Ω. Later this value was verified with the FSCW IPMM-F by directly measuring the phase resistance using a multi-meter.

5.3 Final winding Configuration

The slot dimension of the final design is shown in Fig. 5.21. The determination of the arrangement of phase coils in the prototype FSCW IPMM-F has already been discussed in chapter 4. Fig. 5.22 shows the winding layout of each phase with respect to the slot number.

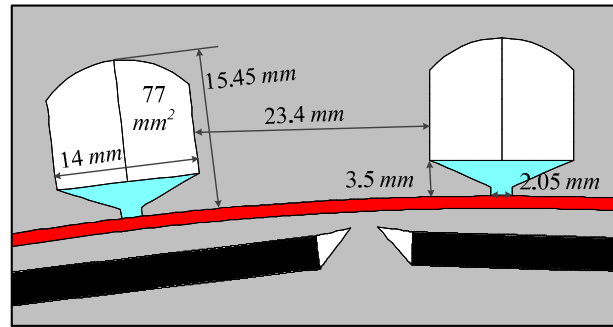


Fig. 5.21. Slot dimension of the final FSCW IPMM-F design

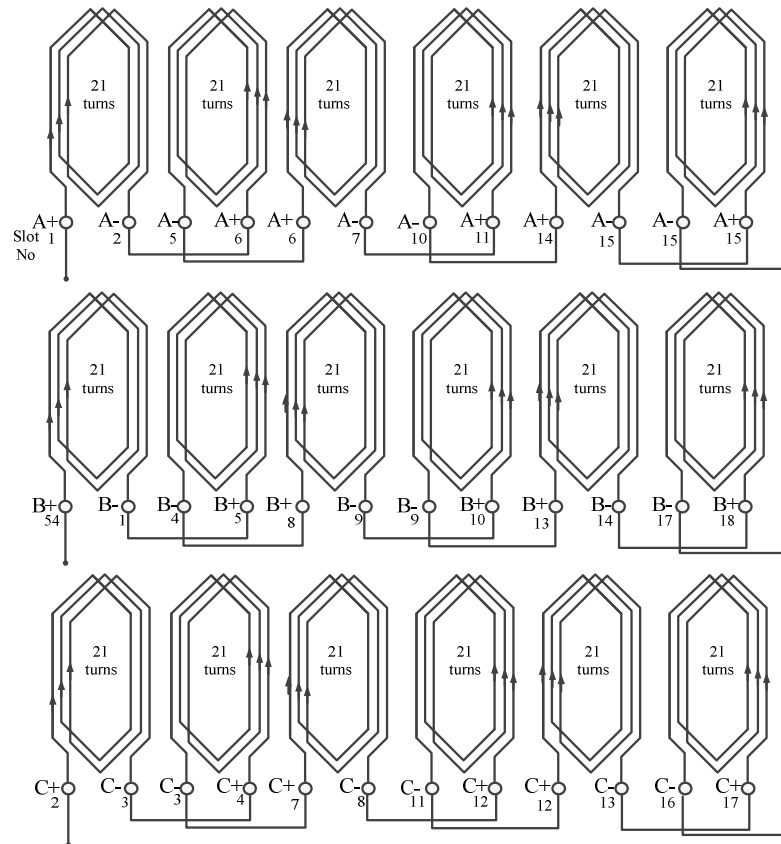


Fig. 5.22. Winding layout of the FSCW IPMM-F

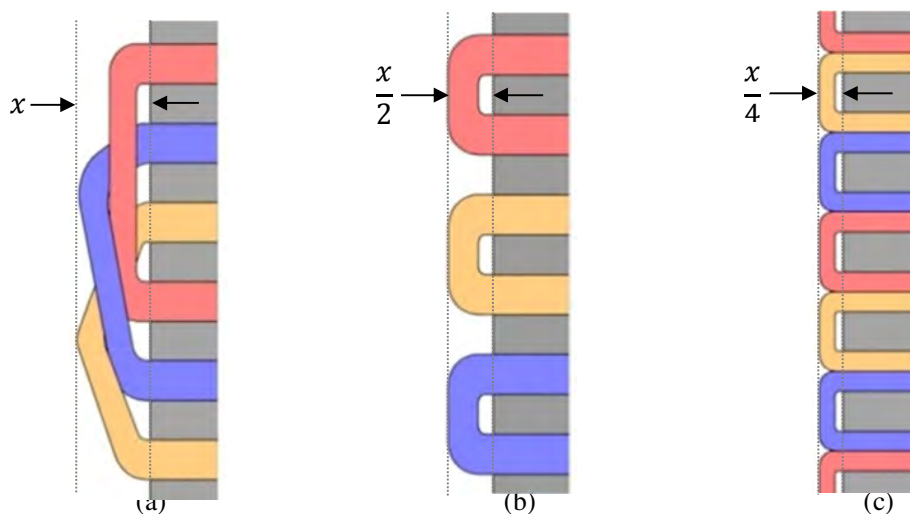


Fig. 5.23. Estimated End winding length for (a) Single layer DW; (b) Single layer FSCW and (c) Double layer FSCW

As the periodicity of the FSCW IPMM-F is three, thus the winding layout in Fig. 5.22 is shown for 18 slots and has to be repeated three times in order to achieve the total winding layout of the FSCW IPMM-F

5.3.1 End winding inductance

A CW layout has non-overlapping coils leading to smaller end-winding length in comparison to a DW design. This leads to lower stack length for a CW machine. Fig. 5.23 compares the end-winding lengths of DW and FSCW.

It can be seen from Fig. 5.23, that the end-winding length of a double layer CW is a quarter of that of a single layer DW. This means that the end-winding leakage flux will also be substantially lower for a FSCW machine. In 2D FEA, the end-winding leakage inductance due to the flow of currents in end-windings cannot be considered in the analysis and needs to be included with the total inductance of the machine. In this thesis, the end-winding leakage inductance is calculated analytically and then added to the total inductance in the FSCW IPMM-F. This value is further validated with a 3D FE

analysis. The end winding leakage inductance was calculated using the equations below [129]:

$$L_{end} = \frac{4m}{s} s_{pp} N_{ph}^2 m_o k \quad (5.6)$$

and

$$k = 2l_{ew} \lambda_{ew} + W_{ew} \lambda_w \quad (5.7)$$

where,

s = total number of phase;

Q = number of slots;

N_{ph} = number of turns in series per phase;

l_{ew} = height of the end winding;

W_{ew} = width of the end winding; and

λ_{ew} and λ_w are reactance factors.

The reactance factors for the end-winding depend on the order of the end-winding layers as well as the structure of the winding. A table of reactance factor values are given in [129] for various machines. In this study, the reactance factors $\lambda_{ew} = 0.518$ and $\lambda_w = 0.138$ were used for a double concentrated winding structure. These values were recommended in [59] for concentrated winding similar to the prototype machine. Fig. 5.24 shows the end-winding arrangement of the FSCW IPMM-F.

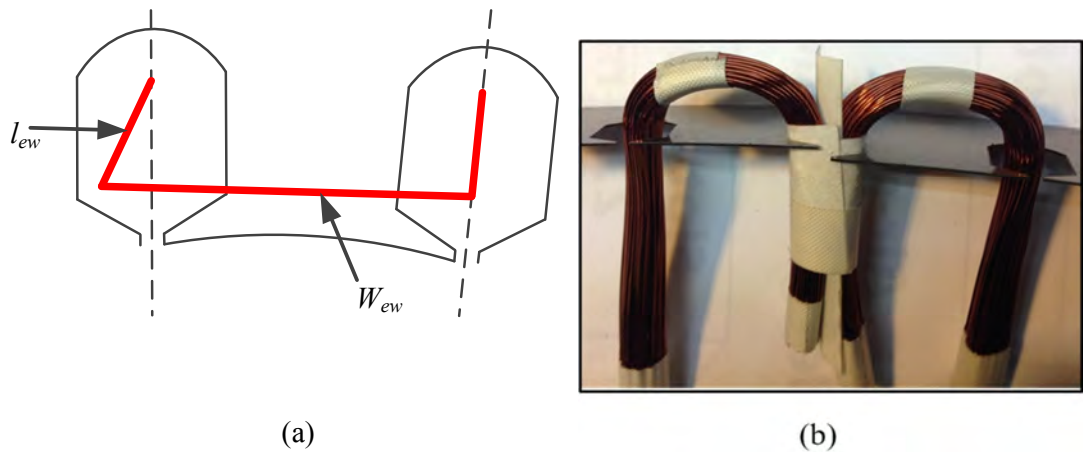


Fig. 5.24. (a) Dimension of an end winding and (b) End winding of the FSCW IPMM-F (side view)

The length of the end winding varies as the turns move further away from the tooth walls. It can be calculated as,

$$l_{end,min} \approx (1 - \lambda_s) \cdot \tau_s \quad (5.8)$$

$$l_{end,max} \approx \frac{\pi \cdot \tau_s}{2} \quad (5.9)$$

$$\tau_s = \frac{2\pi}{s} R_{si} \quad (5.10)$$

where,

$l_{end,min/max}$ = length of the innermost/outermost turn end region;

τ_s = slot pitch;

$\lambda_s = 0.5$ (typical for AC machines);

R_{si} = stator inner radius;

$l_{end,min}$ and $l_{end,max}$ are found to be 66mm and 72 mm respectively for the prototype machine. Using the average of these values, the value for l_{ew} and W_{ew} were calculated as 20mm and 31 mm respectively.

For the prototype FSCW IPMM-F, N_t is 378. Using Eq.(5.6), the end winding inductance, L_{end} for each phase was found to be 0.85 mH. This value of end winding inductance was later verified with a 3D FE model.

5.3.2 Slot fill factor

A slot fill factor (S_{ff}) is defined as the ratio of the total cross-sectional areas of all the conductors in one slot to the total slot area. Typical slot-fill factor for DW is no greater than 35%. In a CW stator, a slot fill factor of 50% can be achieved using the traditional hand winding methods. Fractional slot CW can be automatically wound with a needle-winding machine that results in a smaller slot fill factor as found in [130]. A high slot fill factor of more than 70% can be achieved with needle winding for a joint-lapped core [131] which also makes the production process quicker. However, this

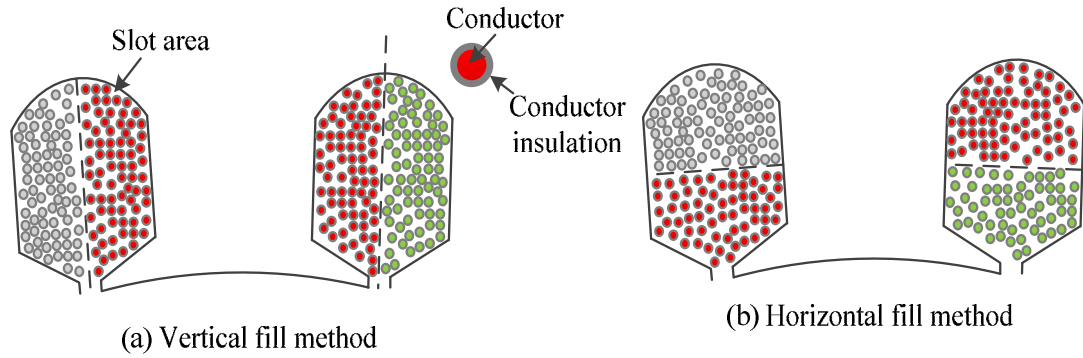


Fig. 5.25. Manual winding methods

method requires investing in a winding machine as well as special laminations are necessary for the stator. For this research, manual hand winding of coils is done on the teeth that make the process slow but economical for the prototype machine.

The slot fill factor S_{ff} also depends on the orientation of the conductors aligned in the stator slots. Fig. 5.25 shows two different methods that can be used to wind a conductor in a double layer CW machine. The vertical fill method reduces the end winding length by approximately half in comparison to the horizontal fill method. This suggests that FSCW IPMM with windings done in vertical fill method will result in a lower copper loss as compared to that of a horizontal fill FSCW IPMM. The only drawback is that the manual vertical fill method is time-consuming (required time is almost twice the time of the horizontal fill method). Despite the expected high production time, the vertical fill method was chosen in the prototype construction to achieve lower copper losses. In the prototype FSCW IPMM, the required conductor area for each slot is 35.6 mm^2 , and available slot area is 77 mm^2 shown in Fig. 5.21. This makes the slot fill factor for the FSCW IPMM-F increase to 46%.

5.4 Rotor of the final design

The rotor outer radius was kept to 310mm as discussed in chapter 4. The structure of the flux barrier and the magnets were optimized in chapter 4 to minimize cogging

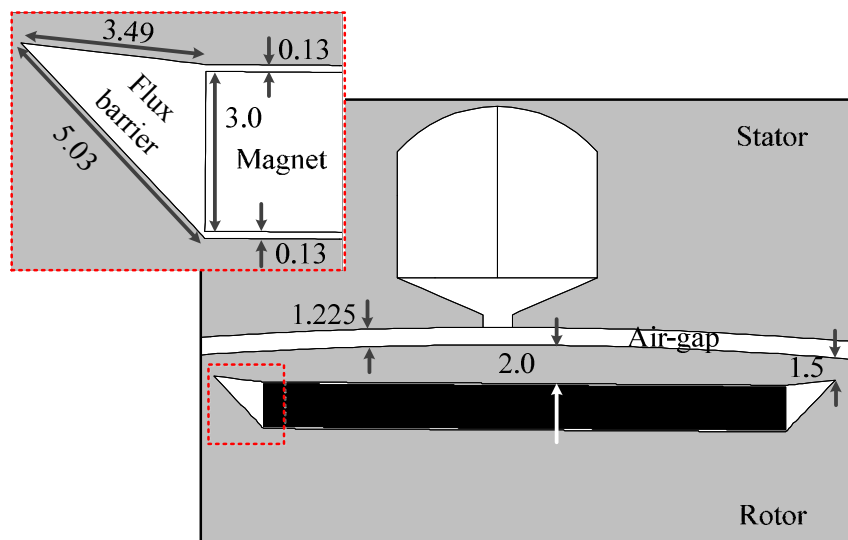


Fig. 5.26. Position of magnet in the rotor for the FSCW IPMM-F (all values are in mm)

torque and torque ripple. The dimension of the flux barrier and the position of a magnet in the rotor with respect to a stator tooth of the prototype machine is shown in Fig. 5.26. The dimensions of the magnets were described in section 5.2.2. It can be seen that, there is a tolerance of 0.13 mm added on both sides of the magnets. Details on this tolerance are presented in Appendix B. The air-gap for the final design is set to 1.225 mm based on the required air-gap flux density to produce 4 KW at 143 RPM. This is seen in Fig. 5.26.

5.5 3-D FEA of the FSCW IPMM-F design

The 3-D FE analysis was conducted for the final design in order to ensure that there were no significant flux leakages in the axial direction. The followings were confirmed with the 3-D FE model:

- Verify the flux density waveform with the flux density waveform obtained using 2D FEA.
- Verify the EMF and its total harmonic distortion.
- Verify the analytical/calculated end-winding leakage inductance.

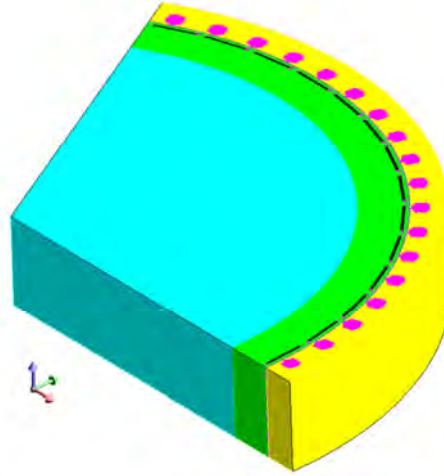


Fig. 5.27. 3-D model of the FSCW IPMM-F

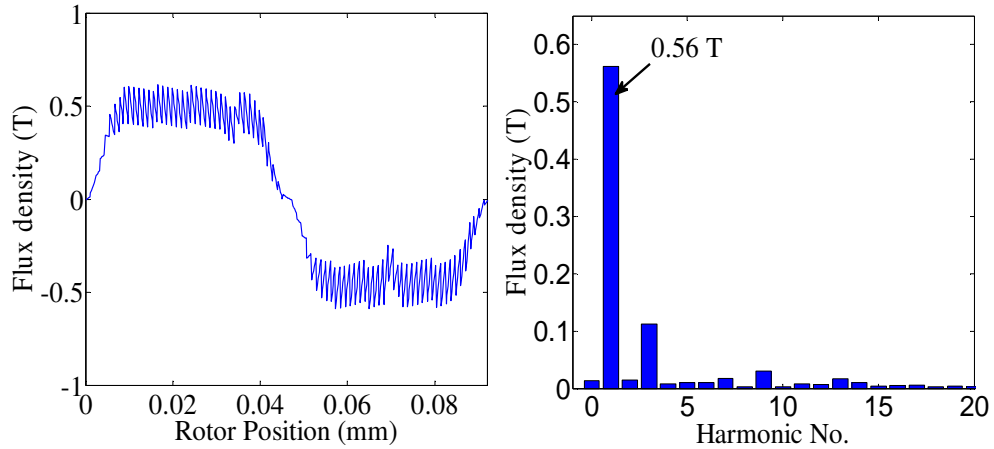


Fig. 5.28. Flux density and its FFT analysis of the FSCW IPMM-F using 3-D FEA

The 3-D FE model of the prototype is shown in Fig. 5.27. The flux density waveform and its FFT are shown in Fig. 5.28. It can be seen that the fundamental flux density is 0.56 T. The fundamental air-gap flux density obtained using 2D FE is 0.576T. This means the inconsistency in the two models is 2.7% which is negligible.

Fig. 5.29 shows the flux density in the axial orientation of the FSCW IPMM-F. The flux density is found to be negligible across the z -axis as seen in Fig. 5.29. This confirms that the electromagnetic analysis obtained from 2-D model was reasonable. The rated L-L RMS voltage is found to be 358 volts at rated speed with a total harmonic

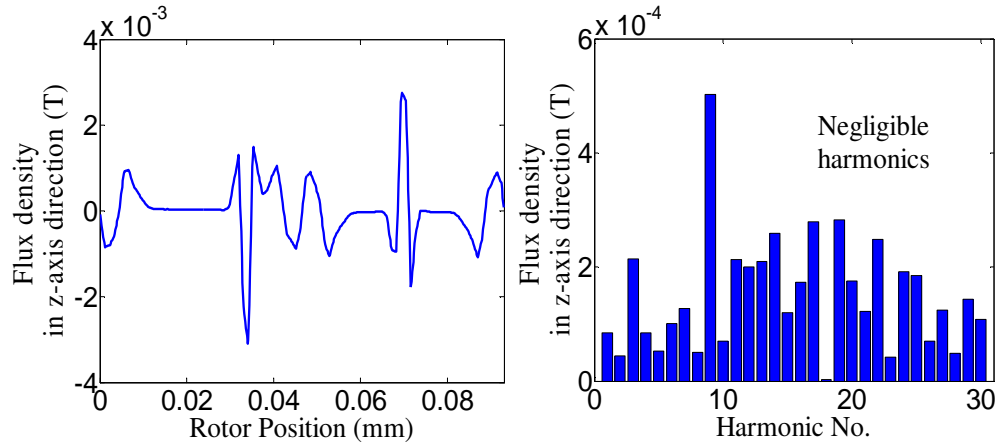


Fig. 5.29. Flux density in the z-axis direction of the FSCW IPMM-F using 3-D FEA

distortion (THD) of 0.77% which is almost identical to the value found during 2-D FEA shown in section 5.7. The inductance in the end-windings was calculated in the 3-D FE model by deriving the energy in the air around the end windings (W_{air}). The end winding inductance can be calculated as,

$$L_a - M_{ab} = 2 \times \frac{4}{3} \times \frac{W_{air}}{I_{max}^2} \quad (5.11)$$

where,

- L_a and M_{ab} = self and mutual inductance;
- $L_a - M_{ab}$ = Cyclic inductance per phase;
- I_{max} = Maximum current;

The end winding inductance of the prototype FSCW IPMM-F was calculated for the 3D FE model as 0.89 mH. The analytical end winding inductance for the prototype machine was 0.85 mH.

5.6 Mechanical stress analysis

The mechanical aspects should be taken into account before construction of a prototype. In an IPMM, the bridge near the flux barriers in the rotor and the air-gap is a mechanically weak region. The bridge has to be strong enough to withstand the

centrifugal forces at high speed [132, 133]. In this study, mechanical stress due to centrifugal forces was analyzed for the FSCW IPMM-F.

The FSCW IPMM-F was modelled in ANSYS Workbench and analyzed by rotating the machine with various speeds. The deflection contour for the rotor of the FSCW IPMM-F at 143 rpm and 4500rpm is shown in Fig. 5.30. According to the manufacturer’s datasheet, Poisson ratio for silicon steel grade 50CS350 is 0.3 [134]. The maximum deformation is found to be 0.06 mm at 4500 rpm that is well below the limit of the material. The mechanical stress applied to the rotor due to centrifugal forces is evaluated by VON-MISES Stress. An irreversible deformation of the rotor will not take place until the VON-MISES Stress exceeds the yield strength of the rotor material [135]. This analysis also looks into the shear stress caused by Poisson effect, which can lead to rotor and magnet cracking and eventually machine failure.

Fig. 5.31 shows the VON-MISES Stress and SHEAR Stress for the rotor and magnets of the FSCW IPMM-F at 143 rpm and 4500rpm. The main conclusions of this analysis are pointed out in Table 5.5. Note that in this analysis, a linear elastic material behavior is assumed. Small deflection theory was used to do the solving process, and no non-linear iterations were included.

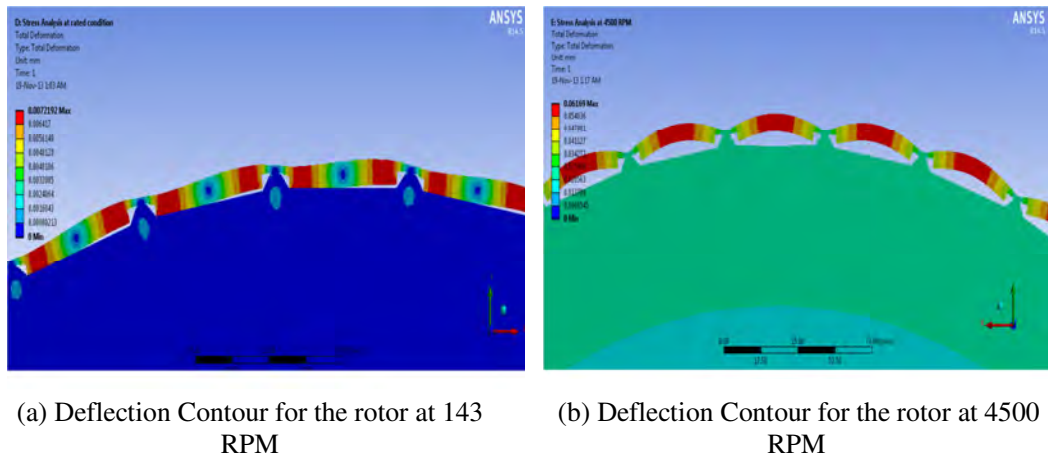


Fig. 5.30. Deflection Contour of the FSCW IPMM-F

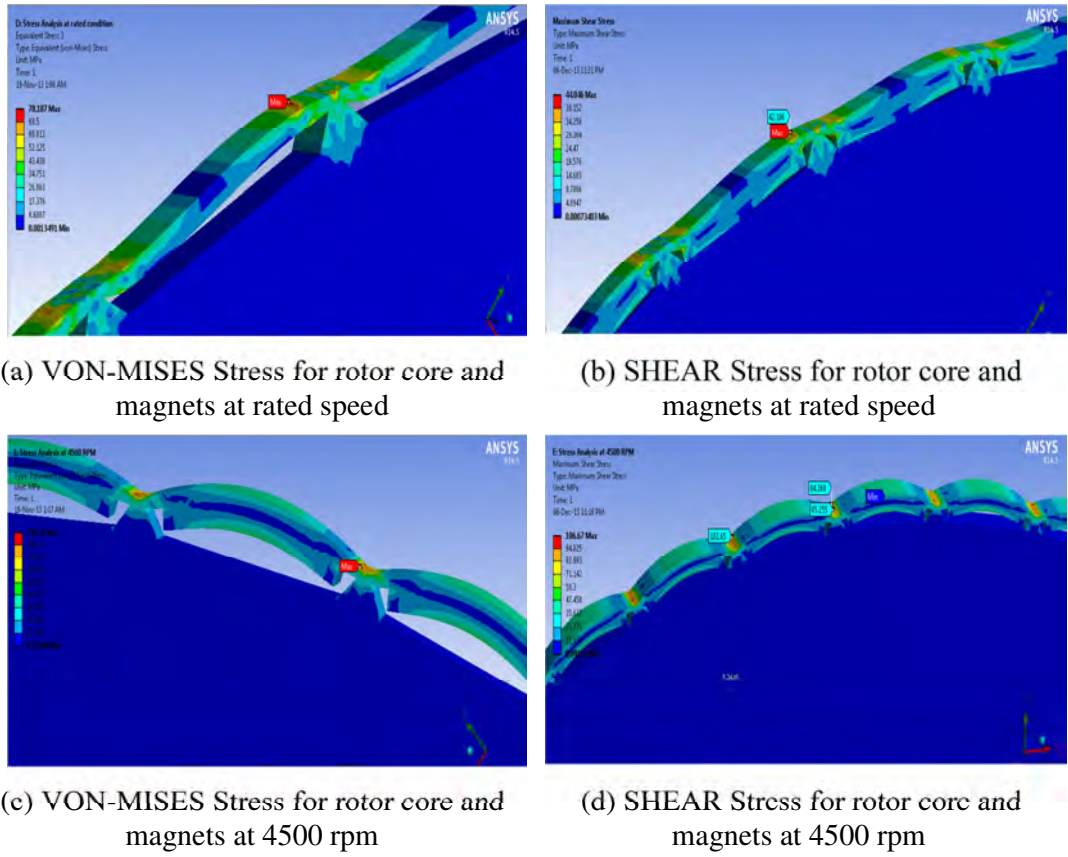


Fig. 5.31. VON-MISES Stress and SHEAR Stress for rotor core and Magnets of the FSCW IPMM-F at Rated Speed (Fig. a & b); 4500 rpm (Fig. c & d);

Table 5.5 Mechanical stress limit for the rotor core

	Speed (Rpm)	Allowable VON-MISES stress (MPa)	Maximum VON-MISES stress (MPa)	Allowable shear stress (MPa)	Maximum shear stress
Rotor Core	143		78.107		44.046
Weight (279 Kg)	4500	400	190.36	230	106.67

The analysis has been performed to determine limiting speed for the rotor. The maximum VON-MISES stresses/Pressure developed in the rotor core at 4500 rpm is 190.36 MPa. The allowable limit for non-oriented silicon steel 50CS350 is 400 MPa. The SHEAR stress is also below the maximum condition during this speed. Hence, the rotor is safe for working in speeds almost 30 times higher than the base speed. As for

the NdFeB magnets, the SHEAR stress during 4500 rpm is 23 MPa, which is well below the maximum allowable SHEAR stress of 48 MPa.

5.7 Final FSCW IPMM-F design

This section presents the key machine parameters of the final FE design of the FSCW IPMM-F. The overall construction process of the FSCW IPMM-F describing the entire development process and the manufacturing timeline is presented in Appendix B. Full specifications of the final design are shown in Table 5.6.

Fig. 5.32 shows the flux density waveform for the final design of the FSCW IPMM-F. The fundamental air-gap flux density is found to be 0.57 T for the proposed machine. The cogging torque minimization technique applied to the FSCW IPMM-F helped in reducing the cogging torque to less than 1% of rated torque. The cogging torque computation was performed with finite element analysis using fine mesh discretization as a multi-static computation for different rotor positions. The cogging torque waveform is displayed in Fig. 5.33. It was already observed in chapter 4, the EMF is nearly sinusoidal for the FSCW IPMM-F. The predicted L-L EMF from the FE model is shown in Fig. 5.34. The rated L-L RMS voltage is found to be 362 volts at rated speed with a total harmonic distortion (THD) of 0.75%. Except for the 3rd harmonic in the phase voltage, there are no significant harmonics in the FFT analysis for both the L-L and phase voltage of the final design.

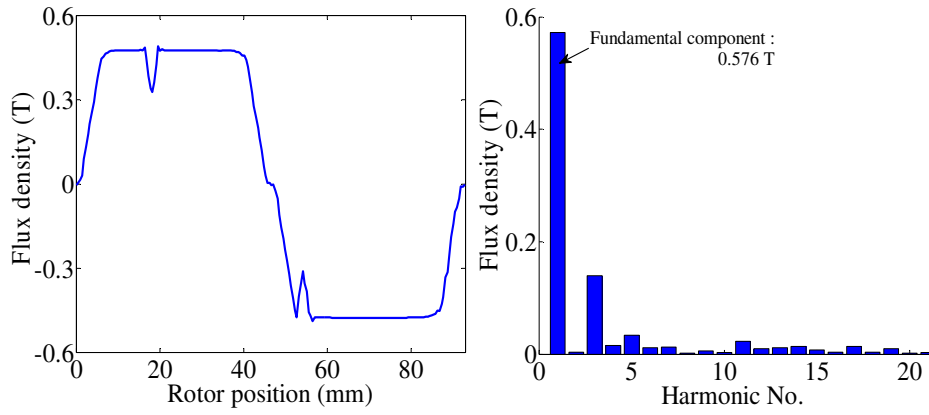


Fig. 5.32. Flux density of the Final design (FSCW IPMM-F) conducted in FEA

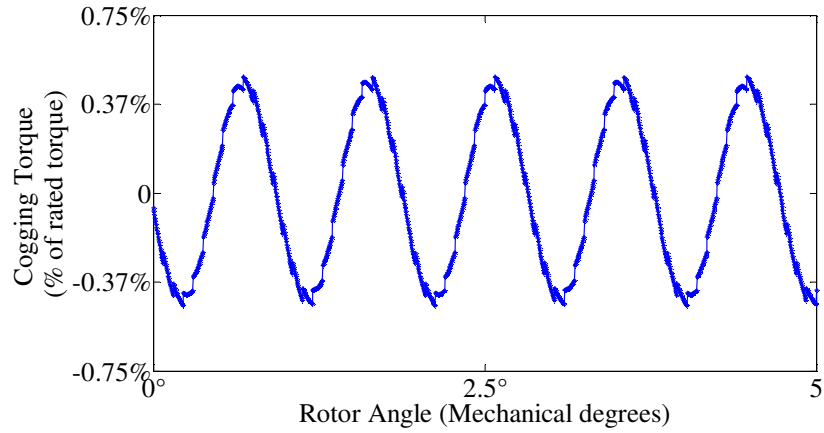


Fig. 5.33. Cogging torque of the Final design

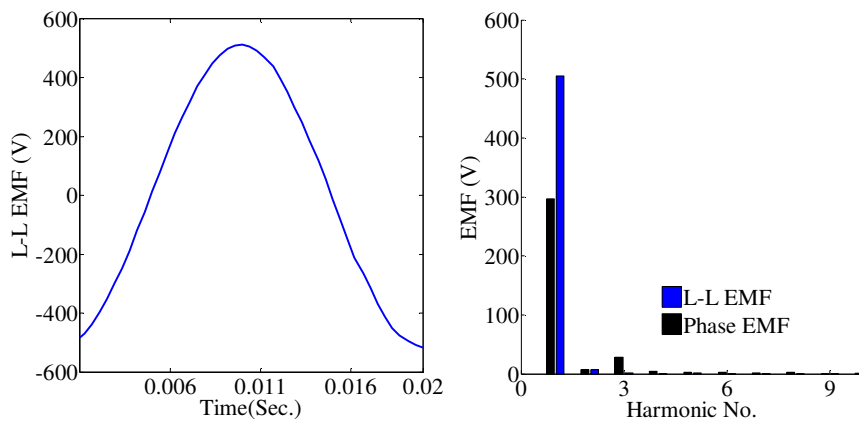


Fig. 5.34. (a) L-L Back EMF & (b) FFT analysis of the L-L and phase Back EMF of the Final Design

Table 5.6 Specifications of the final design

Stator outer diameter	680 mm
Rotor outer diameter	620 mm
Air-gap Length	1.225 mm
Stator inner diameter	621.225 mm
Shaft diameter	60 mm
Stack length	161 mm
Active stack length	201 mm
Stator & Rotor Lamination thickness	0.50 mm
Slot-opening width	2.05 mm
Number of poles	42 poles
Number of magnet pieces	42 pieces
Magnet dimension	161mm x 36.575mm x 3mm
Magnet remanence	1.03 T
Magnet operating temperature rating	$\geq 230^{\circ}$ C
Magnet Coating	Ni-Cu-Ni
Number of slots	54 slots
Winding type	Double-layer concentrated
Slot-fill factor	46%
Number of turns per coil	21 turns
Total number of conductors in parallel	6
Diameter of each conductor	0.6 mm
Conductor insulating material	ULTIMEG 2000/380 Alkyd phenolic
Conductor withstanding temperature	$\geq 180^{\circ}$ C
Cooling arrangement	N/A
Core material	50CS350
Experimental Core loss at 50 Hz/1.7 T	2.65 W/kg
Allowable VON-MISES stress	400 Mpa
Allowable SHEAR stress	230 Mpa
Conductivity of lamination	2272727 s/m
Rated Voltage (RMS)	362 volts
Rated Current (RMS)	6.5 A
Base speed	143 rpm
Maximum rated torque at base speed	274 Nm
<i>d</i> -axis inductance (at rated current)	29.4 mH
<i>q</i> -axis inductance (at rated current)	43.2 mH
Stator winding resistance	1.65 Ω /phase
Magnet flux linkage	0.945 Wb (peak)

5.8 Losses of the final design

The power absorbed in the machine during the conversion of electrical and mechanical energy is referred to losses of that particular machine. The individual losses in the IPM machine are:

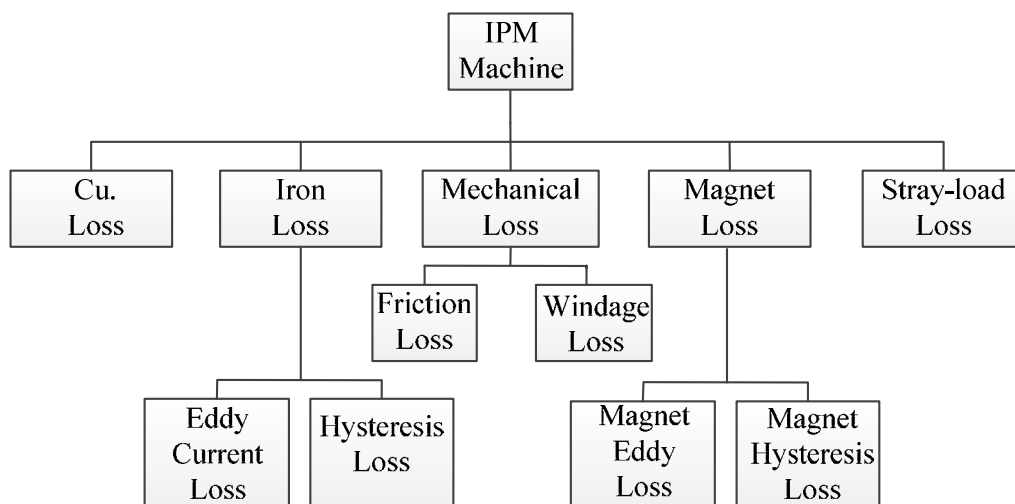


Fig. 5.35. Losses in an IPM machine

The determination of Cu. loss and Iron loss has already been studied in chapter 4. This chapter analyzes the mechanical loss, magnet loss and the stray load loss of the IPMM.

5.8.1 Mechanical losses

In PM machines, the mechanical losses consist of bearing/friction and windage losses [129, 136, 137]. The bearing loss is due to the friction in the bearings of the motor. As for windage loss, it is caused by the rotating elements of the machine. These mechanical losses are identified and calculated individually for the FSCW IPMM-F.

5.8.1.1 Bearing loss

There is a wide variation of bearing types available with rely upon the rolling action of balls or rollers. The bearings used for manufacturing the prototype are hybrid deep

groove ball bearings (SKF: 6212-2RS1). These bearings are usually preloaded axially in high-speed applications. Under these conditions, hybrid deep groove ball bearings behave like angular contact ball bearings with a similar reduced frictional moment. The friction loss is a small portion of the total losses of the machine and in most times are neglected in the calculation. The friction losses in the bearings are a function of bearing size, speed, type of bearing and load. Bearing losses can easily be calculated with the following equation given in [129]:

$$P_{bearing} = 0.5\omega_m K_b F D_b \quad (5.12)$$

where,

ω_m = Speed of the rotor (Mechanical);

K_b = Bearing loss constant;

F = Force acting on the bearing;

D_b = Bearing inner diameter;

Fig. 5.36 shows the schematic rotor and the two bearings to calculate the friction loss of the prototype. In machines with bigger geometrical dimensions, the bearing loss is significant as the force acting on the bearing is high for these machines. According to the manufacturer datasheet, the bearing loss constant is found to be 0.0015. The mass of every portion of the machine is calculated using the volume of the material and its density.

The force acting on the bearings can easily be estimated by using the total mass and multiplying it by the gravitational force (9.81 m/s^2). The calculated force acting downwards on both the bearings is found to be 1821 Nm. The friction loss in the bearings is shown in for various rotor speeds is shown in Fig. 5.37. The total bearing loss is found to be 2.45 W at rated speed. The results indicate that the bearing loss is small compared to other electrical losses in the prototype.

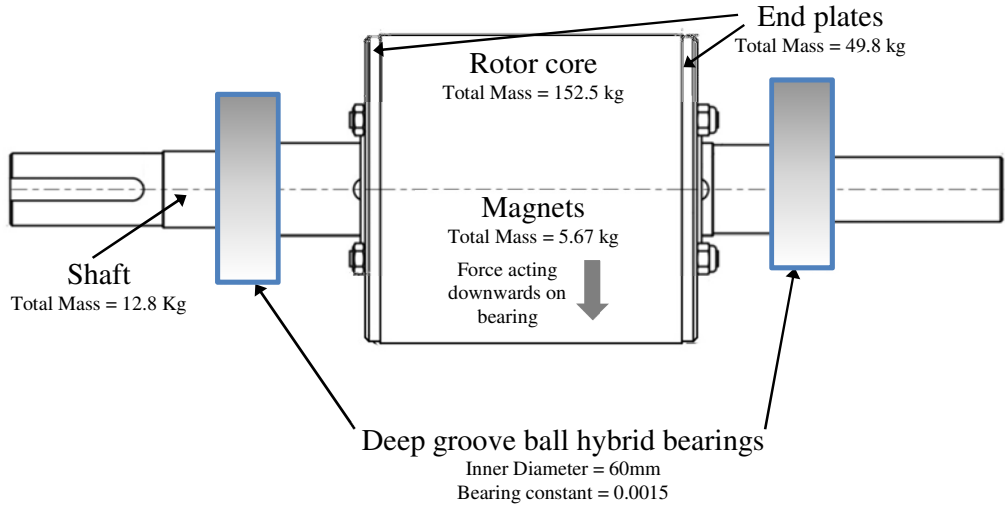


Fig. 5.36. Drawing of the rotor and bearings to calculate the bearing friction loss

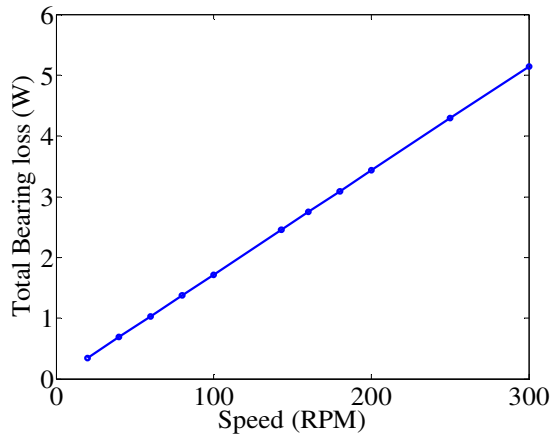


Fig. 5.37. Power loss due to bearing friction at various speeds

5.8.1.2 Windage loss

Windage loss is due to the aerodynamic power loss in the machine. It is generated by friction resulting from relative air movement in reference to the machines rotating part [137]. The fundamental effect of windage power loss that are skin friction, pressure drag, and induced drags are described in details in [138]. According to [129], the windage loss can be expressed as follows:

$$P_{windage} = 0.03125\omega_m^3 \pi k_{cl} k_r \rho_{air} D_r^4 l \quad (5.12)$$

where,

k_{ct} = Torque co-efficient;

k_r = Roughness co-efficient (for a smooth surface, $k_r=1$);

ρ_{air} = Density of air (1.184 kg/m^3);

D_r = Rotor diameter;

l = Length of the rotor;

The torque co-efficient (k_{ct}) is defined by Couette Reynolds number ($R_{e\delta}$). It is given by:

$$R_{e\delta} = \frac{\rho_{air} \omega_m D_r \delta}{2\mu} \quad (5.13)$$

where,

δ = Air-gap length;

μ = Dynamic viscosity of air ($18.6 \mu Pa s$);

The torque co-efficient is obtained as follows:

$$k_{ct} = 10 \frac{(2\delta / D_r)^{0.3}}{R_{e\delta}}, R_{e\delta} < 64, \quad (5.14)$$

$$k_{ct} = 2 \frac{(2\delta / D_r)^{0.3}}{R_{e\delta}^{0.6}}, 64 < R_{e\delta} < 5 \times 10^2, \quad (5.15)$$

$$k_{ct} = 1.03 \frac{(2\delta / D_r)^{0.3}}{R_{e\delta}^{0.5}}, 5 \times 10^2 < R_{e\delta} < 10^4, \quad (5.16)$$

$$k_{ct} = 0.065 \frac{(2\delta / D_r)^{0.3}}{R_{e\delta}^{0.2}}, 10^4 < R_{e\delta}, \quad (5.17)$$

These values are calculated to determine the windage loss of the FSCW IPMM-F, which is shown in Table 5.7.

Table 5.7 Reynolds number, torque coefficient and winding loss at various speeds

Speed (rpm)	$R_{e\delta}$	k_{ct}	$P_{windage}$ (W)
50	126.569	0.0208	8.25×10^{-3}
100	253.173	0.0137	0.0435
143	361.97	0.0110	0.102
200	506.283	9.06×10^{-3}	0.23
250	632.856	7.93×10^{-3}	0.393

5.8.2 Magnet losses

Magnets in an IPM machine are buried inside the rotor that means that they are not directly exposed to the air-gap flux. This suggests that magnet losses in IPMM will be much smaller in comparison to SPM machines [139]. On the other hand, a concentrated winding IPMM results in higher magnet losses as opposed to DW IPMM. This is due to the losses induced by the stator winding MMF spatial sub-harmonics and other higher-order harmonics of a FSCW machine [117, 140-142]. Common strategies used by researchers to reduce magnet losses are:

- The use of Bonded Magnets instead of Sintered Magnets.
- Magnet Segmentation.

Bonded NdFeB magnets are typically made of neodymium powder and Binder. It can be magnetized in any direction or with multiple poles. Ideally, bonded magnets should offer negligible losses in the magnets of a machine. However, the bonded magnets have lower remanence in comparison to sintered magnets. Currently, the maximum remanence available for bonded magnets is well below 1 T. This leads to an increase in the machine volume when using bonded magnets [143]. For this reason, the use of bonded magnets was not considered in this research. The other common way to reduce magnet losses is by the segmentation of the magnets [144-148]. In [149], it was seen that the segmentation of magnets into two magnet pieces reduces the magnet losses by more than 50%. The segmentation of the magnets reduces the eddy currents induced in the magnets thus reducing the overall loss. Analysis of the segmentation of the magnets was conducted in the latter part of this section.

The calculation of magnet losses in FEA is very similar to calculating the core loss of the machine. Magnet loss of the FSCW IPMM-F consists of magnet eddy current loss and magnet hysteresis loss. A lot of researchers have suggested on calculating only the

eddy current loss of a PM machine, but some recent findings show that the magnet hysteresis loss is larger than the eddy current loss in the range of frequencies less than several hundred hertz [150]. The magnet loss can be expressed as [151, 152],

$$p_{mag} = \underbrace{k_h B_{max}^2 f}_{\substack{\text{Losses} \\ \text{by} \\ \text{hysteresis}}} + \underbrace{k_e B_{max}^2 f^2}_{\substack{\text{Eddy} \\ \text{loss}}} \quad (5.18)$$

The calculation of hysteresis loss co-efficient (k_h) is not easy as the value is not readily available in manufacturer's datasheet. The eddy current loss coefficient (k_e) can be easily calculated using the following equation:

$$k_e = \frac{\pi^2 \sigma d_i^2}{6} \quad (5.19)$$

The conductivity (σ) of NdFeB is 55555s/m as found in the manufacturer's datasheet. k_h can be estimated by extrapolating measured data of Sintered NdFeB magnet losses from previously achieved results found the literature. In [150, 152], the authors presented $p_{mag} - B_{max}$ characteristics for a fully magnetized NdFeB magnet at 50 Hz, shown in Fig. 5.38. As seen in the figure, the magnets were exposed to flux densities up to only 0.1T. Fig. 5.39 shows the extrapolated polynomial trend lines that were fitted to the measured results of Fig. 5.38.

The maximum operating point of the FSCW IPMM-F is approximately 0.8 T. At this value, the hysteresis loss is found to be 13.03 W/kg and as for eddy current loss, it is 8.04 W/kg seen from Fig. 5.39. Both the losses increase proportionally with increasing flux density with a linear trend for the hysteresis loss curve, as for the eddy current loss curve, it is exponentially linear. After achieving k_h from Fig. 5.39, and k_e from Eq.(5.19), both the values were used to study of the magnet losses with 2-D FEA.

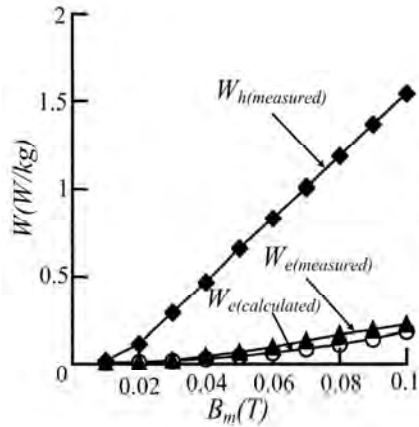


Fig. 5.38. Hysteresis and eddy current loss for sintered NdFeB at 50 Hz [150, 152].

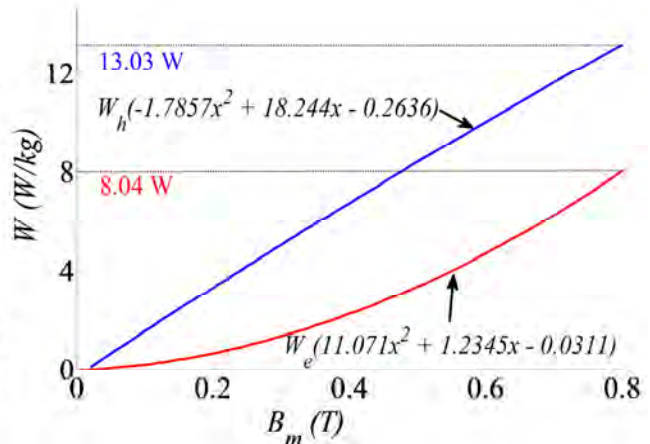


Fig. 5.39. Extrapolated values of measured hysteresis and eddy current loss.

The calculation of the losses in IPMM is done using Eq.(5.18). Fig. 5.40 displays the effect of magnet segmentation on the magnet eddy current loss of the prototype FSCW IPMM-F. It can be seen from Fig. 5.40 that the eddy current loss at 50 Hz is 3.36 watts for non-segmented magnets in the FSCW IPMM-F. The necessity of segmenting the magnets becomes evident when the machine operates at 200 Hz. At this condition, the eddy current loss rises to 52.9 watts, whereas six segments of magnets reduce the loss to only 1.26 watts. The operating region of the prototype FSCW IPMM-F is below 100 Hz frequency, which suggests the magnet eddy current loss will always be less than 5% of the total loss of the machine.

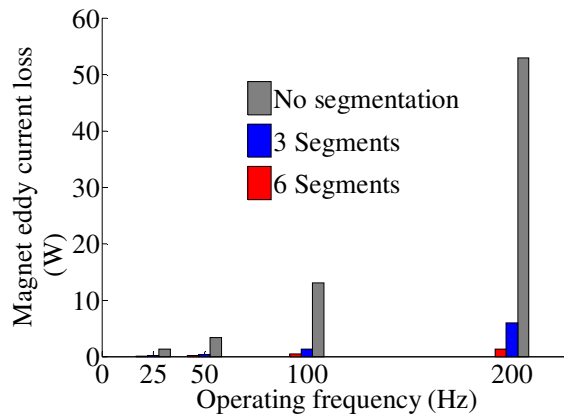


Fig. 5.40. Magnet eddy current losses at various frequencies with the variation in the number of segment in the magnets.

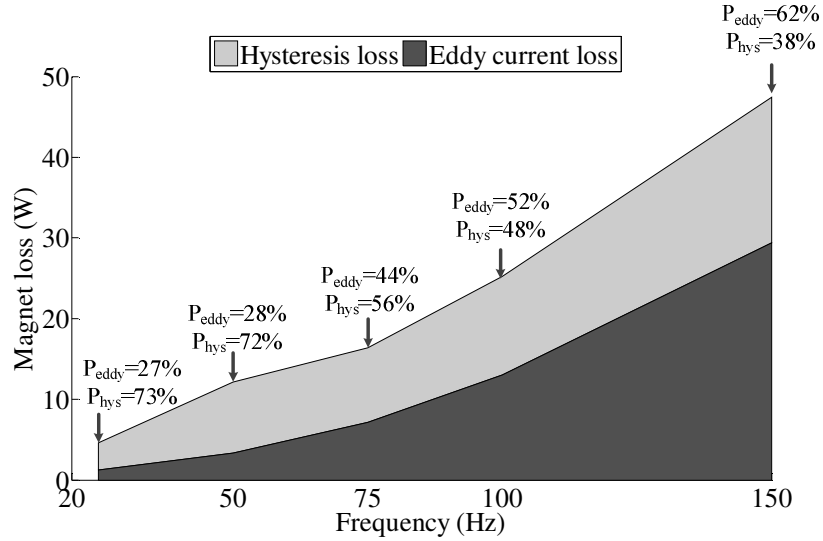


Fig. 5.41. Magnet losses versus frequency in the final design of the FSCW IPMM-F

Segmenting the magnet into more than two pieces will make the whole rotor manufacturing costly and time consuming due to the high pole numbers in the machine. In the final, sintered non-segmented NdFeB magnets were used to prototype the FSCW IPMM-F. The total magnet loss of the final model is shown in Fig. 5.41. The magnet loss found to be 12.18 W at rated condition that is approximately 4% of the total loss of the FSCW IPMM-F. As compared to other IPMM with CW, the magnet loss for this prototype is a bit high due to its large pole numbers. As seen in Fig. 5.41, the hysteresis loss is the dominant loss in the magnet for frequencies below 100 Hz. The magnet loss in the rotor is quite significant in the total core loss of the rotor for the prototype FSCW IPMM-F.

5.8.3 Stray load loss

Stray load losses are residual losses that arise from the skin effect resulting from the same source conductors [153]. Due to skin effect, AC current tends to flow on the outside of the conductor. The skin effect is defined by the skin depth (δ_{skin}) which is the

distance below the surface, where the current density has fallen to $1/e$, where e is equal to 2.718... It can be characterized as

$$\delta_{skin} = \sqrt{\frac{2}{\omega\mu_r\sigma}} \quad (5.19)$$

where,

ω = Angular frequency = $2\pi \times$ frequency;

μ_r = Relative permeability= 0.999994 (For copper);

σ = Electrical conductivity= $1.68 \times 10^{-8} \Omega.m$

The power loss due to this skin effect, as well as the proximity effects of conductors located in the slots of electric machines, can be based on the following equation:

$$P_{stray} = P_{cu} \left(\frac{R_{ac}}{R_{dc}} - 1 \right) \quad (5.20)$$

$\frac{R_{ac}}{R_{dc}}$ can be easily determined using δ_{skin} as shown in Eq.(5.21). It is also readily

available in manufacturer's datasheet for various AWG wires. Fig. 5.42 shows this ratio versus frequency for different sizes of copper wire [128].

$$\frac{R_{ac}}{R_{dc}} = \frac{r^2}{2r\delta_{skin} - \delta_{skin}^2} \quad (5.21)$$

It can be seen in Fig. 5.42, $\frac{R_{ac}}{R_{dc}}$ is one at lower frequencies. For the prototype

FSCW IPMM-F, the diameter of the wire used for winding is 0.6mm. This suggests the ratio of effective AC resistance and the DC resistance will be 1. This indicates that the stray load loss can be considered negligible for the prototype FSCW IPMM-F.

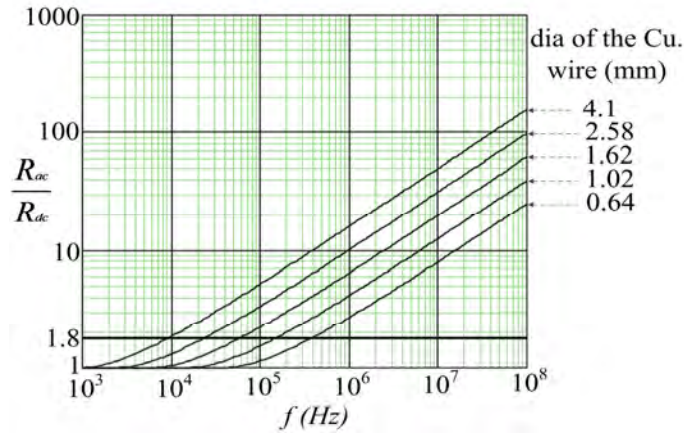


Fig. 5.42. Ratio of $\frac{R_{ac}}{R_{dc}}$ versus frequency for different sizes of copper wire (at 25°C) [128]

5.8.4 Final Efficiency for the FSCW IPMM-F

Fig. 5.43 shows the calculated copper losses, magnet losses and the iron losses for different load settings at rated speed. At rated speed, the iron loss is dominant when the FSCW IPMM-F is loaded 80% of full load configuration. At full capacity, the copper loss accounts for 61% of the total loss of the machine as seen in Fig. 5.43. A surface plot of the efficiency at rated speed for the FSCW IPMM-F is plotted in Fig. 5.44. An efficiency of 92.32 % is achieved for the FSCW IPMM-F at full load during rated speed condition.

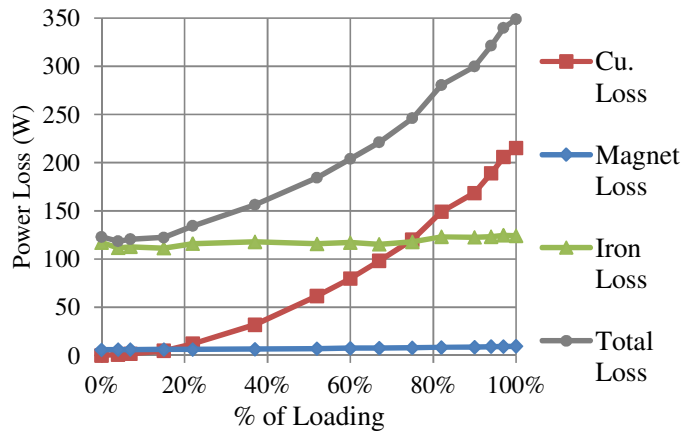


Fig. 5.43. Various losses of the prototype at different load setting during rated speed condition

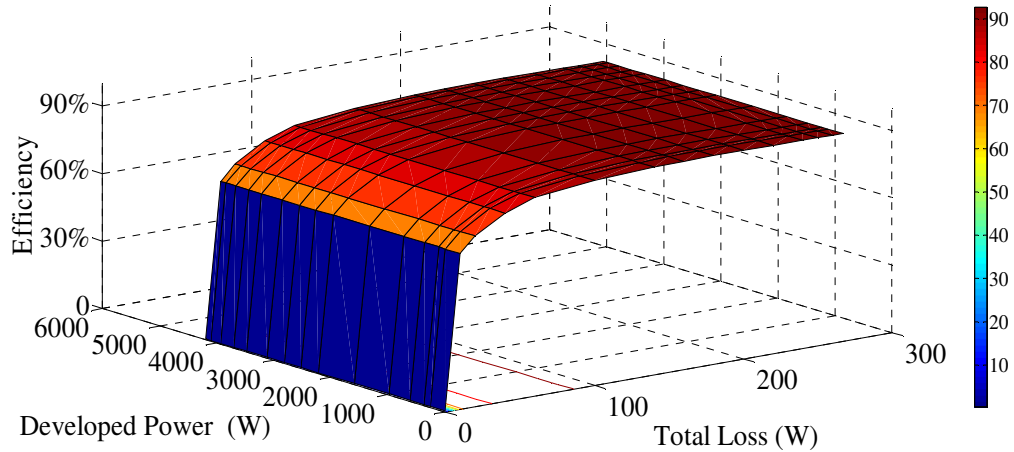


Fig. 5.44. Surface plot of the efficiency at rated speed for the FSCW IPMM-F

The power loss at full load for various speeds was also calculated for the machine and shown in Fig. 5.45(a). The efficiency calculation at full and a half load of the machine is shown in Fig. 5.45(b). It can be seen that the efficiency reaches 92% for both full and half load settings during rated speed condition. The maximum efficiency of 94% is achieved at 100rpm for 50% of full load configuration.

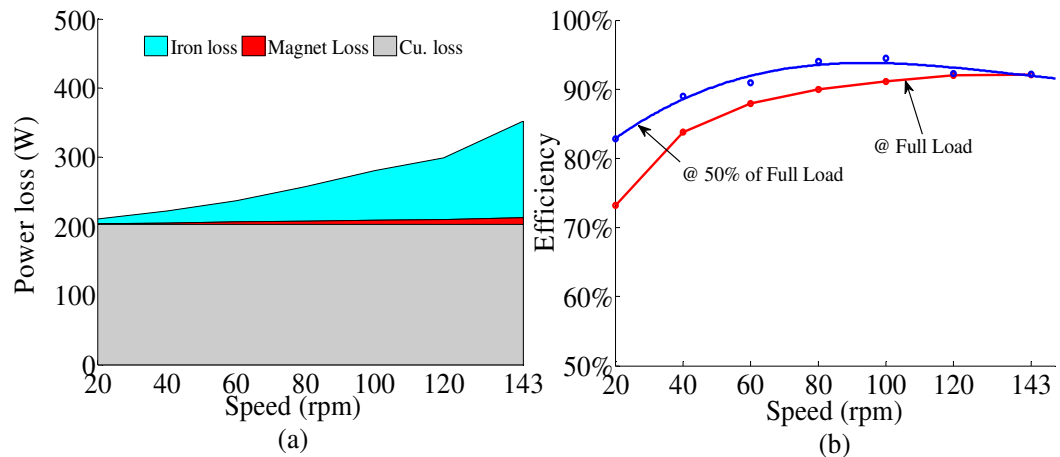


Fig. 5.45. (a) Power loss of the FSCW IPMM-F at full load with the variation in speed; (b) Variation in efficiency with the change in speed for full- and half load;

5.9 Conclusion

In this chapter, the final design of the FSCW IPMM-F was discussed. Initially, the materials of the IPM machine were selected based on the saturation level and design criteria. The final winding configuration together with the end turns inductance have been discussed intensively in this chapter. 3-D FEA was used to analyze the leakage flux in the vertical direction of the machine.

Machine losses were studied, and the final efficiency was calculated. The efficiency was found to be 92% at rated speed during full load conditions. The specifications of the final machine were presented based on the final 2-D FEA of the prototype design. The cogging torque was found to be less than 1% of rated torque. As for the torque ripple, it was less than 2% of rated torque. The FE simulations have shown that the FSCW IPMM-F satisfies all the design criteria stated in chapter 1.

The next chapter evaluates the performance of the prototype FSCW IPMM-F through experiments and comparisons with the FE results.

CHAPTER 6: Experimental Validation of the Steady-State Performance of the Prototype FSCW IPMM-F

6.1 Introduction

This chapter presents the experimental validation of the steady-state performance of the constructed 42-pole/52-slot FSCW IPMM-F. The experiments discussed in this chapter are associated with the generator action of the prototype FSCW IPMM-F. A four-quadrant electrodynamicometer was used to drive the prototype machine as shown in Fig. 6.1. The tests in this chapter were conducted under open loop control. The dynamometer was controlled to apply various speeds to the prototype generator. A variable resistive load was connected to the machine terminals to absorb the generated active power.

The three primary design goals are low cogging torque, low torque ripple and a high efficiency for the prototype FSCW IPMM-F. These were verified in this chapter. The saliency was also measured using the AC standstill test. The obtained results were compared with the predicted results of the FE model (CEDRAT FLUX 2D/3D) as discussed in chapter 5, for validation purposes.

6.2 Open Circuit Parameters

The experimental setup is shown in Fig. 6.2. The components associated with the configuration are given in the Table 6.1. The data sheet for each component is provided in the Appendix G. The numbers shown in Fig. 6.2 represent the numerical of the components in Table 6.1.

CHAPTER 6: Experimental Validation of the Steady-State Performance of the Prototype FSCW IPMM-F

Table 6.1. Components associated with the experimental setup

1: UNSW FSCW IPMM-F	7: Oscilloscope
2: Electrodynamicometer	8: Variable voltage supply
3: Dynamometer control unit	9: 1- ϕ Resistive bank
4: Dynamometer system PC	10: Voltage source inverter
5: Power Analyzer	11: PC for DS1104 control board
6:3- ϕ Resistive bank	

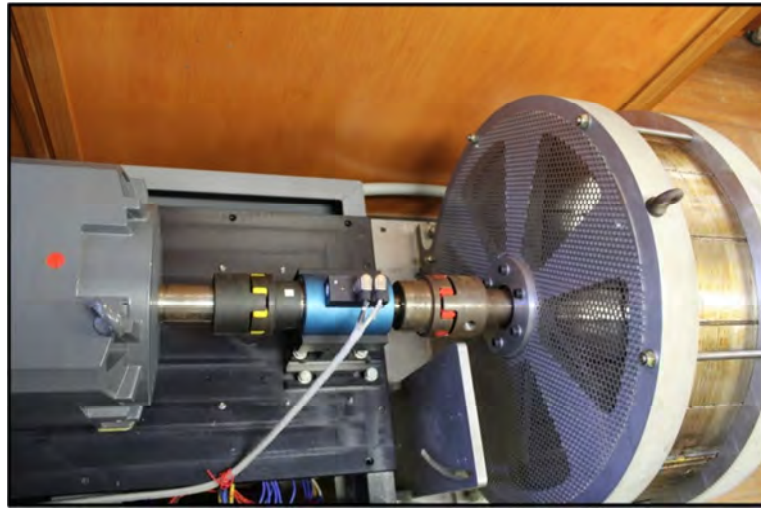


Fig. 6.1. The electrodynamicometer coupled to the prototype FSCW IPMM-F



Fig. 6.2. Experimental setup to determine the new machine parameters

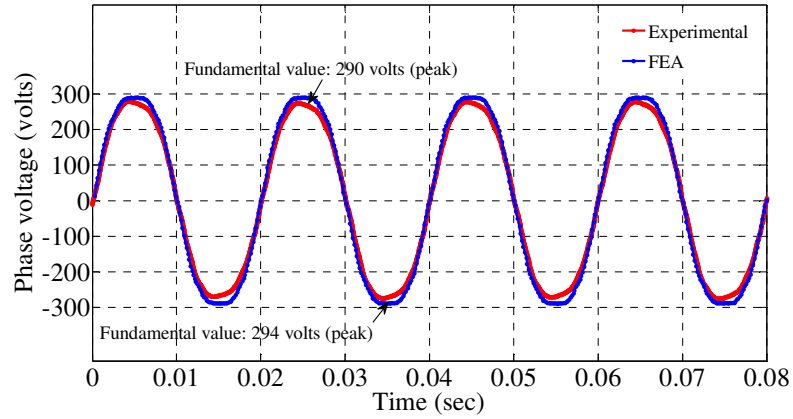


Fig. 6.3. Phase voltage of the prototype

The open-circuit phase back EMF waveform at the base speed of 143 RPM is shown in Fig. 6.3 along with the predicted waveform from the FE model. Fig. 6.4 compares the harmonic spectrum of the measured phase voltage with that of the FE model. The fundamental harmonic content is omitted in this figure for better observing the higher order harmonics. It can be seen from the figure that apart from 3rd order harmonics, no other significant harmonics exist in the back-EMF. This confirms that the $S_{pp} = 3/7$ configuration is capable of inducing a near- sinusoidal L-L back-EMF waveform. The time traces of the measured line to line (L-L) back-EMF of all three phases are displayed in Fig. 6.5. The L-L back EMF of the prototype IPMM is 503 volts (peak) at rated speed, and the THD is 0.76%.

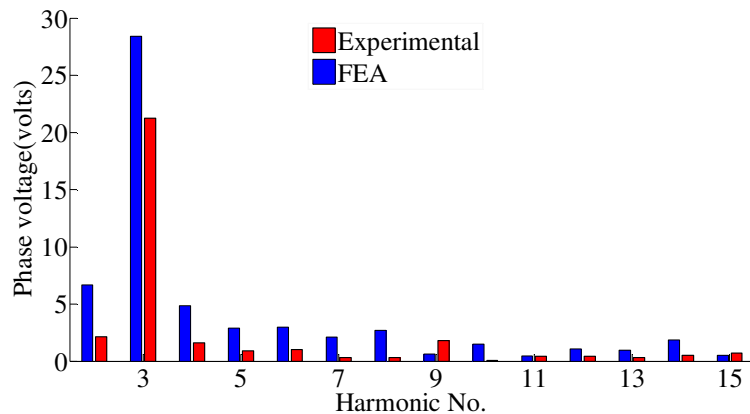


Fig. 6.4 Frequency spectrum of the phase voltage for the prototype

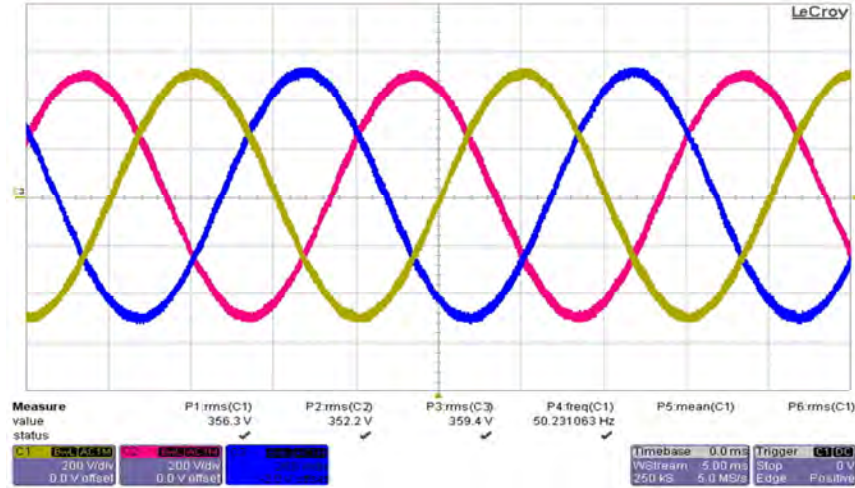


Fig. 6.5. Three phase voltages of the prototype

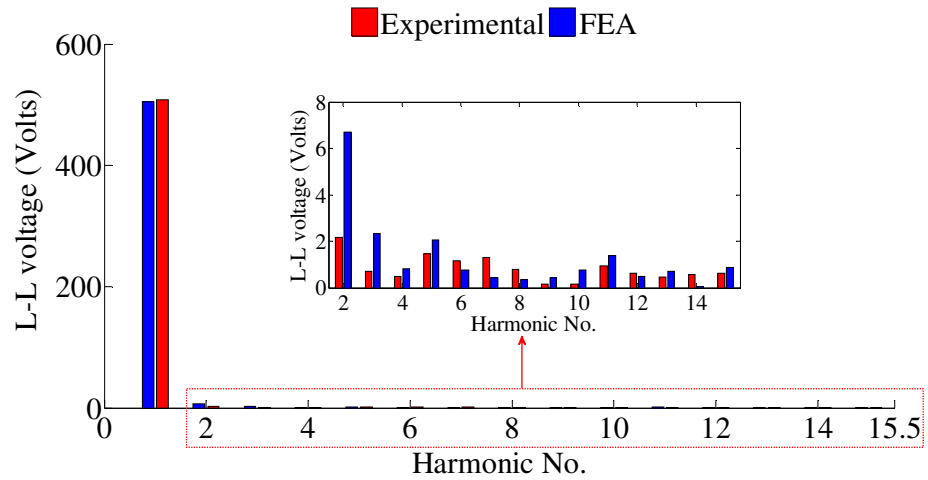


Fig. 6.6. Frequency spectrum of the L-L voltage for the prototype

The FFT analysis of the measured line voltage is compared with the results obtained from the FE model, in Fig. 6.6. The fundamental component of experimentally measured L-L Back-EMF is 505 volts (peak) which is close to the FE value of 509 volts (peak). The difference in the harmonic spectrum of the experimental and the FE results are mainly due to the eccentricity of the rotor [154, 155].

6.2.1 PM Flux linkage

The linear increase of the phase back EMF with the rotational speed is shown in Fig. 6.7.

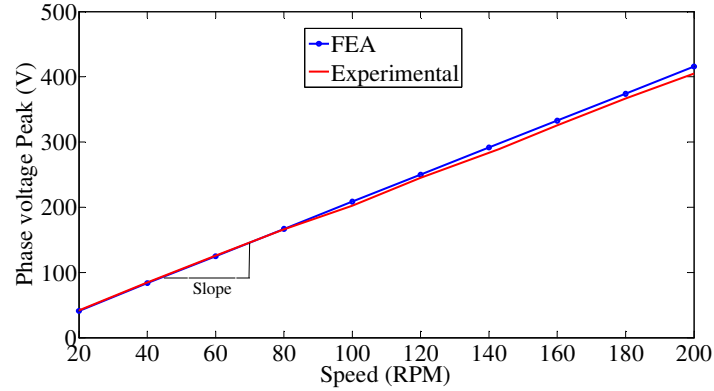


Fig. 6.7. Phase voltage versus Speed of the prototype

The PM flux linkage of the IPMM can be calculated as,

$$\psi_{PM} = \frac{V_{phase(peak)}}{\omega_e} \quad (6.1)$$

In the above expression, ω_e is in electrical *rad/s*. The PM flux linkage is found using Eq.(6.1) and equals to 0.917 Wb. Whereas, the finite element analysis conducted in flux-2D results in a value of 0.945 Wb for the PM flux linkage. As discussed in the previous chapter, due to the discrepancy in the magnet remanence, the experimental PM flux linkage is found to be 2.9% lower than what was predicted in the FE model. This difference is also due to some leakage flux that could not be accurately accounted for in the FE model.

6.2.2 Friction co-efficient and Rotor inertia

The friction coefficient (D) of the prototype machine and the induction machine of the dynamometer can be determined using a simple test.

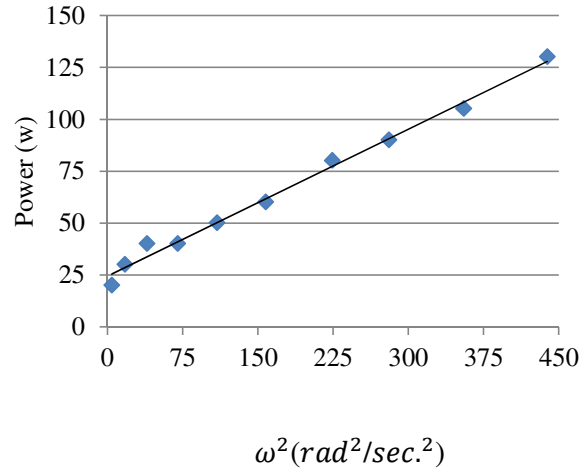


Fig. 6.8(a). Power versus square of the speed of the prototype

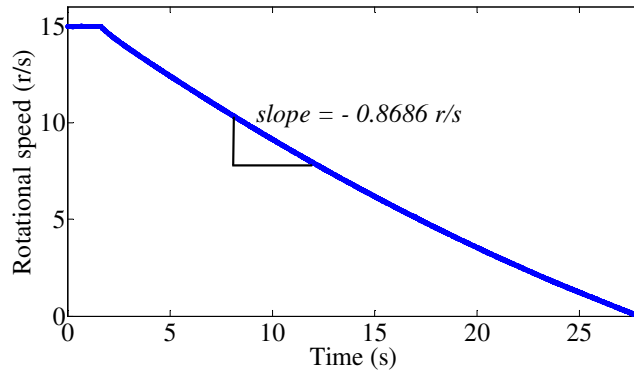


Fig.6.8(b). Rotational speed from rated to 0 with respect to time

The rotational viscous friction of an induction machine is defined in terms of load torque T_v that is directly proportional to the speed w_r [156],

$$T_v = Dw_r \quad (6.2)$$

where $T_v = \frac{P}{w_r}$ and P is the power required to drive a viscous friction load. Rewriting

Eq.(6.2) in terms of P , we can get,

$$D = \frac{P}{w_r^2} \quad (6.3)$$

Fig. 6.8(a) shows the plot of power vs. square of the speed for the IPMM. From the slope of this curve, the friction coefficient was found to be 0.2361 Nm/rad/s in the

prototype machine. The electromagnetic torque is dependent on the friction co-efficient and the rotor inertia (J) that can be shown as,

$$T_e - T_L = J \frac{dw_r}{dt} + Dw_r \quad (6.4)$$

where, T_L is the load torque. Rotor inertia of the FSCW IPMM-F can be easily determined by rotating the machine at rated speed and then switch off the power for which the left hand term of Eq.(6.4) becomes 0,

$$J = -Dw_r \Big|_{t=0} / \frac{dw_r}{dt} \Big|_{t=0} \quad (6.5)$$

Fig. 6.8 (b) shows the plot of w_r vs. time to find the declined slope which is the value of the denominator on the right hand side of Eq.(6.5). Using Eq.(6.5), the value of J is calculated as $4.07 \text{ kg}\cdot\text{m}^2$.

6.2.3 Cogging torque

There are various ways to measure the cogging torque experimentally. The simplest one is to use the torque transducer coupled to the machine shaft while running the machine at a very low speed (1 RPM or less). However, in this method accuracy of the measurement greatly depends on the capability of the shaft torque transducer in use.

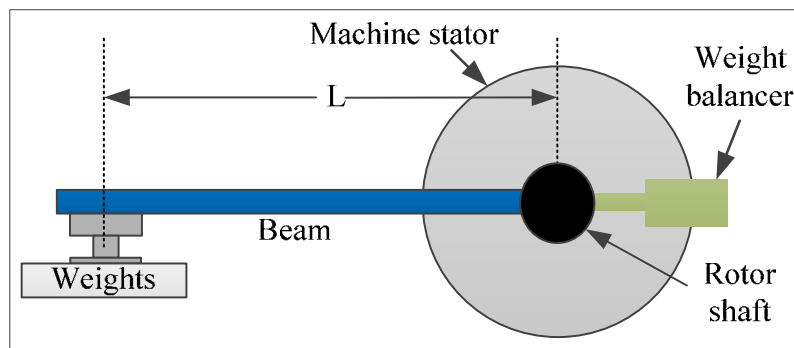


Fig. 6.9. Static measurement test to obtain cogging torque

Another conventional way to measure cogging torque is to do a static measurement [157-159] test that provides an absolute magnitude of the static cogging torque at a particular rotor position of the machine. The schematic of the test set-up is shown in Fig. 6.9. In this method, a force is applied to a lever arm sufficient to move the rotor from one equilibrium state to the next stable position. The experimental validation of the cogging torque was carried out using this simple yet accurate static measurement test. The cogging torque is obtained from the measurement as,

$$T_c = LF_{load} \quad (6.6)$$

where,

F_{load} = Weight acting on the beam;

L = Length of the beam.

The experimental setup for cogging torque measurement is shown in Fig. 6.10. Different values of standard masses were used as weights which have accuracies of +/- 10mg. An incremental encoder connected to the shaft was used to measure the rotor positions. By adding weights at each position, the amount of torque required to rotate the machine to the next rotor position can be calculated using Eq.(6.6). In this measurement method, only the positive cycle for cogging torque can be measured. However, this limitation is not significant since for the prototype machine the positive and negative cycles are symmetrical.

For concentrated windings, cogging torque has high-frequency fluctuations due to its fractional slot distribution. The periodicity of the cogging torque can easily be determined by,

$$T_{cfreq} = \frac{360^\circ}{LCM} \quad (6.7)$$

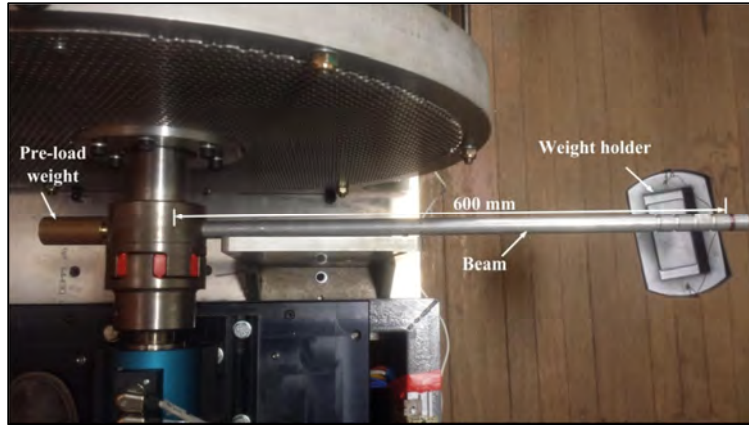


Fig. 6.10. Experimental setup for cogging torque measurement

The lowest common multiple (LCM) for a 42 pole, 52 slots IPMM is 378. Therefore, the periodicity is found to be 0.95° for the prototype FSCW IPMM-F, which means the measured cogging torque points had to be taken in small angular intervals. Fig. 6.11 compares the finite element results with the measured cogging torque of the prototype machine. The curve fitted expected experimental cogging torque was compared to the cogging torque waveform of the FE model in Fig. 6.12. It can be seen that the experimental peak cogging torque is 1.755 Nm as compared to the FE model result of 1.3 Nm peak. This variation in the measurement of cogging torque is likely due to the non-ideal assembly of the prototype during manufacturing [160]. Also, the effect of rotor eccentricity and bearing restriction which were not considered in the FE model would contribute to the magnitude of the measured points.

The experimental peak cogging torque is less than 1% of the rated torque indicating that the design goal of a very low cogging torque was achieved in the prototype machine.

CHAPTER 6: Experimental Validation of the Steady-State Performance of the Prototype FSCW IPMM-F

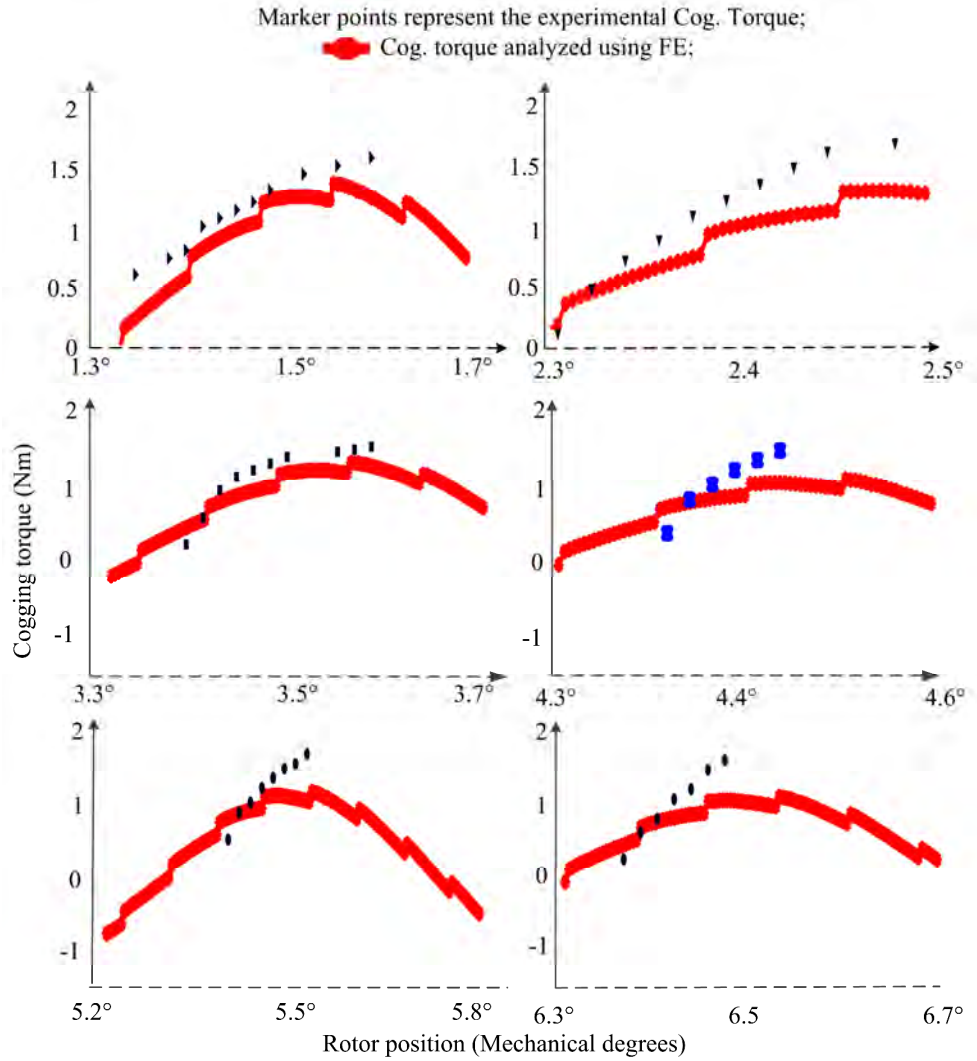


Fig. 6.11. Measured cogging torque for various rotor positions

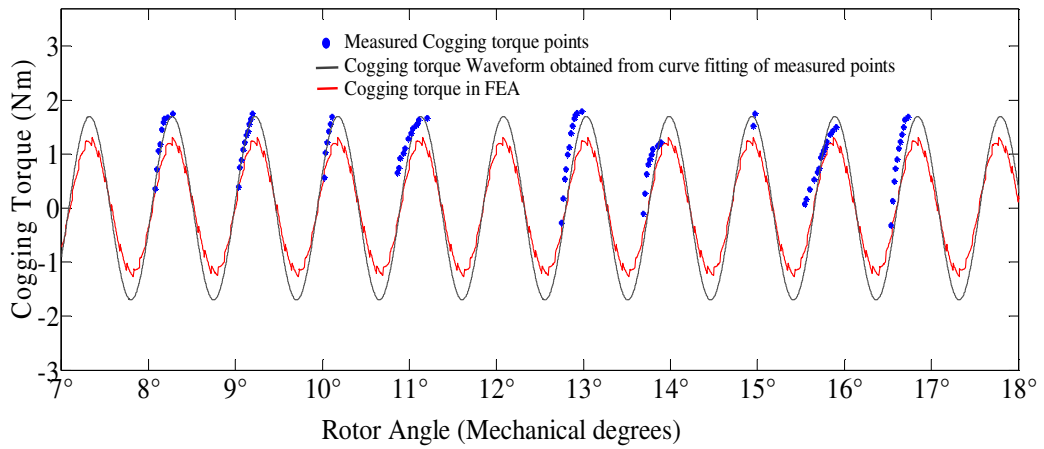


Fig. 6.12. Curve fitted cogging torque waveform

6.3 Developed Torque

The prototype FSCW IPMM-F was loaded with a 3- ϕ resistive bank in order to measure the steady-state performance of the machine under a loaded condition. The torque transducer used for the experiment is a Kistler 4503A torque sensor with an accuracy class of ± 0.1 . Fig. 6.13 shows the measured electromagnetic torque at full load and rated speed condition. The average torque is found to be 263 Nm (shown in Fig. 6.13) which is approximately 4% less than that of the FE result shown in Fig. 6.15. Due to friction, the experimentally measured average torque is less than the FE result. The detailed harmonic analysis of the developed torque is shown in Fig. 6.14.

The experimental torque harmonic spectrum shows dissimilarity in comparison to the FE result provided in Fig. 6.15. The IPM machines modelled in chapter 3 and chapter 4 had significant 6th and 12th order torque ripple which are absent in the final design as seen in Fig. 6.15. This is due to negligible 5th, 7th, 11th and 13th order harmonic contents in the EMF waveform as seen in Fig. 6.6. From Fig. 6.15, it can be seen that the 18th order harmonic component has the highest magnitude that is dominating in the production of the torque ripple using FE analysis.

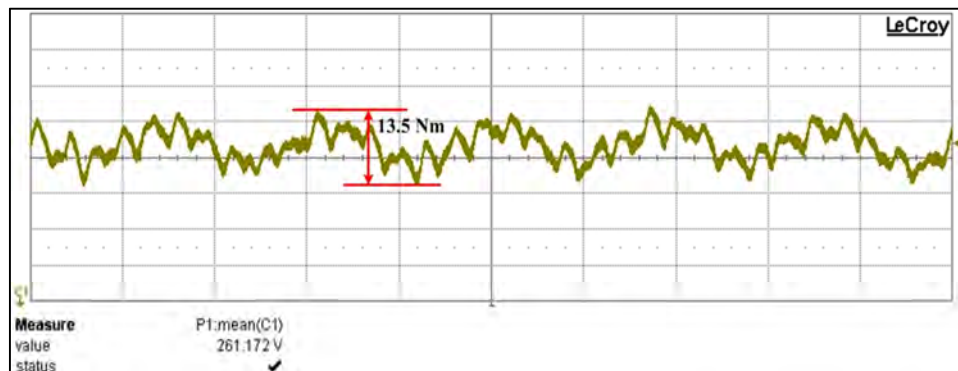


Fig. 6.13. Developed Electromagnetic Torque (Experimental)

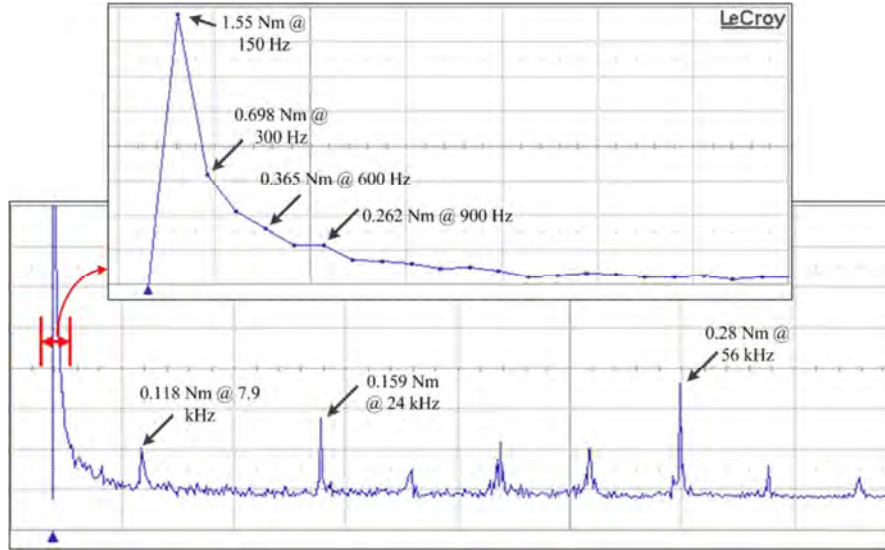


Fig. 6.14. FFT spectrum of Electromagnetic Torque (Experimental)

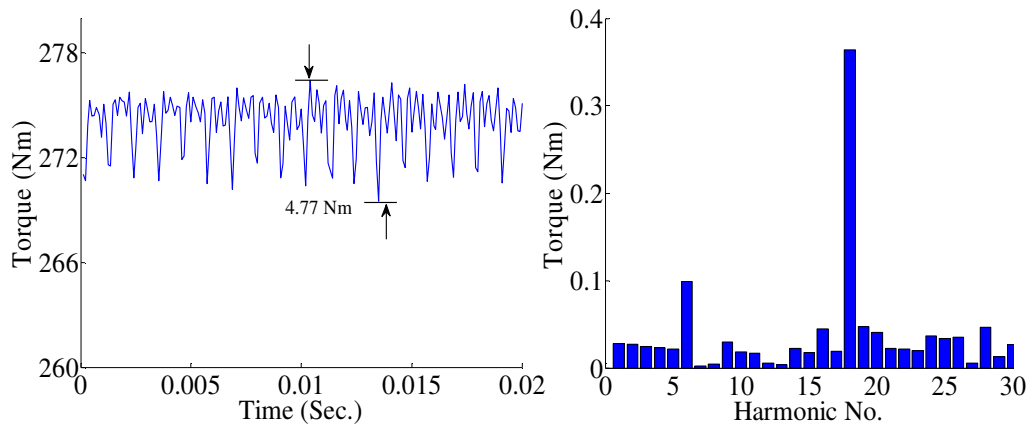


Fig. 6.15. Developed torque of the prototype in FE

The measured torque ripple of the prototype is found to be 4.8%. In FE analysis, the torque ripple was found to be less than 2 %, which means there is a discrepancy in the torque ripple calculated in the FE model and the experiment. The probable reasons for this discrepancy are:

- ❑ The FEA result does not include the induced torque ripples by the dynamometer controller. The prototype IPMM is coupled to the electro-dynamometer which has its own speed control loop. The ripple of this controller will be reflected on the overall torque ripple [161].

- ❑ In FE model, ideal sinusoidal voltage and current were considered while loading the prototype machine as a motor. However, in the experiment, the current waveform is not ideal sinusoid due to the machine inductance and inherent inductance of the resistive load. This effect is referred to as commutation torque [162], which will have a significant effect on torque ripple. The current waveform for various speed and load conditions during motoring and generating operation are shown in Fig. 6.16.
- ❑ Increased torque ripple could also be caused by the slight misalignment of the coupling between the prototype CW IPMM machine and the load machine (Electrodynamometer).

6.4 Inductance and Saliency ratio

Accurate knowledge of inductance is critical for implementing control techniques to PM machines. The most commonly used method to determine the inductance of the IPM machine is the AC standstill test. The self and mutual inductances of the prototype IPMM with respect to rotor positions were measured using the AC standstill test method [123]. In this test, one phase is excited with a known AC current at a specified frequency. The rotor is locked mechanically at each test position. The voltage drop across the excited winding and the neighboring phase winding are measured. The locking mechanism for the AC standstill test developed for the prototype machine is shown in Fig. 6.17. Incremental encoder connected to the shaft was used to measure the rotor mechanical position. One cycle of self and mutual inductance are completed when positions were varied from 0 to 17.14° which is the pole pitch of the prototype machine. In order to have an accurate measurement, inductances were measured at 90 positions within one cycle.

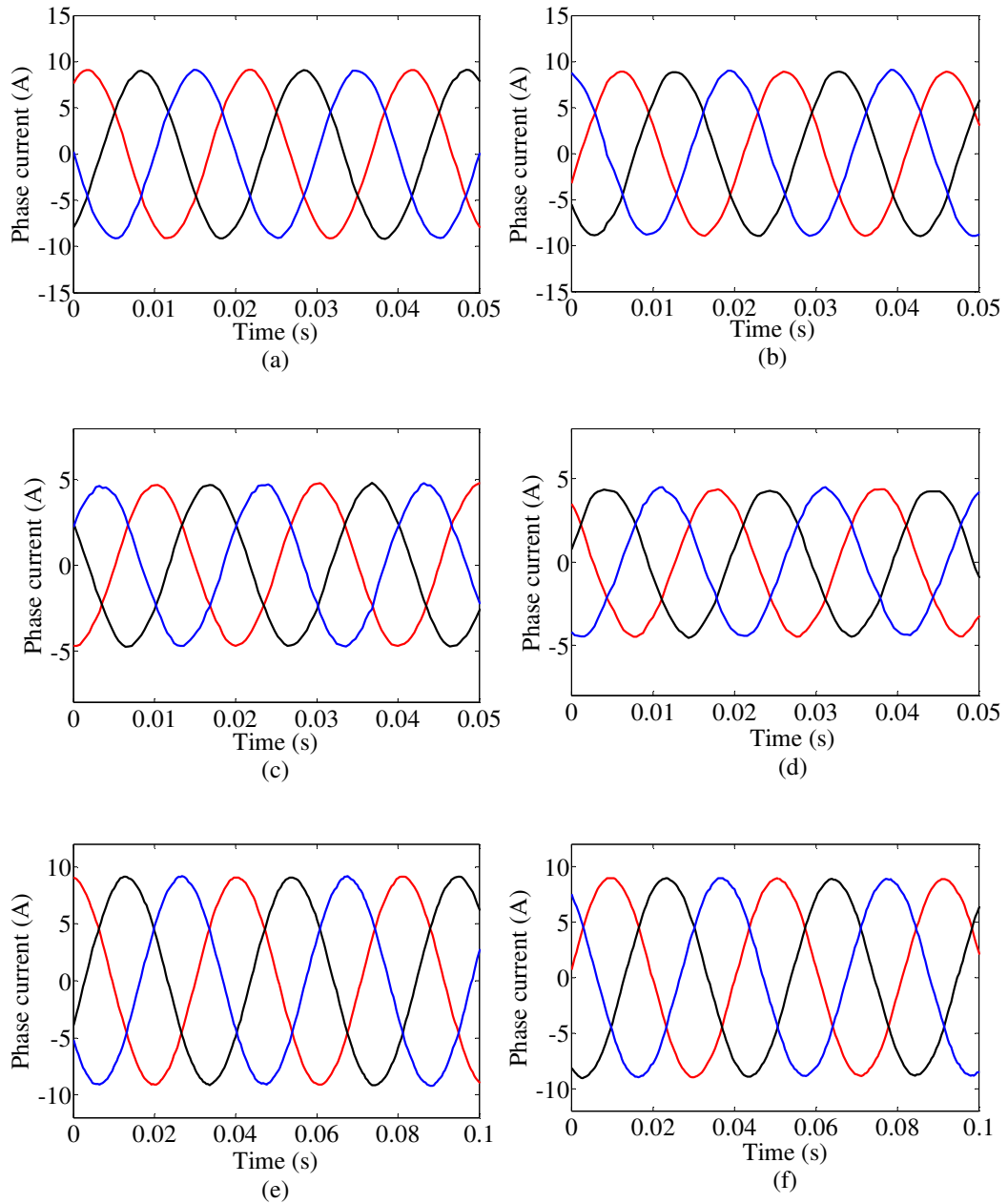


Fig. 6.16. 3-phase current waveform of the prototype FSCW IPMM-F – (a) During motoring at full load and rated speed; (b) During generating at full load and rated speed; (c) During motoring at half load and rated speed; (d) During generating at half load and rated speed; (e) During motoring at full load and half the rated speed; & (f) During generating at full load and half the rated speed;

The test was conducted for various current values. Fig. 6.18 shows the self and mutual inductance at rated current of 6.5A RMS respectively. The values of d - and q -

CHAPTER 6: Experimental Validation of the Steady-State Performance of the Prototype FSCW IPMM-F

axis inductances calculated by using Eq.(4.9) and Eq.(4.10) provided in chapter 4 at this rated condition are compared with that of the FE model in Table 6.2.

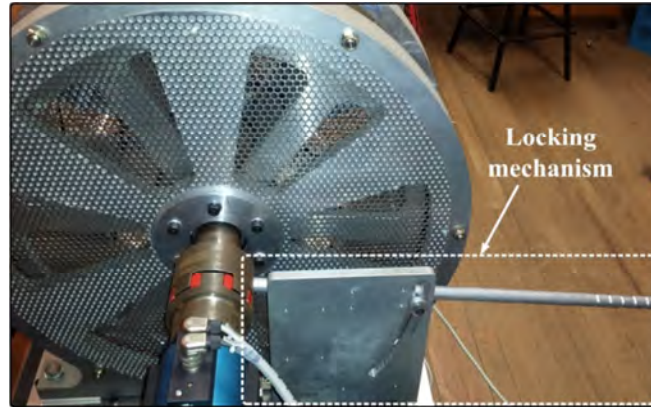


Fig. 6.17. Locking mechanism for the AC standstill saliency test

Table 6.2. d - and q - axis inductances at this rated condition

	Experimental (mH)	FEA (mH)
L_d	30.25	29.48
L_q	42.73	43.24
ξ	1.412	1.466

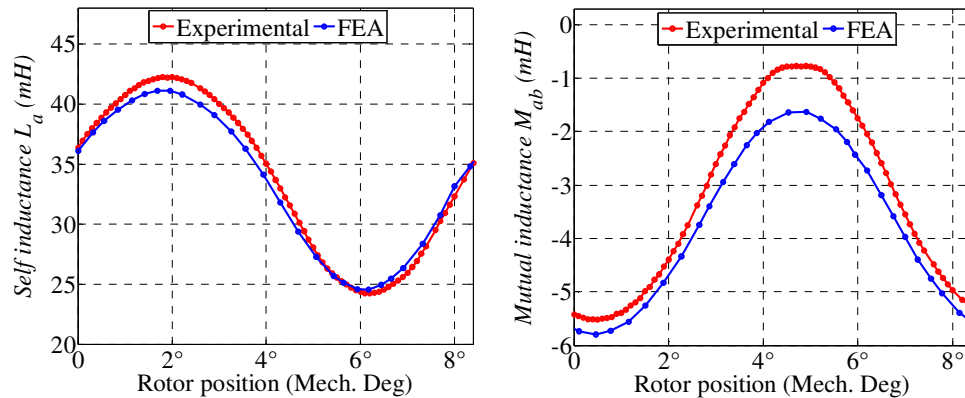


Fig. 6.18. Self- and mutual-inductance waveform of the FSCW IPMM-F at rated current

The average and the peak to peak magnitude of the self-inductance obtained in both FEA and Prototype machine are almost equal. However, in case of the average mutual inductance, FE model has over-estimated the value by approximately 15%. Due to this

difference in mutual inductance has led to a slight lower saliency ratio in the test machine compared to the predicted value of the FE model. The Probable reason for this slight difference in the mutual inductance is due to some end-winding mutual flux leakage which could not be accounted accurately in both 2D and 3D FE model. The measurement error while measuring small values of voltage during the test also could not be ruled out.

The inductance value obtained using the AC standstill saliency test is accurate provided the machine does not go into saturation during high rated current. The experimentally measured voltage and current waveform of the AC standstill test in Fig. 6.19 and their corresponding FFT spectrum in Fig. 6.20 show that even for rated condition, the machine does not go into saturation. Except for a low 3rd order component in the voltage waveform, no significant harmonics are present in both the voltage and current waveforms. The increase in the current excitation causes the core in the machine to get saturated. This causes the inductance to vary slightly with respect to the variation in current. In IPM machines, the q -axis inductance is affected by saturation much more than the d -axis inductance [163].

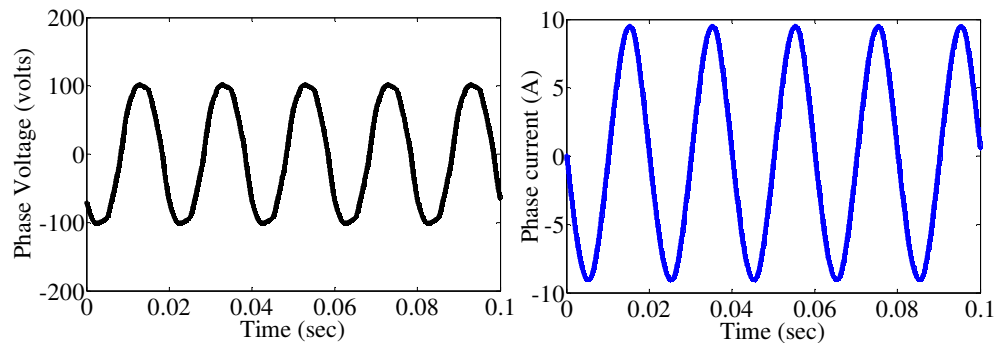


Fig. 6.19. Phase voltage and current during AC standstill saliency test

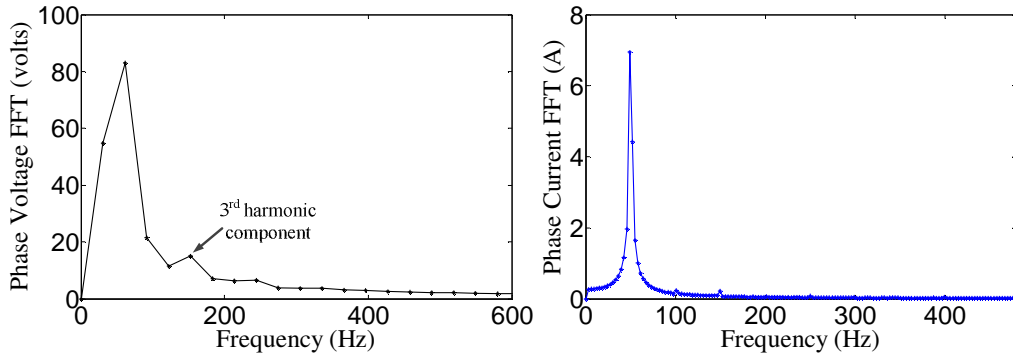


Fig. 6.20. FFT spectrum of phase voltage and current during AC standstill saliency test

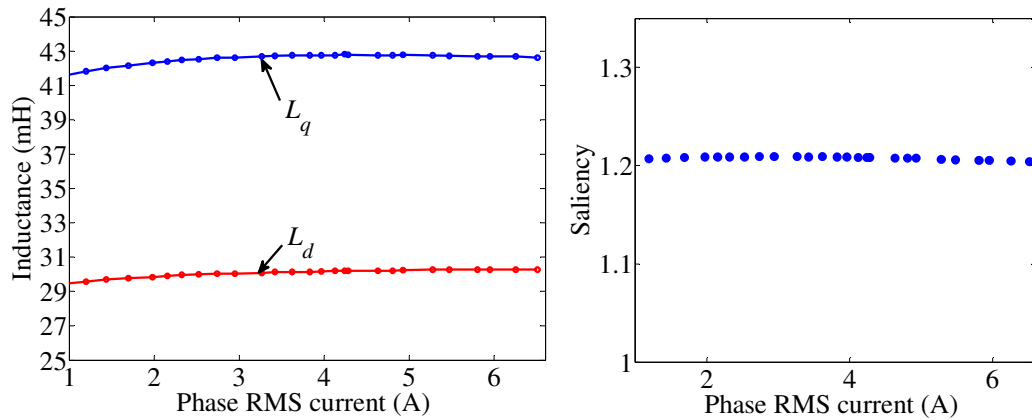


Fig. 6.21. Variation in d - and q -axis inductances and saliency with the change in phase current

Fig. 6.21 shows the variation in d - and q -axis inductances and the saliency with respect to the change in current. As seen in Fig. 6.20, the variation in q -axis inductance is higher than that of the d -axis inductance with changing current excitation. This leads to a slight decrease in the saliency ratio with higher currents. Fig. 6.21 shows that both the inductances vary slightly with respect to the change in current. This is due to the fact that the machine is unsaturated at 6.5A RMS, which is already pointed out in this section.

6.5 Generator Efficiency

This section presents the simple efficiency determination of the FSCW IPMM-F by running it as a generator and loading it with a three-phase resistive load. The efficiency

calculation when applying a control strategy (MTPA and field-weakening) will be presented in the chapter 7 along with dynamic performance. The output power is measured at the machine terminals using a high-performance digital power analyzer (YOKOGAWA WT1800) with a power accuracy of ± 0.1 . The mechanical input power is measured by means of the torque transducer and the speed derived from the position encoder. The signals coming out from the torque transducer and speed sensor can be read from the electro-dynamometer interface but are also fed to the power analyzer for the time synchronization of the input and output power readings. This gives power analyzer the ability to determine the mechanical input power and provide the efficiency directly.

The efficiency is calculated as

$$\text{Efficiency (\%)} = \frac{\text{Electrical Output Power}}{\text{Mechanical input power}} * 100 \quad (6.8)$$

$$= \frac{\text{Electrical Output Power}}{(\text{Electrical Output Power} + \text{Losses})} * 100 \quad (6.9)$$

According to Eq.(6.7), the mechanical input power can be determined by adding up the losses to the electrical output power of the machine. The efficiency analysis for different load settings at three different rotor speed values is shown in Fig. 6.22. The efficiency map of the prototype IPMM is plotted in Fig. 6.23 by which the efficiency value of all the possible combination of rotor speed and torque values is known. The map shows that at rated speed, the efficiency can vary from 90% ~ 92% over half load condition with speed higher than 75 RPM.

The significant losses in an IPM machine are copper loss and core loss. Both these losses can be separated easily by an open-circuit test. When the armature circuits are open-circuited, the total loss includes the iron loss and the mechanical loss of the

CHAPTER 6: Experimental Validation of the Steady-State Performance of the Prototype FSCW IPMM-F

machine [164]. The mechanical loss cannot be separated from the open circuit core loss in the prototype CW IPMM unless the magnet field is removed from the rotor. The copper loss can be easily calculated with a short circuit test in the armature terminals which will provide the losses which include copper loss and mechanical loss. The efficiency is calculated using Eq. (6.6) as the output mechanical power can be easily found in the experimental setup, so the need to measure individual losses of the prototype is not necessary. The copper loss at rated load for the prototype is 210 watts. Fig. 6.24 shows the experimental values for iron and mechanical losses in the prototype for various loading of the machine at the generating condition. At rated speed, the iron loss and mechanical loss sums up to 139 watts as seen in Fig. 6.24.

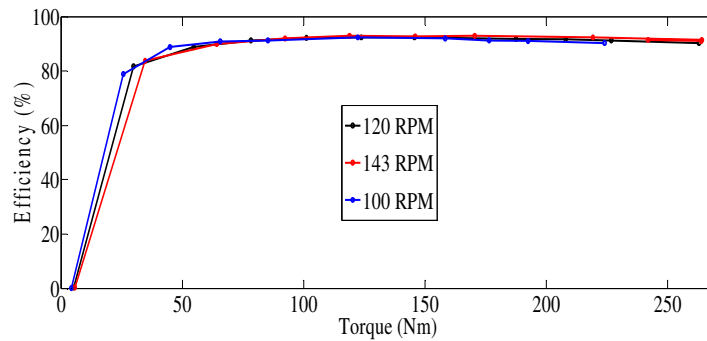


Fig. 6.22. Efficiency calculation of the CW IPMM for three different rotating speeds

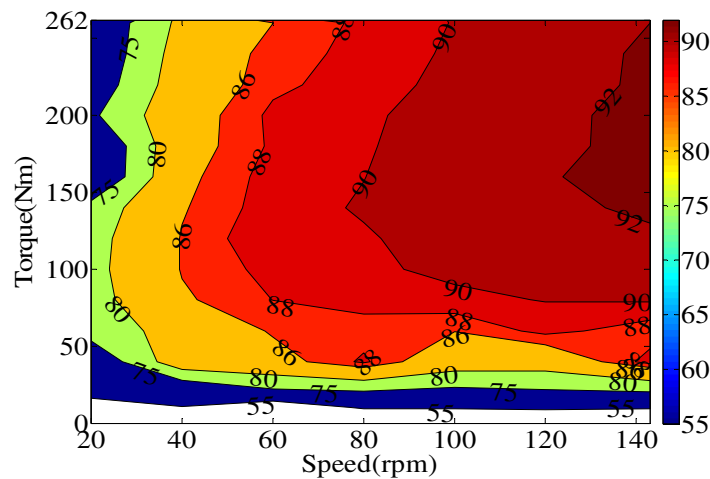


Fig. 6.23. Efficiency map of the CW IPMM during generating condition

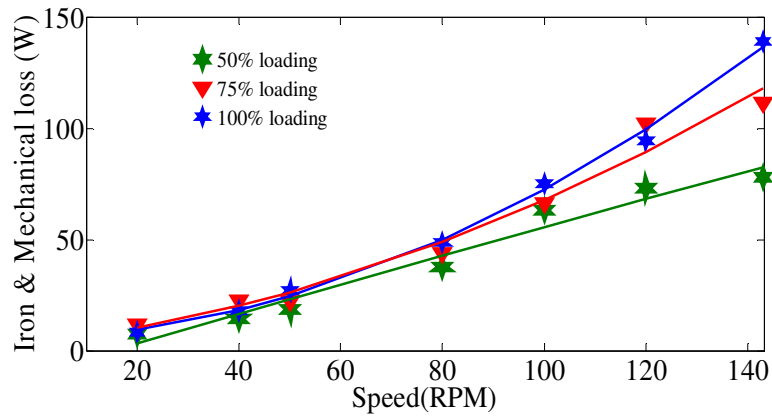


Fig. 6.24. Iron and Mechanical loss of the prototype CW IPMM

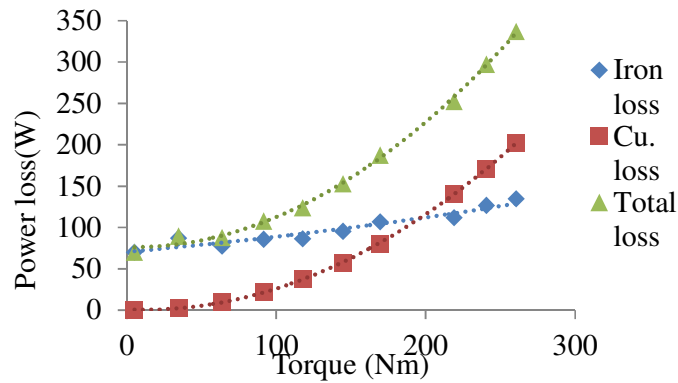


Fig. 6.25. Power loss of the prototype CW IPMM at rated speed

The measured losses of the IPMM at rated speed for various load settings are plotted in Fig. 6.25. From Fig. 6.25, it can be seen that the iron loss is the dominant part of total loss before the prototype machine generates 200 Nm. The total power loss of the FSCW IPMM-F is found to be 337 watts at rated speed for a full load, which is approximately 8% of the total developed power. Copper losses account for 60% of the total losses of the prototype FSCW IPMM-F during full load condition at rated speed.

6.6 Conclusion

The measured performance characteristics of the constructed FSCW IPMM-F were shown and used to verify the performance of the FEA. The concentrated winding IPMM prototype has exhibited sinusoidal back EMF waveform with negligible THD. The experimental verification of the 42 pole/54 slots CW IPMM combination showed low cogging torque ($< 1\%$ of rated torque) and torque ripple ($< 5\%$ of rated torque) with high efficiency ($> 90\%$). This suggests that all the specific design goals set for the FSCW IPMM-F had been achieved.

This chapter has verified the FEA results and the design of the FSCW IPMM-F.

CHAPTER 7: Dynamic Performance of the Prototype FSCW IPMM-F

7.1 Introduction

This chapter discusses the dynamic performance of the prototype machine under current vector control. Fig. 7.1 shows the synchronously rotating rotor reference frame of a 4-pole IPM machine. The d -axis is aligned with the permanent magnet flux linkage and the q -axis is orthogonal to d -axis.

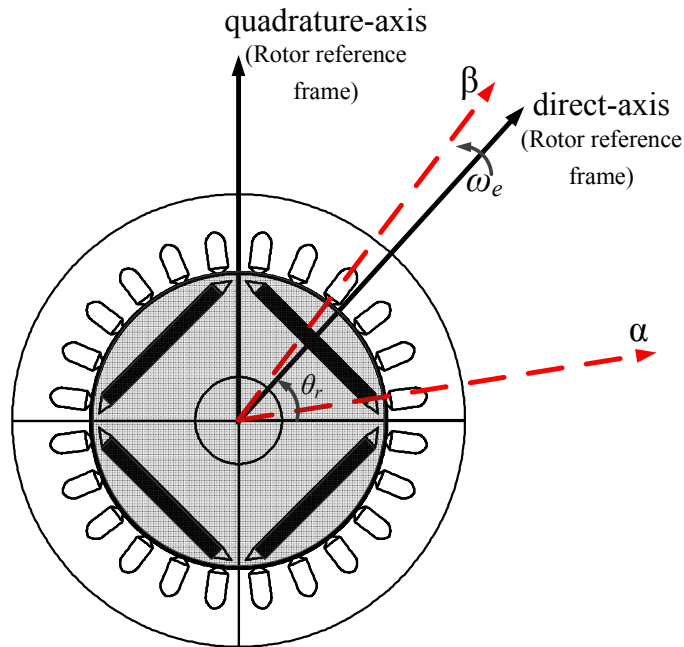


Fig. 7.1. Reference frame for a 4-pole IPM machine

The 3- ϕ time-varying quantities can be transformed into equivalent d - q quantities of the rotor reference frame by using parks transformation [165] given in Eq.(7.1).

$$\begin{bmatrix} d \\ q \end{bmatrix} = \sqrt{\frac{2}{3}} \begin{bmatrix} \cos\theta_m & \cos(\theta_m - \frac{2\pi}{3}) & \cos(\theta_m + \frac{2\pi}{3}) \\ -\sin\theta_m & -\sin(\theta_m - \frac{2\pi}{3}) & -\sin(\theta_m + \frac{2\pi}{3}) \end{bmatrix} \begin{bmatrix} a \\ b \\ c \end{bmatrix} \quad (7.1)$$

Applying parks transformation to phase voltages, currents and flux linkages of the PM machine, we can obtain a dynamic voltage equations in the d - q reference frame as given in Eq.(7.2).

$$\begin{bmatrix} v_d \\ v_q \end{bmatrix} = \begin{bmatrix} R_a & -\omega_e L_q \\ \omega_e L_d & R_a \end{bmatrix} \begin{bmatrix} i_d \\ i_q \end{bmatrix} + \begin{bmatrix} L_d \frac{d}{dt} & 0 \\ 0 & L_q \frac{d}{dt} \end{bmatrix} \begin{bmatrix} i_d \\ i_q \end{bmatrix} + \begin{bmatrix} 0 \\ \omega_e \Psi_{pm} \end{bmatrix} \quad (7.2)$$

where,

$L_{d,q}$ = d - and q - axis inductances;

$i_{d,q}$ = d - and q - axis currents;

ω_e = Electrical speed in rad/s and

Ψ_{PM} = PM flux linkage in $V/rad/s$.

The equivalent d - and q -axis circuits of an IPMM based on Eq. (7.2) are shown in Fig. 7.2. The flux linkages of an IPMM in the dq -axis can be given as

$$\begin{cases} \lambda_d = L_d i_d + \Psi_{PM} \\ \lambda_q = L_q i_q \end{cases} \quad (7.3)$$

7.2 Field oriented control:

The Field Oriented Control (FOC) is one of the commonly used current control strategies to achieve a fast dynamic performance of speed and torque control in the PMSM [166].

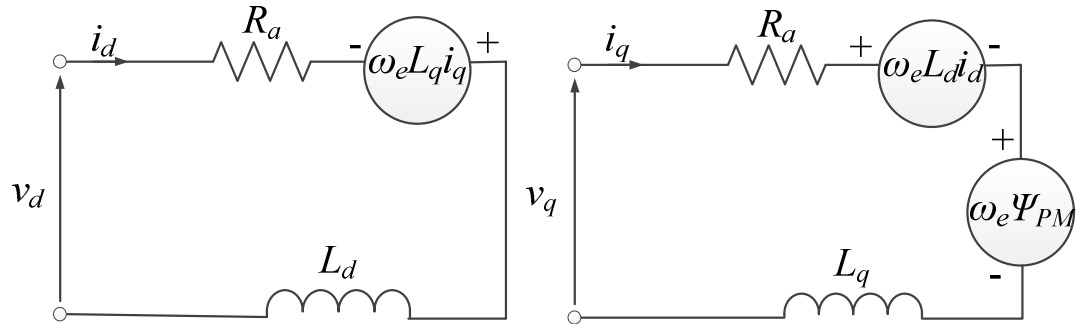


Fig. 7.2. Equivalent circuit of an IPMM

The developed torque can be represented in d - q reference frame as follows [167]:

$$T = \frac{3}{2} P_p \left[\underbrace{\Psi_{pm} i_q}_{\text{Alignment torque}} + \underbrace{(L_d - L_q) i_d i_q}_{\text{Reluctance torque}} \right] \quad (7.4)$$

The first term in Eq. (7.4) represents the alignment torque that makes up most of the total developed torque and the second term represents the reluctance torque component. For IPMM, the d -axis inductance is smaller than q -axis inductance. Therefore, the reluctance torque can contribute to the positive torque, provided that i_d and i_q have opposite polarities. Fig. 7.3 shows the variation of the two torque components with respect to current angle gamma (it is the angle between current phasor and q -axis) of the prototype machine. The block diagram of the FOC algorithm used in this study is presented in Fig. 7.4.

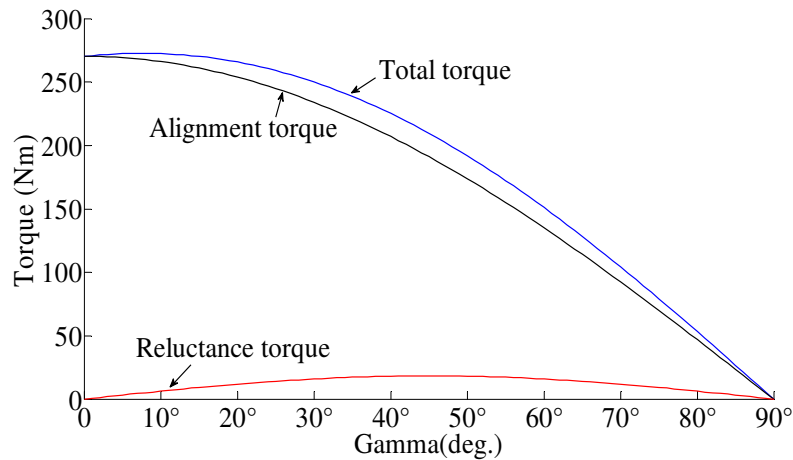


Fig. 7.3. Calculated torque comprising of alignment and reluctance torque from Eq. (7.4)

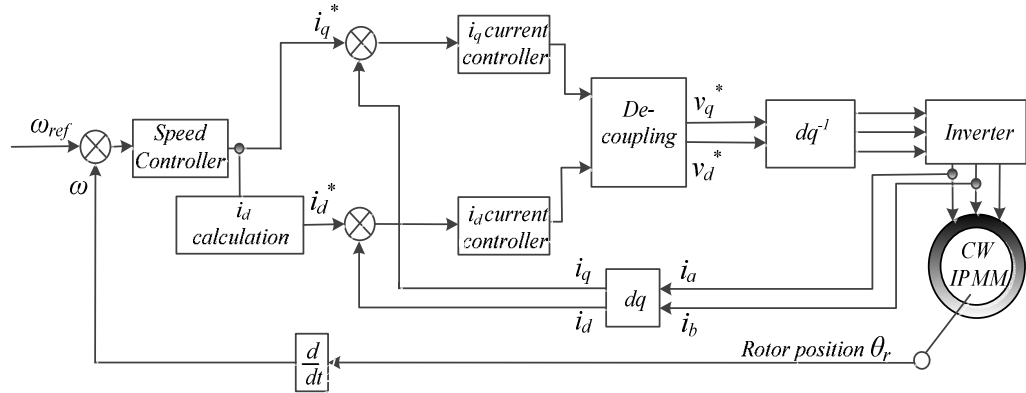


Fig. 7.4. Block diagram of Flux oriented control (FOC)

7.2.1 Effect of current angle variation:

The current angle is defined as the angle between the current phasor and the back EMF which is aligned with the q -axis, as shown in Fig. 7.5. The value of the current angle is directly related to the d - and q - axis current components that are fed to the machine. There are two operating speed regions for the IPM machine: maximum torque per ampere (MTPA) or constant torque region and constant power or field weakening region (FW).

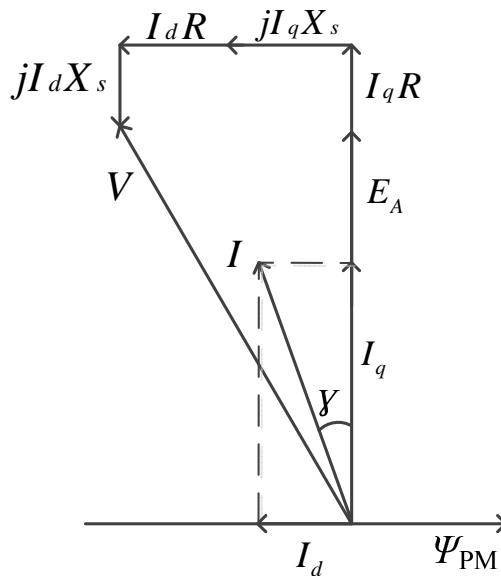


Fig. 7.5. Steady-state Space vector d - and q -axis phasor diagram

During MTPA operation, the current angle is maintained such that maximum torque can be obtained with minimum current. The optimal current angle to produce maximum torque is given as [168]:

$$\gamma_{opt} = \arcsin \left[-\frac{\Psi_{PM}}{4(L_q - L_d)I_{am}} + \sqrt{\frac{\Psi_{PM}^2}{16(L_q - L_d)^2 I_{am}^2} + \frac{1}{2}} \right] \quad (7.5)$$

The optimum value of gamma was found to be 12° for the prototype machine. This value was confirmed by calculating the torque by the FE model.

7.2.2 The d-q current plane

The developed torque gives hyperbolic shapes with respect to i_d and i_q according to Eq. (7.4). Fig. 7.6 shows the constant-torque loci in the four quadrants of an IPM machine. The boundaries of each quadrant are defined by a horizontal line where i_q is zero and a vertical dashed line established by $i_d = \frac{\Psi_{PM}}{(L_q - L_d)}$.

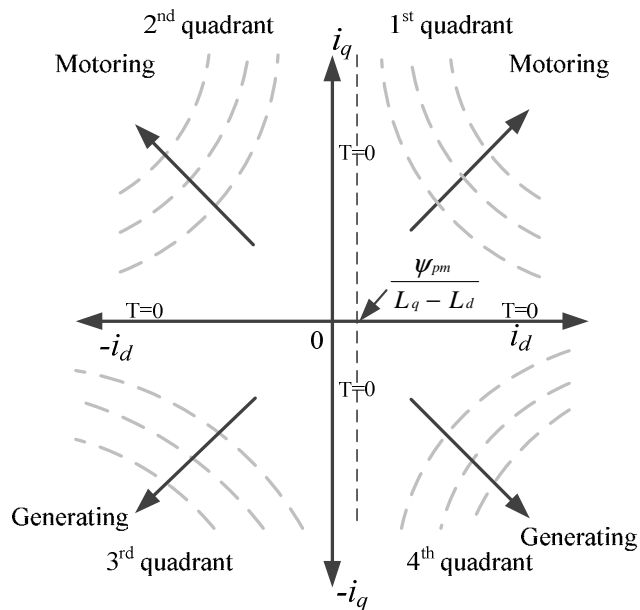


Fig. 7.6. Constant-torque loci of an IPMM

Due to the saliency in an IPMM, the torque per ampere is higher in the second and third quadrant. For this reason, the IPMM is designed to operate in the second and third quadrant where i_d is negative.

7.2.3 Circle diagram

A trajectory diagram represents the machine current and voltage limits in the i_d - i_q plane. It is customary to present the MTPA trajectory, and field weakening trajectory also in the same diagram. The limit and trajectory diagram consists of current limiting circles and voltage limiting ellipses as shown in Fig. 7.7. These limits are bound by the drive system and machine capacity and for satisfactory performance, the voltage and current limits must not be exceeded at all times. The terminal voltage (v_a) and the armature current (I_a) limits can easily be expressed by the following equation:

$$I_a = \sqrt{i_d^2 + i_q^2} \leq I_{am} \quad (7.6)$$

$$V_a = \sqrt{v_d^2 + v_q^2} \leq V_{am} \quad (7.7)$$

Where, I_{am} and V_{am} are the current and voltage limits of the IPMM. v_d and v_q can be formulated using the matrix of Eq. (7.2), that gives the voltage limit as,

$$\begin{aligned} V_a &= \sqrt{(-\omega_e L_q i_q)^2 + (\omega_e L_d i_d + \omega_e \Psi_{pm})^2} \\ &= \omega_e \sqrt{(\Psi_{pm} + L_d i_d)^2 + (L_q i_q)^2} \end{aligned} \quad (7.8)$$

Eq. (7.8) shows that the centre of the voltage ellipse lies at $(-\Psi_{pm}/L_d, 0)$ and becomes smaller with increased speed.

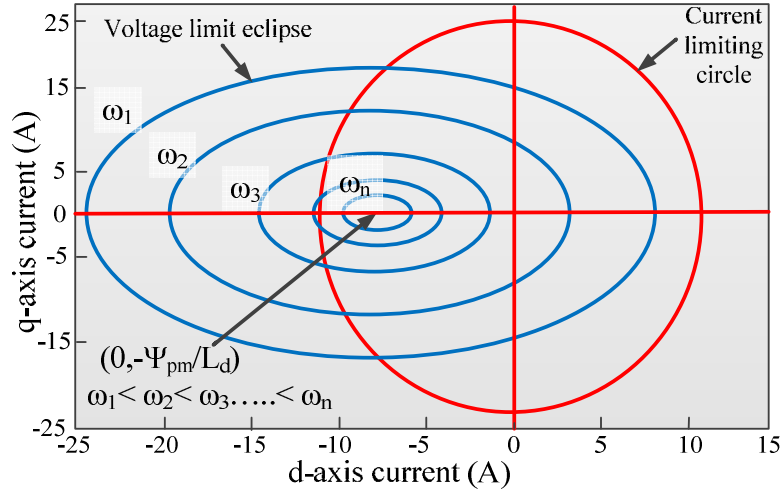


Fig. 7.7. Voltage limit ellipses and current limit circle of an IPMM

7.3 Maximum torque Per Ampere (MTPA):

Due to the reluctance torque component as seen in Fig. 7.3, the armature current vector is controlled such that the maximum torque per ampere is produced [40]. From Eq. (7.4), i_d can be expressed using i_q shown as

$$i_d = \frac{\Psi_{PM}}{2(L_q - L_d)} - \sqrt{\frac{\Psi_{PM}^2}{16(L_q - L_d)^2} + i_q^2} \quad (7.9)$$

The maximum torque is achieved when the armature current is equal to I_{am} . At maximum torque, the MTPA trajectory touches the current limit circle, and the point (referred to as A in Fig. 7.8) can be defined in i_d - i_q plane as

$$i_{da} = \frac{\Psi_{PM}}{2(L_q - L_d)} - \sqrt{\frac{\Psi_{PM}^2}{16(L_q - L_d)^2} + \frac{I_{am}^2}{2}} \quad (7.10)$$

$$\text{and } i_{qa} = \sqrt{I_{am}^2 - i_{da}^2} \quad (7.11)$$

Fig. 7.8 illustrates the circle diagram with the voltage and current limits including the MTPA trajectory for the prototype IPMM.

It shows that point A intersects with the voltage eclipse limit of the base speed, where the base speed is expressed as

$$\omega_b = \frac{V_{om}}{\sqrt{(\Psi_{PM} + L_d i_{da})^2 + L_q i_{qa}^2}} \quad (7.12)$$

where, V_{om} = Voltage limit of the inverter = $V_{am} - I_{am} R$ (for motoring action)

With the base speed of 143 rpm, using Eq. (7.12), the value of i_{da} and i_{qa} for the prototype machine at rated current of 6.5 A (RMS) is found to be -0.88A and 9.14A respectively for the prototype FSCW IPMM-F.

The torque hyperbola indicated for each constant torque values is expressed using the normalized technique described in [40] as a function of normalized i_d and i_q given as

$$T_n = \sqrt{i_{dn} (i_{dn} - 1)^3} \quad (7.13)$$

$$T_n = \frac{i_{qn}}{2} [1 + \sqrt{1 + 4 (i_{qn})^2}] \quad (7.14)$$

where, $T_n = \frac{T_e}{T_{eb}}$; $i_{dn} = \frac{i_d}{i_b}$; $i_{qn} = \frac{i_q}{i_b}$;

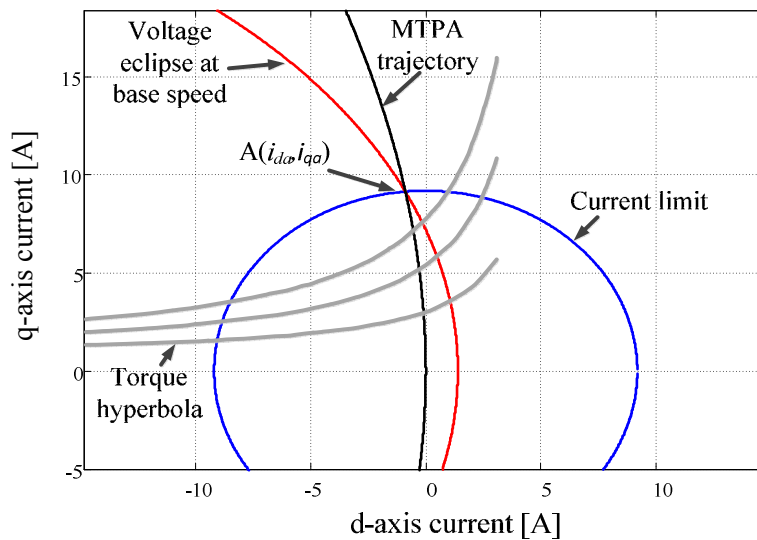


Fig. 7.8. Circle diagram showing torque hyperbolas

7.4 Field weakening region

Above base speed, the negative i_d current needs to be increased for field-weakening so that the terminal voltage of the machine does not exceed V_{om} . The vector diagram in Fig. 7.5 shows that increasing the current phase angle increases the negative i_d which in turns weakens the resultant flux. The control algorithm for current vectors during field weakening can be derived from (7.8) by replacing V_a with V_{om} as,

$$i_d = -\frac{\Psi_{PM}}{L_d} + \frac{1}{L_d} \sqrt{\frac{V_{om}^2}{\omega_e^2} - (L_q i_q)^2} \quad (7.15)$$

where, $|i_q| \leq \frac{V_{om}}{(\omega_e L_q)}$

The limiting values for the d -axis and q -axis currents are the intersecting points of the current limit circles, and the voltage limiting ellipses and can be obtained by,

$$i_{d_max} = -\frac{\Psi_{PM} L_d}{L_d^2 - L_q^2} + \sqrt{\frac{1}{L_d^2 - L_q^2} \Psi_{PM}^2 L_d^2 - (L_d^2 - L_q^2) \left(I_{am}^2 L_q^2 + \Psi_{PM}^2 - \frac{V_{om}^2}{\omega_e^2} \right)} \quad (7.16)$$

$$i_{q_max} = \sqrt{I_{am}^2 - i_{d_max}^2} \quad (7.17)$$

The transition from MTPA to field-weakening is shown in Fig. 7.9. The arrows reflect the path of the current vectors during field-weakening for speeds greater than the base speed up to a speed when the voltage limiting ellipse does not intersect with the current limiting circle.

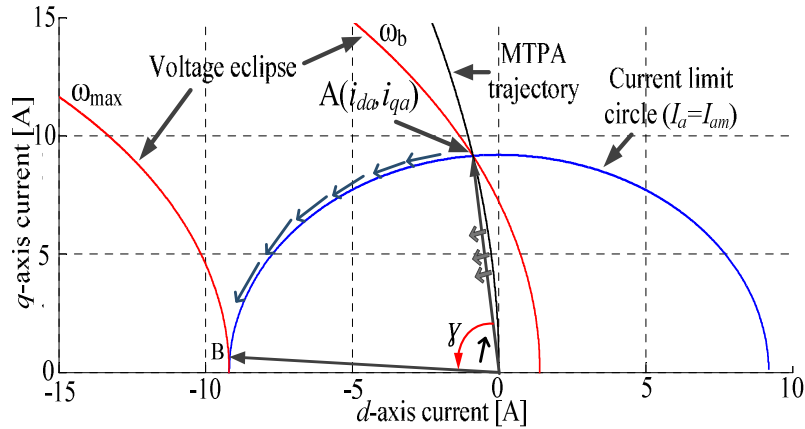


Fig. 7.9. Vector control during field-weakening

The field-weakening of an IPMM can be categorized into two categories based on the machines characteristic current (I_{cr}):

$$\text{Type 1: } |I_{am}| < |I_{cr}|$$

$$\text{Type 2: } |I_{am}| > |I_{cr}|$$

$$\text{where } I_{cr} = \frac{\Psi_{PM}}{L_d} \quad (7.18)$$

Type-1 IPMM have limited field-weakening range as the centre for voltage limit lies outside the current limiting circle and after a certain speed, the voltage and current limit both cannot be satisfied together. So the theoretical maximum speed for field-weakening for Type-1 IPMM can be defined as,

$$\omega_{max} = \frac{V_{om}}{\Psi_{PM} - L_d} \quad (7.19)$$

As for Type-2 IPM machines, the centre for voltage eclipse is inside the current limiting circle thus theoretically resulting in an infinite field-weakening speed range. The voltage limited maximum output trajectory is used to achieve the field-weakening range for Type-2 IPMM.

The voltage limited maximum output trajectory of the prototype is plotted using the i_d and i_q values given as [169]

$$i_d = -\frac{\Psi_{PM}}{L_d} - \Delta i_d \quad (7.20)$$

$$i_q = \frac{\sqrt{\left(\frac{V_{om}}{\omega_e}\right)^2 - (L_d \Delta i_d)^2}}{\xi L_d} \quad (7.21)$$

$$\text{where, } \Delta i_d = \frac{-\xi \Psi_{PM} + \sqrt{(\xi \Psi_{PM})^2 + 8(\xi - 1)^2 \left(\frac{V_{om}}{\omega_e}\right)^2}}{4(\xi - 1)L_d}$$

The voltage limited maximum output trajectory is plotted in Fig. 7.10 for both types to IPMM. For Type-1 IPMM, the voltage limited maximum output trajectory is outside the current limiting circle thus the voltage limited maximum output trajectory control is applicable for Type-2 IPMM. Fig. 7.10(b) shows that the voltage limited maximum output trajectory intersects the current limiting circle and voltage limiting eclipse at point B when the speed is ω_c . Below this speed, the voltage limited maximum output trajectory is outside the current limit circle as seen from the Fig. 7.10(b). So ω_c is the minimum speed for voltage limited maximum output operation which is referred to as critical speed. This speed is defined as,

$$\omega_c = \frac{V_{om}}{\Psi_{PM}} \quad (7.22)$$

For Type-2 IPMM, the current vector follows the line from B to C for flux weakening after the critical speed. The prototype IPMM falls into Type-1 which has limited capability of field-weakening. The characteristic current I_{cr} for the prototype CW IPMM is found to be 33.7A using Eq. (7.18).

The saliency ratio found for the FSCW IPMM-F was 1.41 which is relatively low. This low saliency ratio is also reflected in the small reluctance torque component of the machine shown in the previous chapter. A wider constant power speed range (CPSR) can be achieved in a machine with a low or nil saliency ratio if its characteristic current is equal or close to the machines rated current. However, for the prototype FSCW IPMM, the rated current of the machine is 9.19 A as compared to the characteristic current I_{cr} of 30.3 A. This means that the prototype CW IPMM does not have a broad CPSR. In wind energy conversion applications for which the prototype machine was constructed, the constant power speed range is not a requirement but an added advantage only. The prototype machine has a theoretical CPSR of about 1:1.5.

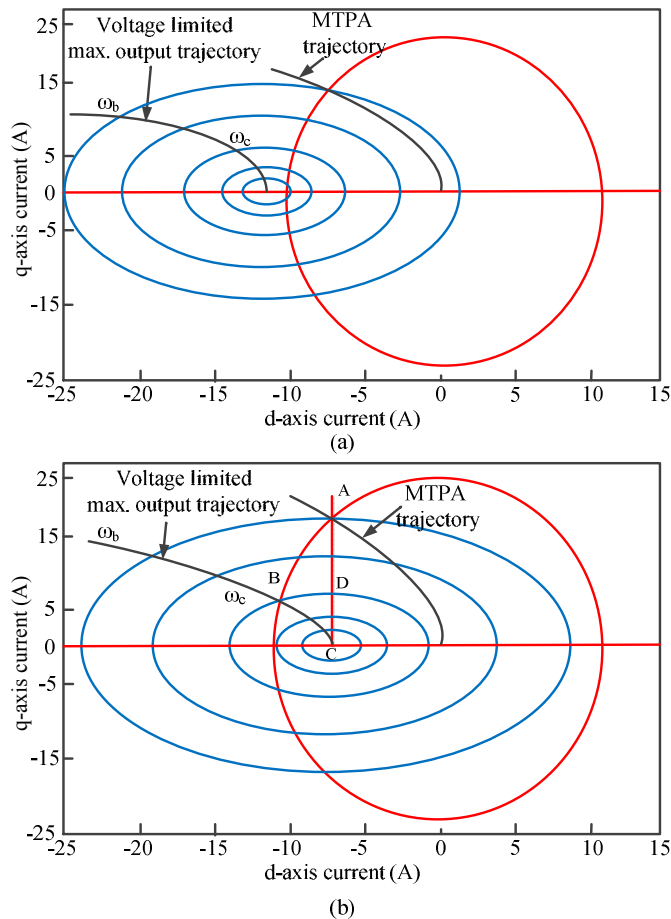


Fig. 7.10. Classification of IPM machine type by characteristic current; (a) Circle diagram for Type-1 IPMM; (b) Circle diagram for Type-2 IPMM;

7.5 Transition of control modes

Below base speed, the IPMM operates with MTPA algorithm. Above the base speed, the field-weakening control algorithm is imposed in order to keep the voltage fixed at rated value. The current vector control block diagram including transition flow of control modes is presented in Fig. 7.11.

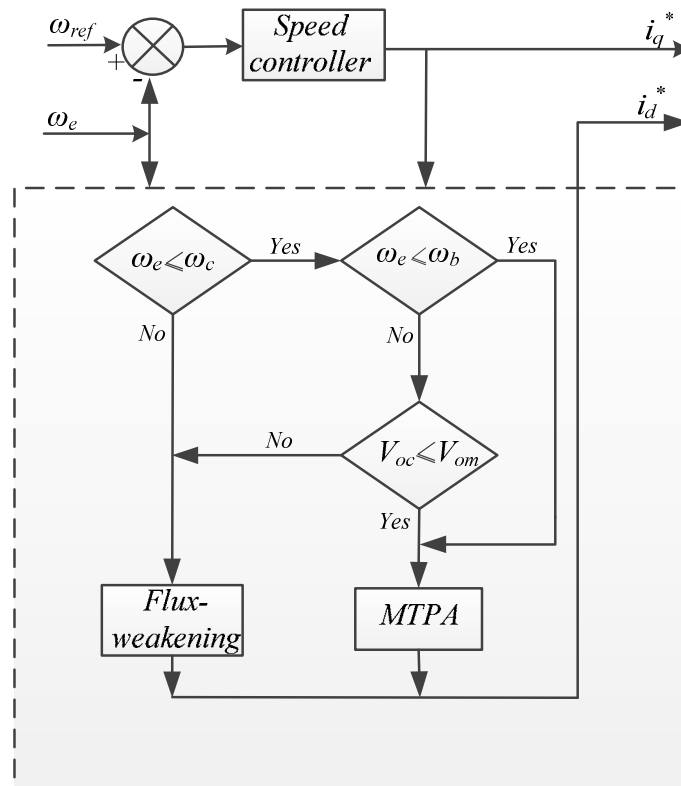


Fig. 7.11. FOC control algorithm

7.6 De-coupling current controllers

The d - and q - axis currents cannot independently control d - and q - axis voltage because of the cross-coupling terms such as $\omega_e(L_d i_d + \psi_{pm})$ and $\omega_e L_q i_q$ are present in the matrix Eq.(7.2) . As these cross-coupling terms are proportional to the rotor speed, the current responses will be affected by the cross-coupling terms at high speeds. In this research, the effects of the cross-coupling terms are compensated by using a feed-

forward compensation [169, 170] at the output of the PI current controllers shown in Fig. 7.12. Where $G_{cd}(s)$ and $G_{cq}(s)$ are the two PI current controller,

$$G_{c(s)} = \frac{G(1 + \tau s)}{\tau s} \quad (7.23)$$

where,

$$G = K_p \text{ (Proportional Gain)}$$

$$\frac{G}{\tau} = K_i \text{ (Integral Gain)}$$

The voltage references are transformed back to three-phase voltages by using inverse Park's transformation shown in Fig. 7.12.

7.7 Control as a Generator:

The FOC control algorithm is also applicable for generating operation. In this case, the speed controller loop is replaced by the DC bus controller that generates the reference i_q^* . The controlled vector operates in the 3rd quadrant as seen in Fig. 7.6 in the i_d - i_q plane, making i_q negative as a consequence of negative torque. The block diagram of the control scheme of the IPMM as a generator in FOC is shown in Fig. 7.13.

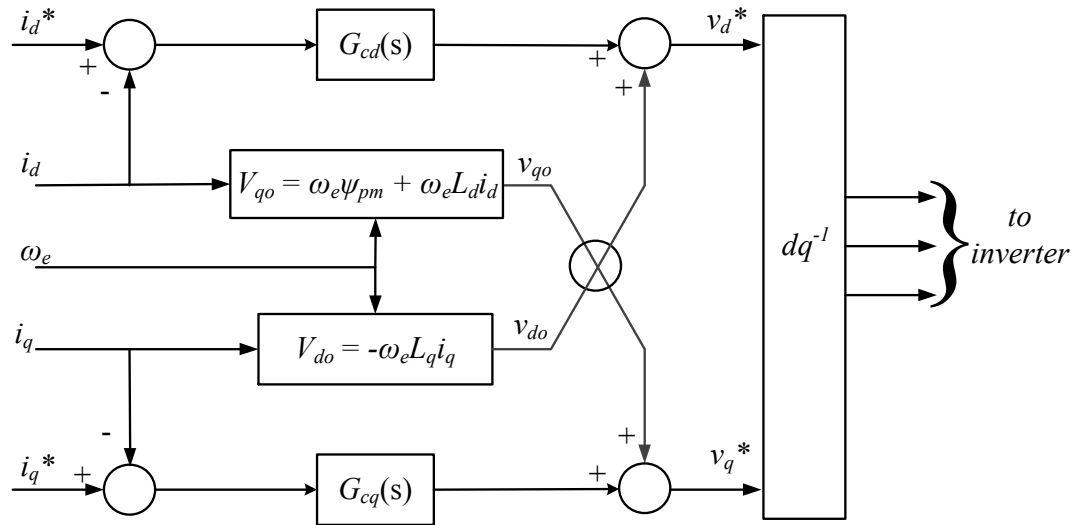


Fig. 7.12. Decoupling current controllers

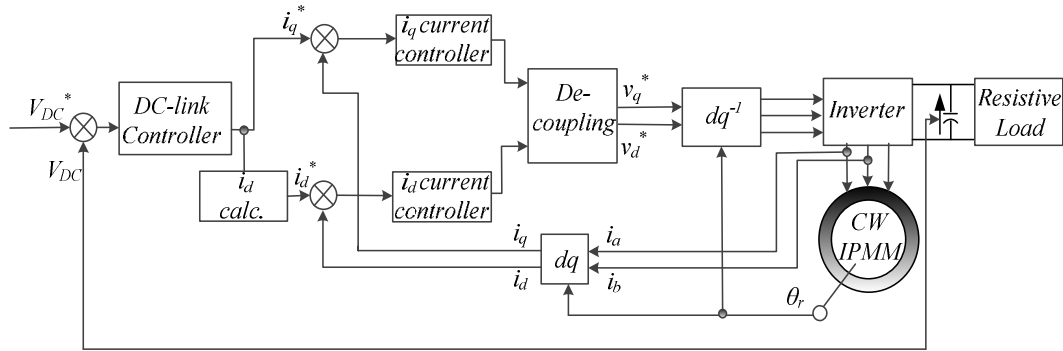


Fig. 7.13. Block diagram of the FOC scheme during generation

7.8 MTPA control during motoring condition:

The MTPA control is applied to the prototype CW IPMM until the rotating speed is below or equal to the rated speed. The dynamic response of speed and \dot{i}_q with respect to a step change in speed from -100 rpm to 100 rpm at 0.07 Hz are shown in Fig. 7.14 and Fig. 7.15 respectively at no load. From Fig. 7.14, it can be seen that the settling time for the speed is 3.7 seconds, and the overshoot is low at 6 rpm. The MTPA trajectory for the FSCW IPMM-F during motoring operation is shown in Fig. 7.16 indicates that the experimental \dot{i}_d and \dot{i}_q points gathered for different torque values follows the MTPA trajectory derived analytically using the machine lumped parameters. At rated speed, the machine delivers a full load, and the MTPA trajectory reaches the current limit. At this point, the values of \dot{i}_d and \dot{i}_q are found to be -1.11 A and 9.12A respectively. The terminal voltage has also reached its limit to 458 volts RMS. The efficiency is also calculated for the prototype CW IPMM during motoring operation while applying MTPA in Fig. 7.17. In Fig. 7.17, the overall system efficiency that includes the CW IPM machine losses, inverter losses, and the dynamometer losses is also compared with just the CW IPM machine efficiency. The efficiency is found to be 92% for the FSCW IPMM-F and the overall system efficiency to be 87.5% at full load for rated speed.

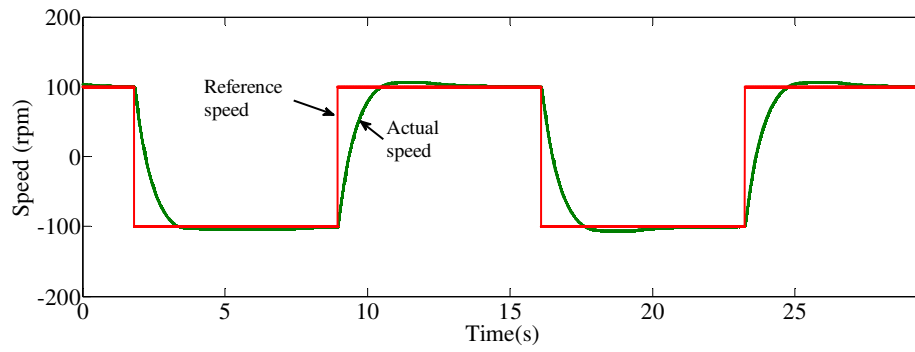


Fig. 7.14. Speed response for speed step of -100 to 100rpm

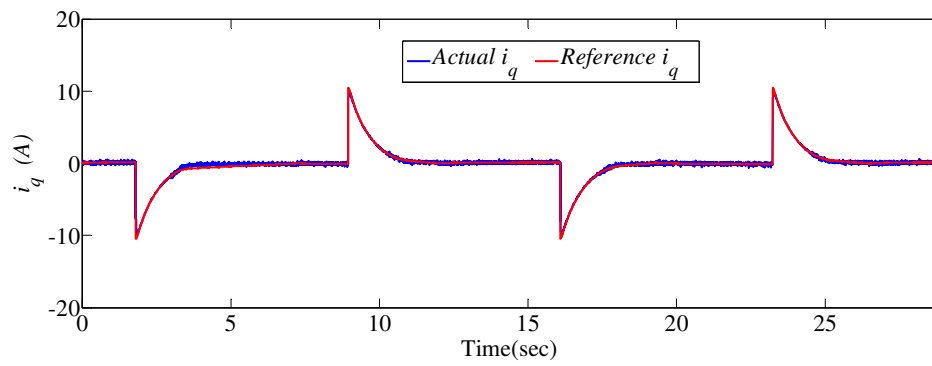


Fig. 7.15. q - axis current response for speed step of -100 to 100rpm

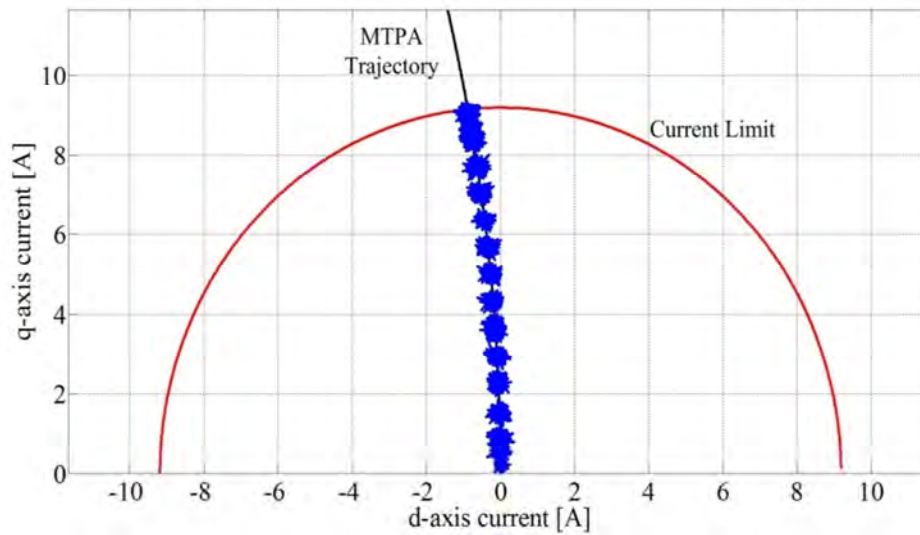


Fig. 7.16. MTPA trajectory achieved experimentally (Blue points) with the current trajectory obtained analytically

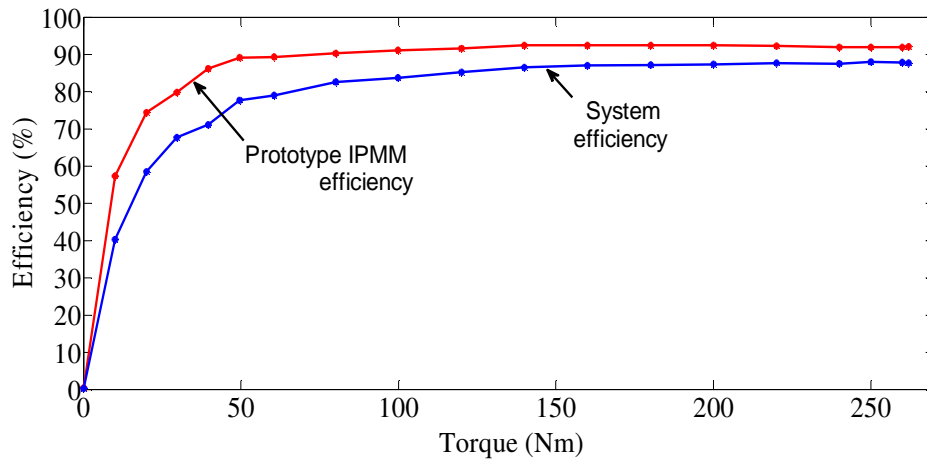


Fig. 7.17. Overall system efficiency and CW IPMM efficiency during MTPA operation during motoring

7.9 Generation:

During generation, the outer speed loop of motoring was replaced with a DC bus regulator loop. The block diagram of the control loop is already shown in Fig. 7.13. The experimental setup for the prototype IPMM during generation is shown in Fig. 7.18. For generating operation, the 42 pole CW IPMM was driven by an MEA electrodynamicometer system that is discussed in appendix G. The dynamometer is supplied with three phase AC supply of 450 volts. The control was implemented using DS1104. The DC bus voltage is regulated at 650 V.

The DC bus regulation at 143 rpm for step load change from 0 to full load is shown in Fig. 7.19. It can be seen in Fig. 7.19, the DC bus voltage drops down to 450 volts as soon as the full load is applied to the machine. After adjusting the PI controllers in the controls, the load disturbance was reduced to 2.14 seconds. The corresponding direct and quadrature axis currents are shown in Fig. 7.20 and Fig. 7.21 respectively. The prototype FSCW IPMM-F operates in the 3rd quadrant during generation as seen in Fig. 7.6, making both the direct and quadrature axis currents negative. After applying full load to the prototype CW IPMM, i_q drops down to -10.8 A before it settles down to the

maximum value of -9.2 A. As for i_d , the reference is set to zero in this condition. Fig. 7.22 shows the torque transient at rated speed when the load changes from zero to full load.

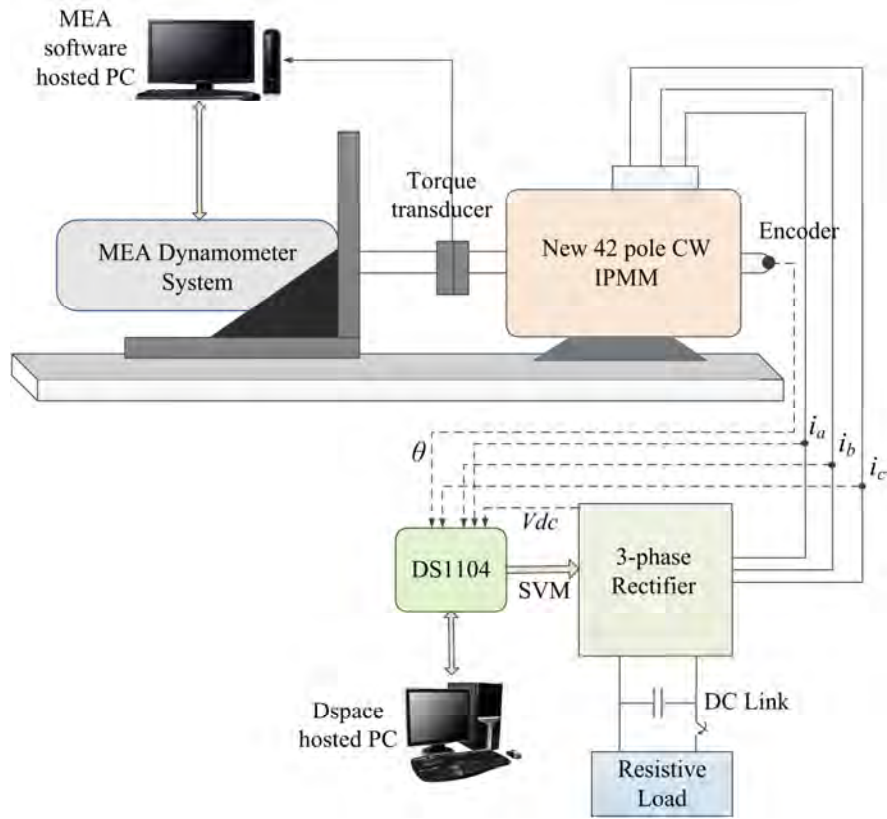


Fig. 7.18. Experimental setup for generation

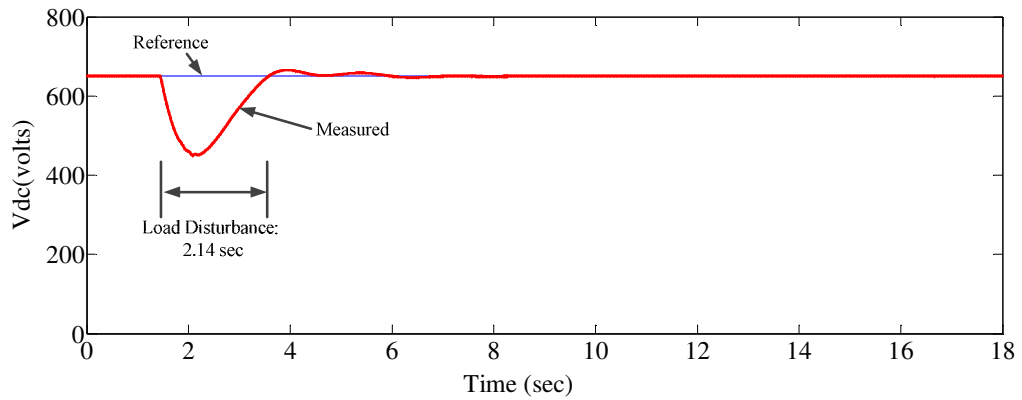


Fig. 7.19. Measured response of the DC bus for a load step change from no load to full load

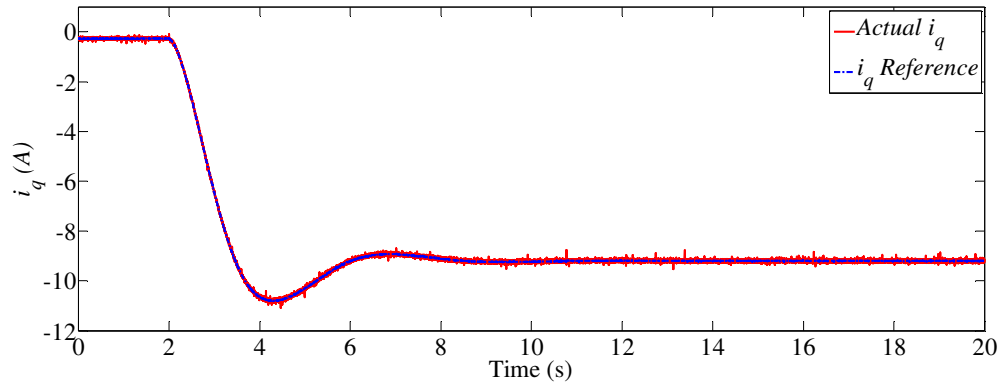


Fig. 7.20. Measured response of i_q for a load step change from no load to full load

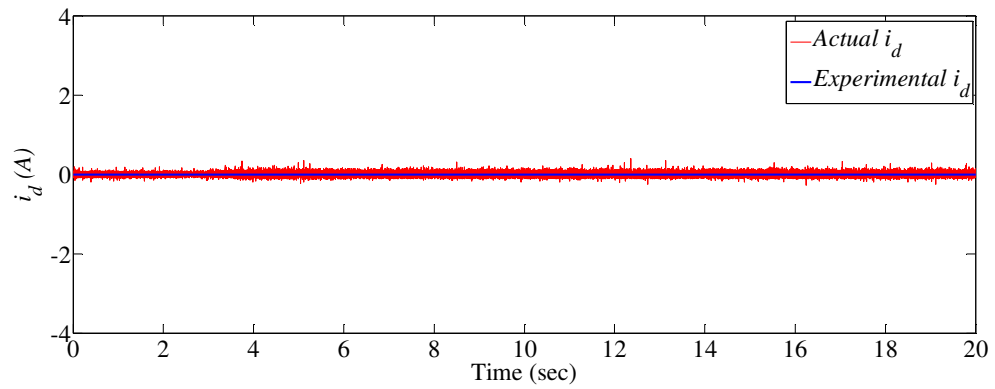


Fig. 7.21. Measured response of i_d for a load step change from no load to full load

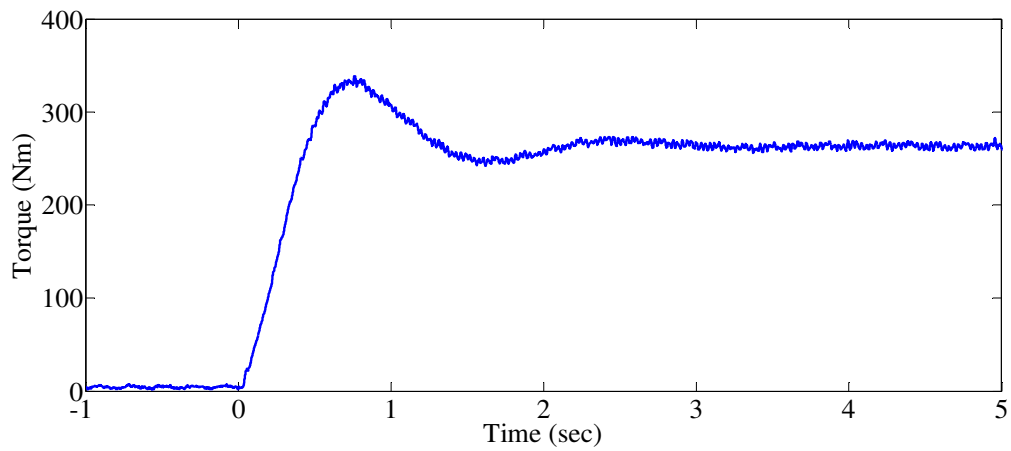


Fig. 7.22. Torque transient when the prototype FSCW-IPMM-F is loaded from zero to full load at rated speed.

7.9.1 MTPA control during generating condition:

In the previous section, the control strategy was implemented with $i_d=0$. For MTPA, i_d is determined according to the value of i_q . The constant torque operation of the drive was investigated with a step change of speed from 80 rpm to 120 rpm. During this experiment, the DC bus was regulated at 440 volts. The dynamic response of the DC bus is given in Fig. 7.23. When the speed reference is changed to 120 rpm, the DC bus voltage drops down to 356 volts and accelerates back to the reference DC voltage. The corresponding values of i_d and i_q is shown in Fig. 7.24. The current trajectory obtained from the measured i_d and i_q is given in Fig. 7.25. As discussed before, the MTPA trajectory operates in the 3rd quadrant as seen in Fig. 7.25.

At rated speed, the CW IPMM is fully loaded, and the MTPA trajectory reaches the voltage limit. As the speed approaches the rated value i_d and i_q jumps to its maximum value of the current to produce the required maximum torque. At this point, the values of i_d and i_q are found to be -1.11A and -9.12A respectively. Fig. 7.25 shows that the dynamic response and the MTPA trajectory obtained through experiments precisely match the results obtained analytically from the modelling.

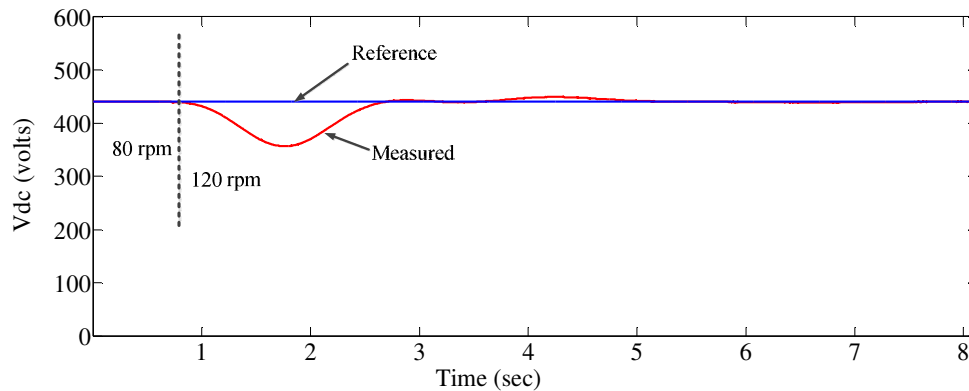


Fig. 7.23. DC bus response for speed step change of 80 to 120 rpm

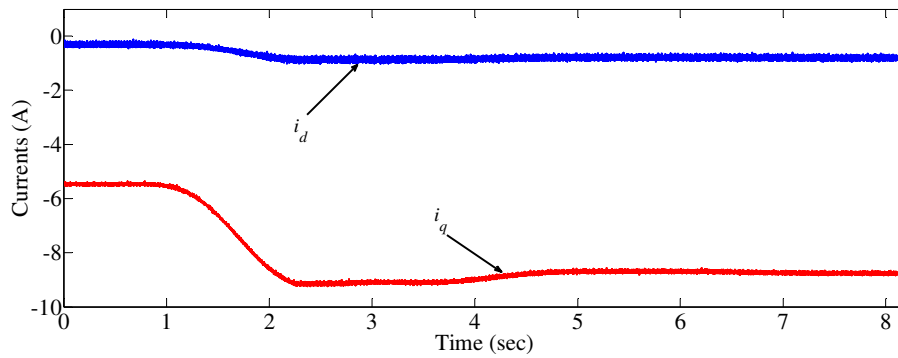


Fig. 7.24. i_d and i_q current response for speed step change of 80 to 120 rpm

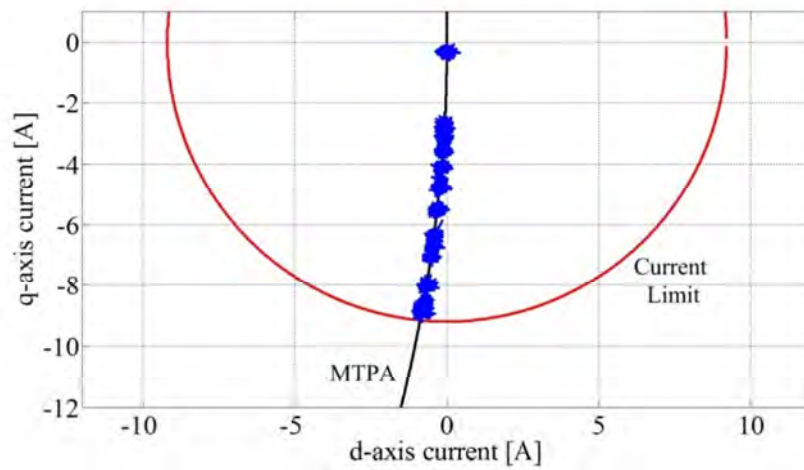


Fig. 7.25. MTPA current trajectory from experiment during generation

The efficiency calculation during MTPA control at the generating condition is given in Fig. 7.26. At full load, the efficiency is found to be 92% that is the same value obtained in chapter 6 during generation mode with the control strategy being absent.

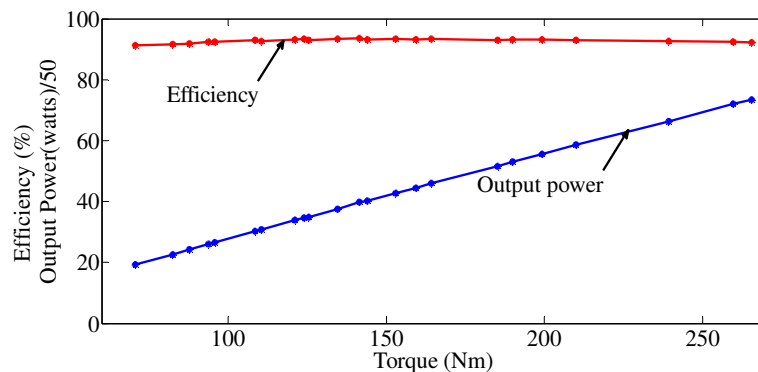


Fig. 7.26. Efficiency calculation of the FSCW IPMM-F with MTPA during generation

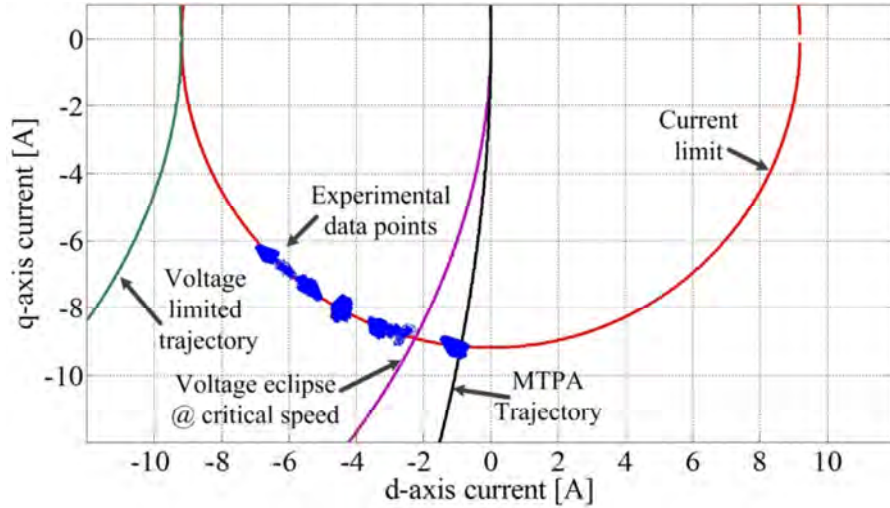


Fig. 7.27. Field-weakening current trajectory from experiment during generation

7.9.2 FW control during generating condition:

Field-weakening region occurs when the speed of the prototype CW IPMM becomes higher than the rated speed. In this region, i_d is used to suppress the flux produced by the magnets and maintain a constant rated power. The theoretical field-weakening range of the FSCW IPMM-F has been already discussed in section 7.4. For the prototype IPMM, the field-weakening control algorithm becomes activated after 143 rpm. The FW trajectory follows the current limiting circle that can be seen in Fig. 7.27. The voltage limited trajectory along with the voltage eclipse at critical speed is also pointed out in Fig. 7.27.

It can be seen from Fig. 7.27, that the d -axis and q -axis currents could not fully reach its maximum values at flux weakening. The maximum speed was found to be 184 rpm during field-weakening at which i_d was -6.9A and i_q at -5.8A. The L-L terminal voltage at field-weakening operation should be constant at its rated value of 450 volts (RMS) that can be seen in Fig. 7.28. At the maximum achievable field-weakening speed, the torque was reduced to 210 Nm as shown in Fig. 7.28. The efficiency during FW is shown in Fig. 7.29. During the FW range, the input power to the prototype CW

IPMM was constant at 4100 watts while the output power varied slightly between 3750 watts to 3780 watts. The output power deviated slightly from the rated power since the machine iron losses increase as the speed increases. The efficiency of the FSCW IPMM-F was found to be in the range of 91% - 92% during the overall field-weakening range. The field-weakening range found in this analysis was less than the range calculated analytically. Fig. 7.30 shows the field-weakening range of the FSCW IPMM-F conducted in FE analysis. Table 7.1 shows the maximum flux weakening speed calculated using various methods.

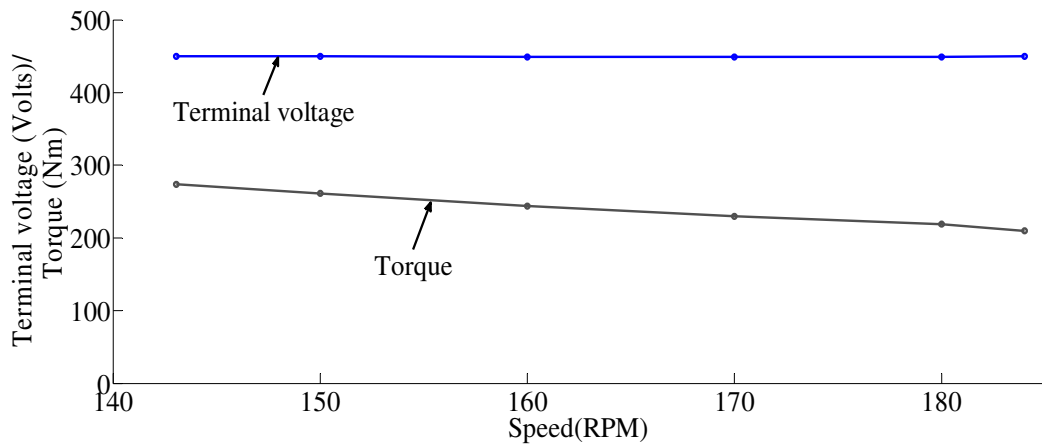


Fig. 7.28. Outcome of terminal voltage and torque with increasing speed

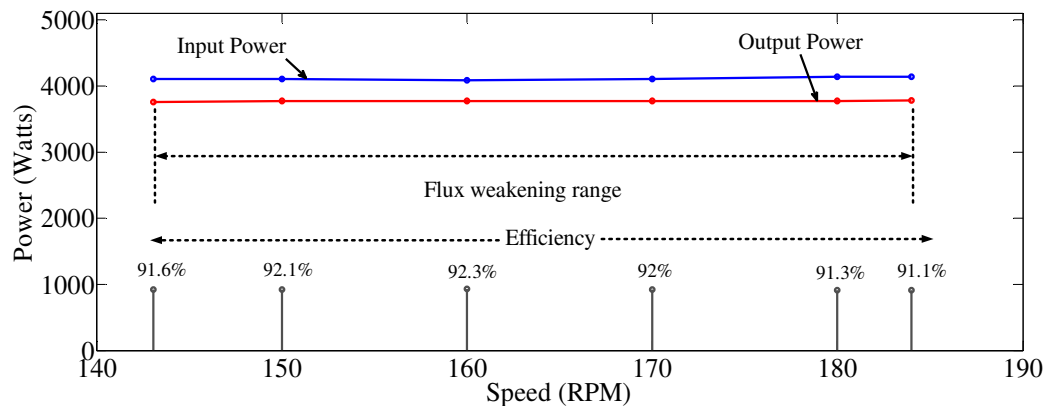


Fig. 7.29. Flux weakening range of the prototype IPMM (Experimental)

Table 7.1. Maximum speed for flux weakening

Calculation method	Max. speed for field-weakening of FSCW IPMM-F (RPM)
Analytical	215
FEA	211
Experimental	184

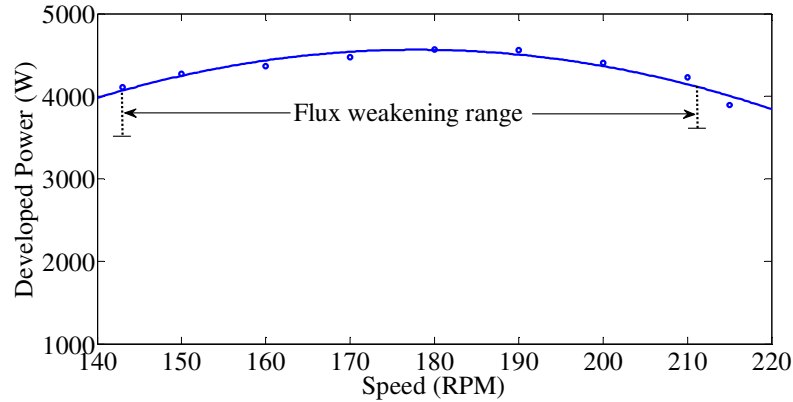


Fig. 7.30. Field-weakening range of the FSCW IPMM-F conducted in FEA

It can be seen from Table 7.1, that the experimentally analyzed maximum speed for FW is a lot lower in comparison to the other two methods. This is because the analytical method and the FEA do not consider the mechanical losses of the IPMM and the inverter losses of the system. The experimental field-weakening range has been verified by using a back-to-back inverter to the FSCW IPMM-F that provides the same maximum speed for FW. This is shown in the next section.

7.10 Wind profile simulation using back-to-back PWM converter

A direct-drive wind turbine topology with back-to-back converters offers many advantages over the existing wind turbine control system [171-174]. However, commercial wind turbines with permanent magnet synchronous machines mainly use a passive rectifier followed by an IGBT inverter [175, 176]. Researchers are focusing on developing highly effective vector controlled system for the wind topology that could be

widely adopted by the wind turbine industry. This section of the research analyzes the constructed FSCW IPMM-F connected to the back-to-back converter with the electro-dynamometer emulating the wind profile. The selected wind profile has been already discussed in chapter 2. Fig. 7.31 shows the configuration of the FSCW IPMM-F connected to a back-to-back PWM converter.

The two voltage source converters shown in Fig. 7.31 are controlled through conventional decoupled dq vector control approach. The machine side three phase converter (MSC) works as a driver controlling the generator to a reference speed. This reference speed is determined by the torque-speed characteristics given by the wind emulator to the dynamometer. Fig. 7.32(b) shows the power efficiency characteristic curve of a typical wind turbine generator. This curve is derived by tracking the maximum power at each wind speed referred to as Maximum power point tracking (MPPT), shown in Fig. 7.32(a). Various MPPT algorithm is available in the literature in order to determine the maximum power at each wind speed [177-179], which is not discussed or implemented in this research.

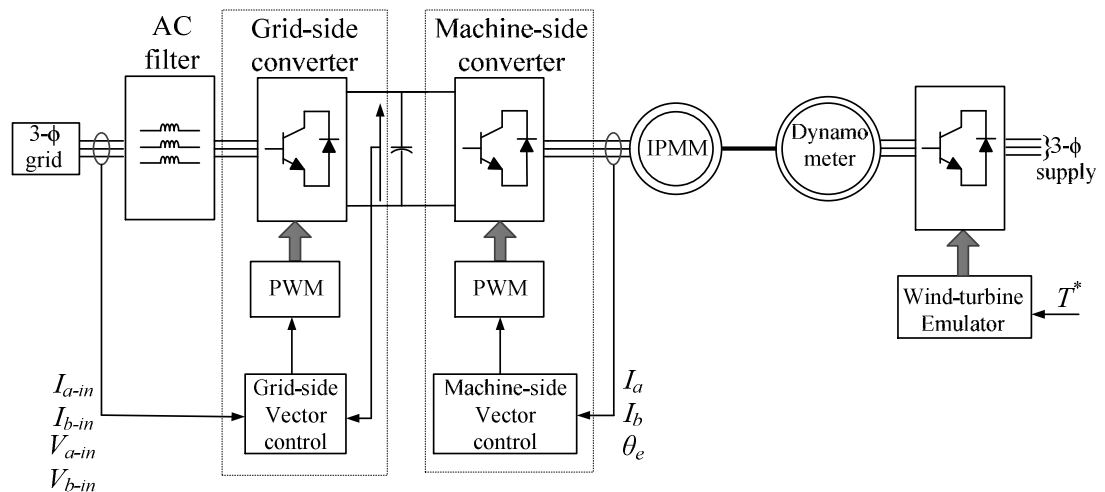


Fig. 7.31. Schematic diagram of the FSCW IPMM-F controlled by a back-to-back PWM converter.

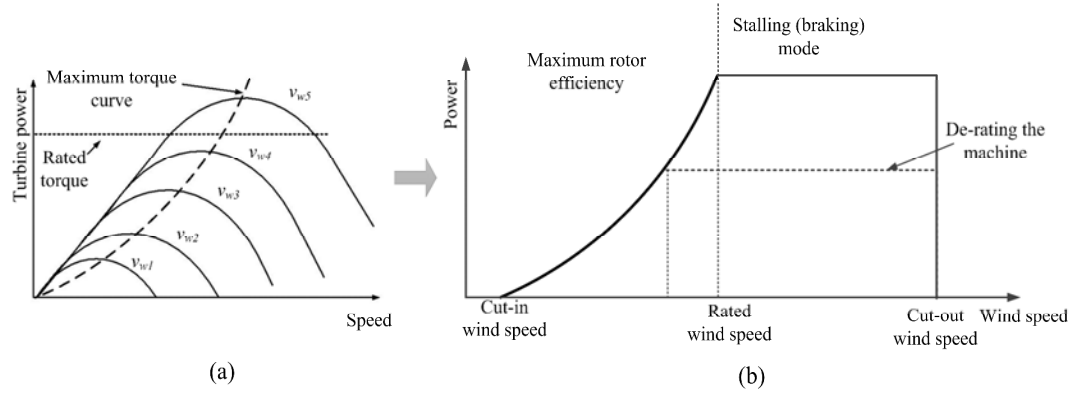


Fig. 7.32. (a) Wind turbine power versus shaft speed for various wind speed; (b) Power-wind speed of a typical small wind turbine generator.

This thesis directly uses the power speed characteristics of a horizontal axis wind turbine derived in chapter 2 for experimenting the FSCW IPMM-F as a wind turbine generator. The grid side converter maintains a constant dc-link voltage and adjusts reactive power absorbed from the grid by the converter. Throughout this experiment, the reactive power was set to zero in order to achieve unity power factor. An inductance value of $5mH$ was used in each phase as the line filter across the grid. Fig. 7.33 shows the power and the torque of the FSCW IPMM-F acting as a wind turbine.

It can be seen that the rated output power of 3710 watts is reached at 143 RPM. During this mode of operation, the control strategy applied to the prototype is convention MTPA. After the rated speed, flux weakening control is applied to the prototype design. During FW operation, the torque reduces, whereas the voltage and the power are kept constant. The efficiency and the L-L Back EMF of the prototype during MTPA and FW are plotted in Fig. 7.34.

During the FW operation, the turbine goes to stalling mode as seen in Fig. 7.32(b). This is because the turbine needs to maintain a certain level of rotational speed in order to control the rotor torque even when the wind speed goes above the rated condition. By

stalling the turbine, it controls the rotational speed to a certain maximal wind speed (referred to as cut-out speed in Fig. 7.32(b)).

Most wind turbine generators do not possess field weakening capability such as DFIG's, SPMM, etc. In such cases, the manufacturers de-rate the machine. De-rating of a machine refers to operating the machine below rated power and rated speed. Fig. 7.32(b) shows the effect of power-speed characteristics when the machine is de-rated. As for IPMM, de-rating is unnecessary as these machines provide field-weakening capability. The prototype FSCW IPMM-F has very limited field-weakening capacity as discussed in the previous section.

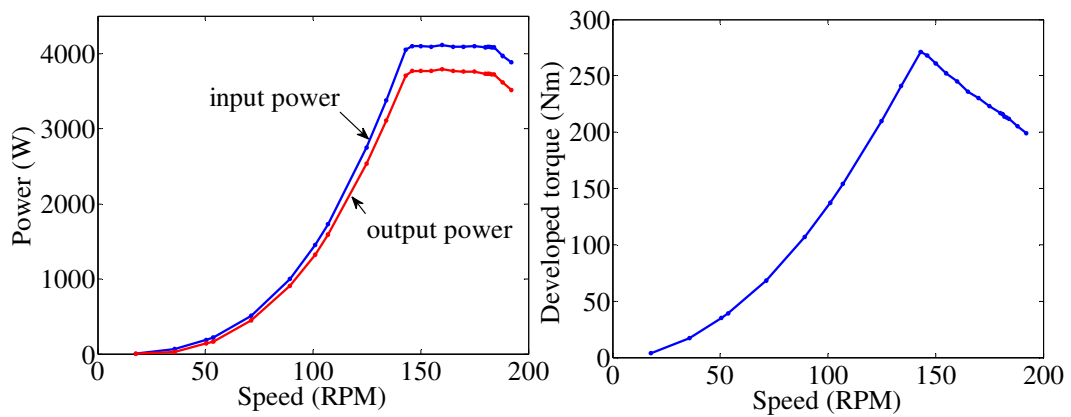


Fig. 7.33. Variation in power and torque with respect to speed

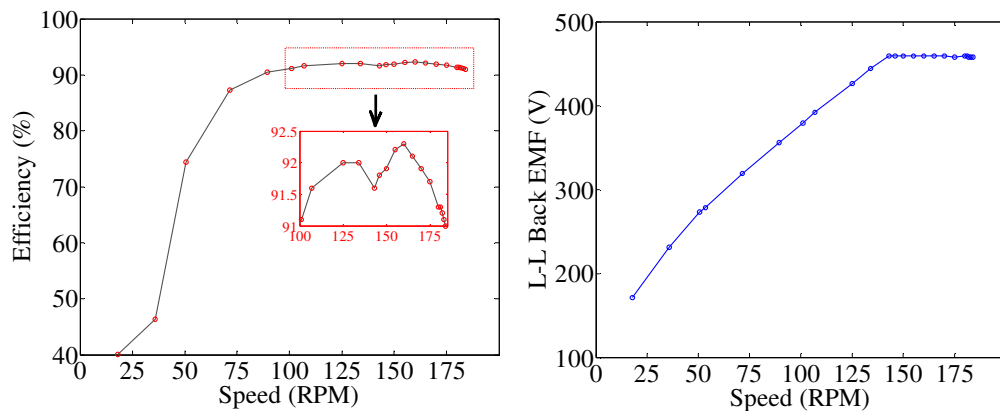


Fig. 7.34. Efficiency and L-L voltage

The maximum speed is found to be at 184 RPM after which the power starts falling as seen in Fig. 7.33. Fig. 7.35 shows the variation of d - and q -axis currents during MTPA and FW. In this section, the effect of the wind gust on the prototype machine is considered. The wind gust phenomenon is simulated by applying a speed step response to the machine operating under MTPA control at full load condition. Fig. 7.36 and Fig. 7.37 show the speed, DC-link voltage and the current responses for a step speed change between 62 rpm and 143 rpm at full load. It can be seen from Fig. 7.36 and Fig. 7.37 that the settling time for speed and the current responses are high which is due to the high inertia of the prototype. It can be seen that the DC-link voltage is constant at 600 volts at all speed conditions.

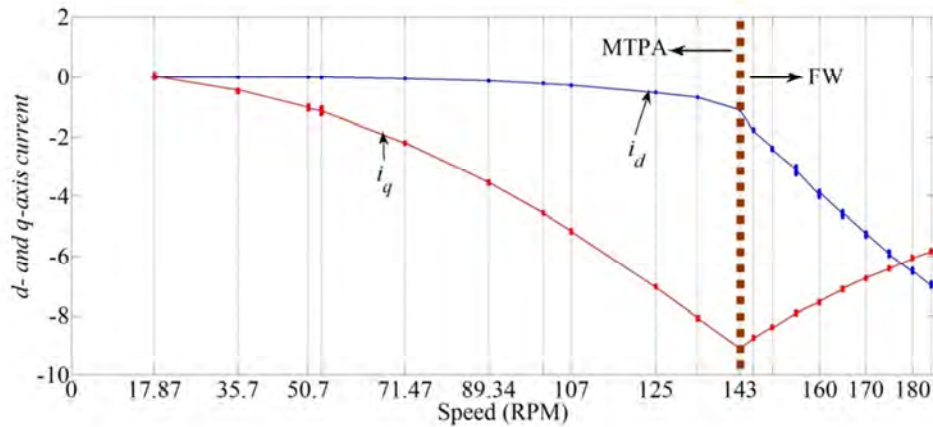


Fig. 7.35. Change in d - and q -axis current of the FSCW IPMM-F

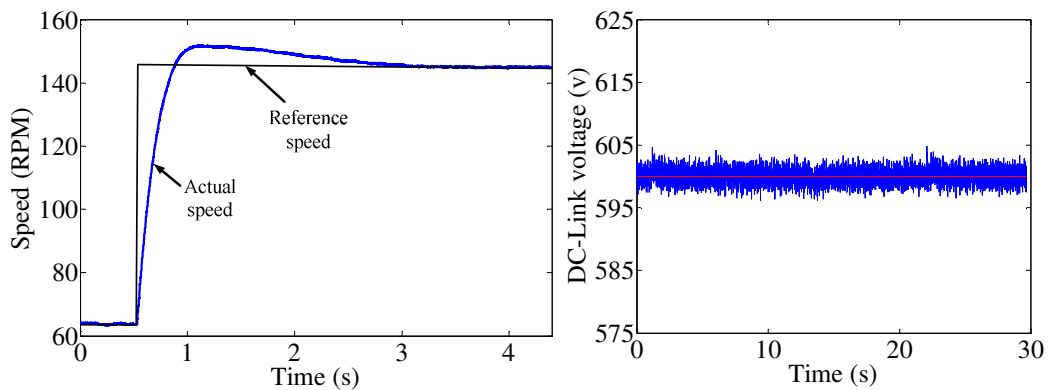


Fig. 7.36. Step change in speed at full load

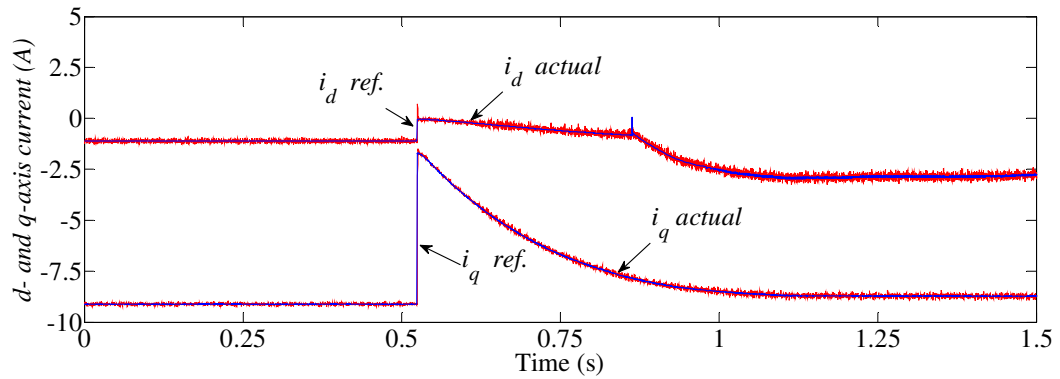


Fig. 7.37. d - and q -axis current during step change in speed from 62 RPM -143 RPM

The dynamic performance of the FOC in the prototype was also investigated for load step change at rated speed conditions. The result is illustrated in Fig. 7.38. As seen in Fig. 7.38, the machine is initially run at 143 rpm with 100 Nm torque loading, and then a 150 Nm torque is applied to the shaft of the prototype. After running with this load for 10 seconds, the load torque is again changed to 100 Nm. The settling time of the speed controller under this load condition is approximately 1 sec. Fig. 7.39 shows the effect of load disturbance on the grid side phase current.

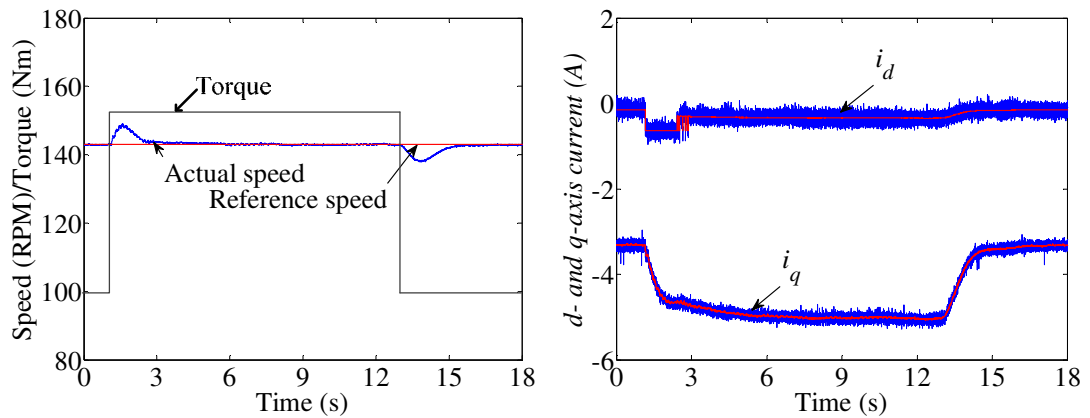


Fig. 7.38. Dynamic performances at 143 RPM with load disturbances

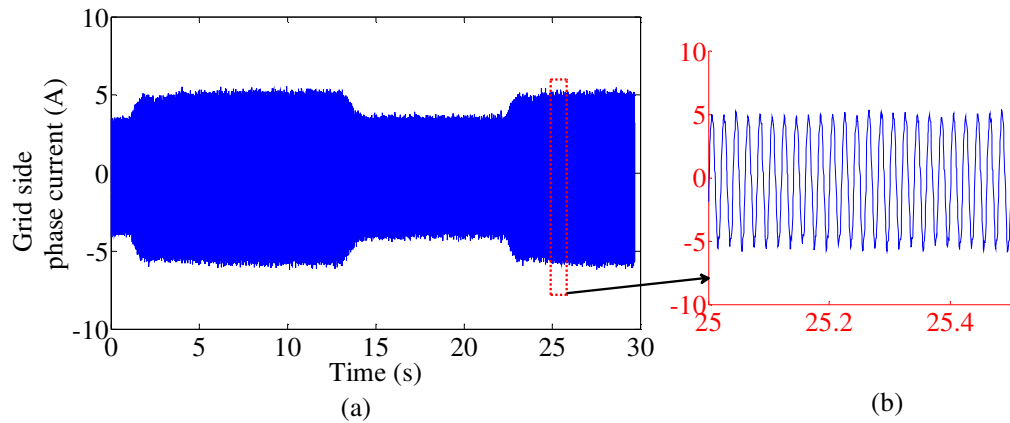


Fig. 7.39. (a) Grid side phase current during load disturbance; (b) Magnified portion of the box shown in (a)

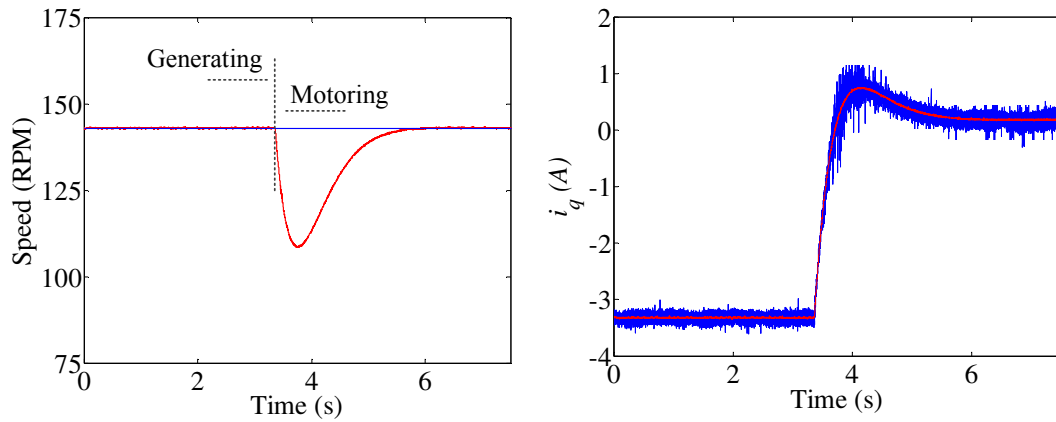


Fig. 7.40. Response of the IPMM with a rapid change from generating to motoring action

Fig. 7.40 shows the speed and current response of the FSCW IPMM-F when the machine is switched from generating action to motoring action. It can be seen that the i_q is negative at -3.25 A when the machine is in generating action. During motoring mode, the i_q current goes positive to 0.15A for a negligible load.

7.11 Conclusion

In this chapter, Field oriented control of the new FSCW IPMM-F was implemented, and the steady-state and dynamic performances of the machine were examined experimentally. For the FSCW IPMM-F, the voltage limited trajectory is not applicable which is due to the centre of the voltage limiting ellipses that lies outside the current limiting circle.

The speed regulation control was performed when the prototype operated in the motoring region. As for the generating region, the DC bus was regulated during MTPA and FW. The experimental results show that the conventional FOC can be effectively applied to the FSCW IPMM-F without any significant modification. As for field-weakening operation, the prototype was not able to reach the maximum theoretical speed. This indicates the possibility of restriction in the existing FOC algorithm during FW of the FSCW IPMM-F. The control strategy to the FSCW IPMM-F fed by a full power back-to-back PWM converter has been also presented in this chapter. The experimental result verifies the vector control algorithm work effectively in the closed loop control system to estimate the generator speed and to control the DC link voltage independently.

CHAPTER 8: Conclusion and Future Works

8.1 Conclusions

This thesis has explored the suitability of fractional-slot CW-IPM machine for low-speed, direct-drive wind turbine applications. A 42-pole, 54-slot FSCW IPMM was developed, constructed and tested. The theoretical and experimental results confirmed that this machine meets the design objectives and will be able to overcome some of the drawbacks of existing direct-drive PM generators. The constructed double-layer FSCW IPMM is compact and offers some saliency that can be exploited to operate the generator without a shaft sensor and also constant power range can be extended close to the cut-out speed of wind conversion system. It displayed an efficiency of over 90% with negligible cogging torque and low torque ripple.

The thesis presents a systematic design comparison between two commonly used rotor geometries of a distributed wound IPMM. Various steps were taken to optimize the magnetic and electric loadings to arrive at the most compact design. The thesis also discusses various steps that were taken to minimize the cogging torque, torque ripple and the overall size of the machine.

After selecting the two most appropriate rotor geometries (Flat-shaped and V-shaped magnet), a study was carried out to check whether a traditional distributed winding (DW) stator or a newly proposed fractional slot concentrated winding (FSCW) stator will be able to satisfy the design goals. First, DW stator with flat-shaped and V-shaped magnet in the rotor were investigated and compared. Results were more favorable toward the rotor with the flat-shaped magnet. A similar study was also carried out with the FSCW stator and again flat-shaped magnet design was found to be

superior. It can be concluded from here that for a machine with large pole numbers, V-shaped magnet design losses out to the flat-shaped magnet design.

A systematic comparison between the FSCW IPMM and the DW IPMM were also carried out which showed that the FSCW IPMM with flat shaped magnets (FSCW IPMM-F) and V-shaped magnets (FSCW IPMM-V) both have lower cogging torque and torque ripple in comparison to the DW IPMM with flat-shaped magnet and can operate with efficiency $>90\%$. However, the winding factor of FSCW IPMM was slightly lower than the DW IPMM leading to a lower power density of the machine. Experimental verifications of the both DW and FSCW IPMSM structures would have been ideal but due to cost constraint, only one machine was considered for prototyping. The FSCW IPMM with flat-shaped magnet was chosen as it was fulfilling the three primary design goals, even though there was a trade-off in the power density. The optimized design was constructed as a 4-kW prototype for experimental verification.

The experimental validation of the steady-state performance was carried out and compared with the FE results. The L-L back EMF of the prototype IPMM displayed sinusoidal waveform with negligible harmonic contents. The experimental peak cogging torque was found to be less than 1% of the rated torque that indicates that the minimization method was successful in reducing the overall cogging torque in the machine. The measured torque ripple of the prototype was found to be 4.8% which was higher than the predicted FE result of 2%. The experimental results of inductance and saliency ratio were also relatively close to that of predicted value from the FEA. Lastly, the experimental efficiency of the FSCW IPMM-F was calculated during the generation which showed the efficiency to vary from 91% ~ 93% depending on the torque of the machine. All these results suggest that all the specific design goals set for the FSCW IPMM-F had been achieved.

The current vector control algorithm of the IPM machine was applied to the prototype FSCW IPMM-F for constant torque region and constant power region. Field oriented control of the new FSCW IPMM-F was implemented, and the dynamic performances of the machine were achieved experimentally. The speed regulation control was performed when the prototype operated in the motoring region. As for the generating region, the DC bus was regulated during MTPA and FW. The field weakening range found in this analysis was less than the range calculated analytically. This chapter also presents the control strategy to the FSCW IPMM-F fed by a full power back-to-back PWM converter with the electrodynamicometer emulating the wind profile. The experimental results showed that the conventional FOC can be applied effectively to the FSCW IPMM-F without any significant modification.

8.2 Future Works

This thesis only focuses on FSCW IPMM with a slot/pole/phase value of 3/7. Some literatures have pointed out other slot/pole/phase values for the FSCW to deliver good performance such as 2/5 or 3/8. Future work may inspect the FSCW with various slot/pole/phase combinations for direct-drive wind applications.

The optimization of torque ripple in a distributed wound IPMM was conducted by adjusting the geometry of the rotor and stator. However, the measured torque ripple was found to be higher than the predicted value. It is difficult to separate the machine generated torque ripple from the ripple due to the mechanical coupling and controllers. Inclusion of these ripple sources in the machine model should be considered while minimizing the torque ripple.

A future study on the power density optimization should be carried out so that more compact design can be achieved. Some work on loss-minimization control (shown in Appendix-A) of the FSCW IPMSM was carried out which indicated conventional minimization algorithm does not provide significant efficiency improvement due to its inability to suppress increasing rotor iron losses due to the MMF harmonics. Further work may be carried out to model the behavior of the rotor iron losses so that it can be incorporated in the loss-minimization algorithm.

The power density of the prototype FSCW IPMM-F can be easily increased by either increasing the rated current or increasing the number of coils in a slot. This is due to the fact that for the prototype, the flux density around the tooth in the stator is way below the saturation point. Some work will be carried out to increase the power density of the prototype by increasing the electrical loading of the machine.

The effect of parameter variation due to saturation on control should also be investigated. Future study should also include the investigation of cross-magnetization and its effect on field-weakening.

Lastly, the prototype FSCW IPMM-F displayed low saliency ratio and limited field weakening range. Even though, wide constant power speed range is not a requirement for the wind turbine application, a higher saliency will be able to provide larger reluctance torque component. Therefore, optimization of the saliency ratio can also be carried out.

Reference

- [1] GWEC, "Global Wind Report- Annual Market Update," Global Wind Energy Council, 2014.
- [2] H. Polinder, F. F. A. van der Pijl, G. J. de Vilder, and P. Tavner, "Comparison of direct-drive and geared generator concepts for wind turbines," in *Electric Machines and Drives, 2005 IEEE International Conference on*, 2005, pp. 543-550.
- [3] F. Wang, Q. Hou, J. Bo, and J. Pan, "Study on control system of low speed PM generator direct driven by wind turbine," in *Electrical Machines and Systems, 2005. ICEMS 2005. Proceedings of the Eighth International Conference on*, 2005, pp. 1009-1012 Vol. 2.
- [4] S. Muller, M. Deicke, and R. W. De Doncker, "Doubly fed induction generator systems for wind turbines," *Industry Applications Magazine, IEEE*, vol. 8, pp. 26-33, 2002.
- [5] D. MR, "Optimized permanent magnet generator topologies for direct-drive wind turbines," PhD dissertation, Delft University Technology, , The Netherlands, 2004.
- [6] E. Muljadi, C. P. Butterfield, and W. Yih-Huie, "Axial-flux modular permanent-magnet generator with a toroidal winding for wind-turbine applications," *Industry Applications, IEEE Transactions on*, vol. 35, pp. 831-836, 1999.
- [7] Y. Xu, D. Patterson, and J. Hudgins, "Permanent magnet generator design and control for large wind turbines," in *Power Electronics and Machines in Wind Applications (PEMWA), 2012 IEEE*, 2012, pp. 1-5.
- [8] H. Li and Z. Chen, "Optimal direct-drive permanent magnet wind generator systems for different rated wind speeds," in *Power Electronics and Applications, 2007 European Conference on*, 2007, pp. 1-10.
- [9] A. Parviainen, "Design of Axial-flux permanent-magnet low-speed machines and performance comparison between Radial-flux and Axial-flux machines," PhD dissertation, Lappeenranta University of Technology, Finland, 2005.
- [10] A. Grauers, "Design of direct-driven permanent-magnet generators for wind turbines," School of Electrical and Computer Engineering, Chalmers University of Technology, 1996.
- [11] M. R. J. Dubois, *Optimized permanent magnet generator topologies for direct-drive wind turbines*: TU Delft, Delft University of Technology, 2004.
- [12] H. Li and Z. Chen, "Overview of different wind generator systems and their comparisons," *Renewable Power Generation, IET*, vol. 2, pp. 123-138, 2008.
- [13] J. H. J. Potgieter and M. J. Kamper, "Modeling and Stability Analysis of a Direct-Drive Direct-Grid Slip–Synchronous Permanent-Magnet Wind Generator," *Industry Applications, IEEE Transactions on*, vol. 50, pp. 1738-1747, 2014.
- [14] E. Ahmed Masmoudi, Z. Zhu, and J. Hu, "Electrical machines and power-electronic systems for high-power wind energy generation applications: Part I-market penetration,

Reference

- current technology and advanced machine systems," *COMPEL-The international journal for computation and mathematics in electrical and electronic engineering*, vol. 32, pp. 7-33, 2012.
- [15] T. Haring, K. Forman, T. Huhtanen, and M. Zawadzki, "Direct drive-opening a new era in many applications," in *Pulp and Paper Industry Technical Conference, 2003. Conference Record of the 2003 Annual*, 2003, pp. 171-179.
- [16] T. Tudorache, L. Melcescu, and M. Popescu, "Methods for cogging torque reduction of directly driven PM wind generators," in *Optimization of Electrical and Electronic Equipment (OPTIM), 2010 12th International Conference on*, 2010, pp. 1161-1166.
- [17] C. Yicheng, P. Pillay, and A. Khan, "PM wind generator topologies," *Industry Applications, IEEE Transactions on*, vol. 41, pp. 1619-1626, 2005.
- [18] H. Polinder, F. F. A. van der Pijl, G. J. de Vilder, and P. J. Tavner, "Comparison of direct-drive and geared generator concepts for wind turbines," *Energy Conversion, IEEE Transactions on*, vol. 21, pp. 725-733, 2006.
- [19] L. Hyung-Woo, P. Chan-Bae, and L. Byung-Song, "Performance comparison of the railway traction IPM motors between concentrated winding and distributed winding," in *Transportation Electrification Conference and Expo (ITEC), 2012 IEEE*, 2012, pp. 1-4.
- [20] J. Sapanen, V. Ruuskanen, J. Nerg, and J. Pyrhonen, "Dynamic Torque Analysis of a Wind Turbine Drive Train Including a Direct-Driven Permanent-Magnet Generator," *Industrial Electronics, IEEE Transactions on*, vol. 58, pp. 3859-3867, 2011.
- [21] M. L. Henriksen and B. B. Jensen, "Comparison of Megawatt-Class Permanent Magnet Wind Turbine Generator Concepts," in *EWEA 2012-European Wind Energy Conference & Exhibition*.
- [22] T. Wakui, Y. Tanzawa, T. Hashizume, and T. Nagao, "Hybrid configuration of Darrieus and Savonius rotors for stand-alone wind turbine-generator systems," *Electrical Engineering in Japan*, vol. 150, pp. 13-22, 2005.
- [23] J. A. V. Alé, M. R. Petry, S. B. Garcia, G. Cirilo, S. Simioni, and G. Konzen, "Performance evaluation of the next generation of small vertical axis wind turbine," *CEP*, vol. 90619, p. 900, 2007.
- [24] M. P. Angell RK, Galbraith RAMcD, "Collected data for tests on a NACA0018 airfoil," G.U. Aero Report 8817,1988.
- [25] A. Solum, P. Deglaire, S. Eriksson, M. Stålberg, M. Leijon, and H. Bernhoff, "Design of a 12kW vertical axis wind turbine equipped with a direct driven PM synchronous generator," in *EWEC 2006-European Wind Energy Conference & Exhibition*, 2006.
- [26] S. Brusca, R. Lanzafame, and M. Messina, "Design of a vertical-axis wind turbine: how the aspect ratio affects the turbine's performance," *International Journal of Energy and Environmental Engineering*, vol. 5, pp. 333-340, 2014.
- [27] J. Y. Chen, C. V. Nayar, and X. Longya, "Design and finite-element analysis of an outer-rotor permanent-magnet generator for directly coupled wind turbines," *Magnetics, IEEE Transactions on*, vol. 36, pp. 3802-3809, 2000.

Reference

- [28] P. Lampola, *Directly driven, low-speed permanent-magnet generators for wind power applications*: Helsinki University of Technology, 2000.
- [29] E. Spooner and A. C. Williamson, "Direct coupled, permanent magnet generators for wind turbine applications," *Electric Power Applications, IEE Proceedings* -, vol. 143, pp. 1-8, 1996.
- [30] A. Ferreira, A. M. Silva, and A. F. Costa, "Prototype of an axial flux permanent magnet generator for wind energy systems applications," in *Power Electronics and Applications, 2007 European Conference on*, 2007, pp. 1-9.
- [31] E. Spooner and A. Williamson, "Direct coupled, permanent magnet generators for wind turbine applications," *IEE Proceedings-Electric Power Applications*, vol. 143, pp. 1-8, 1996.
- [32] A. Parviainen, J. Pyrhonen, and P. Kontkanen, "Axial flux permanent magnet generator with concentrated winding for small wind power applications," in *Electric Machines and Drives, 2005 IEEE International Conference on*, 2005, pp. 1187-1191.
- [33] B. Chalmers and E. Spooner, "An axial-flux permanent-magnet generator for a gearless wind energy system," *Energy Conversion, IEEE Transactions on*, vol. 14, pp. 251-257, 1999.
- [34] D. Bang, Polinder, H & Ferreira, JA, "Review of generator systems for direct-drive wind turbines," in *Proceedings of the 2008 European wind energy conference, EWEC 2008 Brussels*, pp. 1-11.
- [35] N. Bianchi, S. Bolognani, J. Ji-Hoon, and S. Seung-Ki, "Advantages of Inset PM Machines for Zero-Speed Sensorless Position Detection," *Industry Applications, IEEE Transactions on*, vol. 44, pp. 1190-1198, 2008.
- [36] F. Libert and J. Soulard, "Design study of different direct-driven permanent-magnet motors for a low speed application," in *Proceedings of the Nordic Workshop on Power and Industrial Electronics (NORpie), Trondheim, Norway*, 2004.
- [37] M. A. Rahman, "Advances of interior permanent magnet (IPM) wind generators," in *Electrical Machines and Systems, 2008. ICEMS 2008. International Conference on*, 2008, pp. 2228-2233.
- [38] V. B. Honsinger, "The Fields and Parameters of Interior Type AC Permanent Magnet Machines," *Power Apparatus and Systems, IEEE Transactions on*, vol. PAS-101, pp. 867-876, 1982.
- [39] B. J. Chalmers, S. A. Hamed, and G. D. Baines, "Parameters and performance of a high-field permanent-magnet synchronous motor for variable-frequency operation," *Electric Power Applications, IEE Proceedings B*, vol. 132, pp. 117-124, 1985.
- [40] T. M. Jahns, G. B. Kliman, and T. W. Neumann, "Interior Permanent-Magnet Synchronous Motors for Adjustable-Speed Drives," *Industry Applications, IEEE Transactions on*, vol. IA-22, pp. 738-747, 1986.
- [41] R. F. Schiferl and T. A. Lipo, "Power capability of salient pole permanent magnet synchronous motors in variable speed drive applications," *Industry Applications, IEEE Transactions on*, vol. 26, pp. 115-123, 1990.

Reference

- [42] C. R. Steen, "Direct axis aiding permanent magnets for a laminated synchronous motor rotor," ed: Google Patents, 1979.
- [43] M. A. Rahman, T. Little, and G. R. Slemon, "Analytical models for interior-type permanent magnet synchronous motors," *Magnetics, IEEE Transactions on*, vol. 21, pp. 1741-1743, 1985.
- [44] T. M. Jahns, "Flux-Weakening Regime Operation of an Interior Permanent-Magnet Synchronous Motor Drive," *Industry Applications, IEEE Transactions on*, vol. IA-23, pp. 681-689, 1987.
- [45] W. L. Soong and N. Ertugrul, "Field-weakening performance of interior permanent-magnet motors," *Industry Applications, IEEE Transactions on*, vol. 38, pp. 1251-1258, 2002.
- [46] W. L. Soong, D. A. Staton, and T. J. E. Miller, "Design of a new axially-laminated interior permanent magnet motor," *Industry Applications, IEEE Transactions on*, vol. 31, pp. 358-367, 1995.
- [47] Z. Q. Zhu, Y. S. Chen, and D. Howe, "Iron loss in permanent-magnet brushless AC machines under maximum torque per ampere and flux weakening control," *Magnetics, IEEE Transactions on*, vol. 38, pp. 3285-3287, 2002.
- [48] Y. Honda, T. Higaki, S. Morimoto, and Y. Takeda, "Rotor design optimisation of a multi-layer interior permanent-magnet synchronous motor," *Electric Power Applications, IEE Proceedings -*, vol. 145, pp. 119-124, 1998.
- [49] Y. Honda, T. Nakamura, T. Higaki, and Y. Takeda, "Motor design considerations and test results of an interior permanent magnet synchronous motor for electric vehicles," in *Industry Applications Conference, 1997. Thirty-Second IAS Annual Meeting, IAS '97., Conference Record of the 1997 IEEE*, 1997, pp. 75-82 vol.1.
- [50] A. Fratta, A. Vagati, and F. Villata, "On the evolution of AC machines for spindle drive applications," in *Industry Applications Society Annual Meeting, 1989., Conference Record of the 1989 IEEE*, 1989, pp. 699-704 vol.1.
- [51] P. Roshanfekar, T. Thiringer, M. Alatalo, and S. Lundmark, "Performance of two 5 MW permanent magnet wind turbine generators using surface mounted and interior mounted magnets," in *Electrical Machines (ICEM), 2012 XXth International Conference on*, 2012, pp. 1041-1047.
- [52] H. Haraguchi, S. Morimoto, and M. Sanada, "Suitable design of a PMSG for a small-scale wind power generator," in *Electrical Machines and Systems, 2009. ICEMS 2009. International Conference on*, 2009, pp. 1-6.
- [53] H. Haraguchi, S. Morimoto, and M. Sanada, "Suitable design of a PMSG for a large-scale wind power generator," in *Energy Conversion Congress and Exposition, 2009. ECCE 2009. IEEE*, 2009, pp. 2447-2452.
- [54] M. Morandin, E. Fornasiero, S. Bolognani, and N. Bianchi, "Torque/power rating design of an IPM machine for maximum profit-to-cost ratio in wind power generation," in *Electric Machines & Drives Conference (IEMDC), 2011 IEEE International*, 2011, pp. 1113-1118.

Reference

- [55] C. Hong, Q. Ronghai, L. Jian, and Z. Bo, "Comparison of interior and surface permanent magnet machines with fractional slot concentrated windings for direct-drive wind generators," in *Electrical Machines and Systems (ICEMS), 2014 17th International Conference on*, 2014, pp. 2612-2617.
- [56] B. Boazzo, G. Pellegrino, and A. Vagati, "Multipolar SPM Machines for Direct-Drive Application: A General Design Approach," *Industry Applications, IEEE Transactions on*, vol. 50, pp. 327-337, 2014.
- [57] B. C. Mecrow, A. G. Jack, J. A. Haylock, and J. Coles, "Fault-tolerant permanent magnet machine drives," *Electric Power Applications, IEE Proceedings -*, vol. 143, pp. 437-442, 1996.
- [58] J. Cros and P. Viarouge, "Synthesis of high performance PM motors with concentrated windings," in *Electric Machines and Drives, 1999. International Conference IEMD '99*, 1999, pp. 725-727.
- [59] P. Salminen, "Fractional slot permanent magnet synchronous motors for low speed applications," *Acta Universitatis Lappeenrantaensis*, 2004.
- [60] N. Bianchi and M. Dai Pre, "Use of the star of slots in designing fractional-slot single-layer synchronous motors," *Electric Power Applications, IEE Proceedings -*, vol. 153, pp. 459-466, 2006.
- [61] A. M. El-Refaie, T. M. Jahns, and D. W. Novotny, "Analysis of surface permanent magnet machines with fractional-slot concentrated windings," *Energy Conversion, IEEE Transactions on*, vol. 21, pp. 34-43, 2006.
- [62] D. W. Novotny and T. A. Lipo, *Vector control and dynamics of AC drives* vol. 2007: Clarendon Press Oxford, 1996.
- [63] J. Cros and P. Viarouge, "Synthesis of high performance PM motors with concentrated windings," *Energy Conversion, IEEE Transactions on*, vol. 17, pp. 248-253, 2002.
- [64] F. Magnussen and C. Sadarangani, "Winding factors and Joule losses of permanent magnet machines with concentrated windings," in *Electric Machines and Drives Conference, 2003. IEMDC'03. IEEE International*, 2003, pp. 333-339 vol.1.
- [65] K. Reichert, "PM-Motors with concentrated, non overlapping Windings, Some Characteristics," *PS-31, ICEM*, 2004.
- [66] N. Bianchi, S. Bolognani, and G. Grezzani, "Fractional-slot IPM servomotors: analysis and performance comparisons," in *Proceedings of the International Conference on Electrical Machines, Cracow, Poland*, 2004, pp. 1-6.
- [67] A. Di Gerlando, R. Perini, and M. Ubaldini, "High pole number, PM synchronous motor with concentrated coil armature windings," in *Recent Developments of Electrical Drives*, ed: Springer, 2006, pp. 307-320.
- [68] Y. Asano, Y. Honda, H. Murakami, Y. Takeda, and S. Morimoto, "Novel noise improvement technique for a PMSM with concentrated winding," in *Power Conversion Conference, 2002. PCC-Osaka 2002. Proceedings of the*, 2002, pp. 460-465.
- [69] C. Shukang, P. Yulong, C. Feng, and C. Shumei, "The torque pulsation analysis of a starter generator with concentrated windings based hybrid electric vehicles," in *Electric*

Reference

- Machines and Drives Conference, 2003. IEMDC'03. IEEE International, 2003*, pp. 218-221 vol.1.
- [70] M. Nakano, H. Kometani, M. Kawamura, and Y. Ikeda, "Permanent magnet dynamo electric machine, and permanent magnet synchronous generator for wind power generation," ed: Google Patents, 2005.
- [71] B. Wei, X. Wang, and X. Zhao, "Design and research of 5 MW Permanent Magnet Synchronous Generators for wind turbines," in *Electrical Machines and Systems (ICEMS), 2014 17th International Conference on*, 2014, pp. 467-470.
- [72] M. V. Cistelean, M. Popescu, and M. Popescu, "Study of the Number of Slots/Pole Combinations for Low Speed Permanent Magnet Synchronous Generators," in *Electric Machines & Drives Conference, 2007. IEMDC '07. IEEE International, 2007*, pp. 1616-1620.
- [73] L. Chong, "Design of an interior permanent magnet machine with concentrated windings for field weakening applications," University of New South Wales, 2011.
- [74] N. Bianchi, *Electrical machine analysis using finite elements*: CRC press, 2005.
- [75] P. P. Silvester and R. L. Ferrari, *Finite elements for electrical engineers*: Cambridge university press, 1996.
- [76] R. Dutta, "A segmented interior permanent magnet synchronous machine with wide field-weakening range," *School of Electrical Engineering and Telecommunications*, 2007.
- [77] J. Jin, *The finite element method in electromagnetics*: John Wiley & Sons, 2014.
- [78] T. J. Ypma, "Historical development of the Newton-Raphson method," *SIAM review*, vol. 37, pp. 531-551, 1995.
- [79] P. Deuffhard, *Newton methods for nonlinear problems: affine invariance and adaptive algorithms* vol. 35: Springer Science & Business Media, 2011.
- [80] R. Dutta and M. F. Rahman, "Design and Analysis of an Interior Permanent Magnet (IPM) Machine With Very Wide Constant Power Operation Range," *Energy Conversion, IEEE Transactions on*, vol. 23, pp. 25-33, 2008.
- [81] D. Evans, Z. Azar, L. J. Wu, and Z. Q. Zhu, "Comparison of optimal design and performance of PM machines having non-overlapping windings and different rotor topologies," in *Proc. of 5th IET Int. Conf. on Power Electronics, Machines and Drives (PEMD 2010)*, 2010, pp. 1-7.
- [82] Y. Pang, Z. Zhu, and D. Howe, "Analytical determination of optimal split ratio for permanent magnet brushless motors," *IEE Proceedings-Electric Power Applications*, vol. 153, pp. 7-13, 2006.
- [83] J. Pyrhönen, T. Jokinen, and V. Hrabovcová, *Front Matter*: Wiley Online Library, 2008.
- [84] M. S. Islam, R. Islam, and T. Sebastian, "Experimental Verification of Design Techniques of Permanent-Magnet Synchronous Motors for Low-Torque-Ripple Applications," *Industry Applications, IEEE Transactions on*, vol. 47, pp. 88-95, 2011.

Reference

- [85] J. Pyrhonen, T. Jokinen, and V. Hrabovcova, "Main dimensions of rotating machines," in *Design of Rotating Electrical Machines* ed, Lappeenranta University of Technology, 2008, pp. 297-300.
- [86] M. S. Islam, R. Islam, and T. Sebastian, "Experimental verification of design techniques of permanent magnet synchronous motors for low torque ripple applications," in *proc. IEEE Energy Conversion Congress and Exposition (ECCE)*, 2009, pp. 214-219.
- [87] B. Deok-je, H. Polinder, G. Shrestha, and J. A. Ferreira, "Promising Direct-Drive Generator System for Large Wind Turbines," in *Wind Power to the Grid - EPE Wind Energy Chapter 1st Seminar, 2008. EPE-WECS 2008*, 2008, pp. 1-10.
- [88] K. Chang Seop and S. Jin-Soo, "New cogging-torque reduction method for brushless permanent-magnet motors," *Magnetics, IEEE Transactions on*, vol. 39, pp. 3503-3506, 2003.
- [89] Y.-U. P. Ju-Hee Cho, Dae-Kyong Kim, "Study on Reducing Cogging Torque of Interior PM Motor for Agricultural Electric Vehicle," *Journal of International Conference on Electrical Machines and Systems*, vol. 2, pp. 134-140, 2013.
- [90] K. Gyu-Hong and H. Jin, "Analytical prediction and reduction of the cogging torque in interior permanent magnet motor," in *proc. IEEE Int. Conf. Electric Machines and Drives*, San Antonio, TX, 2005, pp. 1620-1624.
- [91] C. Studer, A. Keyhani, T. Sebastian, and S. K. Murthy, "Study of cogging torque in permanent magnet machines," in *Industry Applications Conference, 1997. Thirty-Second IAS Annual Meeting, IAS '97., Conference Record of the 1997 IEEE*, 1997, pp. 42-49 vol.1.
- [92] K. Gyu-Hong, S. Young-Dae, and K. Gyu-Tak, "A Novel Cogging Torque Reduction Method for Interior Type Permanent Magnet Motor," in *Industry Applications Conference, 2007. 42nd IAS Annual Meeting. Conference Record of the 2007 IEEE*, 2007, pp. 119-125.
- [93] K. Gyu-Hong and H. Jin, "Analytical prediction and reduction of the cogging torque in interior permanent magnet motor," in *Electric Machines and Drives, 2005 IEEE International Conference on*, 2005, pp. 1620-1624.
- [94] M. S. Islam, S. Mir, and T. Sebastian, "Issues in reducing the cogging torque of mass-produced permanent magnet brushless DC motor," in *Industry Applications Conference, 2003. 38th IAS Annual Meeting. Conference Record of the*, 2003, pp. 393-400 vol.1.
- [95] R. Islam, I. Husain, A. Fardoun, and K. McLaughlin, "Permanent-Magnet Synchronous Motor Magnet Designs With Skewing for Torque Ripple and Cogging Torque Reduction," *Industry Applications, IEEE Transactions on*, vol. 45, pp. 152-160, 2009.
- [96] S. Huang, M. Aydin, and T. A. Lipo, "Comparison of (non-slotted and slotted) surface mounted PM motors and axial flux motors for submarine ship drives," in *Third Naval Symposium on Electrical Machines, Philadelphia*, 2000.
- [97] Cogent, "SURA M270-35A," ed: Cogent, 2008.
- [98] J. Holtz and L. Springob, "Identification and compensation of torque ripple in high-precision permanent magnet motor drives," *IEEE Trans. Ind. Elec.*, vol. 43, no. 2, pp. 309-320, 1996.

Reference

- [99] L. Alberti, M. Barcaro, and N. Bianchi, "Design of a low torque ripple fractional-slot interior permanent magnet motor," in *proc. IEEE Energy Conversion Congress and Exposition (ECCE)*, Raleigh, NC, 2012, pp. 509-516.
- [100] K. M. Rahman and S. Hiti, "Identification of machine parameters of a synchronous motor," *Industry Applications, IEEE Transactions on*, vol. 41, pp. 557-565, 2005.
- [101] A. Mitcham, G. Antonopoulos, and J. J. A. Cullen, "Favourable slot and pole number combinations for fault-tolerant PM machines," *Electric Power Applications, IEE Proceedings -*, vol. 151, pp. 520-525, 2004.
- [102] A. M. El-Refaie, Z. Q. Zhu, T. M. Jahns, and D. Howe, "Winding Inductances of Fractional Slot Surface-Mounted Permanent Magnet Brushless Machines," in *Industry Applications Society Annual Meeting, 2008. IAS '08. IEEE*, 2008, pp. 1-8.
- [103] A. M. El-Refaie and T. M. Jahns, "Impact of Winding Layer Number and Magnet Type on Synchronous Surface PM Machines Designed for Wide Constant-Power Speed Range Operation," in *Industry Applications Conference, 2006. 41st IAS Annual Meeting. Conference Record of the 2006 IEEE*, 2006, pp. 1486-1493.
- [104] J. Wang, Z. P. Xia, D. Howe, and S. A. Long, "Comparative Study of 3-Phase Permanent Magnet Brushless Machines with Concentrated, Distributed and Modular Windings," in *Power Electronics, Machines and Drives, 2006. The 3rd IET International Conference on*, 2006, pp. 489-493.
- [105] F. Magnussen and H. Lendenmann, "Parasitic effects in PM machines with concentrated windings," in *Industry Applications Conference, 2005. Fourtieth IAS Annual Meeting. Conference Record of the 2005*, 2005, pp. 1044-1049 Vol. 2.
- [106] A. G. Jack, B. C. Mecrow, P. G. Dickinson, D. Stephenson, J. S. Burdett, N. Fawcett, *et al.*, "Permanent-magnet machines with powdered iron cores and prepressed windings," *Industry Applications, IEEE Transactions on*, vol. 36, pp. 1077-1084, 2000.
- [107] H. Akita, Y. Nakahara, N. Miyake, and T. Oikawa, "New core structure and manufacturing method for high efficiency of permanent magnet motors," in *Industry Applications Conference, 2003. 38th IAS Annual Meeting. Conference Record of the*, 2003, pp. 367-372 vol.1.
- [108] N. Bianchi, S. Bolognani, Pre, x, M. D., and G. Grezzani, "Design considerations for fractional-slot winding configurations of synchronous machines," *Industry Applications, IEEE Transactions on*, vol. 42, pp. 997-1006, 2006.
- [109] G. Madescu, M. Biriescu, M. Greconici, and M. Mot, "Low speed PM generator for wind turbines applications," in *Power Electronics and Motion Control Conference (EPE/PEMC), 2012 15th International*, 2012, pp. DS1c.9-1-DS1c.9-4.
- [110] A. M. EL-Refaie, "High Speed Operation of Permanent Magnet Machines," PhD., Electrical and Computer Engineering, UNIVERSITY OF WISCONSIN-MADISON, 2005.
- [111] M. Farshadnia, R. Dutta, J. E. Fletcher, K. Ahsanullah, M. F. Rahman, and H. C. Lovatt, "Analysis of MMF and back-EMF waveforms for fractional-slot concentrated-wound permanent magnet machines," in *Electrical Machines (ICEM), 2014 International Conference on*, 2014, pp. 1976-1982.

Reference

- [112] L. Chong, "Design of an interior permanent magnet machine with concentrated windings for field weakening applications," Ph.D. dissertation, Dept. Elect. Engg, University of new south wales, Sydney,Australia, 2011.
- [113] D. G. Dorrell, M. Popescu, C. Cossar, and D. Ionel, "Unbalanced Magnetic Pull in Fractional-Slot Brushless PM Motors," in *Industry Applications Society Annual Meeting, 2008. IAS '08. IEEE*, 2008, pp. 1-8.
- [114] P. Vijayraghavan and R. Krishnan, "Noise in electric machines: a review," in *Industry Applications Conference, 1998. Thirty-Third IAS Annual Meeting. The 1998 IEEE*, 1998, pp. 251-258 vol.1.
- [115] R. Dutta, L. Chong, and M. F. Rahman, "Design and Experimental Verification of an 18-Slot/14-pole Fractional-Slot Concentrated Winding Interior Permanent Magnet Machine," *Energy Conversion, IEEE Transactions on*, vol. 28, pp. 181-190, 2013.
- [116] P. Ponomarev, P. Lindh, and J. Pyrhonen, "Effect of Slot-and-Pole Combination on the Leakage Inductance and the Performance of Tooth-Coil Permanent-Magnet Synchronous Machines," *Industrial Electronics, IEEE Transactions on*, vol. 60, pp. 4310-4317, 2013.
- [117] N. Bianchi and E. Fornasiero, "Impact of MMF Space Harmonic on Rotor Losses in Fractional-Slot Permanent-Magnet Machines," *Energy Conversion, IEEE Transactions on*, vol. 24, pp. 323-328, 2009.
- [118] K. Sung-Il, B. Ji-Hyung, H. Jung-Pyo, and L. Ki-Chae, "Optimization Technique for Improving Torque Performance of Concentrated Winding Interior PM Synchronous Motor with Wide Speed Range," in *Industry Applications Conference, 2006. 41st IAS Annual Meeting. Conference Record of the 2006 IEEE*, 2006, pp. 1933-1940.
- [119] H. Seok-Hee, T. M. Jahns, and W. L. Soong, "Torque Ripple Reduction in Interior Permanent Magnet Synchronous Machines Using the Principle of Mutual Harmonics Exclusion," in *Industry Applications Conference, 2007. 42nd IAS Annual Meeting. Conference Record of the 2007 IEEE*, 2007, pp. 558-565.
- [120] H. Seok-Hee, T. M. Jahns, W. L. Soong, M. K. Guven, and M. S. Illindala, "Torque Ripple Reduction in Interior Permanent Magnet Synchronous Machines Using Stators With Odd Number of Slots Per Pole Pair," *Energy Conversion, IEEE Transactions on*, vol. 25, pp. 118-127, 2010.
- [121] A. Vagati, M. Pastorelli, G. Francheschini, and S. C. Petrache, "Design of low-torque-ripple synchronous reluctance motors," *Industry Applications, IEEE Transactions on*, vol. 34, pp. 758-765, 1998.
- [122] Z. Peng, G. Y. Sizov, and N. A. O. Demerdash, "Comparison of torque ripple minimization control techniques in Surface-Mounted Permanent Magnet Synchronous Machines," in *Electric Machines & Drives Conference (IEMDC), 2011 IEEE International*, 2011, pp. 188-193.
- [123] R. Dutta, M. F. Rahman, and L. Chong, "Winding Inductances of an Interior Permanent Magnet (IPM) Machine With Fractional Slot Concentrated Winding," *Magnetics, IEEE Transactions on*, vol. 48, pp. 4842-4849, 2012.

Reference

- [124] T. D. Strous, H. Polinder, and J. A. Ferreira, "Inductance calculations for PM machines with concentrated windings," in *Electric Machines & Drives Conference (IEMDC), 2011 IEEE International*, 2011, pp. 447-452.
- [125] K. Ahsanullah, R. Dutta, and M. F. Rahman, "Preliminary Design Analysis of Low Speed Interior Permanent Magnet Machine with Distributed and Concentrated Windings," *Journal of International Conference on Electrical Machines and Systems*, vol. 2, pp. 139-147, 2014.
- [126] J. F. Gieras, *Permanent magnet motor technology: design and applications*: CRC press, 2002.
- [127] D. Martinez, "Design of a Permanent-Magnet Synchronous Machine with Non-Overlapping Concentrated Windings for the Shell Eco Marathon Urban Prototype," 2012.
- [128] T. H. Glisson, *Introduction to circuit analysis and design*: Springer Science & Business Media, 2011.
- [129] J. Pyrhönen, T. Jokinen, and V. Hrabovcová, *Front Matter*, in *Design of Rotating Electrical Machines*: Wiley Online Library, 2008.
- [130] F. Meier, "Permanent-magnet synchronous machines with non-overlapping concentrated windings for low-speed direct-drive applications," 2008.
- [131] H. Akita, Y. Nakahara, N. Miyake, and T. Oikawa, "A new core," *Industry Applications Magazine, IEEE*, vol. 11, pp. 38-43, 2005.
- [132] J. Jae-Woo, L. Byeong-Hwa, K. Do-Jin, H. Jung-Pyo, K. Jae-Young, J. Seong-Min, *et al.*, "Mechanical Stress Reduction of Rotor Core of Interior Permanent Magnet Synchronous Motor," *Magnetics, IEEE Transactions on*, vol. 48, pp. 911-914, 2012.
- [133] H. Kyung-Ho, H. Jung-Pyo, K. Gyu-Tak, C. Young-Hyu, and C. Won-Jee, "Mechanical vibration and stress analysis of the link of interior permanent magnet type synchronous motor," in *Electric Machines and Drives, 1999. International Conference IEMD '99*, 1999, pp. 150-152.
- [134] E. Ladufjäll, "Utvärdering av en Magnetic Harmonic Traction Drive," 2008.
- [135] B. Riemer, M. Leßmann, and K. Hameyer, "Rotor design of a high-speed Permanent Magnet Synchronous Machine rating 100,000 rpm at 10kW," in *Energy Conversion Congress and Exposition (ECCE), 2010 IEEE*, 2010, pp. 3978-3985.
- [136] A. Emadi, *Energy-Efficient Electric Motors, Revised and Expanded*: CRC Press, 2004.
- [137] R. Wrobel, G. Vainel, C. Copeland, T. Duda, D. Staton, and P. Mellor, "Investigation of Mechanical Loss Components and Heat Transfer in an Axial-Flux PM Machine," *Industry Applications, IEEE Transactions on*, vol. PP, pp. 1-1, 2015.
- [138] G. K. Batchelor, *An introduction to fluid dynamics*: Cambridge university press, 2000.
- [139] K. Akatsu, K. Narita, Y. Sakashita, and T. Yamada, "Characteristics comparison between SPMSM and IPMSM under high flux density condition by both experimental and analysis results," in *Electrical Machines and Systems, 2008. ICEMS 2008. International Conference on*, 2008, pp. 2848-2853.

Reference

- [140] K. Atallah, D. Howe, P. H. Mellor, and D. A. Stone, "Rotor loss in permanent-magnet brushless AC machines," *Industry Applications, IEEE Transactions on*, vol. 36, pp. 1612-1618, 2000.
- [141] Z. J. Liu and J. T. Li, "Analytical Solution of Air-Gap Field in Permanent-Magnet Motors Taking Into Account the Effect of Pole Transition Over Slots," *Magnetics, IEEE Transactions on*, vol. 43, pp. 3872-3883, 2007.
- [142] H. Jussila, P. Salminen, A. Parviainen, J. Nerg, and J. Pyrhonen, "Concentrated winding axial flux permanent magnet motor with plastic bonded magnets and sintered segmented magnets," in *Electrical Machines, 2008. ICEM 2008. 18th International Conference on*, 2008, pp. 1-5.
- [143] P. Campbell, *Permanent magnet materials and their application*: Cambridge University Press, 1996.
- [144] H. Toda, X. Zhenping, W. Jiabin, K. Atallah, and D. Howe, "Rotor eddy-current loss in permanent magnet brushless machines," *Magnetics, IEEE Transactions on*, vol. 40, pp. 2104-2106, 2004.
- [145] K. Yamazaki and S. Watari, "Loss analysis of permanent-magnet motor considering carrier harmonics of PWM inverter using combination of 2-D and 3-D finite-element method," *Magnetics, IEEE Transactions on*, vol. 41, pp. 1980-1983, 2005.
- [146] K. Yamazaki and A. Abe, "Loss Investigation of Interior Permanent-Magnet Motors Considering Carrier Harmonics and Magnet Eddy Currents," *Industry Applications, IEEE Transactions on*, vol. 45, pp. 659-665, 2009.
- [147] K. Yamazaki, M. Shina, Y. Kanou, M. Miwa, and J. Hagiwara, "Effect of Eddy Current Loss Reduction by Segmentation of Magnets in Synchronous Motors: Difference Between Interior and Surface Types," *Magnetics, IEEE Transactions on*, vol. 45, pp. 4756-4759, 2009.
- [148] N. Takahashi, H. Shinagawa, D. Miyagi, Y. Doi, and K. Miyata, "Factors affecting eddy current losses of segmented Nd-Fe-B sintered magnets without insulation in large PM motors," in *Electric Machines and Drives Conference, 2009. IEMDC '09. IEEE International*, 2009, pp. 24-29.
- [149] A. M. El-Refaei, *High speed operation of permanent magnet machines*, 2005.
- [150] A. Fukuma, S. Kanazawa, D. Miyagi, and N. Takahashi, "Investigation of AC loss of permanent magnet of SPM motor considering hysteresis and eddy-current losses," *Magnetics, IEEE Transactions on*, vol. 41, pp. 1964-1967, 2005.
- [151] CEDRAT. (2006). *"Flux 10.4 User Guide Vol. 1 - Physical Applications (Magnetic, Electric Thermal)"*.
- [152] S. Kanazawa, N. Takahashi, and T. Kubo, "Measurement and analysis of AC loss of NdFeB sintered magnet," *Electrical Engineering in Japan*, vol. 154, pp. 8-15, 2006.
- [153] C. Huynh, L. Zheng, and D. Acharya, "Losses in high speed permanent magnet machines used in microturbine applications," *Journal of engineering for gas turbines and power*, vol. 131, p. 022301, 2009.

Reference

- [154] Z. Q. Zhu, L. J. Wu, and M. L. Mohd Jamil, "Distortion of Back-EMF and Torque of PM Brushless Machines Due to Eccentricity," *Magnetics, IEEE Transactions on*, vol. 49, pp. 4927-4936, 2013.
- [155] A. Burakov and A. Arkkio, "Comparison of the Unbalanced Magnetic Pull Mitigation by the Parallel Paths in the Stator and Rotor Windings," *Magnetics, IEEE Transactions on*, vol. 43, pp. 4083-4088, 2007.
- [156] H. A. Toliyat and G. B. Kliman, *Handbook of electric motors* vol. 120: CRC press, 2004.
- [157] Z. Q. Zhu, "A simple method for measuring cogging torque in permanent magnet machines," in *Power & Energy Society General Meeting, 2009. PES '09. IEEE*, 2009, pp. 1-4.
- [158] G. Heins, *Control methods for smooth operation of permanent magnet synchronous AC motors*: Charles Darwin University, 2008.
- [159] P. Poels, "Cogging torque measurement, moment of inertia determination and sensitivity analysis of an axial flux permanent magnet ac motor," Technical Report DCT 2007.147, Technische Universiteit Eindhoven 2007.
- [160] Z. Q. Zhu, J. T. Chen, L. J. Wu, and D. Howe, "Influence of Stator Asymmetry on Cogging Torque of Permanent Magnet Brushless Machines," *Magnetics, IEEE Transactions on*, vol. 44, pp. 3851-3854, 2008.
- [161] M. S. Islam, S. Mir, T. Sebastian, and S. Underwood, "Design considerations of sinusoidally excited permanent-magnet Machines for low-torque-ripple applications," *Industry Applications, IEEE Transactions on*, vol. 41, pp. 955-962, 2005.
- [162] C. Shaotang, C. Namuduri, and S. Mir, "Controller induced parasitic torque ripples in a PM synchronous motor," in *Industry Applications Conference, 2000. Conference Record of the 2000 IEEE*, 2000, pp. 171-178 vol.1.
- [163] A. Emadi, *Advanced Electric Drive Vehicles*: CRC Press, 2015.
- [164] "IEEE Guide for Test Procedures for Synchronous Machines Part I Acceptance and Performance Testing Part II Test Procedures and Parameter Determination for Dynamic Analysis," *IEEE Std 115-2009 (Revision of IEEE Std 115-1995)*, pp. 1-219, 2010.
- [165] L. Zhong, M. F. Rahman, W. Y. Hu, and K. W. Lim, "Analysis of direct torque control in permanent magnet synchronous motor drives," *Power Electronics, IEEE Transactions on*, vol. 12, pp. 528-536, 1997.
- [166] B. K. Bose, "Power electronics and motor drives recent progress and perspective," *Industrial Electronics, IEEE Transactions on*, vol. 56, pp. 581-588, 2009.
- [167] S. Morimoto, Y. Takeda, and T. Hirasa, "Current phase control methods for permanent magnet synchronous motors," *Power Electronics, IEEE Transactions on*, vol. 5, pp. 133-139, 1990.
- [168] S. Morimoto, M. Sanada, and Y. Takeda, "Wide-speed operation of interior permanent magnet synchronous motors with high-performance current regulator," *Industry Applications, IEEE Transactions on*, vol. 30, pp. 920-926, 1994.

Reference

- [169] S. Morimoto, Y. Takeda, T. Hirasa, and K. Taniguchi, "Expansion of operating limits for permanent magnet motor by current vector control considering inverter capacity," *Industry Applications, IEEE Transactions on*, vol. 26, pp. 866-871, 1990.
- [170] N. Bianchi and T. M. Jahns, *Design, Analysis, and Control of Interior PM Synchronous Machines: Tutorial Course Notes; Seattle, Oct. 5, 2004*: Cleup, 2004.
- [171] L. Shuhui, T. A. Haskew, R. P. Swatloski, and W. Gathings, "Optimal and Direct-Current Vector Control of Direct-Driven PMSG Wind Turbines," *Power Electronics, IEEE Transactions on*, vol. 27, pp. 2325-2337, 2012.
- [172] S. Jöckel, A. Herrmann, and J. Rinck, "High energy production plus built-in reliability—the new Vensys 70/77 gearless wind turbines in the 1.5 MW class," in *European Wind Energy Conference and Exhibition, EWEC*, 2006.
- [173] G. Michalke, A. D. Hansen, and T. Hartkopf, "Control strategy of a variable speed wind turbine with multipole permanent magnet synchronous generator," in *2007 European Wind Energy Conference and Exhibition*, 2007.
- [174] A. Grauers, "Efficiency of three wind energy generator systems," *Energy Conversion, IEEE Transactions on*, vol. 11, pp. 650-657, 1996.
- [175] K. Tan and S. Islam, "Optimum control strategies in energy conversion of PMSG wind turbine system without mechanical sensors," *Energy Conversion, IEEE Transactions on*, vol. 19, pp. 392-399, 2004.
- [176] F. Valenciaga and P. F. Puleston, "High-Order Sliding Control for a Wind Energy Conversion System Based on a Permanent Magnet Synchronous Generator," *Energy Conversion, IEEE Transactions on*, vol. 23, pp. 860-867, 2008.
- [177] E. Koutroulis and K. Kalaitzakis, "Design of a maximum power tracking system for wind-energy-conversion applications," *Industrial Electronics, IEEE Transactions on*, vol. 53, pp. 486-494, 2006.
- [178] S. Raza Kazmi, H. Goto, H.-J. Guo, and O. Ichinokura, "A novel algorithm for fast and efficient speed-sensorless maximum power point tracking in wind energy conversion systems," *Industrial Electronics, IEEE Transactions on*, vol. 58, pp. 29-36, 2011.
- [179] R. Datta and V. Ranganathan, "A method of tracking the peak power points for a variable speed wind energy conversion system," *Energy conversion, iee transactions on*, vol. 18, pp. 163-168, 2003.
- [180] S. Morimoto, Y. Tong, Y. Takeda, and T. Hirasa, "Loss minimization control of permanent magnet synchronous motor drives," *Industrial Electronics, IEEE Transactions on*, vol. 41, pp. 511-517, 1994.
- [181] F. Fernandez-Bernal, A. Garcia-Cerrada, and R. Faure, "Determination of parameters in interior permanent-magnet synchronous motors with iron losses without torque measurement," *Industry Applications, IEEE Transactions on*, vol. 37, pp. 1265-1272, 2001.
- [182] I. Lar and M. Radulescu, "Equivalent core-loss resistance identification for interior permanent-magnet synchronous machines," in *Electrical Machines (ICEM), 2012 XXth International Conference on*, 2012, pp. 1667-1671.

Reference

- [183] J. G. Ziegler and N. B. Nichols, "Optimum settings for automatic controllers," *trans. ASME*, vol. 64, 1942.
- [184] K. J. Aström and T. Hägglund, "PID controllers: theory, design and tuning," 1995.
- [185] J. Espina, A. Arias, J. Balcells, and C. Ortega, "Speed Anti-Windup PI strategies review for Field Oriented Control of Permanent Magnet Synchronous Machines," in *Compatibility and Power Electronics, 2009. CPE '09.*, 2009, pp. 279-285.
- [186] D. O. Neacsu, "Space vector modulation-an introduction," in *The 27th annual conference of the IEEE industrial electronics society*, 2001, pp. 1583-1592.
- [187] C. Kral, A. Haumer, and L. Sang Bin, "A Practical Thermal Model for the Estimation of Permanent Magnet and Stator Winding Temperatures," *Power Electronics, IEEE Transactions on*, vol. 29, pp. 455-464, 2014.

Appendix A: Loss Minimization Control and Modelling in MATLAB-SIMULINK

A.1 Loss minimization

The iron loss is a function of flux density squared. So by applying d -axis armature reaction, the air gap flux in the machine can be reduced which in turns will reduce the iron loss thus minimizing the total losses of the machine [40, 44].

Previously the iron loss was not considered in the equivalent circuit for IPMM. Considering the iron loss, the IPMM model is represented by an equivalent circuit shown in Fig.A. 1, where R_c represents the equivalent iron loss resistance. The voltage equation of an IPMM can be expressed as [180],

$$\begin{bmatrix} v_d \\ v_q \end{bmatrix} = R_a \begin{bmatrix} i_{od} \\ i_{oq} \end{bmatrix} + \left(1 + \frac{R_a}{R_c}\right) \begin{bmatrix} v_{od} \\ v_{oq} \end{bmatrix} \quad (\text{A.24})$$

$$\begin{bmatrix} v_{od} \\ v_{oq} \end{bmatrix} = \begin{bmatrix} 0 & -\omega_e L_q \\ \omega_e L_d & 0 \end{bmatrix} \begin{bmatrix} i_{od} \\ i_{oq} \end{bmatrix} + \begin{bmatrix} 0 \\ \omega_e \Psi_{pm} \end{bmatrix} \quad (\text{A.25})$$

where, $i_{od} = i_d - i_{cd}$, $i_{oq} = i_q - i_{cq}$

$$i_{cd} = \frac{\omega_e L_q i_{oq}}{R_c} \text{ and } i_{cq} = \frac{\omega_e (\Psi_{pm} + L_d i_{od})}{R_c}$$

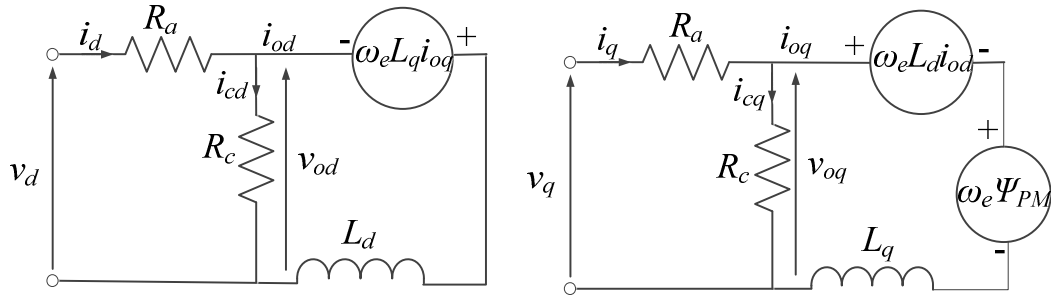


Fig.A. 1. Equivalent circuit of the IPMM taking into account the iron loss resistance

Taking R_c into consideration, the torque equation is expressed as,

$$T_{out} = \frac{3}{2} P_p \left[\Psi_{pm} i_{oq} + (L_d - L_q) i_{od} i_{oq} \right] \quad (A.26)$$

From the figure, the copper loss and the iron loss are shown as,

$$P_{cu} = \frac{3}{2} (i_d^2 + i_q^2) \quad (A.27)$$

$$= \frac{3}{2} R_a \left\{ \left(i_{od} - \frac{\omega_e L_q i_{oq}}{R_c} \right)^2 + \left(i_{oq} + \frac{\omega_e (\Psi_{pm} + L_d i_{od})}{R_c} \right)^2 \right\} \quad (A.28)$$

$$\text{and } P_{iron} = \frac{3}{2} (i_{cd}^2 + i_{cq}^2) \quad (A.29)$$

$$= \frac{3}{2} \left(\frac{(\omega_e^2 L_q i_{oq})^2}{R_c} + \frac{\omega_e^2 (\Psi_{pm} + L_d i_{od})^2}{R_c} \right) \quad (A.30)$$

A.2 Core loss resistance:

The parallel connected core loss resistance can be expressed as

$$R_c = \frac{V_{oc}^2}{P_{iron}} \quad (A.31)$$

where, V_{oc} = no-load induced voltage.

The approximation of the equivalent core loss resistance R_c is very crucial in the loss minimization algorithm. For the prototype, two different methods are used to determine R_c . The first method to measure the core loss resistance is executed at no load condition, where R_c is given as [181],

$$R_c = \frac{v^2 - \omega_e^2 (\Psi_{pm}^2 + (L_d - L_q) i_q^2)}{P_{in} - \omega_e \Psi_{pm} i_q - i_q^2 R_a} \quad (A.32)$$

where, $v^2 = v_d^2 + v_q^2$ and $P_{in} = v_q i_q$;

For no-load condition, i_q is small which makes the saliency term in the numerator negligible. Solving the above equation gives the value R_c to be 1800 Ω at rated speed and 777 Ω at half the rated speed. For further assurance on the approximation of R_c , another method have been applied based on [182] for IPMM. This new estimation method can be implemented on both no-load and loading conditions and is expressed with a fourth order polynomial equation given as,

$$k_1 R_c^4 + k_2 R_c^3 + k_3 R_c^2 + k_4 R_c + k_5 = 0 \quad (\text{A.33})$$

where,

$$k_1 = 3 p_p i_q \left(\Psi_{pm} + (L_d - L_q) i_d \right) - 2 T_{out}$$

$$k_2 = 3 p_p \left[\omega_e L_q (L_d - L_q) i_q^2 - (L_d i_d - \Psi_{pm}) \cdot (\Psi_{pm} + \omega_e i_d (L_d - L_q)) \right]$$

$$k_3 = 3 p_p L_q \omega_e^2 \left[L_d i_q \Psi_{pm} - (L_d - L_q) i_q (L_d i_d - \Psi_{pm}) \right] - 4 T_{out} \omega_e^2 L_d i_q$$

$$k_4 = 3 p_p L_q \omega_e^2 \Psi_{pm} (L_d i_d - \Psi_{pm}) \left[\omega_e (L_d - L_q) - L_d \right]$$

$$\text{and } k_5 = -2 T_{out} \omega_e^4 L_q^2 L_d^2$$

This fourth order equation has two complex solutions and real solutions, one negative and the other positive. For no-load the equation becomes a third-order polynomial. Solving these equations also provides a core loss resistance close to 1800 Ω for no-load and full load condition.

A.3 Control algorithm for LM

Both the iron loss and the copper loss are dependent on i_{od} and i_{oq} . These two losses make up the total electrical loss of the IPMM. The mechanical loss is not controllable by means of current vector control. However, by means of current vector

control, efficiency can be increased by reducing the electrical loss of the machine. The procedure for loss minimization is very similar to MTPA control of the machine. The variable i_{oq} can be cancelled by substituting Eq.(A.26) into Eq.(A.28) and Eq.(A.30). This makes the electrical loss dependent on only i_{od} at rated speed and rated torque. Fig.A. 2 shows the variation in electrical losses with varying i_{od} from -10 A to 10 A for the prototype IPMM simulated in Matlab.

The minimum P_e is found to be 276 watts when i_d is -1.94 A and i_q is at 8.8 A. Using Fig.A. 2, the value for a minimum value of i_d and i_q can be found for different loading conditions [180]. Fig.A. 3 plots the value of i_q versus i_d for various torque conditions. The quadratic curve fitting of these points in Fig.A. 3 gives us a relationship between i_d and i_q , which can be modelled as

$$i_d = Ai_q^2 + Bi_q + C \quad (\text{A.34})$$

where, A , B and C are constant values if the speed is constant. For the prototype, these values are

$$A=-0.0135;$$

$$B=0.011;$$

$$C=-0.8954;$$

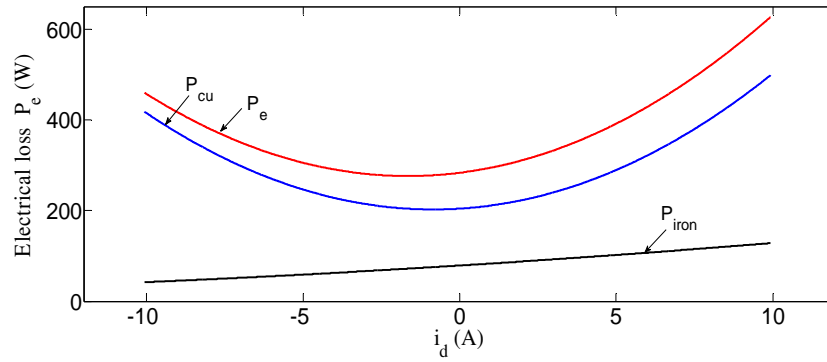


Fig.A. 2. Electrical losses with varying i_{od} under different loading conditions for the prototype IPMM

The loss minimization algorithm works in the same way as maximum torque per Ampere algorithm except for the fact that the i_d reference is selected using Eq.(A.34). The maximum values for i_d and i_q are still governed by the current limiting circle shown in MTPA section. This makes the maximum values as

$$i_{d_max} = -2.03;$$

$$i_{q_max} = 8.99;$$

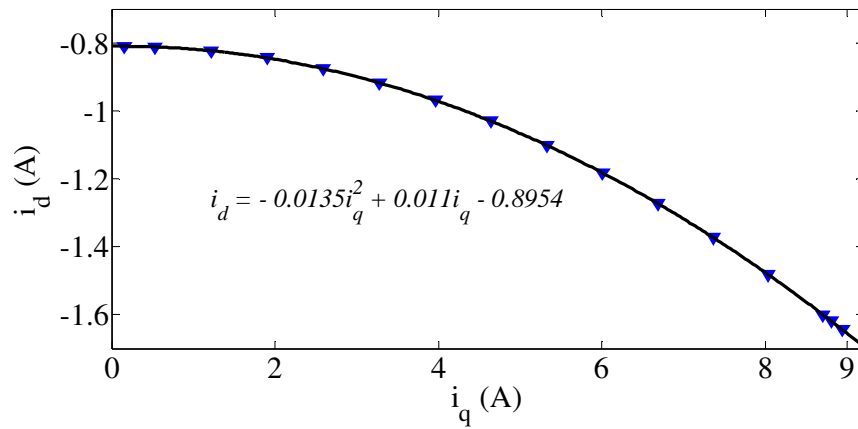


Fig.A. 3. i_q versus i_d for different torque conditions during LM control

A.4 Loss minimization control during motoring condition:

The loss minimization control is similar to that of MTPA control. The only difference is based on the i_d reference signal. The LM trajectory for the prototype CW IPMM during motoring operation is shown in Fig.A. 4 indicates that the experimental i_d and i_q points gathered for different torque values follows the LM trajectory derived analytically using the machine lumped parameters as shown in section A.3. At rated speed with a full load, the values of i_d and i_q are found to be -2.03A and 8.99A respectively. Fig.A. 5 compares the efficiency calculation while applying LM algorithm as compared to normal speed control FOC having $i_d=0$. It can be seen from Fig.A. 5 that the loss minimization control scheme did not improve the efficiency and were similar to the efficiency found when i_d is 0. This is because as the prototype CW IPMM has very little saliency, the demagnetizing effects due to the d-axis armature reaction is very small. Thus, the core loss does not reduce significantly when applying the loss minimization control. Also the cu. loss is the dominant part of losses in the prototype CW IPMM at high speed which is same for both conditions. For these reasons, the efficiency is always 92% at full load for rated speed and is not much influenced by i_d current.

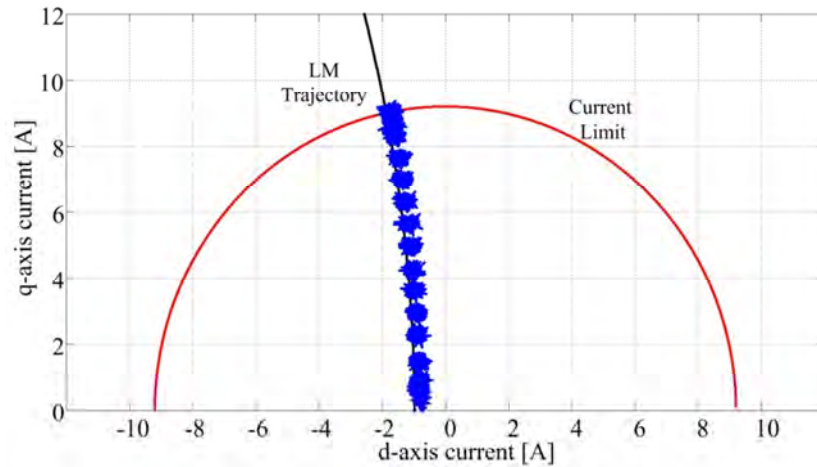


Fig.A. 4. LM trajectory achieved experimentally (Blue points) with current trajectory

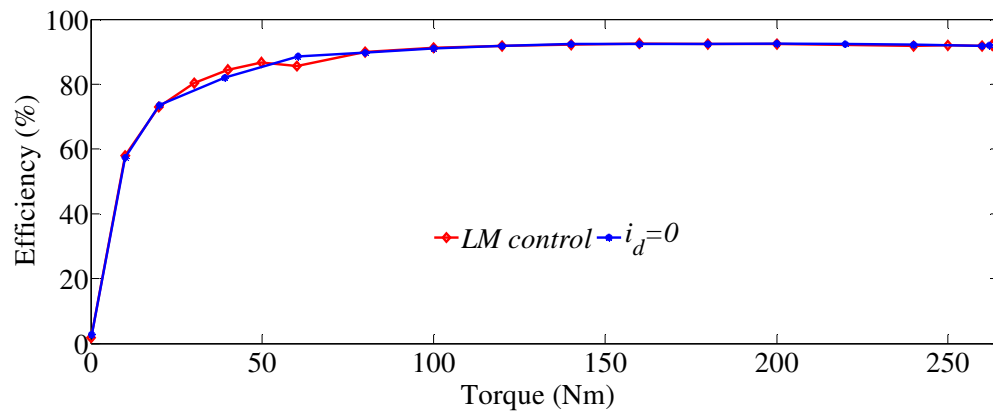


Fig.A. 5. Efficiency calculation of the FSCW IPMM-F during LM operation and when $i_d=0$

A.5 Modelling in Matlab-Simulink for various control strategies:

All control strategies implemented in chapter 7 were first implemented in Matlab-Simulink for the FSCW IPMM-F. The prototype CW IPMM is modelled in Matlab-Simulink with the use of Permanent Magnet Synchronous machine block located in the Simulink library. The tuning of the current, speed and DC link voltage PI controllers are done using the root locus method for FOC of a Permanent Magnet Synchronous Machines. Empirical Ziegler-Nichols PI tuning formula [183] was used to observe the effect in oscillation as compared to the root locus tuning for PI controllers. In order to avoid the unwanted Windup phenomenon [184], an Anti-Windup (AW) strategy is applied to all PI controllers in the Simulink blocks [185]. This lets the

maximum integrator output in the PI controllers to be kept within limits and thus prevents it from un-stabilizing the overall system. Space vector PWM (SPWM) scheme was used for the voltage source inverter as it has some advantages over sinusoidal PWM scheme [186]. Fig.A. 6 shows the MTPA operation in generating mode for the prototype CW IPMM implemented in Matlab-Simulink for rated speed. Fig.A. 7 displays the change in $i_d - i_q$ current with respect to the developed torque during MTPA condition.

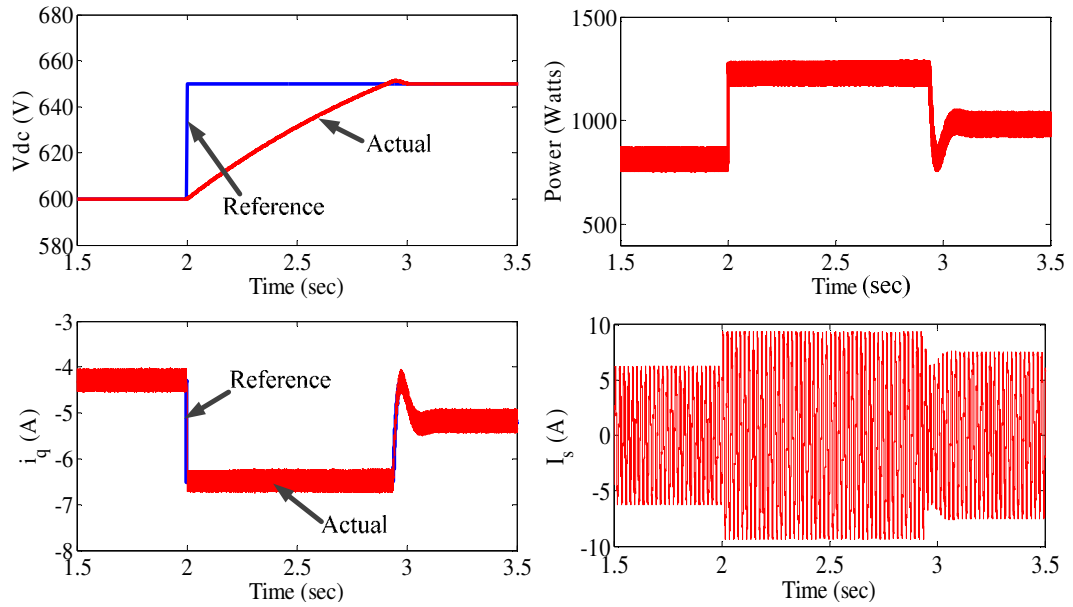


Fig.A. 6. MTPA operation in generating mode for CW IPMM implemented in MATLAB-Simulink

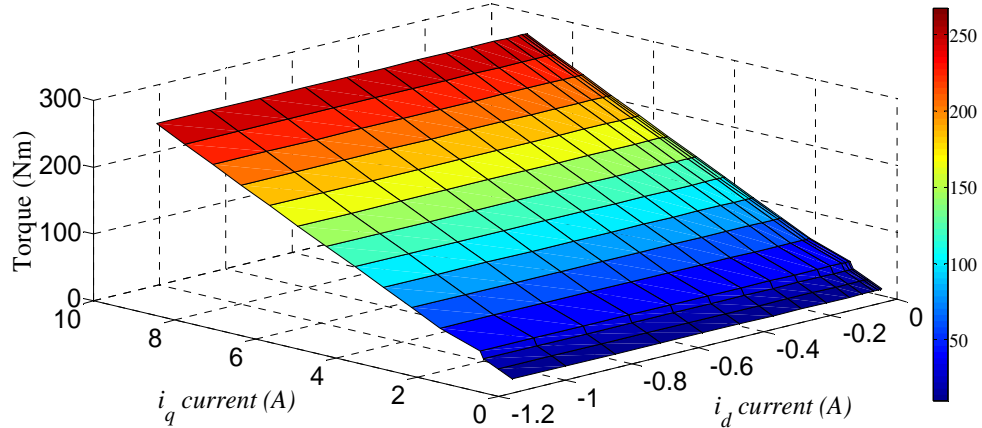


Fig.A. 7. Variation in $i_d - i_q$ current with respect to the developed torque during MTPA condition

Appendix B: Construction Process of the 42 pole FSCW IPMM-F

B.1 Construction Process

The total manufacturing process in prototyping the FSCW IPMM-F took approximately ten months. The construction of the prototype was conducted in CSIRO's lab. It took two months for the design to be approved for construction as there were issues related to manufacturing. Step by step construction process of the CW FS IPMM is shown in Fig.B. 1.

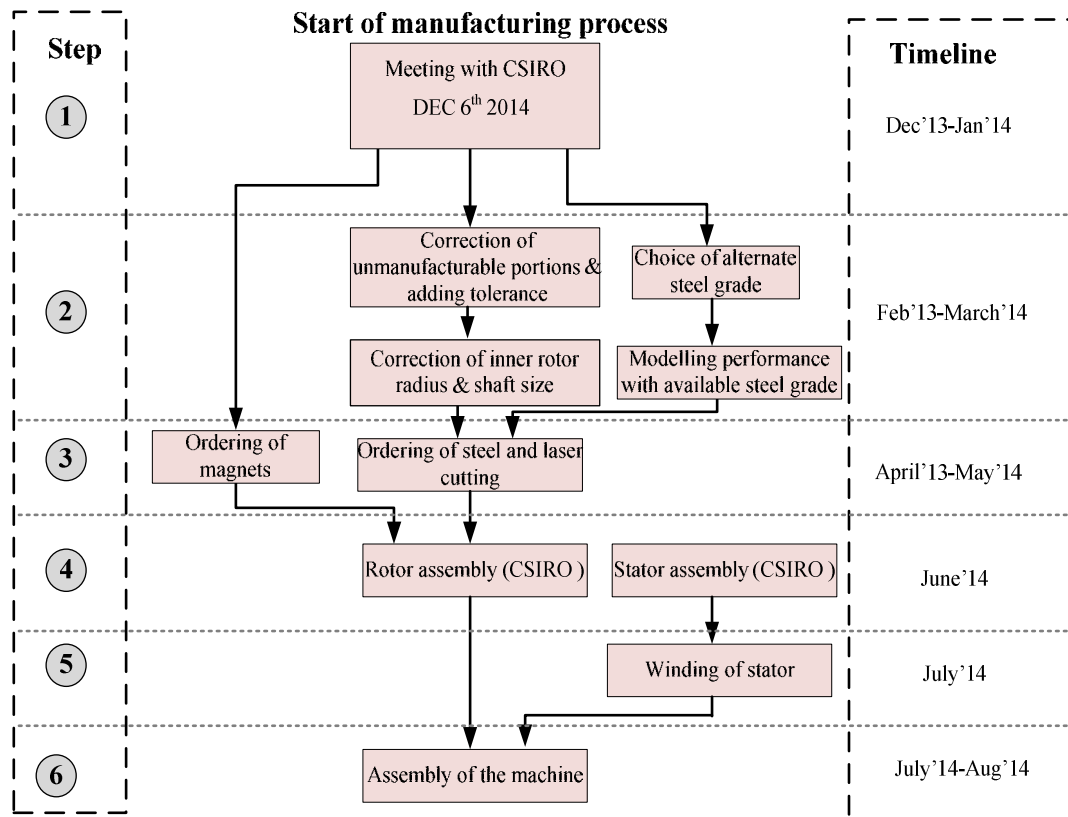


Fig.B. 1. Steps of Construction process

Each of these steps are described in details in this section.

- Step 1: The first step was to meet the manufacturer and provide them with all the machine design files. This took a couple of meetings to let all the requirements be known to the manufacturer. All the FE geometry were converted to CAD data as well is in *.igs* format and provided to the manufacturer.
- Step 2: Ordering of the core material was done after some initial meetings. The primary chosen material was not available during the time of manufacturing. Some simulations were conducted to obtain a material that had a high efficiency and also available in the local market. This topic has already been discussed in chapter 5. The chosen core material was ordered from ‘Sankey’.

After providing the manufacturer with the initial CAD design of the machine, some corrections were done to the design in order to overcome un-manufacturable portions in the design. Tolerance across the magnets was given to the design that changed the overall output of the machine compiled in FE. According to the manufacturer, there should be at least 0.2mm tolerance across each magnet.

Table.B 1 shows the effect of tolerance across the magnets on the torque, torque ripple and the total developed power of the machine. The final tolerance was chosen to be 0.26 mm across each magnet in order to keep the rated power above 4 KW.

Table.B 1 Variation in torque and power with the change in the tolerance across each magnet

	Torque (Nm)	Torque ripple	Power (W)
Without any tolerance	290	1.5%	4366
0.4 mm tolerance	265	1.4%	3966
0.3 mm tolerance	271	3%	4068
0.26 mm tolerance	274	1.7%	4108

The rotor outer diameter is 620mm and the magnets in the rotor are buried only 2mm away from the air-gap. This suggests that there is a large area of unused rotor core where the flux is absent thus it has no use. So in order to reduce the weight of the overall rotor, spokes were built. Fig.B. 2 shows the final rotor configuration of the FSCW IPMM-F indicating the spokes in the rotor core.

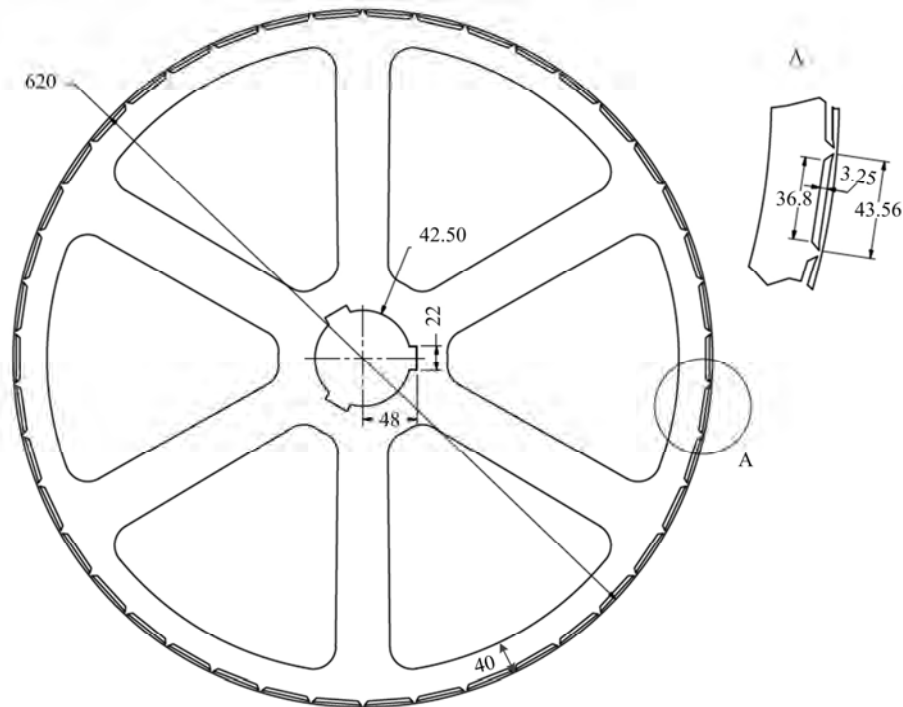


Fig.B. 2. Final rotor configuration

- Step 3: The magnets were ordered from China (RareEarthMagnet Ltd.). The steel and laser cutting was done by the manufacturer that provided the core material. A lamination of iron was taken to the lab and tested for errors and found none. Fig.B. 3 shows the laser cut rotor and stator laminations that were tested in the lab for measurement errors.

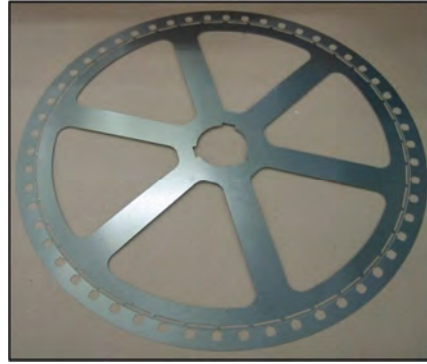


Fig.B. 3. Laser cut rotor and stator laminations

- Step 4: The rotor laminations were assembled with the magnets and the shaft. As for the stator, it was stacked together and sent to the winder for winding according to fractional slot concentrated winding arrangement shown in chapter 5. Fig.B. 4 shows the stacking of laminations to form the rotor core.



Fig.B. 4. Stacking of all rotor laminations

- Step 5: The winding of the stator has been done manually to achieve a high slot-fill factor in the slots. The layout of the search coils has been shown in Appendix C. After the winding of all the phases in the slots had been complete, the windings were varnished using ULTIMEG 2000/380 alkyd phenolic to keep excellent electrical and bond strength of the copper wires. The operating temperature can go up to 180° C for this kind of the Class H varnish. Fig.B. 6 shows the complete winding of the stator for the FSCW IPMM-F.

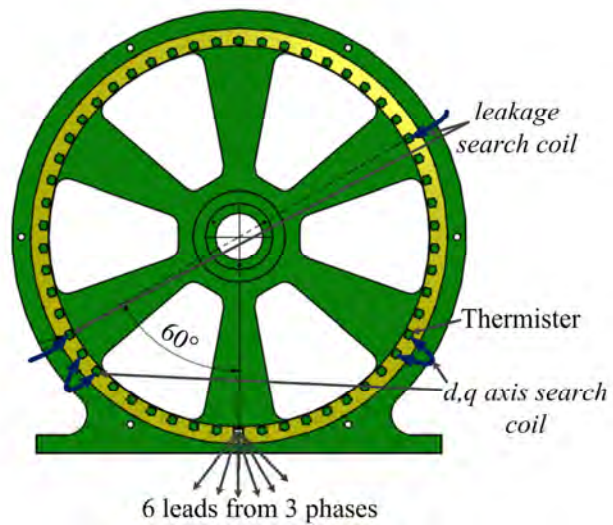


Fig.B. 5. Position of search coils, thermistor, and leads in the CW slot layout



Fig.B. 6. Complete winding of the stator

- Step 6: The final assembly of the rotor and the stator were conducted after ten months of intensive work in the Lab. The prototype machine was checked rigorously for balancing issues. The machine underwent rotating machinery diagnostics and vibration analysis. Dynamic balancing is done with the end plates to achieve rotational weight balance. With all these results coming out to be positive with no errors, the machine was transferred to the UNSW LAB.

Fig.B. 7 shows the complete machine assembly of the FSCW IPMM-F.



Fig.B. 7. FSCW IPMM-F machine assembly

Appendix C: Thermal stress analysis

A permanent magnet IPMM has a complex rotor construction and thermally it is more sensitive in comparison to an asynchronous machine. Thermal overloading of the motor is one of the main causes of degradation in the vulnerable machine components such as the stator winding insulation, permanent magnets and bearings [187]. An essential thermal model was created using Motor-CAD to test the thermal performance of the prototype design. Key specifications for this thermal model are given in Table.C 1.

Table.C 1. Specifications for thermal modelling of the FSCW IPMM-F

Cooling type	Totally enclosed non-ventilated
External/Internal fluid type	Air
Ambient temperature (convection)	40° C
Ambient temperature (radiation)	40° C
Motor current [Arms]	8.485
Iron loss Flux to Power Ratio	1.5
End-cap vents	closed
Shaft speed[rpm]	143
Mat (Liner-Lam)	Impregnation
Liner thickness [mm]	0.25
Air-gap model	Conduction & Convection

It can be seen from Table.C 1, the cooling arrangement has been selected to an enclosed non-ventilated atmosphere. This indicates that the machine was subjected to the worst case scenario where it was completely enclosed without fins and made to run on higher than full load current continuously for 2 hrs. Here, the thermal analysis was carried out using lumped parameter network that is shown in Fig.C.1.

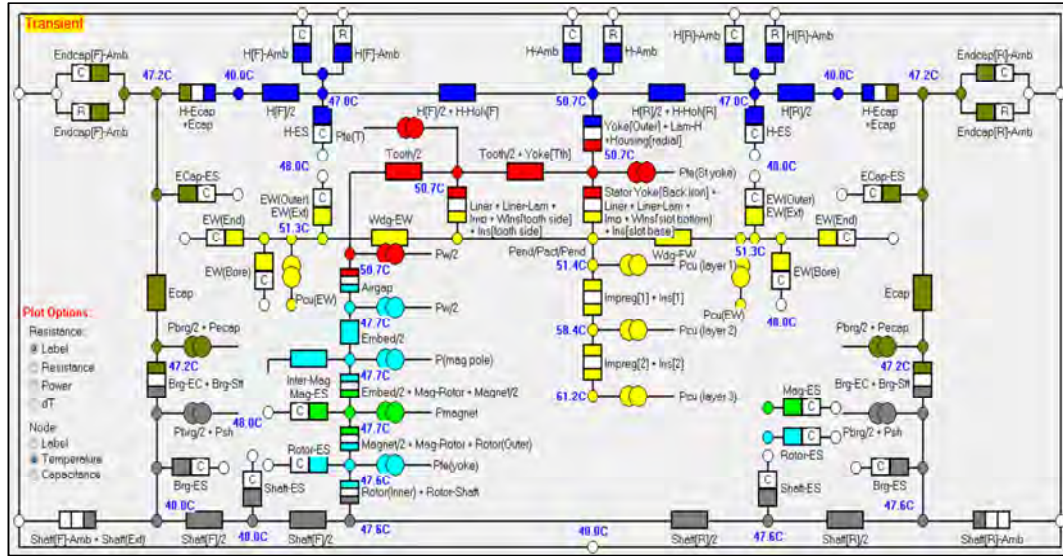


Fig.C.1. Lumped parameter network of the FSCW IPMM-F showing the temperature of various nodes

Table.C 2 shows the temperature rise of different elements of the FSCW IPMM-F during loading of the machine with 8.48 A (RMS) current. The temperature of all the components of the FSCW IPMM-F was well below the maximum temperature. Fig.C.2 shows the change in the stator core temperature when the FSCW IPMM-F is run at full load of 6.5 A (RMS) continuously for 2 hrs. It can be seen that the stator core reaches only 42° C after two hours of running continuously with full load.

Table.C 2 Temperature data for various elements of the FSCW IPMM-F at 8.48 A current after running for three straight hours

Element	Temperature	Element	Temperature
Housing - Active	50.72°C	Airgap Banding	63.45°C
Housing - Overhang (F)	47°C	Magnet	47°C
Endcap - Front	47.18°C	Bearing (F)	47.19°C
Housing - Overhang (R)	47°C	Bearing (R)	47.12°C
Endcap - Rear	47.16°C	End Space (F)	47.9°C
Stator Lam (tooth)	50.69°C	End Space (R)	47.9°C
Stator Lam (back iron)	50.73°C	Winding Layer	61.23°C
Stator Surface	50.66°C	EWdg (F)	51°C
Rotor Surface	47.7°C	EWdg (R)	51°C

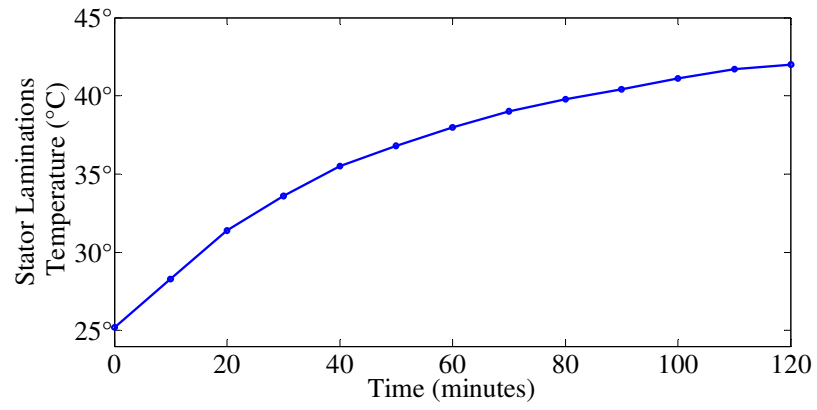


Fig.C.2. Change in stator laminations temperature with respect to time (measured experimentally)

Appendix D : Search coils in the winding

D.1 Search coils

Search coils placed in the stator winding helps to find out the error during inconsistency in the winding arrangement. The voltage can be measured to determine the discrepancy if any with the use of a search coil. There are two types of search coils placed in the stator of the FSCW IPMM-F. They are:

- *d,q* axis search coil: Four search coils are placed in the *d*- and *q*-axis of the stator winding of the FSCW IPMM-F. For *d*-axis, two search coils are placed in slot 1 and 2. Out of these two search coils; one of them is placed as close as possible to the yoke, the other one being placed as close as possible to the air-gap in the slot opening. As for *q*-axis, two other search coils are placed in slot 17 and 18 having the same arrangement as the *d*-axis search coils. Fig.D. 1(a) shows the arrangement of this search coil.
- Leakage search coils: These search coils are placed in slots to determine the amount of leakage flux in a slot. The leakage search coils are placed in slots to determine the discrepancy in voltage due to leakage flux. Slot number 19 and 46 contain leakage search coils. Each of these slots has two search coils respectively. In each slot, one of the search coils is placed as close as possible to the yoke in the middle. The other one being as close as possible to the air-gap in the slot opening located in the center of the slots. Fig.D. 1(b) shows the arrangement of leakage search coils in one slot of the FSCW IPMM-F.

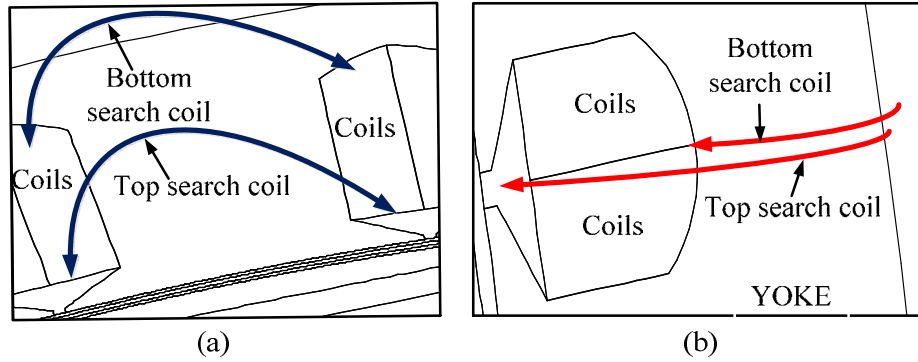


Fig.D. 1. Arrangement of search coils for (a) d,q axis search coils and (b) Leakage search coils

Each of the search coils has three turns, and the winding is done with a 0.6 mm Dia. copper wire. The EMF voltage calculation conducted using search coils have been presented in the next section.

D.2 Phase voltage measurement using search coils

The winding configuration of the prototype FSCW IPMM-F was also examined by determining the voltage across the search coils (location of the search coils are shown Appendix A) and comparing it to the overall voltage of the prototype. Fundamental voltage of Search coil (located between slot 1 & 2 with 3 turns) for phase A is 2.5 volts (peak). The E.M.F. equation is defined as,

$$E = 4.44 * f * N * \phi$$

where,
 $N = 3$;
 $f = 50$ Hz;

From the above equation, the flux is found to be, $\phi = 3.753e-3$ webers. Using this flux to calculate the total voltage for phase A gives

$$\begin{aligned} &= 4.44 * 50 * (3.753e-3) * 378 \\ &= 314.93 \text{ volts} \end{aligned}$$

Appendix D : Search coils in the winding

Taking the winding factor into account, EMF of phase A becomes

$$=314.93*0.902$$

$$= 284.07 \text{ volts (peak)}$$

However, the measured fundamental voltage of phase A is 290 volts. So the inconsistency in the voltage calculated using the search coils is 5.93 volts, which is only 2% of the rated phase voltage.

The analysis on slot leakage flux will be conducted in future work.

Appendix E: Final Machine Drawings

E.1 3-D view of the FSCW IPMM-F

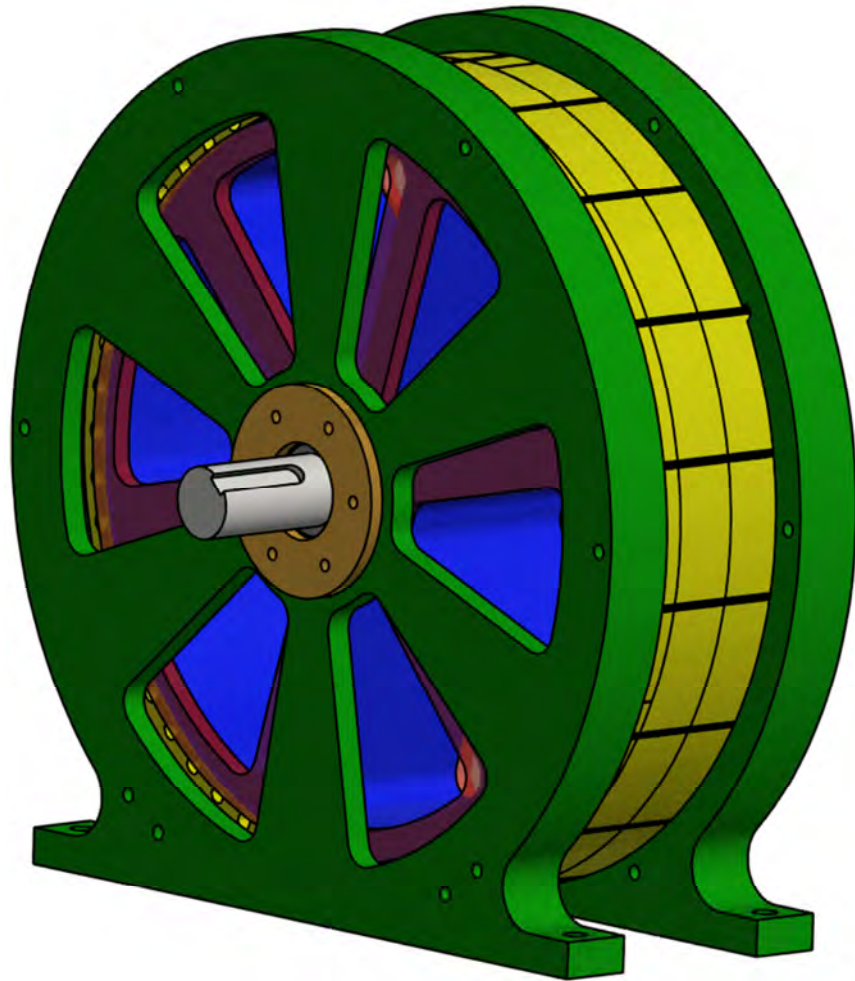
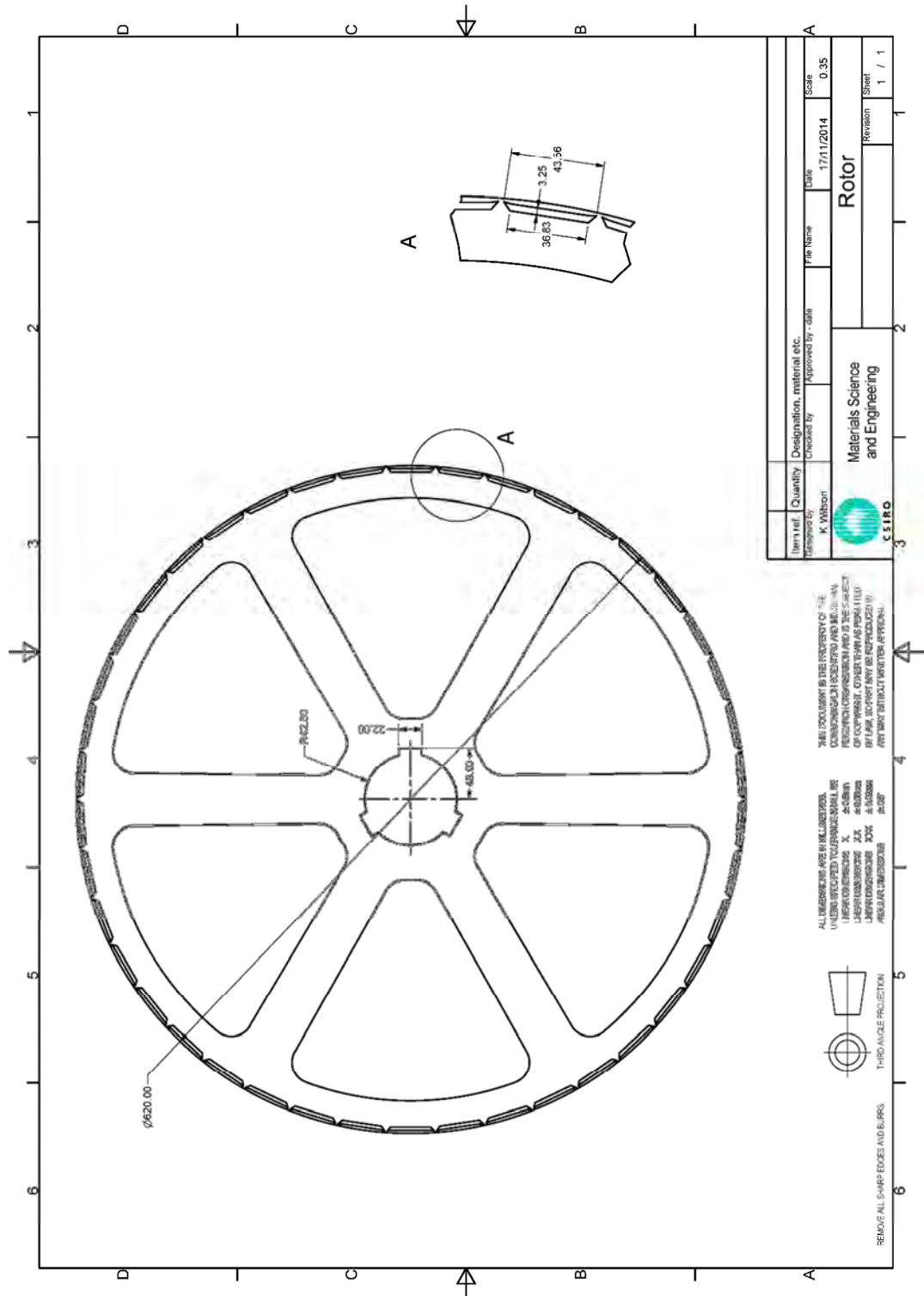
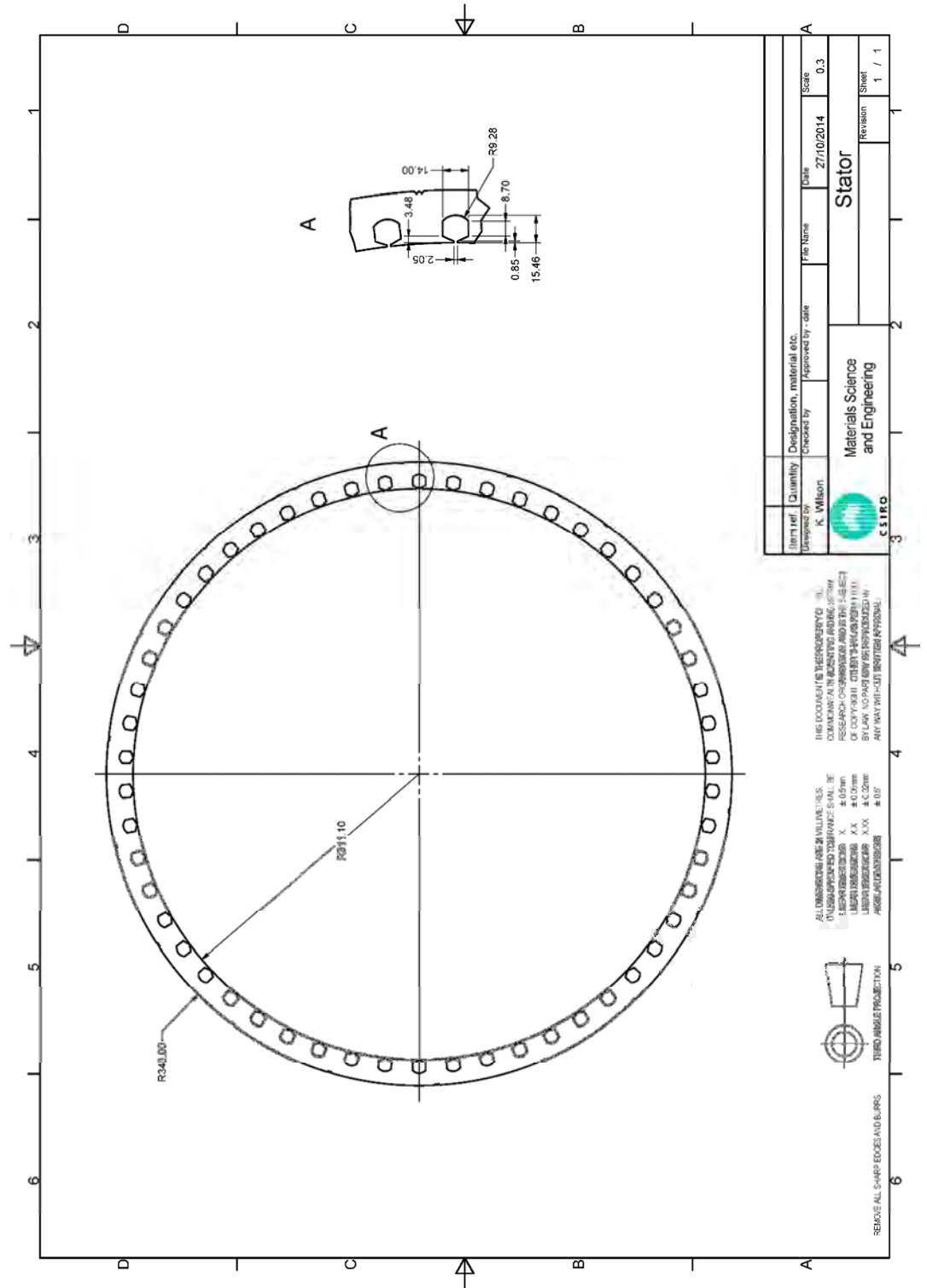


Fig.E. 1. 3-D view of the FSCW IPMM-F

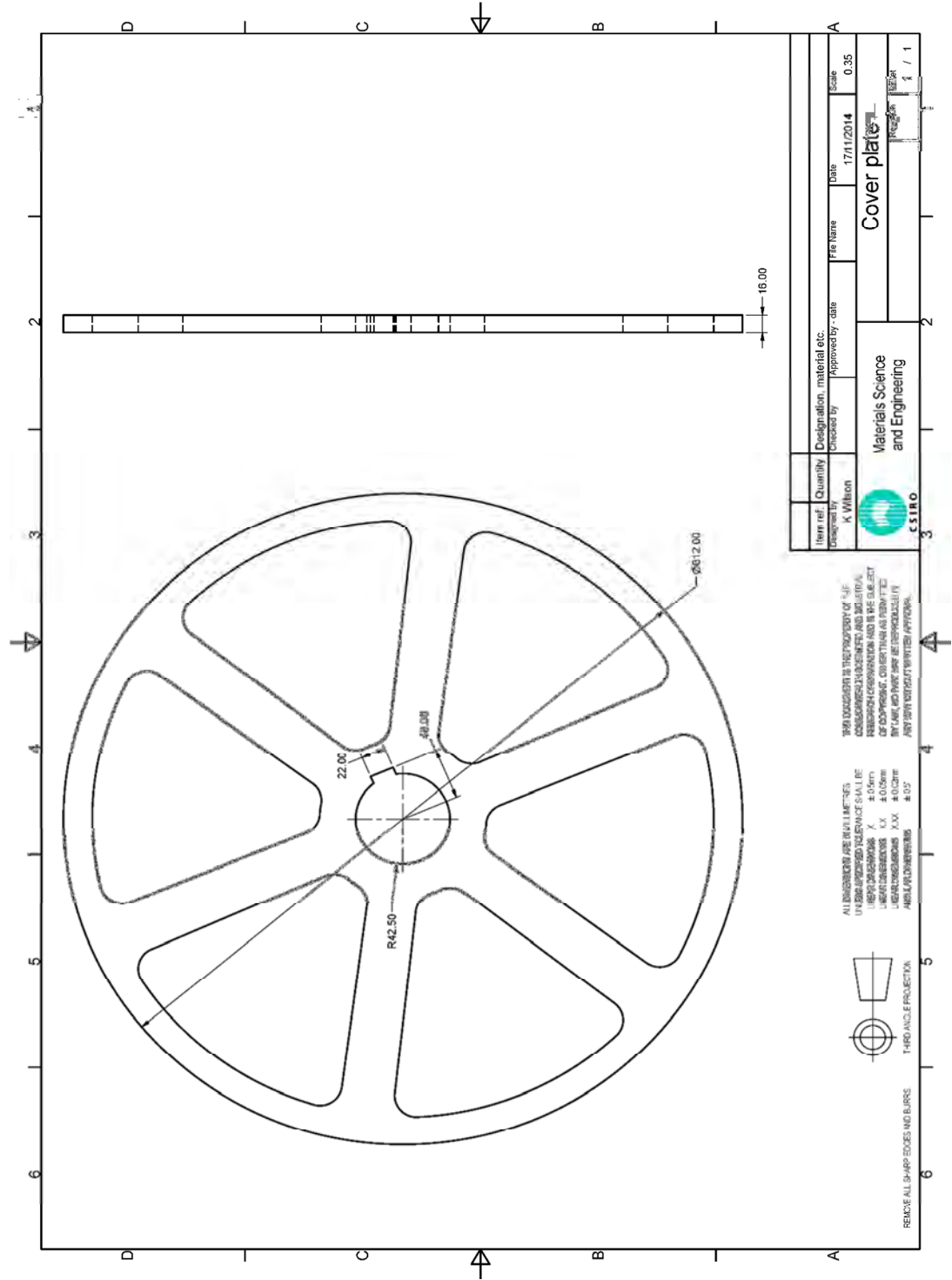
E.2 Rotor of the FSCW IPMM-F



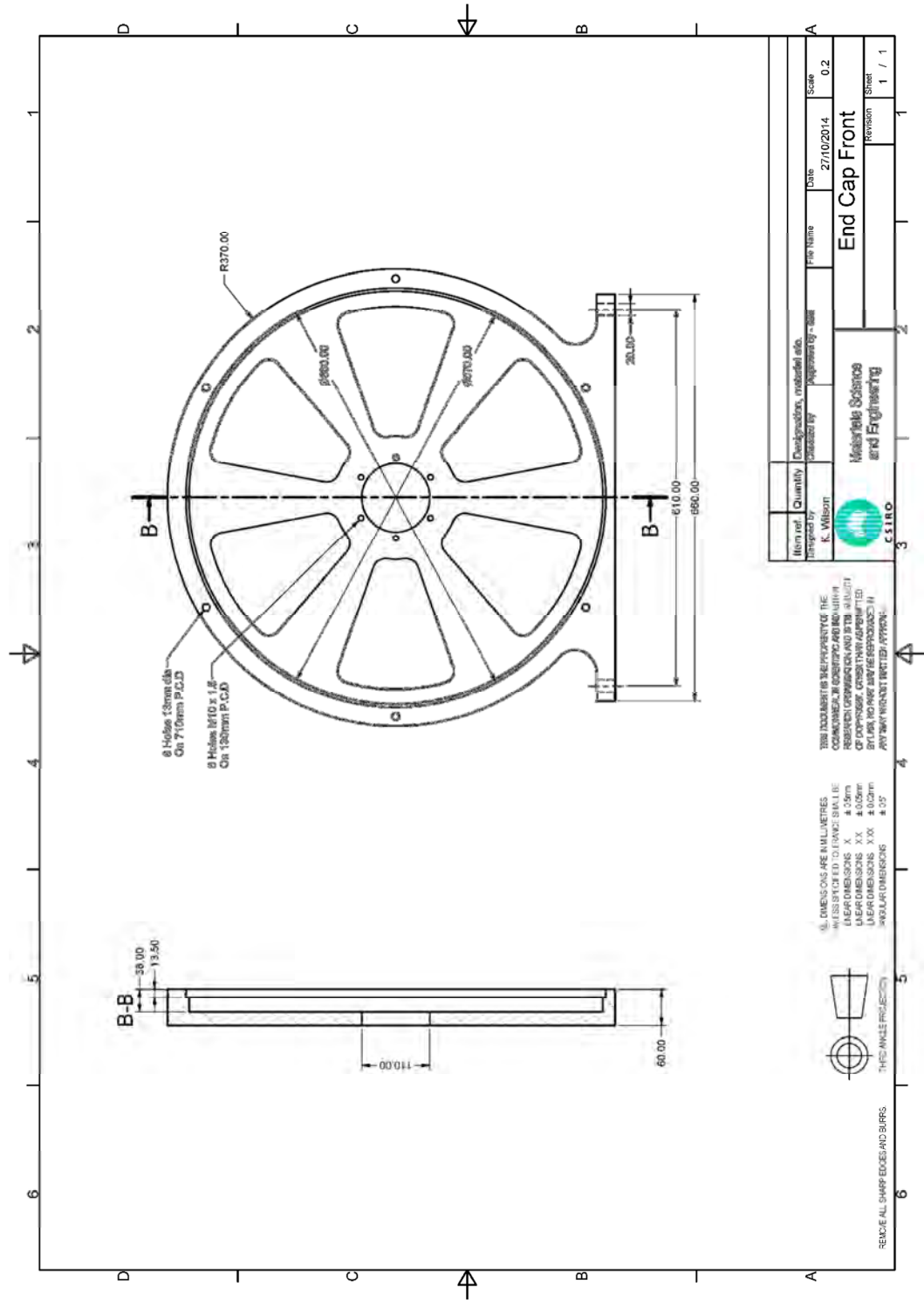
E.3 Stator of the FSCW IPMM-F



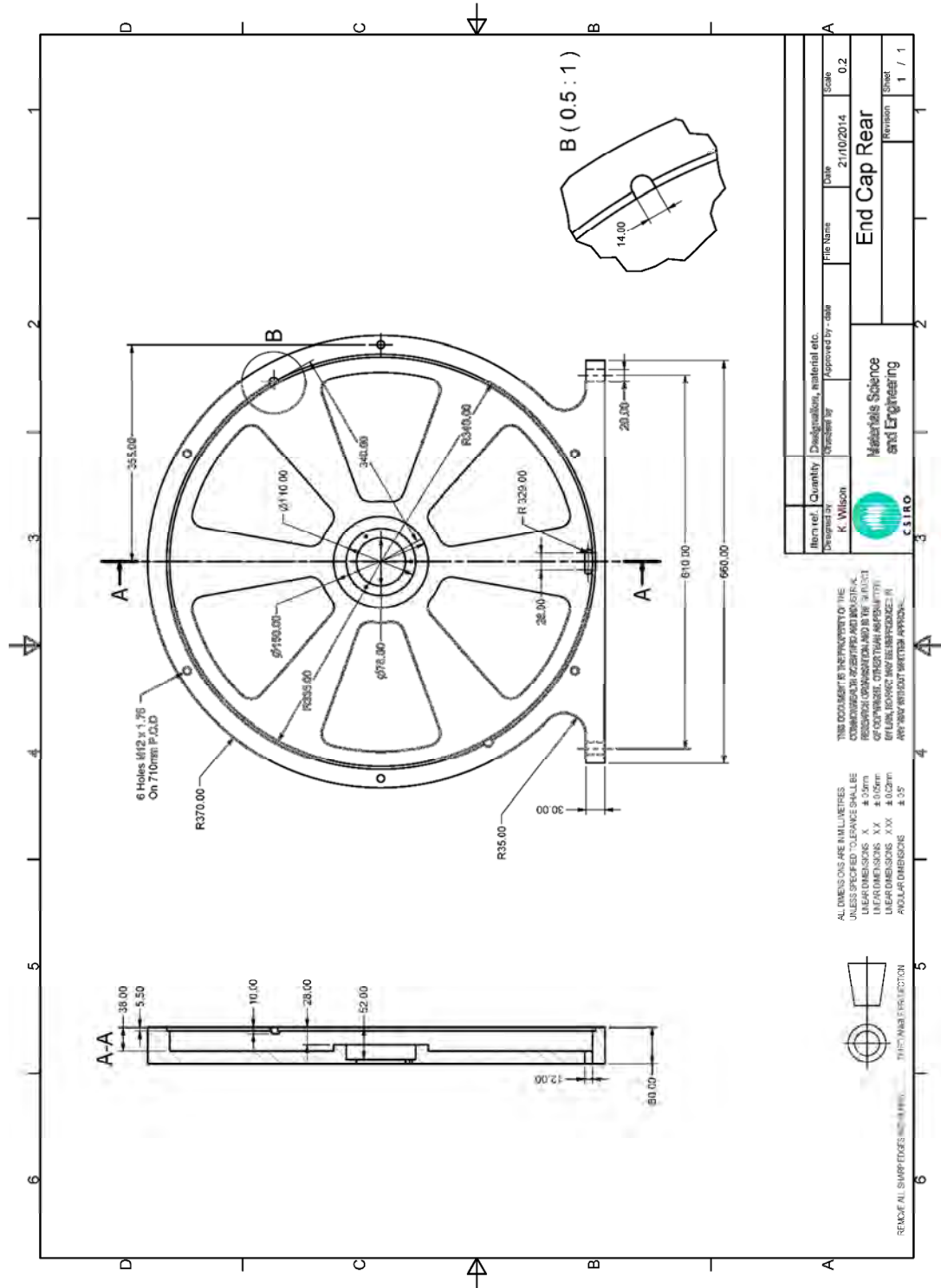
E.4 Cover plate of the FSCW IPMM-F



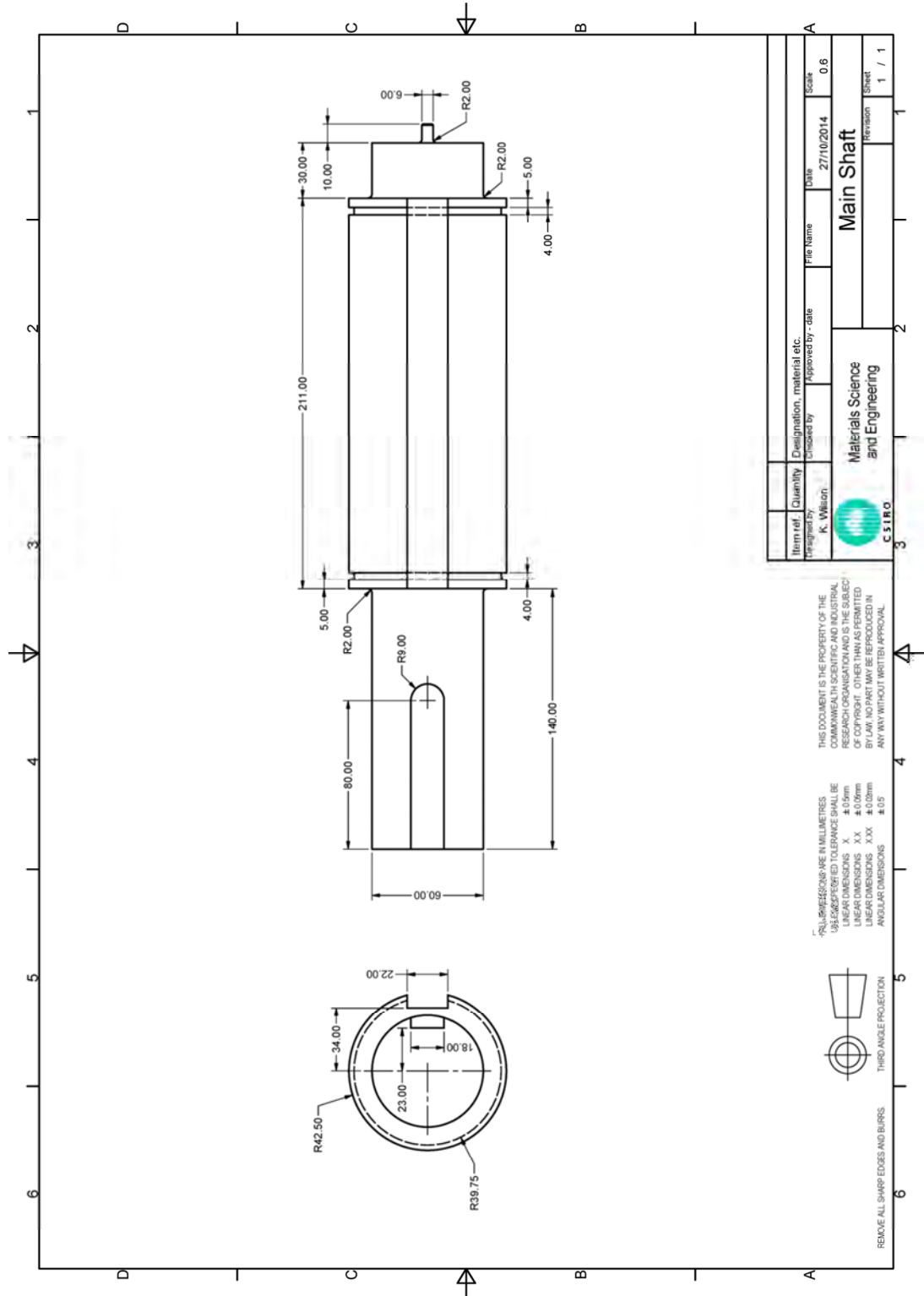
E.5 End plate front of the FSCW IPMM-F



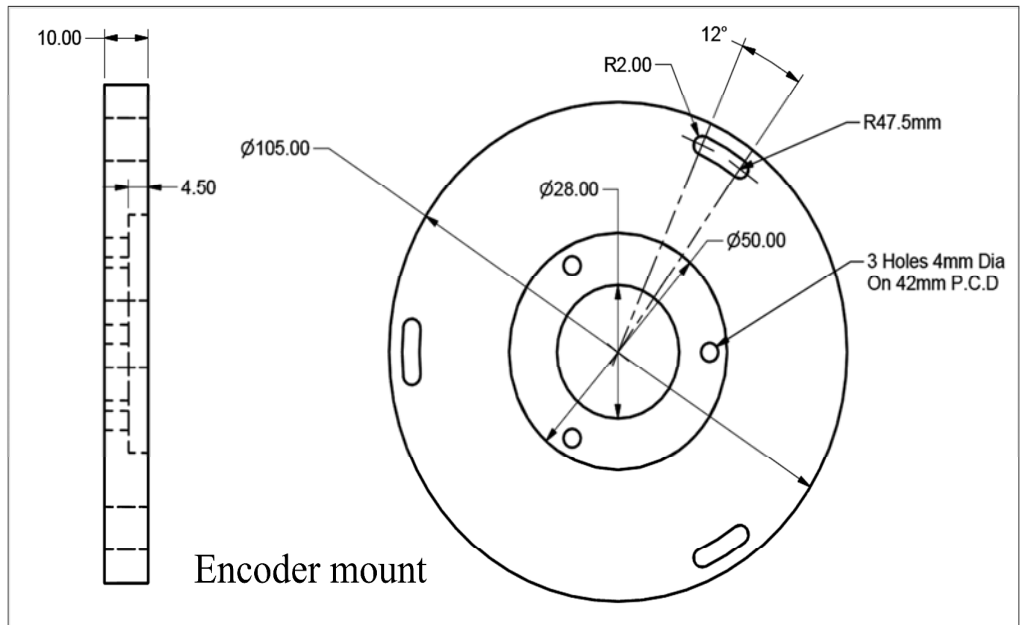
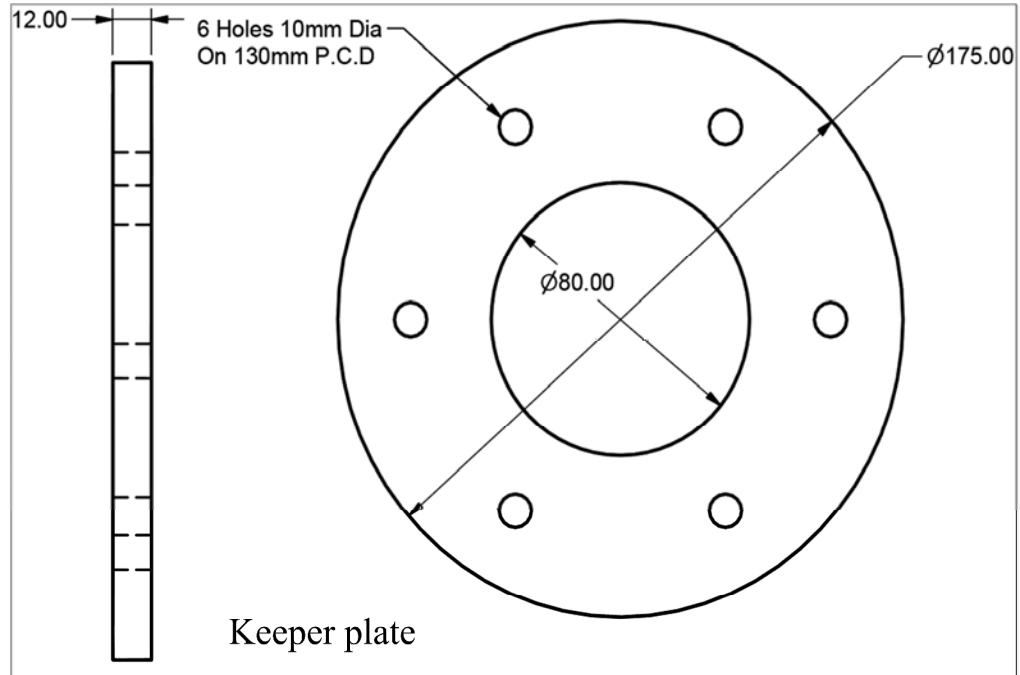
E.6 End plate back of the FSCW IPMM-F



E.7 Shaft of the FSCW IPMM-F



E.8 Encoder Mount and Keeper plate of the FSCW IPMM-F



Appendix F: Space Vector Modulation

F.1 Drive system

The controlling the IPMM in motoring action, the three-phase AC supply is rectified to DC supply using uncontrolled full-bridge rectifier. This DC bus input voltage is then converted to desired AC signal by modulating techniques. Fig.F. 1 shows the inverter architecture for the drive system used during the FSCW IPMM-F in motoring mode.

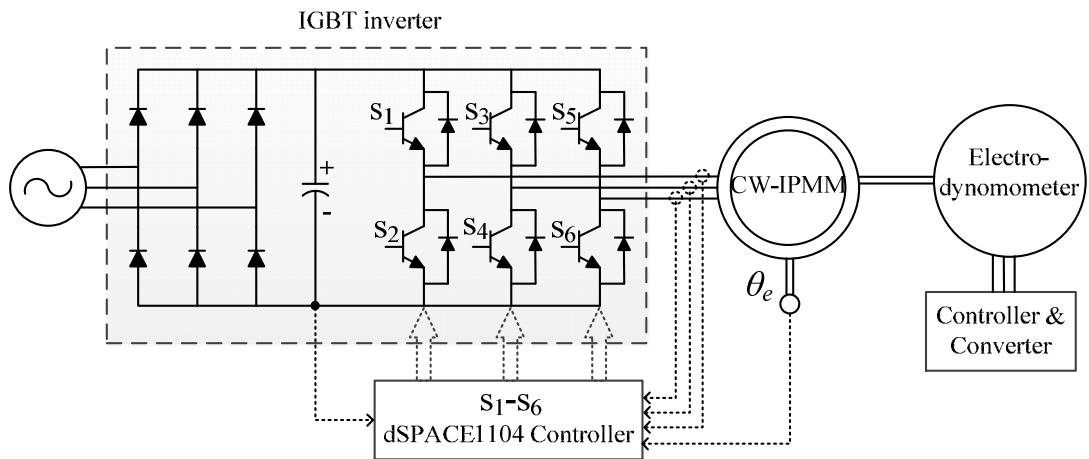


Fig.F. 1. Schematic diagram of the IPMM during motoring operation

The two common modulating techniques are the sinusoidal pulse width modulation (SPWM) scheme, and the space vector modulation (SVM) scheme. SVM provides higher modulation ration that the SPWM. The fundamental phase voltage (max.) in the SPWM and the SVM are given below:

$$V_{SPWM} = \frac{1}{2} V_{DC}$$

$$V_{SVM} = \frac{1}{\sqrt{3}} V_{DC}$$

Here, the SVM is chosen as the modulation scheme for this thesis. The SVM methodology has been described in the next section.

During generation of the FSCW IPMM-F, the uncontrolled diode rectifier is replaced by a resistive load connected directly to the DC-link, shown in Fig.F. 2. The FSCW IPMM-F was also connected to back-to-back inverters for experimental purpose. In this case, two individual inverters and the DC bus in both of them are shorted. The schematic diagram of the back-to-back inverter connected to the FSCW IPMM-F is shown in. The *IGBT inverter 1* in Fig.F. 3 works as the machine side inverter and the *IGBT inverter 2* performs the grid side converter. Two independent SVM scheme are applied individually to the IGBT inverters by using the dSPACE1104 control board.

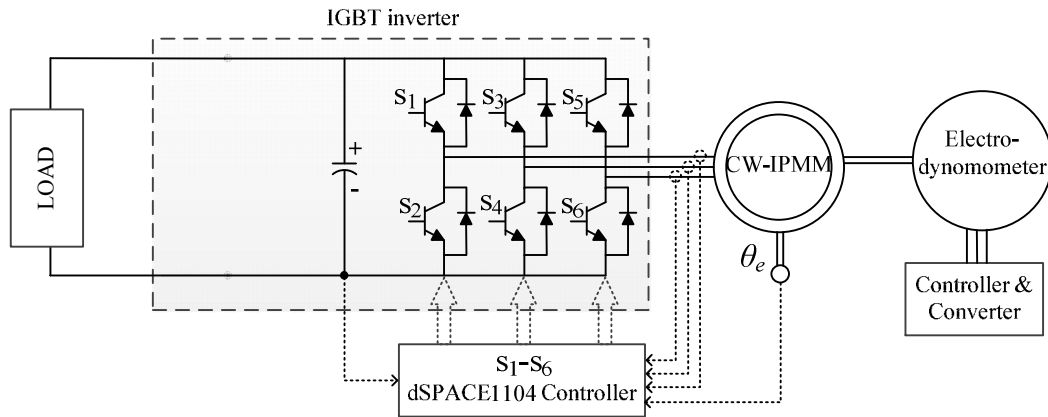


Fig.F. 2. Schematic diagram of the FSCW IPMM-F generator system

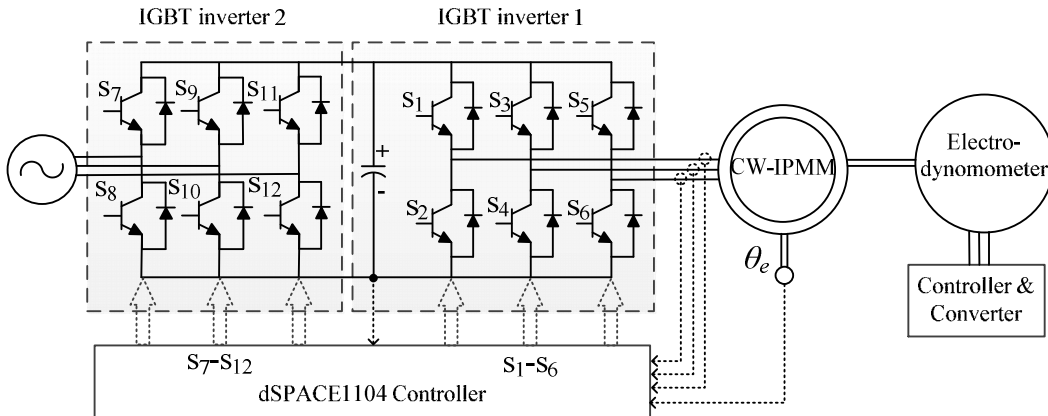


Fig.F. 3. Schematic diagram of the FSCW IPMM-F connected to back-to-back inverters

F.2 Space Vector Modulation scheme

A space vector, which is a simultaneous representation of all three-phase quantities can be defined as

$$v_s = \frac{2}{3}(v_a + \bar{a}v_b + \bar{a}^2v_c)$$

Where, $\bar{a} = \exp(j2\pi/3)$. The desired three phase quantities V_a , V_b and V_c are sampled in time at a specified sampling frequency and are represented in terms of space vectors. The discrete phase voltage space vector positions are shown in Fig.F. 4. These vectors form a hexagon consisting of six sectors each of 60° span. It can be seen from Fig.F. 4, there exist eight possible switching states ($V_0 - V_7$). Two of these vectors (V_0 and V_7) are termed zero vectors while the others are referred to as switching vectors. The phase voltages and their corresponding space vectors can be easily determined with the help of a look-up table shown in Table.F 1 for the SVM scheme.

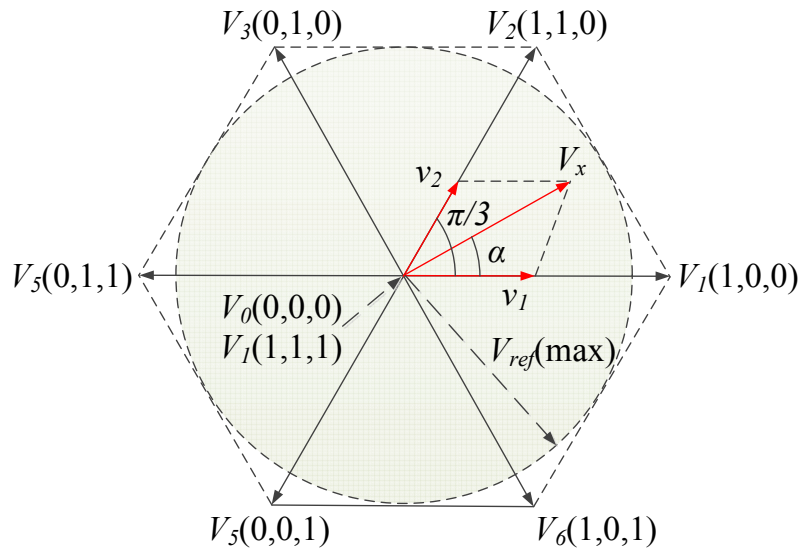


Fig.F. 4 Phase voltage space vectors.

Table.F 1 Space vector modulation look-up table

State	Switch On	V_{an}	V_{bn}	V_{cn}	Space Vector
0	2,4,6	0	0	0	$V_0 = 0,0,0$
1	1,4,6	$\frac{2V_{DC}}{3}$	$-\frac{V_{DC}}{3}$	$-\frac{V_{DC}}{3}$	$V_1 = 1,0,0$
2	1,3,6	$\frac{V_{DC}}{3}$	$\frac{V_{DC}}{3}$	$-\frac{2V_{DC}}{3}$	$V_2 = 1,1,0$
3	2,3,6	$-\frac{V_{DC}}{3}$	$\frac{2V_{DC}}{3}$	$-\frac{V_{DC}}{3}$	$V_3 = 0,1,0$
4	2,3,5	$-\frac{2V_{DC}}{3}$	$\frac{V_{DC}}{3}$	$\frac{V_{DC}}{3}$	$V_4 = 0,1,1$
5	2,4,5	$-\frac{V_{DC}}{3}$	$-\frac{V_{DC}}{3}$	$\frac{2V_{DC}}{3}$	$V_5 = 0,0,1$
6	1,4,5	$\frac{V_{DC}}{3}$	$-\frac{2V_{DC}}{3}$	$\frac{V_{DC}}{3}$	$V_6 = 1,0,1$
7	1,3,5	0	0	0	$V_7 = 1,1,1$

In Fig.F. 4, V_x represents a reference vector in the first sector. V_x can be easily represented with respect to V_1 and V_2 given as

$$V_x \sin\left(\frac{\pi}{3} - \alpha\right) = v_1 \sin \frac{\pi}{3}$$

$$V_x \sin \alpha = v_2 \sin \frac{\pi}{3}$$

Vectors v_1 and v_2 are auxiliary vectors of space vectors V_1 and V_2 respectively. To calculate the time of application of different vectors, consider V_1 and V_2 to be activated for durations t_1 and t_2 respectively over a period t_s . The auxiliary vectors can be represented with respect to the activation time given as

$$v_2 = \frac{t_2}{t_s} V_2$$

$$v_1 = \frac{t_1}{t_s} V_1$$

where t_s is time period.

The activation times can be represented as,

$$t_1 = \frac{V_x \sin(\pi/3 - \alpha)}{v_1 \sin(2\pi/3)}$$

$$t_2 = \frac{V_x \sin(\alpha)}{v_2 \sin(2\pi/3)}$$

$$t_0 = t_s - t_a - t_b$$

The switching pattern for sector 1 of a symmetrical space vector PWM is shown in Fig.F. 5. Similarly for the other sectors, this process is repeated. This shows that the desired output voltage signal specified by the controls can be easily achieved by varying the magnitude, frequency and the phase of the voltage. For SVM, the maximum obtainable fundamental output voltage is 0.577.

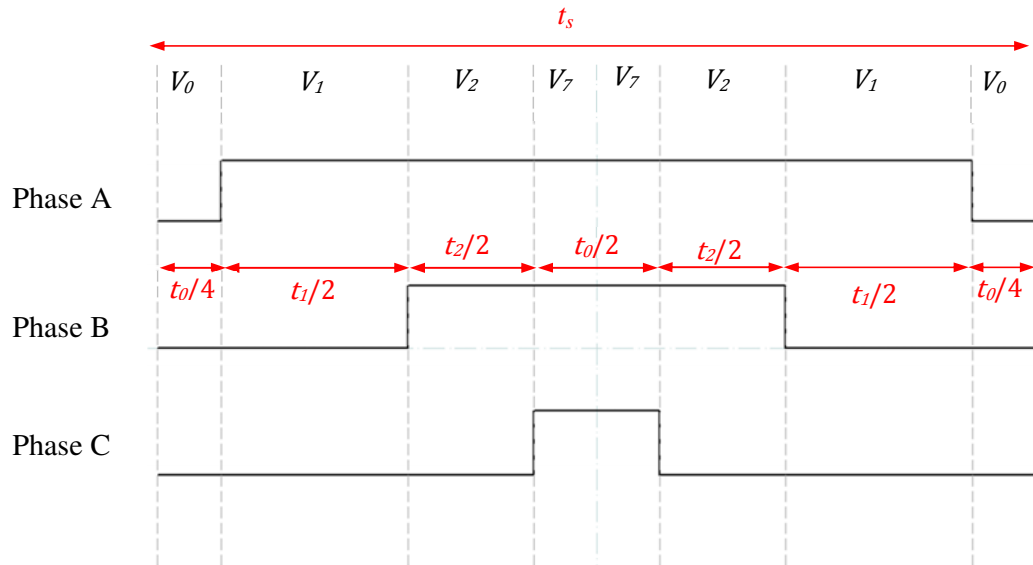


Fig.F. 5. Switching pattern for sector 1.

Appendix G: Experimental setup

G.1 The Experimental setup

The experimental setup (shown in Fig.G. 1) for testing the performance of the FSCW IPMM-F consists of the following:

- i. FSCW IPMM-F
- ii. MEA Regenerative Electro-dynamometer
- iii. Load resister Bank (20Ω - $200\ \Omega$ with a maximum current limit of 5 A)
- iv. DS1104 controller board
- v. Windows based PC
- vi. 3-phase IGBT inverter
- vii. Dual-range torque sensor (KISTLER 4503A)
- viii. Incremental Position sensor (HEIDENHAIN ROD 426)
- ix. Precision Power Analyzer (YOKOGAWA WT1800)
- x. 415V Voltage regulator
- xi. Oscilloscope (Lecroy)
- xii. 3-phase load bank

In this experimental setup, the 3-phase IGBT inverter was supplied by the 3-phase 415V voltage regulator connected to the mains. The output signal of the inverter is connected to the 3-phases of the FSCW IPMM-F through a power analyzer which measures the input/output quantities of the machine. The feedback signals from the inverter, which are the supply current of two phases and the DC link voltage, are fed to the DS1104 controller board. The incremental position sensor that is mounted on the shaft of the prototype also sends its feedback to the controller board. The DS1104 is connected to a windows based PC where the control algorithm is written in C-code and is applied in real time via *d-space control desk* (shown in Fig.G. 2). This control algorithm together with the feedback signals in the controller board and the SVM

produces the desired current references that are fed to the inverter through the controller board.

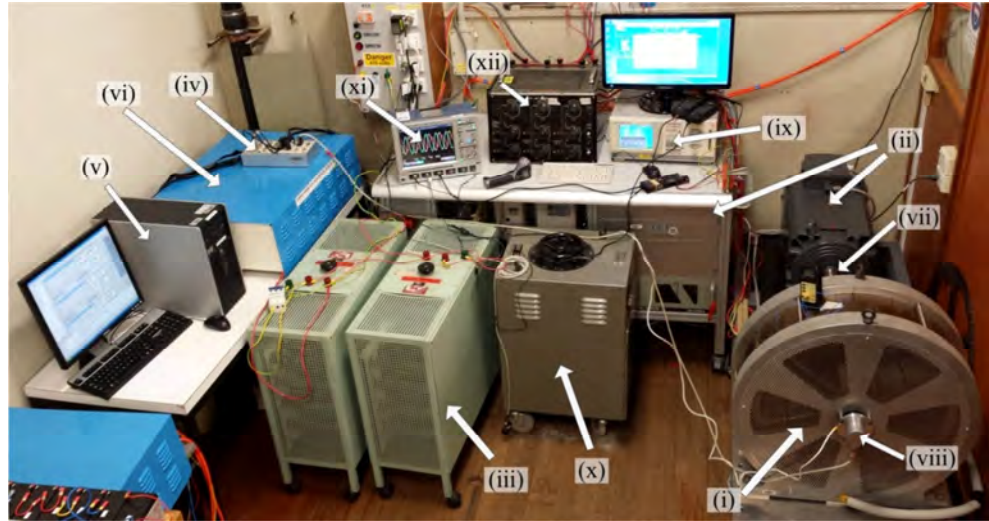


Fig.G. 1. Complete experimental setup

The FSCW IPMM-F is coupled to the MEA electrodynamicometer which acts as the driving motor during generating operation. During motoring operation of the prototype, this dynamometer acts as the loading machine. The mechanical torque of the prototype is measured by a dual-range torque sensor that is coupled in between the shaft of the two machines.

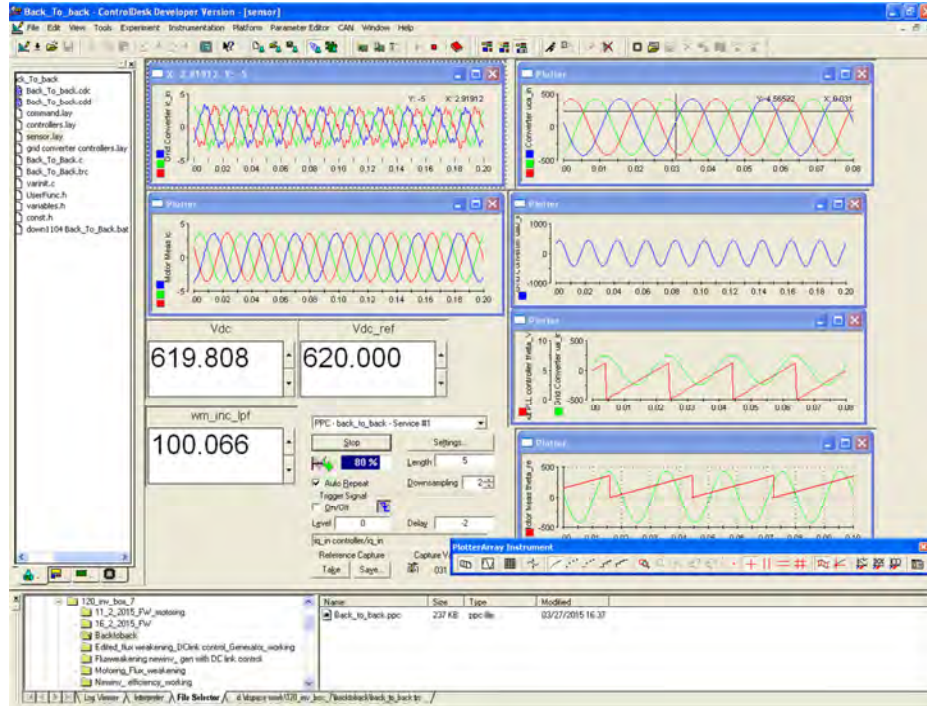


Fig.G. 2 *d*-space control desk

G.2 Regenerative Dynamometer System

The MEA Regenerative Dynamometer System (RDS) is a computerized testing system for electric motors. The system includes the following components:

- Control unit
 - System computer
 - Regenerative unit
 - Inverter
 - PLC
- Torque Sensor
- Loading Motor (Induction Machine shown in Fig.G. 3)

The control unit is supplied with 415 V AC source, Neutral and Earth. The key parameters of the loading motor are provided in Fig.G. 3.

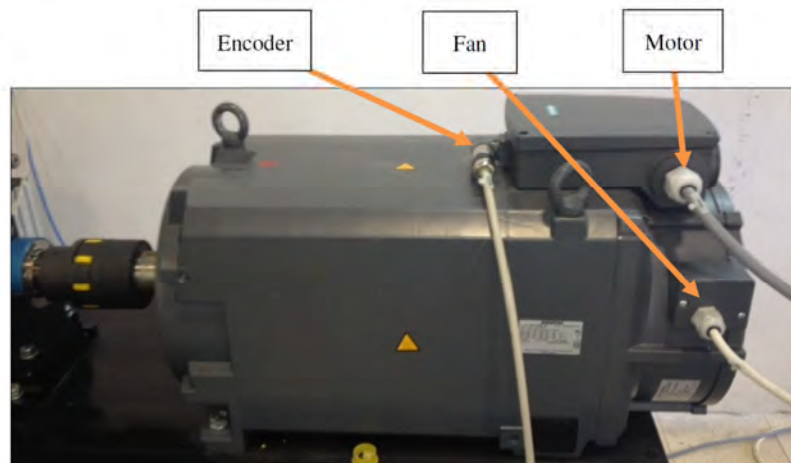


Fig.G. 3. Loading motor

There are four control modes of the MEA RDS for testing the performance of the FSCW IPMM-F. Depending on the experimental setup, these control modes are selected. They are:

- Torque Mode (Generating): This mode (screen shot of the torque mode is shown in Fig.G. 4) is selected when the FSCW IPMM-F is acting as a motor and a certain mechanical torque needs to be applied to it. This means the MEA machine acts as loading motor and can be loaded to 500 Nm. All experimental tests with the prototype in motoring action are conducted in this mode.
- Speed Mode (Generating): In this mode, the prototype machine can be tested by defining the speed of the MEA machine.
- Motoring Mode: The loading unit is running in motoring mode, at a defined speed, with the maximum torque defined by the FSCW IPMM-F. Experiments with the prototype in generating action with a single inverter are conducted in this mode.
- Drive cycle Simulation Mode: Gives the ability to simulate Torque-speed characteristics by loading an Excel file that represents the drive cycle profile. This mode was mainly used to simulate the wind turbine torque-speed

characteristics to the loading motor and the FSCW IPMM-F acting as a wind turbine generator connected to back-to-back inverters.

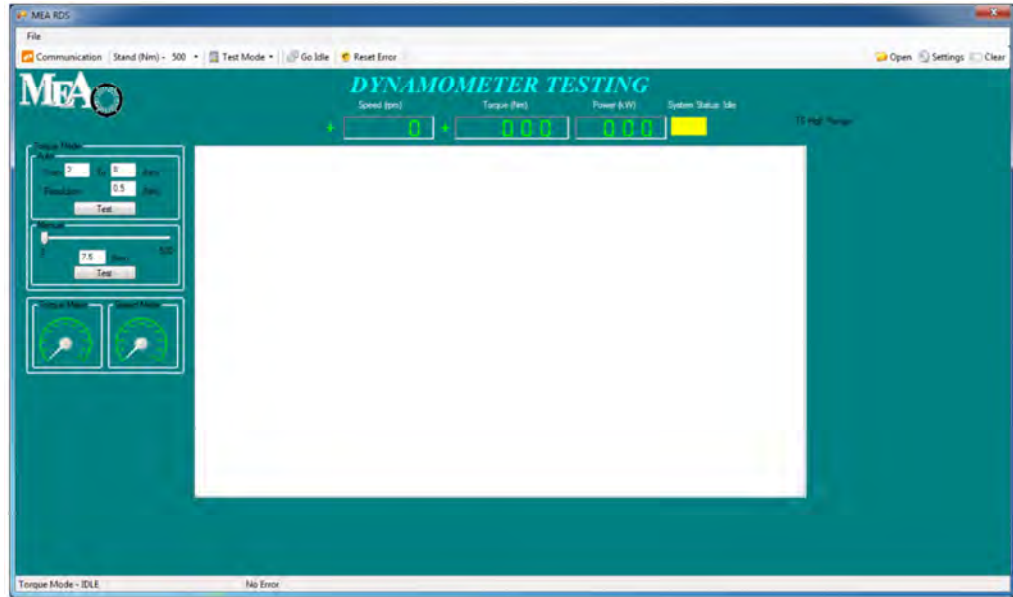


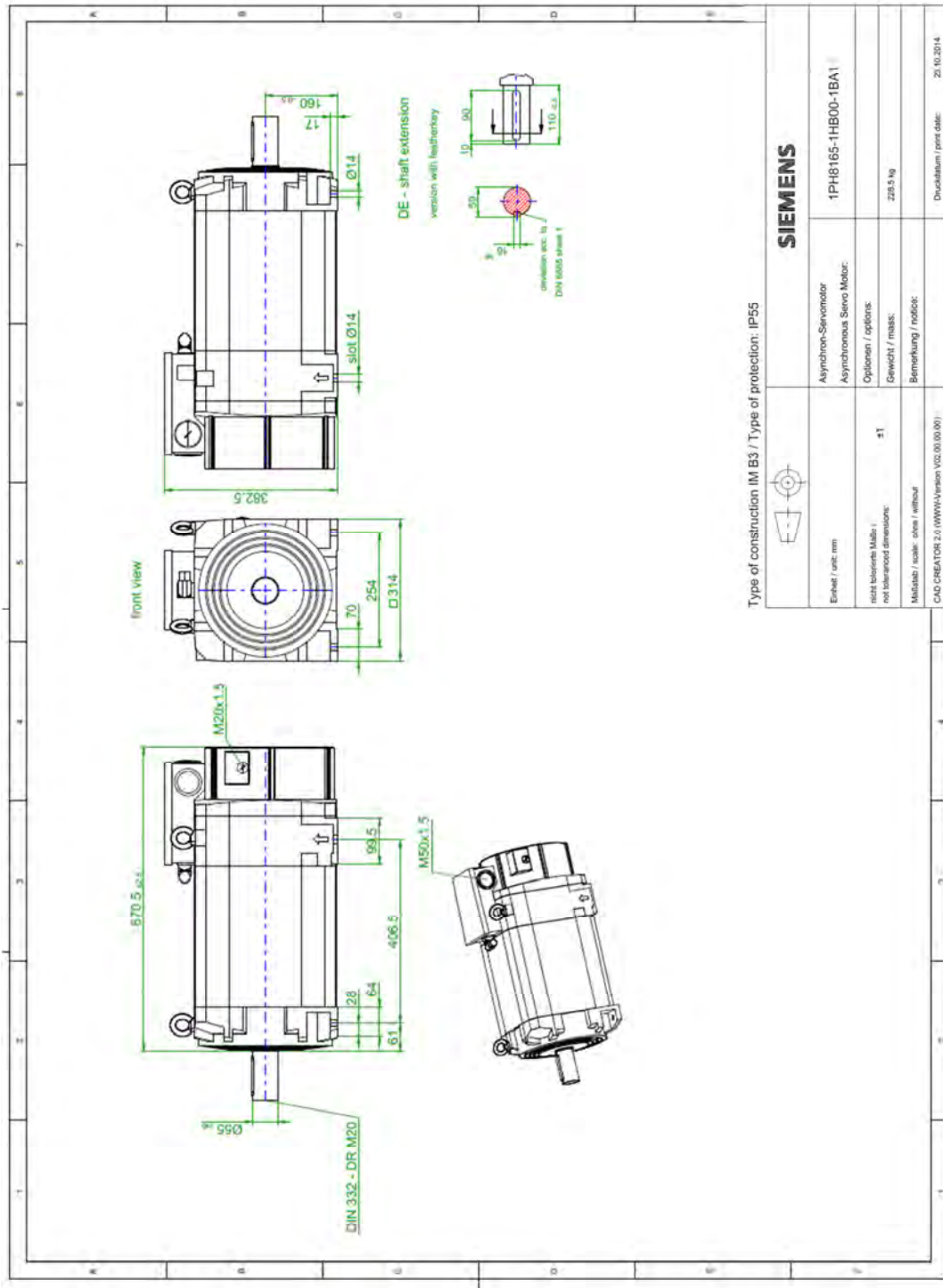
Fig.G. 4. Screen shot of Torque mode option available in MEA RDS

Appendix G: Experimental setup

Table.G 1 Key parameters of the loading motor

- Line data	
Voltage	400 V
Frequency	50 Hz
Number of phases	3
Allowance for short term supply fluctuations	Yes
Drive system / Supply system	
- SINAMICS S120 AC/AC - servo	
- Motor	
Order No.	1PH8165-1HB00-1BA1
Motor / ambient conditions	
Installation altitude	1000 m
Ambient temperature	40 °C
Temperature rise class	F/100K
Motor / catalog data	
Motor type	1PH8 induction motor / synchronous motor
Motor principle	Asynchronous
Interface	Star
Cooling method	Forced ventilation (IP 55)
Bearing / drive type:	Standard
Brake	No
Version	Standard type
Rated power	13.00 kW
Rated torque	310.00 Nm
Rated current	36.00 A
Rated speed	356.21 rpm
Max. mechanical torque	610.00 Nm
Axis height	160 mm
Efficiency	0.826
Encoder	Incremental encoder HTL 1024 S/R
Encoder evaluation	External SMC module
Type of construction	IM B3
Shaft end	With featherkey and full-key balancing
Shaft and flange accuracy	R
Airflow/air-outlet direction	DE → NDE
Terminal box	Terminal box top, outgoing feeder right
Vibration severity grade	R/A
Load data on the motor shaft	
Load type	Simple motor selection
Speed at the operating point	356.21 rpm
Torque at the operating point	310.40 Nm
Current at the operating point	36.04 A
Power at the operating point	11.58 kW

G.3 Mechanical Drawing of the MEA loading motor



G.4 Initial Displacement Angle between the Rotor and the Encoder

Permanent magnet synchronous machines (PMSM) require accurate information of rotor position for high precision control methods. This is acquired by a position sensor mounted on the shaft of the PMSM. As discussed previously, an incremental encoder was used to determine the rotor position in this work. For incremental encoders, the index pulse needs to be aligned to the negative-to-positive zero-crossing point of the phase voltage in order to produce absolute position information. From Fig.G. 5, the index pulse is 30 displaced from the negative-to-positive zero-crossing point of line-to-line back EMF. This means the phase voltage is just aligned with the negative-to-positive zero-crossing point of phase voltage. The measured angle by the encoder is leading the real N-pole of the magnet in the rotor by 7.1° .

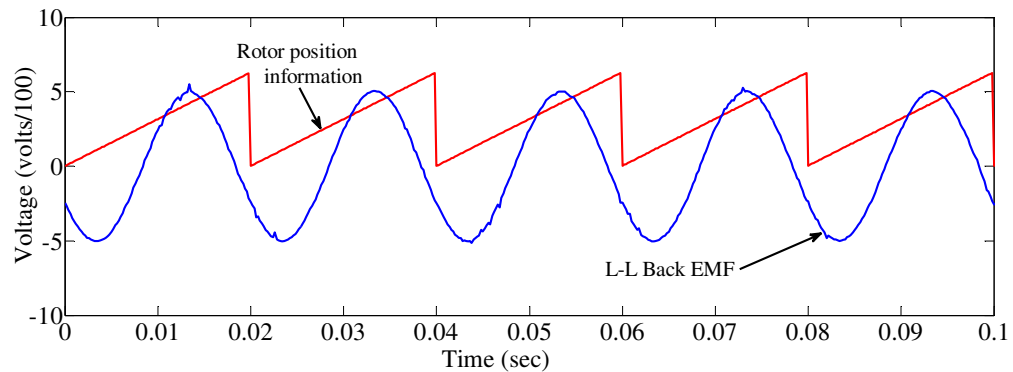


Fig.G. 5. Measured line-to-line back EMF of the prototype FSCW IPMM-F at 143 RPM

G.5 Control algorithm

The major portion of the control algorithm that is written in C and ran with *d-space control desk* is shown below:

```

/* RL_SINGLE_PWM_7.C *****
*
* Rotor Field oriented control of the FSCW IPMM-F during generation *
* using new RtlLib function DS1104_CS_PWM7.c *
* date : MAR. 15, 2014 *
* University of New South Wales, Australia *
*****/
#include <brtenv.h> /* basic real-time environment */
#include <const.h> /* general header for motor control */
#include <UserFunc.h>
#include <variables.h>
#include <varinit.c>

void PWM_sync_interrupt(void)//60us
{
RTLIB_TIC_START(); /* start time measurement */
host_service(1, 0); //ControlDesk service 10us

if (rst==1)
{
varinit();

ds1104_bit_io_clear(DS1104_DIO0);

//----- Measuring Initial Position from Incremental Encoder -----
index_inc=ds1104_inc_index_read(1,DS1104_INC_IDXMODE_ON);
inc_curr= ds1104_inc_position_read_immediately(1,DS1104_INC_LINE_SUBDIV_4)*PI2/5000.0;
theta_rm =(inc_curr +INIT_POS_OFFSET); //adding initial position to mechanical position;
if(theta_rm<0.0) theta_rm=theta_rm+PI2;
else if(theta_rm>=PI2) theta_rm=theta_rm-PI2;
theta_re = Pp * theta_rm;//mech -> elec position
theta_re=theta_re-((unsigned int)(theta_re/PI2))*PI2;/////??
if(theta_re<0.0) theta_re=theta_re+PI2;
else if(theta_re>=PI2) theta_re=theta_re-PI2;

//----- Measuring Position from Incremental Encoder -----
index_inc=ds1104_inc_index_read(1,DS1104_INC_IDXMODE_ON);
inc_curr= ds1104_inc_position_read(1,DS1104_INC_LINE_SUBDIV_4)*PI2/5000.0;
theta_rm =(inc_curr +INIT_POS_OFFSET); //adding initial position to mechanical position;
if(theta_rm<0.0) theta_rm=theta_rm+PI2;
else if(theta_rm>=PI2) theta_rm=theta_rm-PI2;
theta_re = Pp * theta_rm;//mech -> elec position
theta_re=theta_re-((unsigned int)(theta_re/PI2))*PI2;
if(theta_re<0.0) theta_re=theta_re+PI2;
else if(theta_re>=PI2) theta_re=theta_re-PI2;

//-----Calculate the speed of the motor -----
if((inc_curr-inc_old>PI/50.0)||inc_curr-inc_old<-PI/50.0)||index_inc==1) {}
else inc_delta=inc_curr-inc_old;
wm_inc=inc_delta/TS;//rad/s
inc_old=inc_curr;

// position error skipping code

if(fabs(inc_curr-inc_old>PI/50.0))inc_curr=inc_old+wm_inc*TS;

//-----Fist Order Lag to remove the noise from the encoder -----

t_f=fol_w_inc_t;
fol_w_inc.K1 = (2.0*t_f-TS)/(2.0*t_f+TS);
fol_w_inc.K2 = TS/(2.0*t_f+TS);
fol(wm_inc, wm_inc_lpf, fol_w_inc);

//----- Reading ADC -----
ds1104_adc_read_mux(scantable, 4, u);//Channel 1 2 3 4 for DC voltage and phase current of inverter 2
uab_in=GAIN_ADC1*u[0]-ADC1_0;//line-line grid voltage uab ///Vuv motor line voltage for initial position
ubc_in=GAIN_ADC2*u[1]-ADC2_0;//line-line grid voltage ubc
uca_in=-uab_in-ubc_in;//line-line grid voltage ubc
uca_in=GAIN_ADC3*u[2]-ADC3_0;//
Vdc1=GAIN_ADC4*u[3]-ADC4_0;//1000V max DC
//if(Vdc1<1e-3) Vdc1=1e-3;

```

Appendix G: Experimental setup

```

//----- First order Lag Low-pass filter -----
t_f=fo1_Vdc_t;
fo1_Vdc.K1 = (2.0*t_f-TS)/(2.0*t_f+TS);
fo1_Vdc.K2 = TS/(2.0*t_f+TS);
fo1(Vdc1,Vdc,fo1_Vdc);

V_DC=2.0/3.0*Vdc;//Length of the 6 fixed active vectors
//V_DC=U_MAX_LINE*sqrt(1.0/3.0);

ia_in=GAIN_ADC5*ds1104_adc_read_ch_immediately(5)-ADC5_0;//phase current of grid-side converter
ic_in=GAIN_ADC6*ds1104_adc_read_ch_immediately(6)-ADC6_0;//phase current of grid-side converter
ib_in=-ia_in-ic_in;

ia=GAIN_ADC7*ds1104_adc_read_ch_immediately(7)-ADC7_0;//phase current of inverter
ib=GAIN_ADC8*ds1104_adc_read_ch_immediately(8)-ADC8_0;//DC current of inverter
ic=-ia-ib;
//Torque=GAIN_ADC1*ds1104_adc_read_ch_immediately(1)-ADC1_0;

if(Vdc>Vdc_max) Vdc_stat=Vdc_stat+1;//Over-voltage Protection

if(fabs(ia)>Iabc_max) ia_stat=ia_stat+1;//Over-current Protection
if(fabs(ib)>Iabc_max) ib_stat=ib_stat+1;//Over-current Protection
if(fabs(ic)>Iabc_max) ic_stat=ic_stat+1;//Over-current Protection

if(fabs(ia_in)>Iabc_max) ia_in_stat=ia_in_stat+1;//Over-current Protection
if(fabs(ib_in)>Iabc_max) ib_in_stat=ib_in_stat+1;//Over-current Protection
if(fabs(ic_in)>Iabc_max) ic_in_stat=ic_in_stat+1;//Over-current Protection

if(ia_stat>10||ib_stat>10||ic_stat>10||ia_in_stat>10||ib_in_stat>10||ic_in_stat>10||Vdc_stat>0) rst=1;

ial=2.0/3.0*(ia-0.5*ib-0.5*ic);
ibe=SQRT1_3*(ib-ic);

//wt=wt+PI2*Freq*period;//add for RL load theta as no encoder reading
//if(wt>=PI2) wt=wt-PI2;
//if(Freq<0.0) Freq=0.0;
//else if(Freq>0.1/period) Freq=0.1/period;
//theta_re=wt;//add for RL load theta

theta_re_est=theta_re; //should include when running motor

id=ial*cos(theta_re_est)+ibe*sin(theta_re_est);//id calculation
iq=-ial*sin(theta_re_est)+ibe*cos(theta_re_est);//iq calculation

ial_in=2.0/3.0*(ia_in-0.5*ib_in-0.5*ic_in);
ibe_in=SQRT1_3*(ib_in-ic_in);
id_in=ial_in*cos(theta_Vin_PLL)+ibe_in*sin(theta_Vin_PLL);
iq_in=-ial_in*sin(theta_Vin_PLL)+ibe_in*cos(theta_Vin_PLL);
ual_in=2.0/3.0*uab_in+1.0/3.0*ubc_in;
ube_in=SQRT1_3*ubc_in;
Vinmax=sqrt(ual_in*ual_in+ube_in*ube_in);
ua_in=ual_in;
ub_in=1.0/3.0*(-uab_in+ubc_in);
uc_in=-1.0/3.0*uab_in-2.0/3.0*ubc_in;
theta_Vin_atan=atan2(ube_in,ual_in);
if (theta_Vin_atan<0.0) theta_Vin_atan=theta_Vin_atan+PI2;//0 to 2*PI

//----- Anti-windup PI controller Three-phase PLL-----

ud_in=ual_in*cos(theta_Vin_PLL)+ube_in*sin(theta_Vin_PLL);
uq_in=-ual_in*sin(theta_Vin_PLL)+ube_in*cos(theta_Vin_PLL);
Ctrl_PLL.ref=0.0;//control Vq=>0
Ctrl_PLL.fbk=uq_in;// Input: feedback
Ctrl_PLL.Kp=Kp_PLL;// Parameter: proportional loop gain
Ctrl_PLL.Ki=Ki_PLL;// Parameter: integral gain
Ctrl_PLL.Kb=Kb_PLL;// Parameter: anti-windup back-calculation gain
Ctrl_PLL.Umax=0.2*WB;// Parameter: upper saturation limit
Ctrl_PLL.Umin=-0.2*WB;// Parameter: lower saturation limit
PI_BC_MACRO(Ctrl_PLL);
uc_PLL=Ctrl_PLL.out;
we=WB-uc_PLL;
theta_Vin_PLL=theta_Vin_PLL+we*period;
if(theta_Vin_PLL>=PI2) theta_Vin_PLL=theta_Vin_PLL-PI2;
else if (theta_Vin_PLL<0.0) theta_Vin_PLL=theta_Vin_PLL+PI2;
/*

//-----Calculate Electromagnetic torque-----

Te=1.5*Pp*(FLUXM*iq+(Ld-Lq)*id*iq);

//-----MTPA trajectory-----

id_max=FLUXM/4.0/(Lq-Ld)-sqrt(FLUXM*FLUXM/16.0/(Lq-Ld)/(Lq-Ld)+Iam*Iam/2.0);

```

Appendix G: Experimental setup

```

iq_max=sqrt(Iam*Iam-id_max*id_max);

//-----PI Vdc Controller-----

Ctrl_Vdc.ref=Vdc_ref;// Input: reference set-point
Ctrl_Vdc.fbk=Vdc1;// Input: feedback
Ctrl_Vdc.Kp=Kp_Vdc;// Parameter: proportional loop gain
Ctrl_Vdc.Ki=Ki_Vdc;// Parameter: integral gain
Ctrl_Vdc.Kb=Kb_Vdc;// Parameter: anti-windup back-calculation gain
Ctrl_Vdc.Umax=iq_max*100;// Parameter: upper saturation limit
Ctrl_Vdc.Umin=-iq_max*100;// Parameter: lower saturation limit
PI_BC_MACRO(Ctrl_Vdc);

iq_ref=-Ctrl_Vdc.out/100;

//-----PI Current(iq) Controllers-----

Pulse_iq.frq=iq_ref_freq;
Pulse_iq.amp=iq_ref_amp;
Pulse_iq ofs=iq_ref_ofs;
Pulse_iq.dut=iq_ref_dut;
PulseGen_MACRO(Pulse_iq);
Ctrl_iq.ref=iq_ref;// Input: reference set-point
Ctrl_iq.fbk=iq; // Input: feedback
Ctrl_iq.Kb=Kb_iq;// Parameter: anti-windup back-calculation gain
Ctrl_iq.Umax=V_DC;// Parameter: upper saturation limit
Ctrl_iq.Umin=-V_DC;// Parameter: lower saturation limit
Ctrl_iq.Ki=Ki_iq;
Ctrl_iq.Kp=Kp_iq;
PI_BC_MACRO(Ctrl_iq);
uc_iq=Ctrl_iq.out;

//-----PI Current(id) Controllers-----
//MTPA trajectory
id_ref=FLUXM/2.0/(Lq-Ld)-sqrt(iq_ref*iq_ref+FLUXM*FLUXM/4.0/(Lq-Ld)/(Lq-Ld));

if (id_ref <= id_max) id_ref = id_max;//id_max is negative

Ctrl_id.ref=id_ref;// Input: reference set-point
Ctrl_id.fbk=id;// Input: feedback
Ctrl_id.Kp=Kp_id;// Parameter: proportional loop gain
Ctrl_id.Ki=Ki_id;// Parameter: integral gain
Ctrl_id.Kb=Kb_id;// Parameter: anti-windup back-calculation gain
Ctrl_id.Umax=V_DC;// Parameter: upper saturation limit
Ctrl_id.Umin=-V_DC;// Parameter: lower saturation limit
PI_BC_MACRO(Ctrl_id);
uc_id=Ctrl_id.out;

//-----Decoupling-----

Ud_ref=uc_id-Pp*wm_inc_lpf*Lq*iq;
Uq_ref=uc_iq+Pp*wm_inc_lpf*(FLUXM+Ld*id);
Ua1_ref=Ud_ref*cos(theta_re_est)-Uq_ref*sin(theta_re_est);
Ube_ref=Ud_ref*sin(theta_re_est)+Uq_ref*cos(theta_re_est);

//----- Output Voltage Limit-----

Vomax=U_MAX_LINE*sqrt(1.0/3.0);//Vomax is max phase peak
if(0.866*V_DC<Vomax)Vomax=0.866*V_DC*0.95;
Vo_mag=sqrt(Ua1_ref*Ua1_ref+Ube_ref*Ube_ref);//the magnitude of output voltage vector
if(Vo_mag>=Vomax)
{
Ua1_ref=Vomax*Ua1_ref/Vo_mag;
Ube_ref=Vomax*Ube_ref/Vo_mag;
Vo_mag=Vomax;
}
m=SQRT3*Vo_mag/(1.5*V_DC);
theta_Vo=atan2(Ube_ref,Ua1_ref);//[-PI,PI)
if (theta_Vo<0.0) theta_Vo=theta_Vo+PI2;//[0,2PI)
if(theta_Vo>=0.0 && theta_Vo<PI_3)
{
sector=1;//V0(000),V1(100),V2(110),V7(111)
d1=m*sin(PI_3-theta_Vo);
d2=m*sin(theta_Vo);
d0=1.0-d1-d2;
duty[0]=1.0-0.5*d0;//V1(100),V2(110),V7(111)
duty[1]=d2+0.5*d0;//V2(110),V7(111)
duty[2]=0.5*d0;//V7(111)
}
else if(theta_Vo>=PI_3 && theta_Vo<PI2_3)
{
sector=2;//V0(000),V3(010),V2(110),V7(111)
theta_Vo=theta_Vo-PI_3;
d1=m*sin(PI_3-theta_Vo);

```

Appendix G: Experimental setup

```

d2=m*sin(theta_Vo);
d0=1.0-d1-d2;
duty[0]=d1+d0*0.5;//V2(110),V7(111)
duty[1]=1.0-0.5*d0;//V3(010),V2(110),V7(111)
duty[2]=0.5*d0;//V7(111)
}
else if(theta_Vo>=PI2_3 && theta_Vo<PI)
{
sector=3;//V0(000),V3(010),V4(011),V7(111)
theta_Vo=theta_Vo-PI2_3;
d1=m*sin(PI_3-theta_Vo);
d2=m*sin(theta_Vo);
d0=1.0-d1-d2;
duty[0]=d0*0.5;//V7(111)
duty[1]=1.0-0.5*d0;//V3(010),V4(011),V7(111)
duty[2]=d2+0.5*d0;//V3(011),V7(111)
}
else if(theta_Vo>=PI && theta_Vo<PI4_3)
{
sector=4;//V0(000),V5(001),V4(011),V7(111)
theta_Vo=theta_Vo-PI;
d1=m*sin(PI_3-theta_Vo);
d2=m*sin(theta_Vo);
d0=1.0-d1-d2;
duty[0]=d0*0.5;//V7(111)
duty[1]=d1+0.5*d0;//V3(011),V7(111)
duty[2]=1.0-0.5*d0;//V5(001),V4(011),V7(111)
}
else if(theta_Vo>=PI4_3 && theta_Vo<PI5_3)
{
sector=5;//V0(000),V5(001),V6(101),V7(111)
theta_Vo=theta_Vo-PI4_3;
d1=m*sin(PI_3-theta_Vo);
d2=m*sin(theta_Vo);
d0=1.0-d1-d2;
duty[0]=d2+d0*0.5;//V6(101),V7(111)
duty[1]=0.5*d0;//V7(111)
duty[2]=1.0-0.5*d0;//V5(001),V6(101),V7(111)
}
else
{
sector=6;//V0(000),V1(100),V6(101),V7(111)
theta_Vo=theta_Vo-PI5_3;
d1=m*sin(PI_3-theta_Vo);
d2=m*sin(theta_Vo);
d0=1.0-d1-d2;
duty[0]=1-d0*0.5;//V1(100),V6(101),V7(111)
duty[1]=0.5*d0;//V7(111)
duty[2]=d1+0.5*d0;//V6(101),V7(111)
}
}

/* set DACH1 to ia */
ds1104_dac_write(3,sp_ref/10);
ds1104_dac_write(2,uca_in/5000);
/* activate the previously written DAC values synchronously */
ds1104_dac_strobe();

/*duty[0,1,2]=duty[4,5,6]*/
duty[4]=duty[0];
duty[5]=duty[1];
duty[6]=duty[2];
duty[0]=duty[3];//chopper SPWM1

/* write PWM Duty cycle to slave DSP and test for error */
ds1104_slave_dsp_pwm_duty_write(task_id, ch2_index, duty[4]);
ds1104_slave_dsp_pwm_duty_write(task_id, ch3_index, duty[5]);
ds1104_slave_dsp_pwm_duty_write(task_id, ch4_index, duty[6]);

/* write PWM3 Duty cycle to slave DSP and test for error */
ds1104_slave_dsp_pwm3_duty_write(task_id, index, duty[0], duty[1], duty[2]);

exec_time =RTLIB_TIC_READ();
}

main()
{
init();

/*initial the master-slave communication*/
ds1104_slave_dsp_communication_init();

ds1104_bit_io_init(DS1104_DIO0_OUT);

```

Appendix G: Experimental setup

```
varinit();

/* init D/A converter in latched mode */
ds1104_dac_init(DS1104_DACMODE_LATCHED);

/*init incremental encoder channel 1*/
ds1104_inc_init(1, DS1104_INC_MODE_RS422);
ds1104_inc_set_idxmode(1, DS1104_INC_IDXMODE_ON); //DS1104_INC_IDXMODE_ON);

ds1104_syncout_edge_setup(DS1104_SYNC_TRIGGER_FALLING);
ds1104_inc_trigger_setup(1,DS1104_TRIGGER_ENABLE);
ds1104_dac_trigger_setup(DS1104_TRIGGER_ENABLE);
ds1104_adc_trigger_setup(2,DS1104_TRIGGER_ENABLE);
ds1104_adc_trigger_setup(3,DS1104_TRIGGER_ENABLE);
ds1104_adc_trigger_setup(4,DS1104_TRIGGER_ENABLE);
ds1104_adc_trigger_setup(5,DS1104_TRIGGER_ENABLE);
ds1104_syncin_trigger();

/* init and start of 3-phase PWM generation on slave DSP */
ds1104_slave_dsp_pwm3_init(task_id, period,duty[0], duty[1], duty[2],deadband, sync_pos);
ds1104_slave_dsp_pwm3_start(task_id);

/* registration of PWM duty cycle update command */
ds1104_slave_dsp_pwm3_duty_write_register(task_id, &index);

/* initialization of PWM generation on slave DSP */
ds1104_slave_dsp_pwm_init(task_id, period, 0.5, mode, pol,
                          SLVDSP1104_PWM_CH2_MSK |
                          SLVDSP1104_PWM_CH3_MSK |
                          SLVDSP1104_PWM_CH4_MSK);

/* start of PWM generation on slave DSP */
ds1104_slave_dsp_pwm_start(task_id,
                           SLVDSP1104_PWM_CH2_MSK |
                           SLVDSP1104_PWM_CH3_MSK |
                           SLVDSP1104_PWM_CH4_MSK);

/* registration of PWM duty cycle update commands */
/* channel 2 */
ds1104_slave_dsp_pwm_duty_write_register(task_id, &ch2_index, 2);

/* channel 3 */
ds1104_slave_dsp_pwm_duty_write_register(task_id, &ch3_index, 3);

/* channel 4 */
ds1104_slave_dsp_pwm_duty_write_register(task_id, &ch4_index, 4);

/* initialization of PWM sync interrupt */
ds1104_set_interrupt_vector(DS1104_INT_SLAVE_DSP_PWM, (DS1104_Int_Handler_Type)
&PWM_sync_interrupt,SAVE_REGS_ON);
ds1104_enable_hardware_int(DS1104_INT_SLAVE_DSP_PWM);
RTLIB_INT_ENABLE();

/* Background tasks */
while(1)
{
RTLIB_BACKGROUND_SERVICE(); /* background service */
}
}

*****                                     END                                     *****
```

G.6 3-phase IGBT inverter

Fig.G. 6 shows the back-to-back 3-phase IGBT inverter which during the experiment is connected to the FSCW IPMM-F. The circuit diagrams of the 3-phase IGBT inverter are provided in Fig.G. 7 and Fig.G. 8.

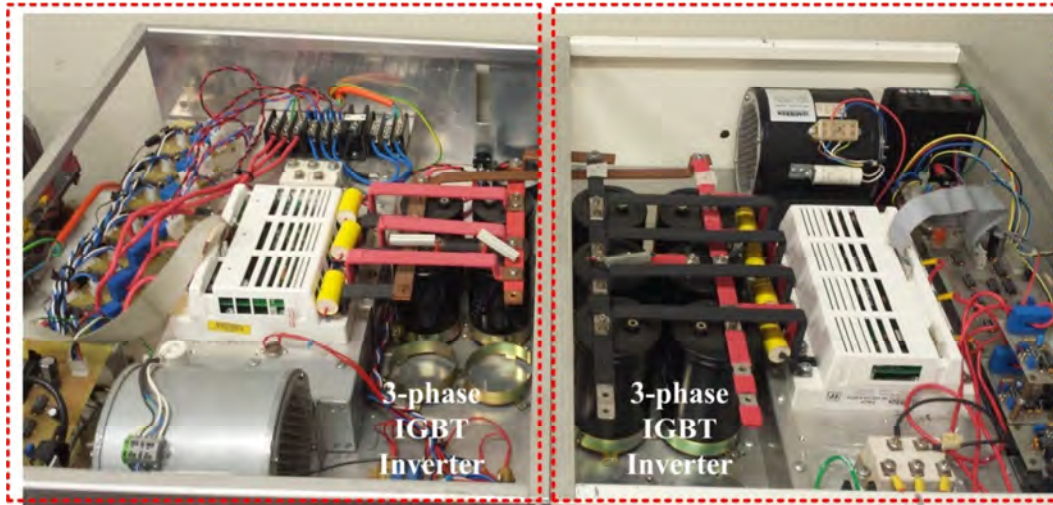


Fig.G. 6. Back-to-Back 3-phase IGBT inverter (casing off)

Appendix G: Experimental setup

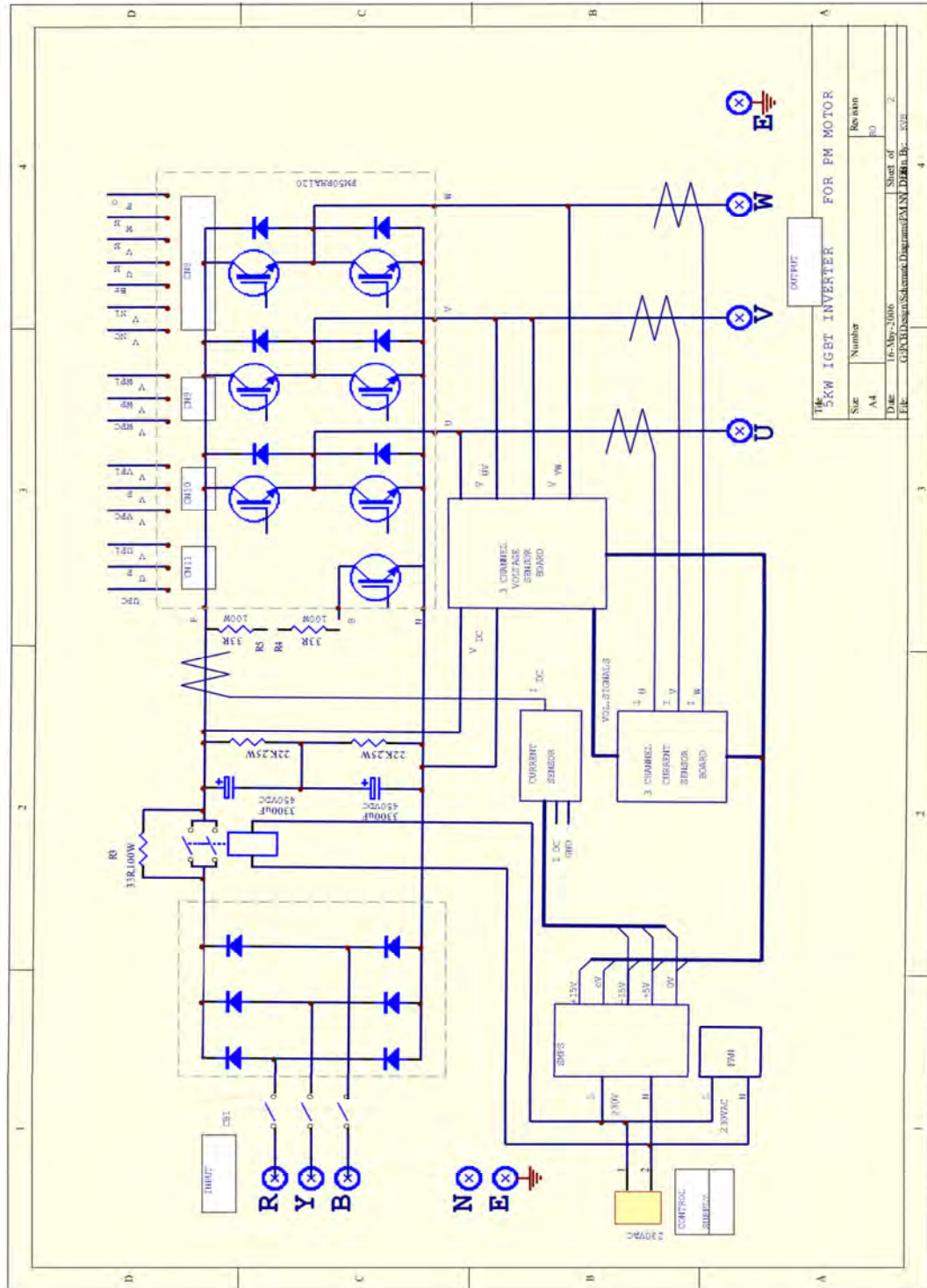


Fig.G. 7. IGBT inverter schematic

Appendix G: Experimental setup

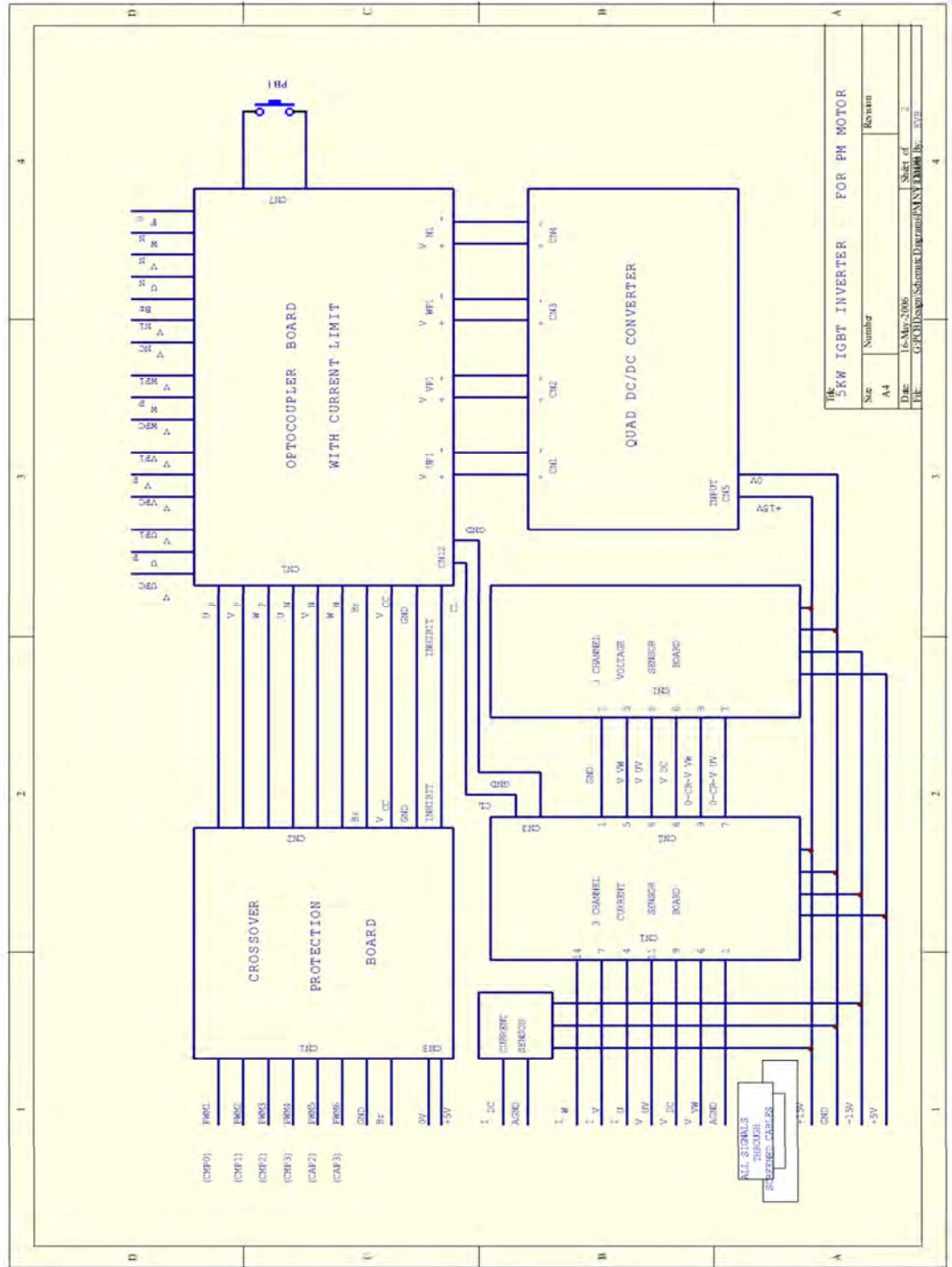


Fig.G. 8. Interconnection between the IGBT inverter and the control boards

Appendix H: Publication list

Journal Publications:

- [1] K. Ahsanullah, R. Dutta, M.F. Rahman, "Preliminary Design Analysis of Low Speed Interior Permanent Magnet Machine with Distributed and Concentrated Windings " ,Journal of International Conference on Electrical Machines and Systems, vol.2 , no.2 , pp. 139-147, 2014 .

Conference Publications:

- [2] K. Ahsanullah, R. Dutta, and M. F. Rahman, "Review of PM generator designs for direct-drive wind turbines," in 22nd Australasian Universities Power Engineering Conference (AUPEC), 2012, Indonesia. ISBN: 978-1-4673-2933-0
- [3] K. Ahsanullah, R. Dutta, J. Fletcher, and M. F. Rahman, "Design of an interior permanent magnet synchronous machine suitable for direct drive wind turbine," in 2nd IET Renewable Power Generation Conference (RPG 2013), 2013, China. ISBN: 978-1-84919-758-8
- [4] K. Ahsanullah, R. Dutta, and M. F. Rahman, "Investigation of flat and V-shaped magnets in interior permanent magnet machine for direct drive wind turbine application," in proc. IEEE Int. Conf. Energy Conversion Congress & Expo (ECCE) Asia Down under (ECCE Asia), 2013, Australia. ISBN: 978-1-4799-0483-9
- [6] K. Ahsanullah and J. Ravishankar, "Fault ride-through of doubly-fed induction generators," in International Conference on Power, Signals, Controls and Computation (EPSCICON), 2012, India. ISBN: 978-1-4673-0446-7
- [7] K. Ahsanullah, R. Dutta, and M. F. Rahman, "Distributed and concentrated winding Interior PM Synchronous Machine (IPMSM) for direct drive wind turbine," in 39th Annual Conference of the IEEE Industrial Electronics Society, IECON 2013, Austria.
- [8] K. Ahsanullah, R. Dutta, and M. F. Rahman, "Design of a 4KW interior permanent magnet machine suitable for low speed application," in IEEE Int. Conf. on Electrical Machines and Systems (ICEMS), 2013, South Korea. ISBN: 978-1-4799-1446-3
- [9] M. Farshadnia, R. Dutta, J. E. Fletcher, K. Ahsanullah, M. F. Rahman, and H. C. Lovatt, "Analysis of MMF and back-EMF waveforms for fractional-slot concentrated-wound permanent magnet machines," in proc. IEEE Int. Conf. on Electrical Machines (ICEM), 2014, Germany.